

Copyright

by

Eric Richard Weeks

1997

**Experimental Studies of Anomalous Diffusion, Blocking  
Phenomena, and Two-Dimensional Turbulence**

by

**Eric Richard Weeks, B.S.**

**Dissertation**

Presented to the Faculty of the Graduate School of

The University of Texas at Austin

in Partial Fulfillment

of the Requirements

for the Degree of

**Doctor of Philosophy**

**The University of Texas at Austin**

December 1997

**Experimental Studies of Anomalous Diffusion, Blocking  
Phenomena, and Two-Dimensional Turbulence**

**Approved by  
Dissertation Committee:**

---

---

---

---

---

---

For my parents, Richard and MaryBeth Weeks.

# Acknowledgments

First and foremost, thanks to Harry Swinney for being an outstanding advisor and mentor. His enthusiasm, insight, support, and sense of humor made my five and a half years here extremely enjoyable and productive. Much of the impact of this dissertation stems from Harry's ability to choose excellent problems to study. I also thank him for allowing me the time to pursue side projects such as Refs. [156, 162], as well as writing a laboratory manual for Physical Science 303.

Tom Solomon and Jeff Urbach were also valuable mentors, and they taught me most of what I know about experimental techniques. Tom Solomon also exposed me to *awk*, aiding with the data analysis used in Chap. 4, and the public domain graphics package “GLE” which was used to produce nearly all of the figures in this dissertation. Two additional experimental collaborators are Charles Baroud and Brendan Plapp; thanks for being hard-working and cheerful companions. Yudong Tian provided invaluable assistance for the topography experiments. Eshel Faraggi did excellent work improving our hot film system. Essential assistance in writing data acquisition software was provided by Muhammad Shazad Pervez and Muhammad Ali Bawany.

It was very beneficial to me when I started as a graduate student to “inherit” this experiment from previous workers. I would like to acknowledge the previous workers who designed, built, and improved this experiment: Joel Sommeria, Steve Meyers, Bob Behringer, Tom Solomon, and Bill Holloway. Thanks also to Les

Deavers, Dan Boyd, Jim Pinget, and others working in the machine shop for helping me continue to improve the experiment.

Several people contributed in less direct ways to the success of my work. Thanks to Diego del-Castillo-Negrete for teaching me Hamiltonian theory and some geophysics. Thanks to Michael Ghil for motivating and assisting with the topography work, and thanks to Kayo Ide for assisting with that work and answering my many questions about geophysics. Figure 5.3 is due to Graham Carey, who taught me least-squares fitting, and Mike Marder, who encouraged me to learn PostScript. The work of Chaps. 3 and 4 benefitted by discussions with Joseph Klafter, Michael Shlesinger, Gert Zumofen, George Zaslavsky, Ed Ott, Shankar Venkataramani, Ray Goldstein, and John Lowenstein; a special thanks to the first three for writing a Physics Today article mentioning my work [68]. Discussions with Lee Panetta greatly improved my understanding of the work done in Chap. 5 and geophysics in general.

Thanks to Scott Franklin and Steve Van Hook for endless discussions over lunch, including much advice and support for my experimental problems. Thanks also to John Burgess for good discussions and a fun collaboration. Helpful advice was provided by Josef Kas, Bill McCormick, Phil Morrison, Mike Marder, and Misha Vishik. I greatly appreciate the interactions I had with everybody at the Center for Nonlinear Dynamics; especially I thank the people who taught me various experimental techniques: Alexei Predtechensky, Paul Umbanhowar, and Greg Lewis. Thanks to everybody who lent a hand lifting heavy equipment. Thanks to Dorothy Featherling and Theresa Hancock for much patience and help with paperwork.

Finally, a big thanks to everybody who helped with their encouragement and friendship. There are too many of these people to list everyone, but a special thanks goes to Linas Buntinas, John Burgess, Scott and Merrie Franklin, Jenny Lew, Jill Polites, Steve and Jenny Van Hook, and Dan Young. Thanks to Theresa

Hancock for providing her support, encouragement, friendship, and for getting me to leave the lab now and then. And most importantly, thanks to my parents for their encouragement of my pursuit of physics,

Financial support for this research was provided by the Office of Naval Research Grant N00014-89-J-1495, a Department of Education Fellowship, a University of Texas Livingston Fellowship, and an Office of Naval Research Augmentation Award for Science and Engineering Training.

ERIC RICHARD WEEKS

*The University of Texas at Austin*

*December 1997*

# Experimental Studies of Anomalous Diffusion, Blocking Phenomena, and Two-Dimensional Turbulence

Publication No. \_\_\_\_\_

Eric Richard Weeks, Ph.D.  
The University of Texas at Austin, 1997

Supervisor: Harry L. Swinney

We study three problems which have been studied theoretically, but problems for which little or no experimental work has been done: anomalous diffusion leading to enhanced mixing, dynamics of atmospheric blocking patterns, and two-dimensional turbulence. Our experimental apparatus is a 1 m diameter rapidly rotating annular tank filled with fluid. The Coriolis force constrains the fluid flow inside the tank to be nearly two-dimensional.

The first problem studied is mixing in a simple flow. Usually, mixing is describable by diffusion: dye in fluid spreads, with the typical size of the dye spot growing as  $\sim (Dt)^{1/2}$  with diffusion constant  $D$ . We examine flows with jets carrying tracer particles long distances. Ensembles of tracer particles grow in size as  $\sim t^h$  with  $h > 1/2$  ( $D = \infty$ ). In our experiments, this anomalous diffusion is due to Lévy flights: the mean square time spent in a jet before being trapped in a vortex is infinite. This is the first direct experimental observation of Lévy flights. Our experiments suggest that jet structures in general may lead to anomalous diffusion.



We also study a model which determines circumstances which produce anomalous diffusion.

The origin of atmospheric blocking in the Northern Hemisphere is our second problem. Normally mid-latitude weather is determined by the zonal flow of the jet stream, but several times each winter this flow is diverted poleward by a blocking vortex, which lasts several weeks. Models have proposed that blocking patterns are due to interactions of the zonal flow with the Rockies and Alps. We place two ridges on the bottom of our tank; by forcing a zonal flow across the ridges we observe blocking and zonal patterns. These are the first experimental observations of such patterns. The experiments also find a broad parameter range for which the flow intermittently switches between zonal and blocked, as is observed for the atmosphere.

The interaction between two-dimensional (2D) and three-dimensional (3D) turbulence is our third problem. Rotating 2D turbulence is especially relevant to geophysical flows, but remains largely unexamined by experiments. The possibility of studying the transition from 2D to 3D turbulence in our apparatus is examined.

# Contents

|  |             |
|--|-------------|
| <b>Acknowledgments</b>   | <b>v</b>    |
| <b>Abstract</b>  | <b>viii</b> |
| <b>List of Tables</b>  | <b>xiv</b>  |
| <b>List of Figures</b>   | <b>xv</b>   |
| <b>Chapter 1 Introduction</b>                                      | <b>1</b>    |
| 1.1 Motivation . . . . .   | 1           |
| 1.2 Quasi-geostrophic flow . . . . .                               | 4           |
| 1.2.1 Equations of motion . . . . .                                | 5           |
| 1.2.2 Geostrophic Limit . . . . .                                  | 7           |
| 1.2.3 Ekman layers . . . . .                                       | 8           |
| 1.2.4 The Stream Function . . . . .                                | 9           |
| 1.2.5 Potential vorticity . . . . .                                | 10          |
| 1.2.6 Relation between topography and spherical geometry . . . . . | 12          |
| 1.2.7 Free surface effects . . . . .                               | 14          |
| 1.2.8 Axisymmetric flow in the experiment . . . . .                | 15          |
| 1.3 Previous experiments . . . . .                                 | 15          |

|                  |  |           |
|------------------|--|-----------|
| <b>Chapter 2</b> | <b>Experimental Apparatus and Procedures</b>             | <b>18</b> |
| 2.1              | Rotating tank . . . . .                                  | 18        |
| 2.2              | Particle tracking system . . . . .                       | 22        |
| 2.3              | Particles as passive tracers . . . . .                   | 26        |
| 2.4              | Calculating Stream Functions . . . . .                   | 32        |
| 2.4.1            | Basis Functions . . . . .                                | 32        |
| 2.4.2            | Least Squares Analysis . . . . .                         | 35        |
| 2.4.3            | Preprocessing of Data . . . . .                          | 36        |
| 2.4.4            | No-slip boundary condition . . . . .                     | 38        |
| 2.5              | Hot film probes . . . . .                                | 39        |
| 2.6              | Ultrasound probe . . . . .                               | 42        |
| 2.6.1            | Ultrasound hardware . . . . .                            | 42        |
| 2.6.2            | Ultrasound software . . . . .                            | 44        |
| 2.6.3            | Choosing parameters . . . . .                            | 47        |
| 2.6.4            | Clock signal box . . . . .                               | 49        |
| 2.6.5            | Additional considerations . . . . .                      | 51        |
| 2.7              | Temperature control . . . . .                            | 51        |
| 2.8              | Flow meter . . . . .                                     | 53        |
| 2.9              | Pressure sensor . . . . .                                | 57        |
| 2.10             | Achieving high rotation rates . . . . .                  | 57        |
| <b>Chapter 3</b> | <b>Theory of Random Walks</b>                            | <b>61</b> |
| 3.1              | Introduction to Random Walks . . . . .                   | 61        |
| 3.2              | Random Walks in Experiments . . . . .                    | 65        |
| 3.3              | Higher dimensions . . . . .                              | 66        |
| 3.4              | Previous Theoretical Work . . . . .                      | 67        |
| 3.5              | A model for asymmetric random walks . . . . .            | 70        |
| 3.6              | Results: symmetric and asymmetric random walks . . . . . | 73        |

|   |  |            |
|---|--|------------|
| 3.7   | Strongly Asymmetric Random Walks . . . . .         | 78         |
| 3.7.1   | Model . . . . .                                    | 80         |
| 3.7.2   | Results . . . . .                                  | 81         |
| 3.8   | Discussion . . . . .                               | 86         |
| 3.8.1   | Exponential PDFs . . . . .                         | 86         |
| 3.8.2   | Correlated Random Walks . . . . .                  | 88         |
| 3.8.3   | Higher order terms . . . . .                       | 88         |
| 3.8.4   | Conclusions . . . . .                              | 89         |
| <b>Chapter 4 Random Walks in Experiments</b>                  |  | <b>91</b>  |
| 4.1   | Motivation . . . . .                               | 91         |
| 4.2   | Flows Studied . . . . .                            | 93         |
| 4.3   | Analysis techniques . . . . .                      | 99         |
| 4.4   | Results . . . . .                                  | 103        |
| 4.4.1   | Time-independent flow: no chaotic mixing . . . . . | 103        |
| 4.4.2   | Time-periodic flows: power law flights . . . . .   | 104        |
| 4.4.3   | Chaotic flows . . . . .                            | 116        |
| 4.4.4   | Weakly turbulent flow: no long flights . . . . .   | 123        |
| 4.5   | Discussion . . . . .                               | 126        |
| <b>Chapter 5 Interaction of Eastward Jets with Topography</b> |  | <b>129</b> |
| 5.1   | Atmospheric Observations of Blocking . . . . .     | 129        |
| 5.2   | Models of Blocking . . . . .                       | 132        |
| 5.3   | Previous Experiments . . . . .                     | 134        |
| 5.4   | Experimental Observations . . . . .                | 134        |
| 5.4.1   | Apparatus . . . . .                                | 135        |
| 5.4.2   | Results . . . . .                                  | 138        |
| 5.4.3   | Symmetry of Flow Patterns . . . . .                | 148        |

|  |   |            |
|--|---|------------|
| 5.5  | Conclusions . . . . .                       | 152        |
| <b>Chapter 6 Two-Dimensional Turbulence</b>      |   | <b>154</b> |
| 6.1  | Introduction . . . . .                      | 154        |
| 6.2  | Considerations for our experiment . . . . . | 158        |
| 6.3  | Previous Experiments . . . . .              | 167        |
| 6.4  | Experiments . . . . .                       | 168        |
| <b>Appendix A Random Walk Second Order terms</b> |   | <b>171</b> |
| A.1  | Notation . . . . .                          | 171        |
| A.2  | Second order terms . . . . .                | 171        |
| <b>Appendix B Software documentation</b>         |   | <b>177</b> |
| B.1  | Ultrasound Data Acquisition . . . . .       | 177        |
|  | B.1.1 Matec controller software . . . . .   | 177        |
|  | B.1.2 Data acquisition software . . . . .   | 179        |
| B.2  | Hot Film Probe Data Acquisition . . . . .   | 181        |
| B.3  | Stream Function Programs . . . . .          | 184        |
| <b>Bibliography</b>                              |   | <b>192</b> |
| <b>Vita</b>                                      |   | <b>209</b> |

# List of Tables

|     |   |     |
|-----|---|-----|
| 2.1 | Definition of symbols used in Sec. 2.3 [39]. . . . .  | 27  |
| 3.1 | List of common symbols used in Sec. 3.6. . . . .  | 73  |
| 3.2 | Anomalous diffusion results for symmetric random walks. . . . .                                 | 75  |
| 3.3 | Scaling of the mean position for asymmetric random walks. . . . .                               | 78  |
| 3.4 | Anomalous diffusion results for asymmetric random walks. . . . .                                | 79  |
| 3.5 | Scaling of the mean position for strongly asymmetric random walks. . . . .                      | 83  |
| 3.6 | Anomalous diffusion results for strongly asymmetric random walks. . . . .                       | 85  |
| 4.1 | Summary of conditions for transport experiments. . . . .  | 101 |
| 4.2 | Results for all transport experiments. . . . .  | 127 |
| A.1 | List of common symbols used in this appendix. . . . .   | 172 |
| A.2 | Scaling of the mean position for asymmetric random walks: first and second order terms. . . . . | 174 |
| A.3 | Anomalous diffusion results for symmetric random walks: first and second order terms. . . . .   | 175 |
| A.4 | Anomalous diffusion results for asymmetric random walks: first and second order terms. . . . .  | 176 |

# List of Figures

|      |   |    |
|------|---|----|
| 1.1  | Tracer trajectory in seven vortex flow. . . . .                               | 2  |
| 1.2  | Blocked flow in atmosphere and experiment. . . . .                            | 3  |
| 2.1  | Schematic diagram of rotating annulus. . . . .                                | 19 |
| 2.2  | Two atypical particle trajectories. . . . .                                   | 25 |
| 2.3  | Azimuthal velocity at annulus walls. . . . .                                  | 38 |
| 2.4  | Schematic diagram of multiplexed hot film probe system. . . . .               | 41 |
| 2.5  | Schematic of ultrasound pulses from Matec box. . . . .                        | 44 |
| 2.6  | Ultrasound pulses reflected from buffer rod. . . . .                          | 46 |
| 2.7  | Ultrasound reflections from a particle. . . . .                               | 48 |
| 2.8  | Clock signal box operation. . . . .   | 50 |
| 2.9  | Flow rate before and after active control installed. . . . .                  | 55 |
| 2.10 | Accelerometer data used to balance the annulus. . . . .                       | 60 |
| 3.1  | Examples of a normal and anomalous random walk. . . . .                       | 63 |
| 3.2  | Phase diagrams for variance of symmetric and asymmetric random walks. . . . . | 76 |
| 3.3  | Phase diagram for the variance of strongly asymmetric random walks. . . . .   | 84 |
| 3.4  | Example showing approach to asymptotic behavior of the variance. . . . .      | 89 |

|      |   |     |
|------|---|-----|
| 4.1  | Phase space portraits for time-independent and time-dependent Hamiltonians. . . . . | 92  |
| 4.2  | Velocity time series and power spectra for six flows. . . . .                       | 95  |
| 4.3  | Seven vortex flow shown by many particle trajectories. . . . .                      | 96  |
| 4.4  | Four vortex flow shown by many particle trajectories. . . . .                       | 98  |
| 4.5  | Two trajectories for the weakly turbulent flow. . . . .                             | 100 |
| 4.6  | Particle trajectories for the time-independent flow. . . . .                        | 105 |
| 4.7  | Particle trajectories for the six-vortex flow. . . . .                              | 106 |
| 4.8  | $\theta(t)$ for Fig. 4.7. . . . .   | 108 |
| 4.9  | Plot related to the velocity profile of a vortex. . . . .                           | 109 |
| 4.10 | $\Delta\theta$ versus $\Delta t$ for particle flights. . . . .                      | 110 |
| 4.11 | Flight and sticking PDFs for seven-vortex flow. . . . .                             | 112 |
| 4.12 | Variance $\sigma^2(t)$ for the seven-vortex flow. . . . .                           | 113 |
| 4.13 | Flight and sticking PDFs for the six-vortex flow. . . . .                           | 114 |
| 4.14 | Variance $\sigma^2(t)$ for the six-vortex flow. . . . .                             | 115 |
| 4.15 | Particle trajectories for the four-vortex flow. . . . .                             | 116 |
| 4.16 | $\theta(t)$ corresponding to Fig. 4.15. . . . .                                     | 118 |
| 4.17 | Flight and sticking PDFs for the five-vortex flow. . . . .                          | 119 |
| 4.18 | Variance $\sigma^2(t)$ for the five-vortex flow. . . . .                            | 120 |
| 4.19 | Flight and sticking PDFs for the four-vortex flow. . . . .                          | 121 |
| 4.20 | Variance $\sigma^2(t)$ for the four-vortex flow. . . . .                            | 122 |
| 4.21 | Mean particle position for the four-vortex flow. . . . .                            | 123 |
| 4.22 | $\theta(t)$ corresponding to Fig. 4.5. . . . .                                      | 124 |
| 4.23 | PDF for the turbulent flow. . . . .   | 125 |
| 4.24 | Variance $\sigma^2(t)$ for the weakly turbulent flow. . . . .                       | 126 |
| 5.1  | Atmospheric pictures of blocked and zonal flow. . . . .                             | 130 |
| 5.2  | Bottom topography placed in the rotating annulus. . . . .                           | 135 |



|      |  |     |
|------|--|-----|
| 5.3  | Experimental streamfunctions showing blocked and zonal flow. . . .                               | 139 |
| 5.4  | Azimuthally averaged azimuthal velocity profile for blocked and zonal<br>flow. . . . .           | 141 |
| 5.5  | Azimuthal velocity profile relative to center of jet for blocked and<br>zonal flow. . . . .      | 142 |
| 5.6  | Streak photographs for zonal flow. . . . .   | 143 |
| 5.7  | Streak photographs for blocked flow at low forcing. . . . .                                      | 144 |
| 5.8  | Streak photographs for blocked flow for high forcing. . . . .                                    | 145 |
| 5.9  | Velocity time-series and power spectra for blocked and zonal flows. .                            | 146 |
| 5.10 | Velocity time series for several values of $Ro$ . . . . .  | 147 |
| 5.11 | Experimental phase diagram for flows over topography. . . . .                                    | 149 |
| 5.12 | Velocity time series showing intermittent transitions between blocked<br>and zonal flow. . . . . | 150 |
| 6.1  | Theoretical energy spectrum for 2D turbulence. . . . .   | 156 |
| 6.2  | $L$ and $U$ for turbulence experiments. . . . .  | 160 |
| 6.3  | $Ro$ and $Re$ for turbulence experiments. . . . .  | 161 |
| 6.4  | $Ek$ and $\tau_E$ for turbulence experiments. . . . .  | 162 |
| 6.5  | Length scales for turbulence experiment, logarithmic scale. . . . .                              | 164 |
| 6.6  | Length scales for turbulence experiment, linear scale. . . . .                                   | 165 |
| 6.7  | Dissipation rates for turbulence experiments. . . . .  | 166 |
| A.1  | Phase diagram for the tables in this appendix. . . . .   | 173 |
| B.1  | Schematic view of ultrasound pulses generated by Matec system. . .                               | 178 |
| B.2  | Partitioning scheme for the program <b>amp2con</b> . . . . .                                     | 187 |
| B.3  | Azimuthal velocity at annulus walls. . . . .   | 191 |

# Chapter 1

## Introduction

### 1.1 Motivation

This dissertation discusses three sets of experiments done in a rotating annulus experiment. The apparatus is a large 86 cm diameter rotating annular tank filled with 100 L of fluid. Despite the large size, this tank can be rotated at speeds up to 4 Hz ( $8\pi$  rad/s), thus allowing us to conduct unique, quasi-two-dimensional experiments: for rapid rotation, the fluid is constrained to move in the plane perpendicular to the rotation axis (see Sec. 1.2.2). We exploit this two-dimensionality to examine three distinct problems.

1. *Transport and Mixing:* Mixing in the atmosphere and ocean is an important question: mixing of ozone, heat, moisture have meteorological significance, and quantities such as heat, salinity, and oil spills mix in the ocean. Because of the two-dimensionality of the fluid motion, it is easy to visualize flow in the annulus via a camera co-rotating above the experiment, allowing us to conduct in-depth studies of mixing in a simplified laboratory system.

A novel long-term tracking technique has been developed by Pervez and Solomon ([104]) for use with this experiment, allowing individual tracer particles

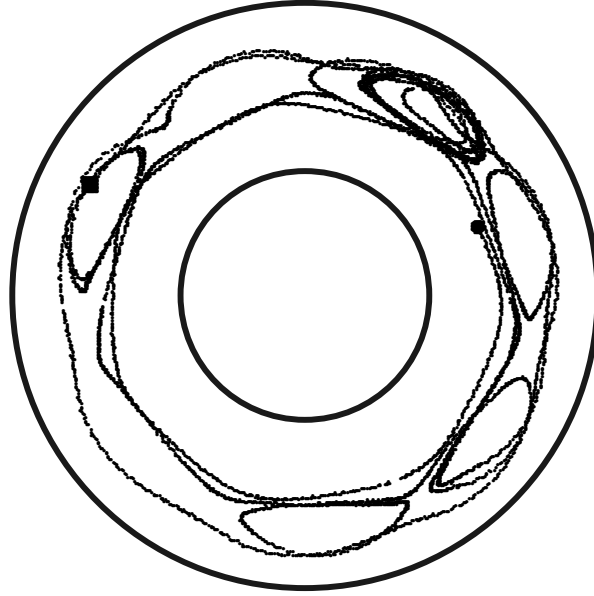


Figure 1.1: Trajectory of a tracer particle in the rotating annulus experiment, showing seven vortices of the same sign sandwiched between two jets (in opposite directions). The particle moves randomly between vortices and the jets; see Chap. 4 for more details. The beginning of the trajectory is marked with a square, the end with a circle.

to be followed for long periods of time (typically up to  $\sim 3000$  rotation periods of the annulus, or  $\sim 100$  vortex turnover times). This long-term tracking of individual tracers allows us to examine the mixing of various flows (see Fig. 1.1). This is one of the first few experiments to examine many particle trajectories for long times, and the first which directly observes *Lévy flights*: random walks where tracer particles move azimuthally for random times before changing direction, with an infinite mean square time between direction changes. This work is described in Chap. 4, after calculation of theoretical results pertaining to random walks in Chap. 3.

2. *Flows over Topography*: One to three times each winter, in the Northern Hemisphere a flow pattern known as *blocking* occurs: a large vortex blocks

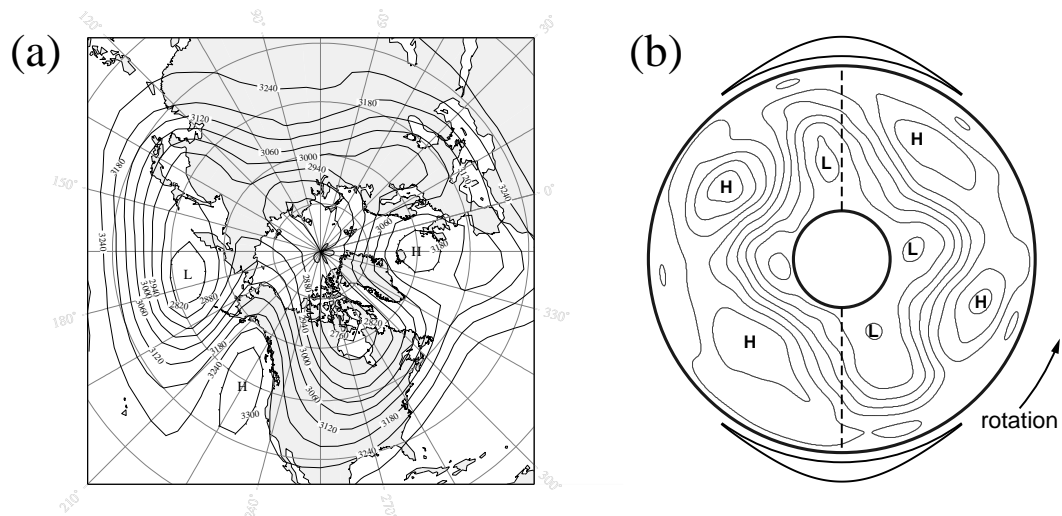


Figure 1.2: (a) Blocked flow in the atmosphere; the flow follows the contour lines. See Fig. 5.1 for more details. Blocked flow advects cold Arctic air southward over eastern North America or Europe, while decreasing precipitation in the continent's western part [118]. (b) A blocked flow in the rotating annulus experiment. Ridges are placed in the bottom of the experiment, with peaks indicated by heavy dashed lines and their profiles indicated by black curves above and below the annulus. For details see Chap. 5. HELP: Fix shading of (a).

the normal jet stream flow, diverting it poleward [117, 118] (see Fig. 1.2(a)). The diverted jet then carries cool Arctic air across the southwestern United States, occasionally resulting in extreme weather conditions such as snowfall in Texas. Blocking has other detrimental effects such as increasing the intensity of storms along the eastern coast of the United States, and decreasing rainfall in certain parts of the world with harmful results for agriculture. These blocking events typically last two weeks, and have been conjectured to result from the interaction of the jet stream with mountain ranges (specifically the Rockies and the Alps) [24].

Several atmospheric flow models have seen blocked flows [24, 72, 146]: specifically, the models assume (1) two-dimensional flow, (2) jet-stream-like forcing, and (3) two symmetrically placed mountain ridges. The rapid rotation rate of

the experiment results in flows satisfying the first condition. By placing two symmetric ridges in the bottom of the rotating annular tank, and forcing a jet to flow around the annulus (and thus over the topographic ridges), we find a flow which strongly resembles blocked flow (Fig. 1.2(b)). Because of the rapid rotation of the experiment, observations of thousands of “days” of behavior (annulus rotation periods) can be conducted in an hour, facilitating rapid exploration of parameter space. Our observations are discussed in Chap. 5; these are the first experimental observations supporting the results of the models, that is, that atmospheric blocking may have a topographic origin.

3. *Two-Dimensional and Three-Dimensional Turbulence:* For sufficiently rapid rotation, the experimental flows are predominantly two-dimensional. However, for low rotation rates flows will become three-dimensional [129]. Previous experiments ([34, 57]) examined the transition from three-dimensional flow to two-dimensional flow, but the parameters characterizing the transition varied in space, and thus it was difficult to closely examine this transition. We examine the dimensionality of the flow as a function of the forcing and rotation rate of the experiment; these results are presented in Chap. 6.

A discussion of the equations governing rotating fluid flows is presented in the following section, and Sec. 1.3 discusses previous work done with this experimental apparatus. Other relevant work done by other researchers is discussed in each chapter. The experimental apparatus and procedures are described in Chap. 2.

## 1.2 Quasi-geostrophic flow

This section gives a brief summary of important results pertaining to rotating flows. Many introductory texts discuss the following topics and are the source of the following material [30, 31, 73, 102, 150].

### 1.2.1 Equations of motion

The Navier-Stokes equation for the fluid velocity field  $\vec{u}(\vec{r}, t)$ , in reference frame rotating with rotation  $\vec{\Omega}$ , is given by

$$\frac{D\vec{u}}{Dt} = -\frac{1}{\rho}\vec{\nabla}p + \nu\nabla^2\vec{u} - 2\vec{\Omega} \times \vec{u} - \vec{\Omega} \times (\vec{\Omega} \times \vec{r}) \quad , \quad (1.1)$$

for a fluid with density  $\rho$  and kinematic viscosity  $\nu$ , and where the operator  $D/Dt$  is the substantive derivative [150], given by

$$\frac{D}{Dt} = \frac{\partial}{\partial t} + \vec{u} \cdot \vec{\nabla} \quad . \quad (1.2)$$

The left hand side of Eq. (1.1) is the advective term, and the terms on the right hand side are due to the pressure ( $p$ ), the viscous dissipation, the Coriolis force, and the centripetal force. This equation is simplified by noting that the centripetal term can be written as the gradient of a scalar,  $-\vec{\Omega} \times (\vec{\Omega} \times \vec{r}) = (1/2)\vec{\nabla}|\Omega^2 r^2|$ , and thus can be taken into the pressure term by considering an effective pressure,  $p' = p + (1/2)|\Omega^2 r^2|$ . This effective pressure will be used in all subsequent formulas, with the prime dropped. Physically, the centripetal force is exactly balanced by a component of the pressure field, which in turn has no other effect on the flow.

Equation (1.1) can be nondimensionalized using a characteristic length  $L$ , characteristic velocity  $U$ , characteristic time  $L/U$ , characteristic pressure  $P$ , and using for the rotation  $\vec{\Omega} \equiv \Omega\hat{z}$ :

$$\frac{U}{2\Omega L} \frac{D\vec{u}^*}{Dt^*} = \frac{-P}{2\rho UL\Omega} \vec{\nabla}^* p^* + \frac{\nu}{2\Omega L^2} \nabla^{*2} \vec{u}^* - \hat{z} \times \vec{u}^* \quad , \quad (1.3)$$

where the asterisks indicate the nondimensional variables. Dropping the asterisks from this point onward, we can write a simpler version of the Navier-Stokes equation as

$$Ro \frac{D\vec{u}}{Dt} = -Ro \left( \frac{P}{\rho U^2} \right) \vec{\nabla} p + Ek \nabla^2 \vec{u} - \hat{z} \times \vec{u} \quad , \quad (1.4)$$

using the nondimensional Rossby number  $Ro \equiv U/(2\Omega L)$  and the nondimensional Ekman number  $Ek \equiv \nu/(2\Omega L^2)$ .  $Ro$  expresses the relative importance of the advection to the Coriolis force and  $Ek$  expresses the relative importance of the dissipation to the Coriolis force. The nondimensional term in parenthesis modifying the pressure term,  $P/\rho U^2$ , must be of order  $Ro^{-1}$ , as the pressure term balances the Coriolis term in the limits of small  $Ro$  and  $Ek$  (see Eq. (1.7)) and  $\vec{\nabla} p$  is  $O(1)$ . Note that the Rossby number and Ekman number can be combined to yield the nondimensional Reynolds number,  $Re = Ro/Ek = UL/\nu$ , which is the traditional measure of how turbulent the flow is.

Often the rotation rate  $\Omega$  is replaced with the Coriolis parameter  $f = 2\Omega \sin \theta$ , where  $\theta$  is the angle between  $\vec{\Omega}$  and  $\vec{u}$ . This allows the cross product in Eq. (1.1) to be written as  $2\vec{\Omega} \times \vec{u} = f\hat{z} \times \vec{u}$ , with  $\hat{z}$  the local vertical direction (rather than the direction of  $\vec{\Omega}$ ). On a spherical planet,  $\theta$  is the latitude. For large scale flows on a planet, the Coriolis parameter is not a constant, but changes due to the  $\theta$ -dependence (see Sec. 1.2.6).

A continuity equation is also needed to describe the flow:

$$\frac{\partial \rho}{\partial t} + \vec{\nabla} \cdot (\rho \vec{u}) = 0 \quad . \quad (1.5)$$

If the fluid is incompressible ( $\rho$  is constant), this yields the simpler equation

$$\vec{\nabla} \cdot \vec{u} = 0 \quad . \quad (1.6)$$

Flows with constant  $\rho$  are *barotropic*; the term barotropic applies to any flow with  $\rho$  being a function of the pressure (i.e.,  $\rho = \rho(P)$ ; surfaces of constant pressure and constant density are equivalent). *Baroclinic* flows violate this condition, and typically arise in situations where there is a buoyant force due to differential heating of the fluid or stratified flows.

### 1.2.2 Geostrophic Limit

For geophysical flows, typically  $Ro$  is small and  $Ek$  is small; in the *geostrophic limit* with  $Ro \rightarrow 0$  and  $Ek \rightarrow 0$ , Eq. (1.1) becomes the geostrophic equation,

$$2\vec{\Omega} \times \vec{u} = -\frac{1}{\rho}\vec{\nabla}p \quad (1.7)$$

(written in dimensional units). According to this equation, the flow is along lines of constant pressure, rather than perpendicular to these lines (as would be the case for non-rotating flow).

A very useful result can be derived by taking the curl of the geostrophic equation, yielding  $\vec{\nabla} \times (\vec{\Omega} \times \vec{u}) = 0$ . Expanding this and using the incompressibility (and continuity)  $\vec{\nabla} \cdot \vec{u} = 0$  gives the result

$$(\vec{\Omega} \cdot \vec{\nabla})\vec{u} = 0 \quad . \quad (1.8)$$

Taking  $\vec{\Omega} = \Omega\hat{z}$ , this equation becomes  $\partial\vec{u}/\partial z = 0$ . This result is known as the Taylor-Proudman theorem. A useful consequence of this equation is that if the  $z$ -component of the velocity is zero anywhere (such as at an impenetrable bottom surface or at the lid of an annular tank), the  $z$ -component of the velocity is zero everywhere. A second consequence of this equation is that the horizontal velocity components are also  $z$ -independent. Thus, the fluid moves horizontally in coherent columns.

Flows with small but nonzero  $Ro$  are quasi-geostrophic flows. Such flows can have slightly relaxed constraints on their two-dimensionality. This allows for interesting non-trivial flows. For example, a geostrophic flow over varying topography without a free surface has the constraint that fluid columns must follow the lines of constant height — otherwise they would be stretched or compressed in the  $z$ -direction, violating the Taylor-Proudman theorem. In a quasi-geostrophic flow, fluid columns can be stretched or compressed slightly by moving uphill or downhill. The Taylor-Proudman constraint then provides a restoring force against these sorts



of fluid motions. Other effects are discussed at the end of Sec. 1.2.5. In general, the smaller  $Ro$  becomes, the more nearly the flow becomes two-dimensional.

### 1.2.3 Ekman layers

For flows with rigid top and/or bottom boundaries, the Taylor-Proudman theorem must be violated sufficiently close to these boundaries, in order to satisfy the no-slip condition at the boundaries. The Taylor-Proudman theorem holds true in the limit  $Ek \rightarrow 0$ , and it is this limit that breaks down near the boundaries, where viscous dissipation serves to take the fluid from the bulk velocity to the boundary velocity. This occurs within the *Ekman boundary layer*. These boundary layers have a thickness given by  $Ek = \nu/(2\Omega\delta^2) \sim 1$ , or

$$\delta \sim \sqrt{\nu/(2\Omega)} \quad . \quad (1.9)$$

In our experiment, the parameters typically are  $\nu \sim 0.01 - 0.03 \text{ cm}^2/\text{s}$  and  $\Omega/2\pi \sim 1 - 4 \text{ Hz}$  (see Chap. 2), so  $\delta \sim \sqrt{0.01/(16\pi)} - \sqrt{0.03/(4\pi)} = 0.14 - 0.5 \text{ mm}$ .

These boundary layers have an effect on the bulk flow. They inject fluid into low-pressure regions of the flow (regions of cyclonic flow, that is, vortices with the same sense of rotation as  $\Omega$  – see Eq. (1.7)), and withdraw fluid from high-pressure regions (anticyclones). This results in a reduction of vorticity,  $\omega = (\vec{\nabla} \times \vec{u}) \cdot \hat{z}$ . An unforced flow being damped by this *Ekman pumping* is damped as  $\vec{u}(t) \sim \vec{u}_0 e^{-t/\tau_E}$  with  $\tau_E = h_0/(2\sqrt{\nu\Omega})$  for a fluid with two Ekman layers (i.e., a fluid with a top and bottom boundary) spaced  $h_0$  apart.  $\tau_E$  is termed the Ekman time. A typical time scale for viscous damping of the bulk fluid is  $L^2/\nu$ , which is often larger than  $\tau$ ; thus, *Ekman damping* is often more important for rotating flows than direct viscous damping. For the experiment,  $h_0 \approx 20 \text{ cm}$ , and  $\tau_E \sim 12 - 40 \text{ s}$ .

We can recast the Ekman number in terms of the Ekman time and the

rotation period of the annulus, with

$$Ek = \frac{T_{\text{annulus}}^2}{\tau_E^2} = (8\pi^2) \frac{\nu}{\Omega(h_0/2)^2} \quad . \quad (1.10)$$

This definition differs from the previous one by the choice of  $h_0/2$  rather than  $L$  for the length scale, and the factor of  $8\pi^2 \approx 79$ . This definition is used for  $Ek$  in Chap. 5.

### 1.2.4 The Stream Function

For two-dimensional incompressible flows, the continuity equation (Eq. (1.6)) becomes

$$\frac{\partial u_x}{\partial x} + \frac{\partial u_y}{\partial y} = 0 \quad . \quad (1.11)$$

This constraint allows velocity field to be written in terms of derivatives of one scalar field  $\psi(x, y, t)$ :

$$u_x = \frac{\partial \psi}{\partial y}, \quad u_y = -\frac{\partial \psi}{\partial x} \quad . \quad (1.12)$$

$\psi(x, y, t)$  is known as the *stream function*, as it is constant along a streamline [150]. Equation (1.12) can also be written as

$$\vec{u} = \hat{z} \times (\vec{\nabla} \psi) \quad . \quad (1.13)$$

The existence of the stream function is valid for any two-dimensional incompressible flow; its usefulness for rotating flows is due to the Taylor-Proudman theorem. Equations (1.12) are equivalent to Hamilton's equations of motion, with  $\psi$  being the Hamiltonian and  $x$  and  $y$  being the phase space coordinates.

Another interesting equivalence can be noted by taking  $\hat{z} \times$  [Eq. (1.7)],

$$\hat{z} \times (2\Omega \hat{z} \times \vec{u}) = \hat{z} \times \left(-\frac{1}{\rho} \vec{\nabla} p\right), \quad (1.14)$$

producing (after dividing by  $2\Omega$ )

$$\vec{u} = \frac{1}{2\rho\Omega} \hat{z} \times (\vec{\nabla} p) \quad . \quad (1.15)$$

By comparing this equation with Eq. (1.13), it can be seen that for geostrophic flows,

$$\psi = \frac{1}{2\rho\Omega} p \quad . \quad (1.16)$$

This equivalence between the stream function and the pressure field is strictly true only for purely geostrophic flows; in practice, for small but nonzero  $Ro$  this is still a reasonable approximation.

### 1.2.5 Potential vorticity

An important conserved quantity for quasi-geostrophic flows is potential vorticity,  $q = (f + \omega)/h$ , where  $h$  is the fluid depth and  $\omega$  is the vorticity in the rotating reference frame. The following derivation of the conservation of potential vorticity is based on the derivation of Ref. [30] (Chap. 4).

Start with Eq. (1.1), taking  $\nu = 0$  and using the Coriolis parameter  $f$ :

$$\frac{D\vec{u}}{Dt} = \frac{\partial\vec{u}}{\partial t} + (\vec{u} \cdot \vec{\nabla})\vec{u} = \frac{1}{\rho}\vec{\nabla}P + f\hat{\times}\vec{u} \quad . \quad (1.17)$$

Take the curl of this equation, allowing the Coriolis parameter  $f$  to vary in  $x$  and  $y$ ; the pressure term will vanish as  $\vec{\nabla} \times \vec{\nabla} = 0$ . This produces the following equation:

$$\frac{D}{Dt}(f + \omega) + (\vec{\nabla} \cdot \vec{u})(f + \omega) = 0 \quad . \quad (1.18)$$

Next consider a column of fluid with cross sectional area  $dA$ . This area will undergo changes due to the flow; these changes are given by the equation

$$\frac{D}{Dt}dA = (\vec{\nabla} \cdot \vec{u})dA \quad , \quad (1.19)$$

which can be understood as a horizontal divergence will increase the cross section; a convergence decreases this area. By multiplying Eq. (1.18) by  $dA$ , Eq. (1.19) by  $(f + \omega)$ , and adding the results together, the result is

$$dA \frac{D}{Dt}(f + \omega) + (f + \omega) \frac{D}{Dt}dA = \frac{D}{Dt}[(f + \omega)dA] = 0 \quad . \quad (1.20)$$

This product,  $(f + \omega)dA$ , is the circulation of the fluid parcel for small  $dA$ , and Eq. (1.20) expresses Kelvin's theorem for a rotating, two-dimensional flow (conservation of circulation  $[= \int dA\omega]$  for an inviscid fluid) [30].

Next we derive an equation governing changes in the height of the fluid,  $h(x, y, t)$ . Note that these changes may be either due to a free surface, or fixed topography, or both. Assume that the bottom of the fluid is a fixed surface at  $z = 0$  for the moment. Writing out the equation for conservation of mass (Eq. (1.6)), we get

$$\frac{\partial u_x}{\partial x} + \frac{\partial u_y}{\partial y} + \frac{\partial u_z}{\partial z} = 0 \quad . \quad (1.21)$$

Integrating this equation over  $\int_0^h dz$ , we get

$$\left(\frac{\partial u_x}{\partial x} + \frac{\partial u_y}{\partial y}\right)h + u_z|_{z=h} - u_z|_{z=0} = 0 \quad . \quad (1.22)$$

Previously we have neglected any vertical velocity component, but now we recognize that a vertical velocity will occur due to the possibility of variations in  $h$ . Equation (1.22) neglects any variations in  $u_x$  and  $u_y$  in the vertical direction, which would result in a higher order correction to this equation. If the vertical velocity  $u_z$  varies linearly with height  $z$ , the horizontal divergence given by the first two terms will cancel exactly with the last term, and  $u_x$  and  $u_y$  will still be independent of  $z$ . The vertical velocity at the bottom  $u_z|_{z=0}$  must be zero, as the bottom surface is assumed to be fixed and flat. The vertical velocity at the top depends on the fluid height,

$$u_z|_{z=h} = \frac{\partial h}{\partial t} + (\vec{u} \cdot \vec{\nabla})h = Dh/Dt \quad . \quad (1.23)$$

As the fluid height changes in time,  $u_z|_{z=h}$  must change with it, yielding the  $\partial h/\partial t$  term. As a column of fluid moves horizontally, it is stretched to conform to  $h(x, y, t)$ , producing the  $(\vec{u} \cdot \vec{\nabla})h$  term. Rewriting Eq. (1.22) using this result produces

$$\frac{D}{Dt}h + (\vec{\nabla} \cdot \vec{u})h = 0 \quad . \quad (1.24)$$

Multiplying this equation by  $dA$ , multiplying Eq. (1.19) by  $h$ , and adding, produces

$$dA \frac{D}{Dt} h + h \frac{D}{Dt} dA = \frac{D}{Dt} [hdA] = 0 \quad . \quad (1.25)$$

This equation expresses the conservation of volume for a fluid column. Taking Eq. (1.20) and dividing by Eq. (1.25) produces the desired result,

$$\frac{D}{Dt} \left( \frac{f + \omega}{h} \right) = \frac{Dq}{Dt} = 0 \quad , \quad (1.26)$$

the equation expressing conservation of potential vorticity. For a slightly different derivation, see Ref. [102]. A more careful derivation taking in account variations in bottom topography produces the same result.

It is useful to consider the implications for a vortex column in a rotating flow. A column of fluid with vorticity  $\omega$  (relative to the rotating reference frame) which moves uphill (in the direction of decreasing  $h$ ) must conserve its potential vorticity. Thus cyclones (vortices with  $\omega$  having the same sign as  $f$ ) slow down, while anticyclones ( $\omega$  having opposite sign as  $f$ ) spin up. Conversely, cyclones moving downhill spin up and anticyclones moving downhill slow down.

In general, this result (Eq. (1.26)) is true only in the limit of negligible dissipation ( $Ek \rightarrow 0$ ) and for barotropic flows [102]. When Ekman pumping is occurring (Sec. 1.2.3), potential vorticity is dissipated as

$$\frac{Dq}{Dt} = -\frac{f \delta_E}{2h^2} \omega \quad (1.27)$$

with  $\delta_E$  the Ekman layer thickness [73].

### 1.2.6 Relation between topography and spherical geometry

Through the conservation of potential vorticity, a connection can be made between flows in a spherical geometry (such as planetary-type flows) and flows in a rectangular geometry with topography. For planetary flows, the variation of the Coriolis

parameter  $f$  with latitude is important. If the scale of the flow in the north-south direction is sufficiently small,  $f$  can be linearized about a typical value,

$$f = 2\Omega \sin \theta \approx 2\Omega \sin \theta_0 - \delta\theta(2\Omega \cos \theta_0) \quad . \quad (1.28)$$

Using local coordinates on the sphere with  $+\hat{x}$  in the east direction,  $+\hat{y}$  in the north direction, and  $+\hat{z}$  in the local vertical direction,  $\delta\theta = y/R$  where  $R$  is the radius of the sphere. Now the Coriolis term can be written as  $f = f_0 - \beta y$  with  $\beta = 2\Omega \cos \theta_0/R$ . Thus the potential vorticity becomes

$$q = \frac{f_0 + \omega - \beta y}{h} \quad . \quad (1.29)$$

Now consider a separate case where  $f = f_0$  is constant but with  $h$  varying linearly in  $y$ ,  $h(y) = h_0 + sy$  where  $s$  is the slope. The potential vorticity is

$$\begin{aligned} q &= \frac{f_0 + \omega}{h(y)} = \frac{f_0(1 + \omega/f_0)}{h_0(1 + sy/h_0)} \approx \frac{f_0(1 + \omega/f_0)(1 - sy/h_0)}{h_0} \\ &\approx \frac{f_0(1 + \omega/f_0 - sy/h_0)}{h_0} = \frac{f_0 + \omega - \beta y}{h_0} \quad , \end{aligned} \quad (1.30)$$

where now  $\beta = sf_0/h_0$ . This result has the same form as Eq. (1.29), showing that topography sloping in the  $y$ -direction can approximate the curvature of a spherical geometry, to first order. Note that this result was derived by assuming that  $\omega/f_0$  and  $sy/h_0$  are small quantities, which is true if  $Ro$  and the slope  $s$  are both small.

This equivalence of the two  $\beta$ 's is termed the beta-plane approximation [102]. A similar result holds for a cylindrical geometry, with  $y$  (the poleward variable) being replaced by  $r$ . Ideally, for the annular geometry used in the experiments (see Chap. 2)  $\beta$  should vary linearly with  $r$  [138]. For simplicity, the experiments are conducted with constant  $\beta$ , and the results found in previous experiments agree with predictions for the atmosphere (e.g. Ref. [131]).

### 1.2.7 Free surface effects

The experimental setup described in Chap. 2 is filled with fluid up to a rigid lid, and thus has no free surface. However, we briefly consider how the potential vorticity conservation would be modified in situations with a free surface. This discussion is based on Ref. [31].

We start with Eq. (1.26), noting now that  $h = h_0 + sy + \eta$ , where  $s$  is a bottom slope as discussed in the previous subsection, and  $\eta(x, y, t)$  is the free surface variation ( $\eta/h_0 \ll 1$ ). Equation (1.30) now is

$$q = \frac{f_0(1 + \omega/f_0 - sy/h_0 - \eta/h_0)}{h_0} . \quad (1.31)$$

In general, the pressure can be written as  $p = p_0 + \rho g \eta$ , which along with Eq. (1.16) can be solved for  $\eta$ :

$$\eta = \frac{f_0}{g} \psi - \frac{p_0}{\rho g} . \quad (1.32)$$

Using this result in Eq. (1.30) allows us to write the potential vorticity as

$$q = \frac{f_0(1 + \omega/f_0 - sy/h_0 - \psi/R_D^2)}{h_0} + \text{constant} , \quad (1.33)$$

where

$$R_D \equiv \frac{\sqrt{gh_0}}{f_0} \quad (1.34)$$

is the *Rossby deformation radius*. As the vorticity can be written as  $\omega = \nabla^2 \psi$ , it can be seen that the magnitude of the local vorticity term in Eq. (1.33) is  $O(L^{-2}\psi)$  and the magnitude of the free surface term is  $O(R_D^2\psi)$ . Thus, for flows on length scales  $L > R_D$ , free surface variations are important, and for  $L < R_D$  the free surface can be neglected — the variation of  $\eta$  is slight enough to be treated as a rigid surface. A slightly different interpretation is that  $R_D$  is the distance over which the gravitational tendency to flatten the free surface is balanced by the tendency of the Coriolis force to deform the surface [102] (see for example Eq. (1.32) relating  $h$  and  $\psi$ ). The ratio  $L/R_D$  is known as the Froude number. For cases without a free surface (such as the experiment), we use  $R_D \rightarrow \infty$ .

### 1.2.8 Axisymmetric flow in the experiment

A theoretical result of particular importance to this dissertation is the axisymmetric flow generated at low forcing in the rotating annulus experiment. Consider a rotating annular tank filled up to a rigid lid. Fluid is pumped into the tank axisymmetrically through the bottom at radius  $r_{\text{source}}$ , and out of the tank axisymmetrically at radius  $r_{\text{sink}}$ . In Ref. [31] D. del Castillo Negrete derives the flow that results from this type of forcing. Fluid between the two radii moves in an axisymmetric jet, which is co-rotating with the tank rotation if  $r_{\text{source}} > r_{\text{sink}}$ , and counter-rotating otherwise. Assume  $r_{\text{source}} > r_{\text{sink}}$ ; fluid between the forcing rings has a velocity

$$u_{\theta}(r) = u_{\text{max}} r_{\text{sink}} / r \quad , \quad (1.35)$$

with

$$u_{\text{max}} = \sqrt{\frac{\Omega}{\nu} \frac{F}{2\pi r_{\text{sink}}}} \quad . \quad (1.36)$$

$F$  is the pump flux. Fluid elsewhere in the annulus has  $\vec{u} = 0$ . This result is in good agreement with experimental measurements [131]. Often a co-rotating jet is termed an eastward jet, and a counter-rotating jet termed a westward jet; in this dissertation we will use co- and counter- rotating jets for clarity.

In Chap. 5 we use  $v_{\text{max}}$  as the characteristic velocity scale  $U$  in order to define  $Ro$  and  $Ek$ .

## 1.3 Previous experiments

The experimental apparatus described in Chap. 2 was originally constructed in 1986-8 by J. Sommeria, S. D. Meyers, and H. L. Swinney. The original inspiration was provided by P. S. Marcus, who proposed that a large coherent vortex would form under certain conditions, analogous to Jupiter's Great Red Spot [77]. Thus the first experiments done using the rotating annulus were investigations into vortex



formation and dynamics for turbulent westward (counter-rotating) jets [78, 86, 136]. These experiments confirmed Marcus's results, observing a large long-lived vortex which could be visualized with red dye.

The next set of experiments examined co-rotating jets [6, 87, 137, 138]. These jets tended to be narrower than the counter-rotating jets. The experiments found that the jet had a strong gradient of potential vorticity inside, with potential vorticity fairly uniform on either side of the jet. This potential vorticity gradient was a powerful barrier to mixing, as would be expected as fluid columns should conserve their potential vorticity (Sec. 1.2.5). Dye rapidly mixed outside of the jet, but was extremely slow to mix across the jet.

These earlier experiments were all conducted with a large pump, that had pump rates up to  $350 \text{ cm}^3/\text{s}$ . Next, T. H. Solomon, W. J. Holloway and H. L. Swinney investigated the onset of instabilities at low pump rates [131], and thus a smaller pump was installed that had a carefully controlled flow rate up to  $50 \text{ cm}^3/\text{s}$ . At very low pump rates, the axisymmetric jet profile discussed in Sec. 1.2.8 was observed. Above each forcing ring was a shear layer between the axisymmetric jet and the motionless fluid outside the jet. As the forcing was increased, these shear layers became unstable to a vortex chain which propagated around the annulus at roughly half the speed of the jet at that point (i.e., the average speed of the fluid in the jet and the fluid outside the jet). The formation of the vortex chains later proved useful for conducting the transport experiments discussed in Chap. 4. At still higher pump rates, the vortex chain above the inner ring of holes would “lock” with the vortex chain above the outer ring of holes. For the co-rotating case, the wavy jet between the locked vortex chains was interpreted as a Rossby wave, a wave structure caused by the presence of a  $\beta$ -effect (Sec. 1.2.6; see Ref. [102] for a careful explanation of Rossby waves). For the counter-rotating case, the interpretation was less clear, and it is possible that the observed locking was only a coincidence of the two vortex

chains rotating at similar rates [134].

During these onset experiments, a novel particle tracking system was developed by M. S. Pervez and T. H. Solomon [104]. This system is briefly discussed in Sec. 2.2 and led to the investigation of transport and mixing discussed in Chap. 4; the transport experiments in turn motivated the theoretical calculations discussed in Chap. 3.

## Chapter 2

# Experimental Apparatus and Procedures

### 2.1 Rotating tank

The experiment consists of a large annulus, which rotates rapidly, filled completely with fluid, and a pump and plumbing system which is used to generate flows inside the annulus. The annulus has an inner radius  $r_1 = 10.8$  cm, outer radius  $r_2 = 4r_1 = 43.2$  cm, and a height linearly varying from 17.1 cm (at  $r_1$ ) to 20.3 cm (at  $r_2$ ); see Fig. 2.1. The conical bottom slope ( $s = 0.1$ ) provides for the  $\beta$ -effect discussed in Sec. 1.2.6, modeling the variations of the Coriolis force with latitude for a spherical planet. The annulus is covered by a rigid Plexiglas lid which prevents fluid from spilling when the experiment is rotated rapidly.

The inner wall of the annulus is constructed from aluminum (with Magnaplatting HCR treatment to prevent corrosion), as well as the sloping bottom (also Magnaplated). The outer walls and lid are constructed from Plexiglas, to allow for flow visualization (see Sec. 2.2). The entire apparatus rotates rigidly (at speeds ranging from  $\Omega/2\pi = 0\text{--}4$  Hz), rather than differential rotation as for Taylor-

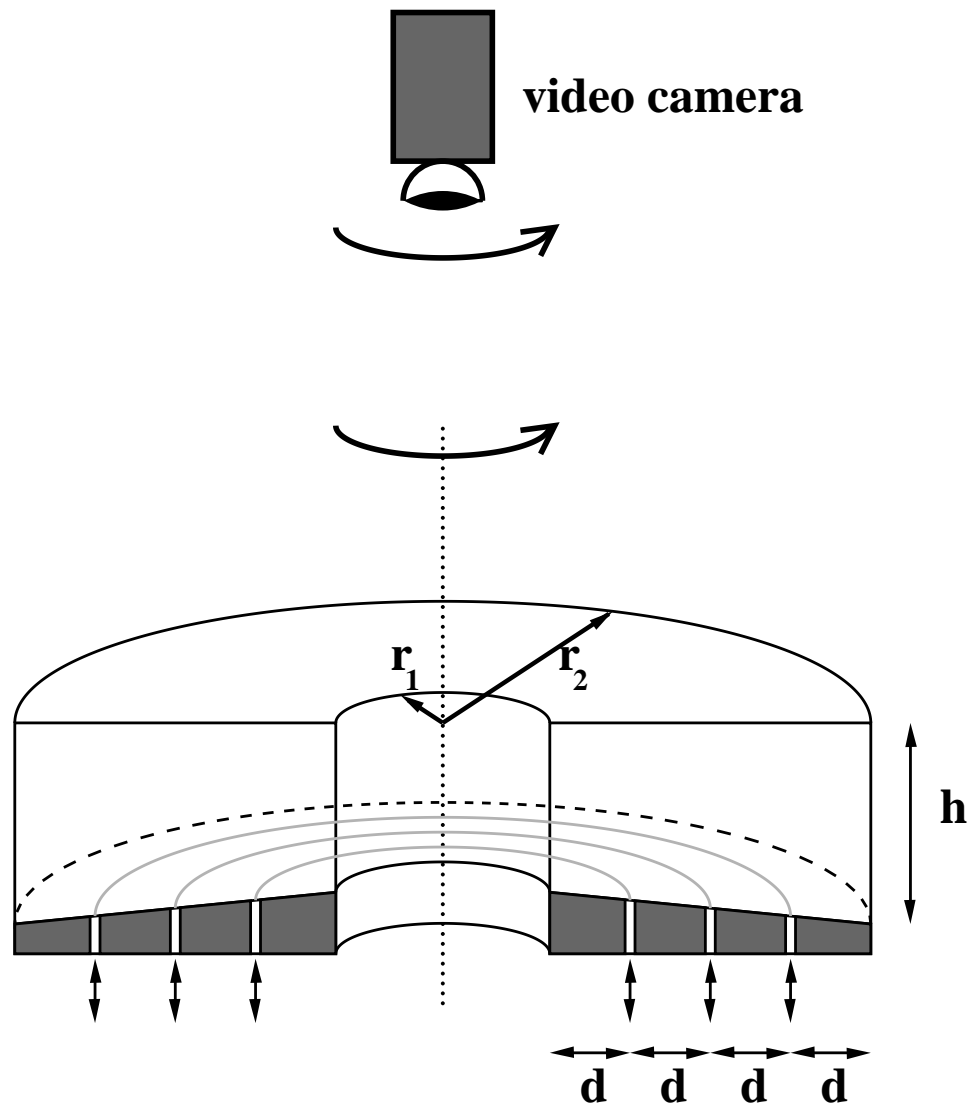


Figure 2.1: Schematic diagram of rotating annulus.  $r_1 = 10.8$  cm,  $r_2 = 43.2$  cm,  $d = 8.1$  cm, and  $h = 20.3$  cm at  $r_2$ . The bottom has a slope of 0.1. See text for other details.

Couette experiments. When the apparatus is rotating at a steady rate, the only source of energy to drive flows in the tank is the pump, discussed below. Details of the motor system driving the tank are in Ref. [88].

For the experiments discussed in this dissertation, two fluids are used. When a high Reynolds number is desired, distilled water is used with kinematic viscosity  $\nu = 0.009 \text{ cm}^2/\text{s}$ . Experiments conducted at lower Reynolds numbers use a mixture of 38% glycerol (by weight) in water with kinematic viscosity  $\nu = 0.030 \text{ cm}^2/\text{s}$ . Experiments are conducted at or near room temperature, and the viscosity of these two fluids strongly depends on temperature. Temperature measurement and control are discussed in Sec. 2.7.

Flows are generated in the annulus by pumping fluid into and out of the annulus through small holes (0.26 mm diameter) in the bottom. The annulus floor has three concentric rings of 120 holes each, at radii 18.9 cm, 27.0 cm, and 35.1 cm (see Fig. 2.1). Underneath the aluminum annulus floor are 18 separate channels, each controlled by one valve. Thus each channel allows flow through one  $60^\circ$  arc of 20 holes. By opening and closing valves, the flow can be individually controlled through each  $60^\circ$  sector. From the pump, a hose carries the flow to a three-way divider; the three hoses from the divider each go to a secondary divider, and from the secondary dividers the nine hoses go to the valves beneath the annulus floor. The flow from the annulus back to the pump repeats this plumbing in reverse with additional dividers. The hoses are connected with Swagelok connectors. By connecting the hoses appropriately and opening the appropriate valves, fluid can be pumped into the experiment through 1–9 separate  $60^\circ$  sectors of holes, and out of the experiment through 1–9 sectors.

In practice, we typically use two complete rings of forcing holes, and pump uniformly through each ring. The hoses are connected so that the flow impedance through the plumbing is uniform for each  $60^\circ$  sector: typically the six hoses for

a forcing ring are taken two from each secondary flow divider. The additional hose from each secondary flow divider is attached to a sector of the unused forcing ring, and the valve is closed. By pumping fluid in uniformly at one radius and out uniformly at a different radius, azimuthal flow can be generated as discussed in Sec. 1.2.8. Future experiments may consider pumping fluid uniformly into the annulus through two rings of holes, and out of the annulus through the third ring of holes; the flow dividers will need to be redesigned for this configuration.

The experiments discussed in this dissertation were done with two different pumps. Originally a small Micropump positive-displacement magnetically coupled gear pump was installed. This pump produces carefully controlled flow rates ranging from 1 to 52 cm<sup>3</sup>/s, and was used for the experiments discussed in Chap. 4. More recently, a larger 800 W Tri-Rotor positive-displacement rotary piston pump (model 20DV) was installed. This pump has larger fluctuations in flow rate, and produced flows up to 900 cm<sup>3</sup>/s in our table-top tests (the pump is rated for flows up to 1250 cm<sup>3</sup>/s). In practice, pumping through the hoses and forcing holes reduces the maximum flow rate to approximately 450 cm<sup>3</sup>/s. To achieve a flow rate of 450 cm<sup>3</sup>/s, the plumbing was upgraded to increase the diameter of most of the hoses on the annulus, and replacing the smaller valves used with the Micropump with larger valves. It is likely that still higher flow rates can be achieved with additional plumbing modifications, although given the limitations of space beneath the experiment, there is not much room for larger hoses. Because of the fluctuations with the Tri-Rotor pump, a flow meter has been installed; this is discussed in Sec. 2.8. This flow meter is a significant contribution to the flow impedance, and is the place where the most improvements could be made to increase the maximum possible flow (see Sec. 2.8).

The Tri-Rotor pump is powered by a PMI model U16M4 motor, connected with a flexible-chain coupler to the pump. This motor is capable of speeds up to

3000 RPM; the pump is designed for speeds up to 1800 RPM, so we have built a circuit which controls the motor power limiting the maximum allowed motor speed.

A flow-reversing valve was used with the Micropump, installed immediately downstream of the pump. We have chosen not to install such a valve with the Tri-Rotor pump, as it would increase the impedance of the plumbing and lower the maximum pump rate. The Tri-Rotor pump is capable of running backwards, although the flow rate fluctuations are larger, and the flow meter (Sec. 2.8) is more accurate in the “forward” direction. This pump is not designed to be reversed for extended periods of time; to reverse the flow, it is necessary to rearrange the plumbing.

Beneath the plumbing is a set of 16 slip rings, used to carry electrical signals onto and off of the annulus. The electrical connections include power for the pump, connections for the hot film probe system (Sec. 2.5), connections for the thermistor (Sec 2.7), power for and signals from the flow meter (Sec. 2.8), and signals from the pressure sensor (Sec. 2.9).

## 2.2 Particle tracking system

In order to visualize the flow, a Sony CCD video camera and a Olympus OM-1 SLR 35 mm camera are mounted on a rotating platform above the tank [88]. Usually this platform has the same rotation rate as the experiment, although the rotation rate can be adjusted independently to focus on traveling structures. Our primary technique for flow visualization is particle tracking, discussed in this subsection. Another technique which we have used is injecting fluorescent dye into the tank; however, this is not used for the experiments discussed in this dissertation.

For particle tracking, small neutrally buoyant particles are added to the fluid. We then use the video camera and an automated technique to track individual particles for long times (up to 1000 s; see the discussion in Sec. 4.5). The long term

particle tracking is useful for the mixing studies discussed in Chap. 4, while particles have been tracked for much shorter durations to generate the stream functions shown in Chap. 5 (see Sec. 2.4). Also, the tracer particles can be used to generate streak photographs using the 35 mm camera.

Several methods have been used to produce these particles. The method used for the experiments described in this dissertation uses Crayola © fluorescent crayons (colors: sunflow, laser lemon, unmellow yellow, outrageous orange, and atomic tangerine; sometimes these crayons are sold as “Neon” crayons rather than “fluorescent”). These colors were chosen as they fluoresce the brightest under black lights. However, the illumination we use are halogen lamps (see below) rather than black lights. Black lights were tried and the resulting fluorescence did not sufficiently contrast with the background to be useful for flow visualization. The crayons used have a density very close to  $1.0 \text{ g/cm}^3$ , typically slightly larger. To make particles neutrally buoyant in water, we melt and mix the crayons with a small amount of paraffin wax (with a density slightly less than  $1.0 \text{ g/cm}^3$ ). The melted mixture is allowed to harden, and is then chopped and sieved to produce particles approximately 1 mm in diameter.

The resulting particles typically have a spread of densities close to  $1.0 \text{ g/cm}^3$ . We place the particles in a small jar filled with distilled water, which has been boiled and allowed to cool in order to reduce the amount of dissolved gas in the water. The jar is sealed and allowed to sit overnight, to further allow for gas bubbles trapped on the particles to dissolve. The following day, the jar is shaken and allowed to sit for 3-5 minutes. Using a pipet, particles which have neither sunk to the bottom nor floated to the top are removed from the middle of the jar. They are placed in a separate container which is then sealed and allowed to sit for another day. The process is repeated with that container and the particles are added to the tank fluid.

For particles intended to be neutrally buoyant in the water-glycerol mixture,



with a larger density, cement fixer dust is added to the melted wax mixture (which in this case does not have paraffin wax added). The resulting particles generally have a wide spread in densities and, using the techniques described above, it is possible to select the particles with the correct density for the experimental fluid. Carnoba wax has also been used occasionally to increase the density of particles, rather than cement fixer dust.

The particles are illuminated from the side by eight 100 W halogen lamps, through the Plexiglas walls of the annulus. Using a felt-tipped permanent marker to make the bottom of the annulus black improves contrast.

A novel long-term particle tracking technique is used to find the particle trajectories. For details of this method, see Ref. [104]. Briefly, the CCD video camera rotates at the same rate as the annulus, above the experiment. The signal from this camera goes to a Matrox frame-grabber card, which is able to compare the image to a threshold, and write to a hard disk only the pixel coordinates brighter than a threshold. This is done at speeds from 10–30 frames per second; typically we use 10 or 15 frames per second. After the experiment is over, a program identifies clusters of pixels in each frame, and then identifies particles which are close to each other between frames as the same particle trajectory. Refinements are made to improve accuracy when many particles are visible [104]. This method results in at least several hundred particle trajectories, often over a thousand, depending on the duration of the experiment and the number of particles in the fluid. Two atypical particle trajectories are shown in Fig. 2.2.

One problem occurs with these particles: at high pump rates, particles are suctioned into the sink forcing holes. On the underside of the annulus bottom, netting is placed which catches the particles to prevent them from passing through the pump. Thus the particles clump around the forcing holes. This restricts the flow through the holes, and can change the flow rate. The active pump control

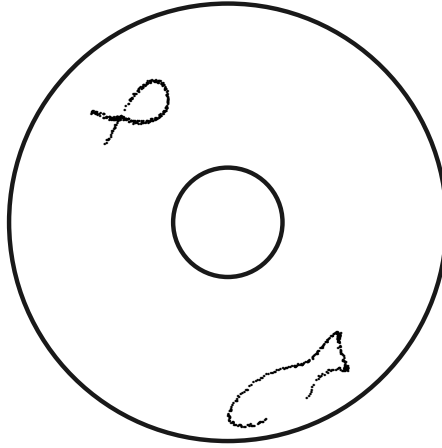


Figure 2.2: Two atypical particle trajectories actually seen in the rotating annulus experiment, tracked with the technique of Ref. [104]. Other more typical examples appear in Chap. 4.

system discussed in Sec. 2.8 is used to compensate for this problem (by increasing the power provided to the pump). However, an additional concern is that this particle clogging problem is non-axisymmetric, and results in uneven forcing. The magnitude of this problem is unknown. For most experiments with pump flux rates above  $100 \text{ cm}^3/\text{s}$ , after 15-60 minutes, significant clogging has occurred. When this is observed, the pump is temporarily reversed to force the particles out of the holes. Quite often, several holes remain clogged despite the pump reversal. For experiments where we desire to take long time series with the hot film probes (Sec. 2.5), we completely remove the particles from the tank to avoid the clogging problems. This is additionally useful as particles can bump against the hot film probes and change how the probes are cooled by the flow.

In addition to the particles placed in the experiment, we place a light emitting diode (LED) on the lid of the annulus, typically attaching it to a hot film probe (Sec. 2.5). The LED is tracked just as the particles are tracked. This provides a known location on the annulus which is useful for locating stationary features inside

the annulus (topography used in Chap. 5, and the hot film probes themselves). The LED also can provide information about the exact rotation rate of the annulus relative to the camera; the two rotation rates are never perfectly matched.

### 2.3 Particles as passive tracers

It is important that the particles act as passive tracers and accurately follow the flow. Much work has been done deriving equations of motion for spherical particles in flows at low relative Reynolds numbers. Two good reviews are Refs. [90] and [135], which are the primary sources for this section; see also Ref. [55]. This is still an active field of research; the literature has a number of incorrect results (discussed in [90]) and it is sometimes unclear which equations are best suited for a given system. This section considers the various forces on particles in our experiment. The following forces may be relevant: (a) the gravitational (buoyant) force; (b) the centripetal force; (c) the viscous drag force; (d) fluid inertia; (e) lift (due to rotation – the “Magnus” force); and (f) the pressure gradient [135].

The notation used in this section is in Table 2.1. The equation of motion for a spherical, non-rotating particle is given by [39, 90]:

$$\begin{aligned}
m_p \frac{d\vec{u}_p}{dt} &= 6\pi a \rho_f \nu (\vec{u}_f - \vec{u}_p) && \text{Stokes drag} \\
&+ m_f \frac{D\vec{u}_f}{Dt} && \text{pressure, viscous stresses} \\
&+ \frac{1}{2} m_f \left( \frac{D\vec{u}_f}{Dt} - \frac{d\vec{u}_p}{dt} \right) && \text{added mass} \\
+ 6a^2 \rho_f \sqrt{\pi \nu} \int_0^t \frac{(d/d\tau)(\vec{u}_f - \vec{u}_p)}{\sqrt{t - \tau}} d\tau &&& \text{Basset history} \\
&+ (m_p - m_f) \vec{F} && \text{buoyant, centripetal.} \tag{2.1}
\end{aligned}$$

The left hand side gives the acceleration of the particle; the right hand side terms are the drag force, the force due to the pressure gradient and viscous stresses, the inertia force of added mass (fluid dragged along with the moving sphere), the Basset history term (viscous force due to unsteady relative acceleration), and the combined

Table 2.1: Definition of symbols used in Sec. 2.3 [39].

| Symbol            | Meaning   |
|-------------------|---|
| $a$               | particle radius ( $\approx 0.05$ cm for our experiment)   |
| $d/dt$            | derivative with respect to time following the moving particle   |
| $D\vec{u}_f/Dt$   | $\partial\vec{u}_f/\partial t + (\vec{u}_f \cdot \vec{\nabla})\vec{u}_f$ evaluated at the particle position |
| $\vec{F}$         | gravitational and centripetal acceleration, $\vec{F} = -g\hat{z} + r\Omega^2\hat{r}$                        |
| $m_f$             | mass of fluid displaced by particle   |
| $m_p$             | mass of particle = $(4\pi/3)a^3\rho_p \approx 0.01$ g (for our experiment)                                  |
| $u_{p,f}$         | velocity of particle, fluid   |
| $u_{\text{term}}$ | terminal velocity of particle ( $F_B = F_D$ )   |
| $\rho_{p,f}$      | density of particle, fluid  |
| $\nu$             | kinematic viscosity of fluid  |
| $F_B$             | magnitude of buoyant force (Eq. (2.2))  |
| $F_C$             | magnitude of centripetal force (Eq. (2.4))  |
| $F_D$             | magnitude of drag force (Eq. (2.3))   |
| $F_{AM}$          | magnitude of “added mass” force (Eq. (2.5))   |
| $F_{BH}$          | magnitude of Basset history force (Eq. (2.6))   |

force of the buoyant and centripetal forces. Historically the terms on the right hand side were considered independent forces; however, recent evidence suggests that for any  $Re > 0$ , even  $Re \ll 1$ , these terms are not actually independent [90]. Fortunately this will not affect our discussion; for low  $Re$  this equation has been found to be empirically correct [90]. Equation (2.1) was independently derived by Basset, Boussinesq, and Oseen, and is sometimes referred to as the BBO equation [90, 135]. Earlier related work was done by Poisson, Green, Clebsch, and Stokes [90].

It is easiest to consider forces acting on a particle in the reference frame co-moving with the fluid, that is, where  $D/Dt = 0$ . We wish to consider the magnitude of each force, so we will drop vector notation in the following discussion. We start by considering the buoyant force, which is a constant for each particle:

$$F_B = (m_f - m_p)g \quad . \quad (2.2)$$

The mass of the particle  $m_p$  depends on the density of the particle  $\rho_p$ . We estimate

$\rho_p$  by considering the settling time for particles. As discussed previously, particles are selected for the experiment with a settling time larger than 5 min. We estimate the terminal velocity of particles as  $\sim 2$  cm/min = 0.033 cm/s (from observations of particles in the experiment when it is not rotating). The drag force on a sphere is given by [150]:

$$F_D = 6\pi\nu\rho_f a u_p \quad (2.3)$$

where  $u_p$  is now the velocity of the particle relative to the fluid. (This equation is only valid for  $Re < 1$ , that is,  $u_p < \nu/2a = 0.1$  cm/s. This is reasonable as the terminal velocity is smaller than this; particles moving quickly enough for  $Re \approx 1$  would be quickly damped by the drag force.) Solving Eqs. (2.2) and (2.3), we find  $|\rho_p/\rho_f - 1| \approx 0.0006$  (using water for the fluid). Thus, particles selected for neutral buoyancy in water have densities ranging from 0.9994–1.0006 g/cm<sup>3</sup>. This may be too generous; a more likely range is 0.9990–1.0010 g/cm<sup>3</sup>, with a terminal velocity of  $u_{\text{term}} = 0.056$  cm/s. Using  $\rho_p = 1.001$  g/cm<sup>3</sup> allows us to estimate the magnitude of the buoyant force as  $F_B = 5 \times 10^{-4}$  dynes (1 dyne =  $10^{-5}$  N). Note that the buoyant force acts in the vertical direction, while the flow is predominantly two-dimensional and vertical particle motions are not measured; the buoyant force only affects how long particles remain in the illuminated horizontal section of the annulus.

From the drag force a characteristic time can be extracted, given by  $\tau_{\text{drag}} = 2a^2/9\nu = 0.06$  s (for particles with  $\rho_p \approx \rho_f$ ). Thus, particles rapidly reach their terminal velocity; particles for which the velocity relative to the fluid  $u_p > u_{\text{term}}$  are quickly damped. This helps compensate for the forces discussed below by opposing motion relative to the fluid.

The remaining forces depend on quantities which are unknown and variable; we estimate the conditions necessary for each force to be  $O(F_B)$ . The centripetal force is related to the buoyant force by

$$F_C = \frac{r\Omega^2}{g} F_B \quad . \quad (2.4)$$

At a typical rotation rate of  $\Omega = 3\pi$  rad/s, a particle at a radius  $r = 40$  cm experiences a centripetal force 3.6 times larger than the buoyant force. At higher rotation rates ( $\Omega = 6\pi$  rad/s)  $F_C = 14F_B = 7.4 \times 10^{-3}$  dynes. Clearly the centripetal acceleration is a significant force, and is the main reason we strive to use neutrally buoyant particles ( $\rho_p \approx \rho_f$ ).

The drag force counteracts somewhat the action of the gravitational and centripetal forces. We can consider a new terminal velocity  $u_{\text{term}} = 0.8$  cm/s which balances the worst case  $F_C = 7.4 \times 10^{-3}$  dynes. Typical experimental flow velocities are from 1–20 cm/s; at low flow rates and high rotation rates  $u_{\text{term}}$  is comparable to the flow velocity, and thus the centripetal force can result in significant perturbations to the flow. At lower rotation rates ( $\Omega = 3$  rad/s;  $\Omega/2\pi = 1.5$  Hz), the terminal velocity is  $u_{\text{term}} = 0.2$  cm/s, which is reasonably small. Note that particles with densities significantly different from water move even faster than these estimated terminal velocities, and thus centrifuge to the edges of the annulus and are not visible to the camera.

Next we consider the added mass force, given by

$$F_{AM} = \frac{1}{2}m_f \frac{du_p}{dt} \quad . \quad (2.5)$$

$F_{AM} = F_B$  when  $du_p/dt = 2$  cm/s<sup>2</sup>; recall that  $u_p$  is the relative particle motion.  $du_p/dt$  for a typical flow can be estimated as the acceleration due to  $F_C$  (which occurs if  $u_p = 0$  temporarily and thus  $F_D = 0$ ). The acceleration from the buoyant force is  $F_B/m_p \approx 1$  cm/s<sup>2</sup>, and using Eq. (2.4) we see that at  $\Omega = 3$  rad/s, the maximum acceleration is 3.6 cm/s<sup>2</sup>. At  $\Omega = 6$  rad/s, the maximum acceleration can be 14 cm/s<sup>2</sup>. Thus, the added mass force can be fairly significant when the drag force disappears. These estimates may overemphasize  $F_{AM}$ , as typically the drag force is significant and acts to reduce the accelerations caused by  $F_C$ . By inspecting Eq. (2.1) it can be seen that the effect of the added mass force is to effectively increase the mass of the particle, that is, it decreases the acceleration of the particle

in response to the forces on the right hand side of Eq. (2.1). This is useful for helping the particle track the flow; forces which would cause the particle not to follow the flow act on a larger effective mass, that is, they must accelerate a small volume of fluid around the particle as well as the particle itself.

Next we consider the Basset history force, named after Basset despite Boussinesq’s derivation of this force 3 years prior to Basset [90]. This force is a viscous force arising from unsteady relative acceleration [39]:

$$F_{BH} = 6a^2 \rho_f \sqrt{\pi\nu} \int_0^t \frac{(du_p/d\tau)d\tau}{\sqrt{t-\tau}} \quad (2.6)$$

where  $u_p$  is the relative velocity of the particle. This force is from “the effect of the deviation in flow pattern from steady state” [55], and is caused by the flow readjusting to the particle motion when the particle is accelerated.

It is difficult to estimate the magnitude of this term due to the integral. We make the assumption that the history is important only for a time  $T$ : the integral only needs to be evaluated for times  $t - T < \tau < t$ . We further assume that  $du_p/d\tau$  is constant (a dubious assumption). We then estimate that  $F_{BH} = F_B$  when  $du_p/dt \approx 0.094/\sqrt{T}$  cm/s<sup>2</sup> (measuring  $T$  in seconds). A guess for  $T$  is 1 s, suggesting that even small accelerations  $O(0.1$  cm/s<sup>2</sup>) can result in a significant contribution of  $F_{BH}$  to the total force. It is likely that this is an overly conservative estimate; numerical work provides evidence that  $F_{BH}$  is typically small [39] compared to the other forces. Fluctuations of  $du_p/dt$  would result in a much smaller  $F_{BH}$ . Note that by decreasing  $a$  (the radius of the particle)  $F_{BH}$  decreases quickly, especially compared to the drag force; the larger the drag force is relative to the other forces, the more the particle acts as a passive tracer.

The lift force acting on a rotating particle<sup>1</sup> is proportional to the velocity gradient in the fluid normal to the direction of particle motion [135]. This force is more important very close to walls [90], which is not an important consideration

---

<sup>1</sup>a particle rotating relative to the fluid, not necessarily a particle in a rotating experiment.

for our experiment as often particles close to walls cannot be seen by the camera due to reflections from the walls and parallax problems with the camera. The nondimensional Taylor number  $Ta = \Omega a^2/\nu$  is a measure of the importance of particle rotation, where here  $\Omega$  is rotation relative to the fluid. For  $a = 0.05$  cm and  $\nu = 0.01$  cm<sup>2</sup>/s,  $\Omega$  must be  $O(\pi$  rad/s) for  $Ta \sim 1$ . It is unlikely our particles are rotating this quickly relative to the fluid. It is not clear that lift forces need to be considered for flows far from walls, where the velocity gradients are gentler [90].

The preceding discussion only provides estimates, and some of the numbers are arbitrary. Several additional caveats are necessary. Equation (2.1) is only correct in the limit  $Re \rightarrow 0$ , that is, the relative velocity  $u_p$  is very small. For finite  $u_p$  this equation can be modified with empirically determined corrections [90], although this only works for small  $Re$ . The empirical corrections increase  $F_D$  by a factor of  $(1 + 0.15Re^{0.667})$ , decrease  $F_{AM}$ , and increase  $F_{BH}$ ; the latter two forces are modified by terms related to the nondimensional acceleration of the particle rather than  $Re$ . Another important consideration is that almost all of the work done studying particle transport has been for spherical particles. Studies considering simple elliptical particles suggest that non-spherical particles cannot be merely considered as spherical particles with an equivalent radius, as has been done in the estimates above. However, there are no methods yet to be used for non-spherical particles [90].

An encouraging fact is that many numerical experiments strongly suggest that neutrally buoyant particles are excellent tracers, even with a finite size [39, 121]. To further improve our particles, we should use smaller particles if possible, and work to find particles that are closely density matched. Also, spherical particles would make the above estimates more applicable, to increase our confidence that the particles are passive tracers. It is also clear that when possible, experiments should be conducted at a lower rotation rate, although of course this increases the



Rossby and Ekman numbers and decreases the two-dimensionality of the flow. It is likely that measurements at large  $Re$  will be for  $\Omega/2\pi$  up to 5 Hz, in which case the centrifugal force will impose more stringent conditions on the density of particles.

## 2.4 Calculating Stream Functions

As discussed in Sec. 1.12, the velocity field of an incompressible two-dimensional fluid flow can be represented by a stream function  $\psi(x, y, t)$ . If the stream function is known, then the velocity field is given by  $\vec{u}(x, y, t) = \vec{\nabla} \times (\psi(x, y, t)\hat{z})$  (where  $\hat{z}$  is the unit vector in the  $z$  direction). The contours of the stream function give an indication of the flow pattern, and the spacing of the contours give an indication of the strength of the flow: closely spaced contour lines correspond to stronger velocities (similar to the lines in a two-dimensional electric field line diagram [162]).

We use the method of least squares to derive stream functions from experimental data. The particle trajectories obtained using the method discussed in Sec. 2.2 are analyzed to find velocities, which are then time-averaged before the least-squares routine is used; this is discussed in more detail below.

### 2.4.1 Basis Functions

The basis functions were chosen to match the boundary conditions of the experiment, an annular shape with inner (outer) radius 10.8 cm (43.2 cm). For some experiments, the Plexiglas barrier was in place which restricted the flow to an inner radius of 18 cm. A tensor product basis was used,  $\{\psi_{mn}(r, \phi)\} = \{R_m(r)\} \otimes \{\Phi_n(\phi)\}$ . The zero-flux boundary condition is:

$$u_r(r_{\text{in}}) = u_r(r_{\text{out}}) = \left(\frac{1}{r}R_m\frac{d\Phi_n}{d\phi}\right)\Big|_{r_{\text{in or out}}} = 0. \quad (2.7)$$

To satisfy this condition,  $R_m(r)$  must be zero on the inner and outer boundaries, or  $\Phi(\phi)$  must be a constant. An additional boundary condition is the no-slip condition:

$$u_\phi(r_{\text{in}}) = u_\phi(r_{\text{out}}) = -\left(\Phi_n \frac{dR_m}{dr}\right)\Big|_{r_{\text{in}} \text{ or } r_{\text{out}}} = 0. \quad (2.8)$$

To satisfy the no-slip condition, the first derivative of  $R_m$  should also go to zero on the boundary. We choose to relax the no-slip condition and demand basis functions to only satisfy the zero-flux condition. Often the flow is considered in a reference frame which rotates slowly relative to the tank frame of reference, and in such a reference frame the no-slip condition is “violated” with respect to a stationary wall. In such rotating reference frames the flow has a fixed non-zero velocity at the boundaries, and to allow the stream function program to be as general as possible it is useful to allow for slip boundary conditions. This works reasonably well; see the discussion in Sec. 2.4.4.

Trigonometric basis functions are used. Specifically,

$$\psi_{mnl} = R_m(r)\Phi_{n,l}(\phi), \quad (2.9)$$

with the radial basis functions given by

$$R_m(r) = \sin\left(m\pi\left(\frac{r - r_{\text{in}}}{r_{\text{out}} - r_{\text{in}}}\right)\right) \equiv \sin(mC(r - r_{\text{in}})) \quad (2.10)$$

(with  $C \equiv \pi/(r_{\text{out}} - r_{\text{in}})$ ) and the azimuthal basis functions given by

$$\begin{aligned} \Phi_{n,l=0}(\phi) &= \sin(n\phi) \\ \Phi_{n,l=1}(\phi) &= \cos(n\phi). \end{aligned} \quad (2.11)$$

The radial index  $m$  ranges from 1 to  $M$ , and the azimuthal index  $n$  ranges from 0 to  $N$  (with the function  $\Phi_{0,0} = 0$  unused;  $\Phi_{0,1} = 1$  is used). Thus there are  $(2N + 1)M$  total trigonometric basis functions.

Special consideration is needed for the case with  $n = 0$ , that is, when  $\Phi_{0,1} = 1$  is the azimuthal basis function. In such cases the zero-flux condition (Eq. (2.7))

holds for any function  $R(r)$ . This situation can be considered as a one-dimensional function  $R^*(r)$  being approximated by a set of basis functions  $R_m(r)$ . In fact, for  $M \rightarrow \infty$  the set of trigonometric basis functions considered above (Eq. (2.10)) is a complete set and can perfectly approximate  $R^*(r)$ . However, for finite  $M$ , it is difficult to approximate a function  $R^*(r)$  where  $R^*(r_{\text{in}}) \neq R^*(r_{\text{out}})$ , as for each individual basis function  $R_m(r_{\text{in}}) = R_m(r_{\text{out}}) = 0$ , and it is only in the limit that an infinite number of these basis functions are used that the endpoints can be nonzero<sup>2</sup>.

This is not merely a mathematical technicality but also an important problem for approximating experimental stream functions. The condition  $\psi(r_{\text{in}}) \neq \psi(r_{\text{out}})$  means that there is net azimuthal flux carried around the annulus:

$$\text{Net Flux} = \int_{r_{\text{in}}}^{r_{\text{out}}} dr u_\phi(r, \phi_0) = \int_{r_{\text{in}}}^{r_{\text{out}}} dr \left( -\frac{\partial \psi(r, \phi_0)}{\partial r} \right) = \psi(r_{\text{in}}, \phi_0) - \psi(r_{\text{out}}, \phi_0) \quad (2.12)$$

where  $\phi_0$  is arbitrary because of the incompressibility condition. In order to aid the approximation, we add an additional basis function:

$$\psi_{001} = R_0(r) = Cr \quad . \quad (2.13)$$

(The constant  $C$  makes the basis function dimensionless.) Thus any function  $R^*(r)$  can be rescaled by a linear transformation to a new function that is zero on the endpoints, and such a function is typically easy to approximate using our original set of basis functions (Eq. (2.10)). This linear rescaling is accomplished by adding in this extra basis function which can be used in the least squares routine. (Note that a basis function which is just a constant is not needed, as the stream function is arbitrary to within a constant.)

Now there are  $(2N + 1)M + 1$  basis functions which serve as a reasonable approximation to the complete space of functions satisfying the zero-flux boundary conditions on an annulus. Note that there may be better choices of basis functions

---

<sup>2</sup>Mathematically,  $\lim_{r \rightarrow r_{\text{end}}} \lim_{M \rightarrow \infty} \sum_{m=1}^M c_m R_m(r) = R^*(r_{\text{end}})$  for the two endpoints, with the proper coefficients  $c_m$ .

in the radial direction which would simplify some of the mathematical operations discussed below [20]; in particular, radial basis functions which are orthogonal to each other would be useful.

### 2.4.2 Least Squares Analysis

The approximate solution is:

$$\tilde{\psi}(r, t) = \sum_{m,n,l} c_{mnl} \psi_{mnl}(r, t). \quad (2.14)$$

We want to minimize the integral:

$$I = \int_A dA \left| \vec{u}_{\text{experiment}} - \vec{\nabla} \times (\tilde{\psi} \hat{z}) \right|^2 = \int_A dA \left[ \left( u_r - \frac{1}{r} \frac{\partial \tilde{\psi}}{\partial \phi} \right)^2 + \left( u_\phi + \frac{\partial \tilde{\psi}}{\partial r} \right)^2 \right] \quad (2.15)$$

with respect to the coefficients  $c_{mnl}$ ;  $\int_A dA = \int_0^{2\pi} \int_{r_{\text{in}}}^{r_{\text{out}}} r dr d\phi$ . This produces:

$$\begin{aligned} \frac{\partial I}{\partial c_{m'n'l'}} = \int_A dA & \left[ \left( -\frac{1}{r} R_{m'} \frac{d\Phi_{n'l'}}{d\phi} \right) \left( u_r - \frac{1}{r} \sum_{mnl} c_{mnl} R_m \frac{d\Phi_{nl}}{d\phi} \right) \right. \\ & \left. + \left( \Phi_{n'l'} \frac{dR_{m'}}{dr} \right) \left( u_\phi + \sum_{mnl} c_{mnl} \Phi_{nl} \frac{dR_m}{dr} \right) \right] = 0 \quad . \end{aligned} \quad (2.16)$$

Two useful integrals are:

$$\int_0^{2\pi} d\phi \Phi_{n_1, l_1} \Phi_{n_2, l_2} = \pi \delta_{n_1, n_2} \delta_{l_1, l_2} (1 + \delta_{n_1, 0}) \quad (2.17)$$

and

$$\int_0^{2\pi} d\phi \frac{d\Phi_{n_1, l_1}}{d\phi} \frac{d\Phi_{n_2, l_2}}{d\phi} = \pi \delta_{n_1, n_2} \delta_{l_1, l_2} n_1^2, \quad (2.18)$$

where  $\delta_{jk}$  is the Kronecker delta symbol,  $\delta_{jk} = 1$  if  $j = k$  and 0 otherwise. Using these two integrals Eq. (2.16) can be rewritten as:

$$\begin{aligned} \int_A dA \left( \frac{1}{r} R_{m'} \frac{d\Phi_{n'l'}}{d\phi} u_r - \frac{dR_{m'}}{dr} \Phi_{n'l'} u_\phi \right) = \\ \pi \sum_m c_{mn'l'} \int_{r_{\text{in}}}^{r_{\text{out}}} r dr \left[ \frac{n^2}{r^2} R_m R_{m'} + (1 + \delta_{n', 0}) \frac{dR_m}{dr} \frac{dR_{m'}}{dr} \right]. \end{aligned} \quad (2.19)$$

If we define the following two constants:

$$A_{m_1 m_2} \equiv \int_{r_{\text{in}}}^{r_{\text{out}}} r dr \left( \frac{1}{r} R_{m_1} \right) \left( \frac{1}{r} R_{m_2} \right)$$

$$B_{m_1 m_2} \equiv \int_{r_{\text{in}}}^{r_{\text{out}}} r dr \frac{dR_{m_1}}{dr} \frac{dR_{m_2}}{dr} \quad , \quad (2.20)$$

then Eq. (2.16) can be further simplified as:

$$\int_A dA \left( \frac{1}{r} R_{m'} \frac{d\Phi_{n'l'}}{d\phi} u_r - \frac{dR_{m'}}{dr} \Phi_{n'l'} u_\phi \right) = \pi \sum_m c_{mn'l'} (n'^2 A_{mm'} + (1 + \delta_{n',0}) B_{mm'}) . \quad (2.21)$$

This is a system of  $(2N + 1)M + 1$  equations for the  $(2N + 1)M + 1$  unknowns  $c_{mnl}$ . The left hand side of this equation depends on the data  $u_r$  and  $u_\phi$  obtained from the particle trajectories. To solve using Gaussian elimination would take  $O(8N^3 M^3)$  operations. However, for fixed values of  $n$  and  $l$ , this can be regarded as  $M$  equations for the  $M$  unknowns  $c_{mnl}$  (with an additional equation and unknown for  $n = 0$ , for the additional basis function  $\psi_{001} = Cr$ ), and thus the entire system of  $(2N + 1)M + 1$  unknowns can be solved in  $O(2NM^3)$  operations. The matrices  $A_{m_1 m_2}$  and  $B_{m_1 m_2}$  are precomputed to decrease the overall computation time.

Typically we use  $M = 9$  and  $N = 17$ , resulting in 316 basis functions total. These choices for  $M$  and  $N$  are somewhat arbitrary. Trials with more basis functions did not appear to improve the results, while fewer basis functions did not produce pictures that were convincing. In general the results were not very sensitive to the number of basis functions.

### 2.4.3 Preprocessing of Data

Difficulty was encountered in evaluating the left hand side of Eq. (2.21). This integral depends on the experimental data, which do not fully cover the annular region of integration. The first method tried was to approximate this integral by summing over all of the data and normalizing by the number of data points. This was somewhat analogous to a Monte Carlo integration technique. However, this method failed to work as well as desired. The distribution of data points in the integration region was nonuniform, with sparse data near the inner and outer edges of the

annulus due to lighting problems. While this produced stream function pictures that looked qualitatively correct, the azimuthal velocity of the flow along the edges was incorrect. Typically this velocity showed large fluctuations and was too large by an order of magnitude in the approximate solution.

A second method would be to interpolate the data onto a uniform mesh that covers the entire domain. This is difficult in some ways, as some locations have very little data to interpolate from. We use this method as a pre-processing once the velocity data are obtained. This unfortunately gives equal weight to regions with few data and regions with lots of data. In some regions, it is possible that a velocity datum is determined by only one trajectory, while other regions are covered by many trajectories which are then averaged to find the velocity at each point on the uniform mesh.

We then consider all of the integrals as sums over the data points. We originally considered replacing the right hand side of Eq. (2.21) by a calculation, rather than using the analytical expressions. This would result in a large, full matrix, however, and would increase the amount of calculation necessary back to  $O(8N^3M^3)$ . A compromise solution is to assume that the angular integrals can be calculated analytically, while the radial integrals could be computed by summing over the data. This is a reasonable compromise, as the data are fairly evenly distributed over the angular direction; the nonuniform distribution is primarily in the radial direction. This “compromise” method is the method that we use. For sparse data sets it would be necessary to do the full computation if the data are nonuniform in the angular direction; we do not compute any stream functions for sparse data sets.

A possible improvement to the program would be to use the velocity data to interpolate locally to spline functions; then the integrations could be done analytically.

Note that due to a general lack of instantaneous data, instantaneous stream

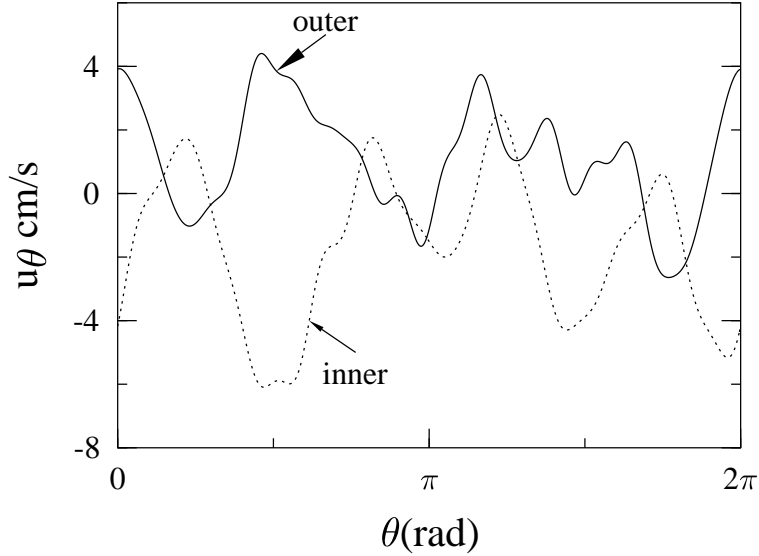


Figure 2.3: Azimuthal velocity at outer wall (solid line) and inner wall (dashed line). Due to insufficient data, the velocity does not go to a constant at the walls. These data correspond to Fig. 5.3(b), the blocked flow. (The no-slip condition corresponds to a velocity  $u_\theta = 0$  for these data.)

functions cannot be obtained. The stream functions shown in this dissertation are exclusively time-averaged stream functions. An improved particle visualization system could probably be used to find instantaneous or quasi-instantaneous stream functions using the current stream function programs (see Appendix B).

#### 2.4.4 No-slip boundary condition

In general the velocity of the approximated solution along the inner and outer walls is moderately consistent with a no-slip boundary condition in the appropriate rotating frame of reference. Figure 2.3 shows an example of the velocity found at the walls. While the velocity is fluctuating, the fluctuations are smaller than the velocities in the bulk (  $\sim 10\text{--}20$  cm/s).

It is possible to modify the least-squares program to enforce a no-slip bound-

ary condition, without changing the basis functions. The easiest way to impose the boundary condition is through the use of a penalty term added to  $I$  (Eq. (2.15)) [20]. Consider a new term  $I'$  to be minimized:

$$I' = I + A \int_0^{2\pi} d\phi [(\tilde{u}_\phi(r_{\text{in}}, \phi) - u_\phi^{\text{no-slip}}(r_{\text{in}}))^2 + (\tilde{u}_\phi(r_{\text{out}}, \phi) - u_\phi^{\text{no-slip}}(r_{\text{out}}))^2]. \quad (2.22)$$

The velocities  $u_\phi^{\text{no-slip}}$  are determined by the reference frame that the no-slip boundary condition must hold in, and the constant  $A$  gives the relative weight to be attached to the no-slip boundary condition.  $\tilde{u}_\phi = -\partial\tilde{\psi}/\partial r$  is the azimuthal velocity determined from the approximate solution. Thus, by minimizing  $I'$  an attempt to minimize the new integral term will help impose a no-slip boundary condition. By increasing  $A$ , added importance will be given to satisfying this boundary condition, at the expense of best satisfying the fit to the data in the bulk region.

## 2.5 Hot film probes

The particle tracking methods discussed in Sec. 2.2 are best for obtaining time averages of the velocity field at all points in space. To measure the time dependence of the velocity at a given point, we use hot film probes. Hot film probes are constructed by placing a thin film of conductive material over a quartz fiber, and then coating the conductor with an insulator. The resistance of the conductor is strongly temperature dependent. As fluid flows past the probe, it cools the resistor (with the rate of cooling related to the velocity of the flow). By measuring the resistance of the probe, the velocity of the fluid is obtained. The outer insulator coating prevents electrolysis of the fluid.

We have several holes in the annulus lid to insert the probes. They are at the same radii as the forcing holes (Sec. 2.1), at 18.9 cm, 27.0 cm, and 35.1 cm. We use TSI model 1210-60W probes, a general purpose probe. These probes are designed to measure one component of the velocity. We orient them to measure azimuthal



velocities, as usually our forcing creates a strong azimuthal flow. Additionally, for the turbulence experiments discussed in Chap. 6, we use X-array probes (TSI models 1240-60W, 1243-60W). These allow measurement of two components of the velocity, in the plane of the crossed probe fibers. The two different models are used to measure flow in the horizontal plane (azimuthal and radial directions) and the vertical plane (azimuthal and vertical directions). The resolution of these probes is set by the wire length of the probe, which is 2 mm.

The probes require fairly high levels of power as their resistance is typically  $\sim 5\Omega$  and the voltage applied to the probes is  $O(1\text{ V})$ . Originally we used a pair of lock-in amplifiers (models PAR 121, PAR 124) to measure two separate probes. One lock-in provides a 9 kHz signal. This is amplified and sent to the rotating annulus through a pair of slip rings. The probes each form part of Wheatstone bridges, which are powered by the amplified 9 kHz signal. The bridge outputs are returned back through a pair of slip rings each, pass through a transformer, and back to the lock-in amplifiers. The lock-in amplifiers are adjusted to be maximally sensitive to fluctuations in the bridge signal. The lock-ins provide a voltage which is read by a computer (see below). As the signals of interest are typically of low frequency (less than 0.5 Hz), the lock-ins are used with a time constant of 1 s to reduce high frequency noise.

A computer with a National Instruments AT-MIO-16 card is used to collect the hot film probe data (both a 386 and a Pentium have been used). Muhammad Ali Bawany has written a data acquisition program which reads the analog-to-digital inputs of the NI card.

More recently we have replaced the lock-in amplifier system with a a system allowing more than two hot film probes to be used. This change was motivated by the desire to use the X-array probes, each with two sensors which need to be measured. To use two X-array probes (or four regular probes) would require four

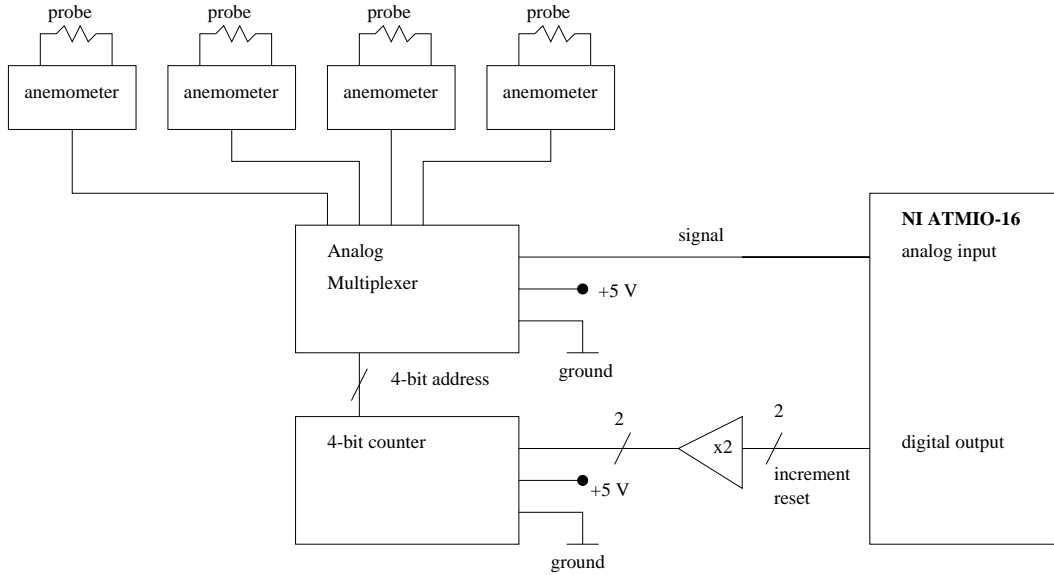


Figure 2.4: Schematic diagram of multiplexed hot film probe system. The NI ATMIO-16 board is in a Pentium computer.

lock-in amplifiers, and an additional four slip rings for the additional Wheatstone bridges. We have installed four constant temperature anemometers (TSI models 1053B and 1750) on the rotating annulus, which read the hot film probes. These replace the lock-in amplifiers of the previous system. Power is provided to these anemometers by a TSI model 1051-6 power supply. The anemometers provide a voltage corresponding to the flow rate.

Eshel Faraggi has built a multiplexer circuit which multiplexes the analog voltages from these anemometers (Fig. 2.4). Thus, as many as eight separate voltages can be read through one slip ring (although four extra slip rings are needed to power and control the multiplexer). Currently this system is set up for four anemometers, and the remaining multiplexer inputs could be used for other purposes if necessary. Faraggi has extended Bawany's original data acquisition program to control the multiplexer.

## 2.6 Ultrasound probe

Particle tracking reveals the time-averaged horizontal velocity field, and hot film probes measure the velocity at particular points. In order to measure the vertical velocity component along a line, we have installed an ultrasound Doppler probe. This probe emits pulses of ultrasound and also receives the reflections of the ultrasound pulses from particles. The information from the reflections gives the velocities and positions of the particles, relative to the probe. Our probe is attached to the lid and aimed straight down at the bottom of the tank, and so measures the vertical velocities of particles in a column of fluid beneath the probe. We are *not* using a Doppler shift method ([141, 142, 143]); instead, our system uses the phases of the reflected ultrasonic pulses to precisely locate the particles in order to determine the velocity.

### 2.6.1 Ultrasound hardware

Ultrasound probes are typically made of piezoelectric material. Such material physically deforms when a voltage is applied. Thus, by applying a radio-frequency signal (RF) the probe emits ultrasonic waves. Piezoelectric materials also generate a voltage when deformed by external forces, and so by turning off the RF voltage to the probe, the probe acts as a receiver for any reflected ultrasound.

We use two probes. The first is a Matec model IM-1025-R probe, a cylindrical probe with a diameter  $D = 0.8$  cm and a resonant frequency of 10 MHz. The second is a Matec model IP-0502-GP probe, a cylindrical probe with the same diameter and a resonant frequency of 5 MHz. Typically we use the 5 MHz probe at its resonant frequency. The attenuation of sound in water at 25° C is  $\alpha = (46.0 \times 10^{-15})f^2$ ; the power decreases as  $e^{-\alpha x}$  at a distance  $x$  from the probe [2] ( $f$  is the frequency). Thus, the power attenuation in dB for an ultrasonic pulse traveling to the bottom of the tank and back to the probe ( $x = 40$  cm) is given by  $0.075f^2$  when  $f$  is measured

in MHz. At 5 MHz, 1.9 dB of attenuation occurs (the power has decreased by a factor of 1.5). At 10 MHz, the attenuation is 7.5 dB (the power has decreased by a factor of 5.5).

As the speed of sound in water is  $c = 1.5 \times 10^5$  cm/s, the wavelength is  $\lambda = c/f = 0.03$  cm, allowing for high spatial resolution. The divergence half-angle from a circular source is  $\phi_d = \sin^{-1}(1.22\lambda/D) = 2.6^\circ$  [27], so the volume measured is a truncated cone extending from the probe, at the lid with diameter  $D = 0.8$  cm, to the bottom of the annulus, 18.7 cm below the probe, with diameter 0.9 cm. These are only approximate numbers, as the field has a complicated shape in actuality [27].

We use a Matec model GA-822 system to generate the RF pulses and to amplify and measure the reflected signal. This system generates a specified number of cycles of RF, typically 40, which is sent to the probe (duration  $\tau_{\text{width}} = 40/f$ ). The RF signal is then quickly (within  $1/f$ ) switched off and the probe then acts as a receiver. The reflections seen by the probe are amplified by the Matec system. The reflected signal is then compared with the original RF signal, and also the original signal phase shifted  $90^\circ$ . The two outputs are low-pass filters for the reflected signal, extracting the amplitude of the signal in phase with the original signal, and the amplitude of the signal  $90^\circ$  phase shifted. (Thus, the reflected signal is proportional to  $v_a \cos(\omega t) + v_b \cos(\omega t + 90^\circ)$ .) The Matec system generates bursts of ultrasound with a specified between-burst interval (see Fig. 2.5). Typically many reflections are seen from one particle before it leaves the cone of ultrasound, and by using information from subsequent reflections from one particle, the velocity of that particle is determined (as discussed below). Typically the spacing between ultrasound bursts is 4000 cycles of the RF signal ( $\tau_{\text{spacing}} = 4000/f$ ). The parameters  $\tau_{\text{width}}$  and  $\tau_{\text{spacing}}$  (Fig. 2.5) are set using a GPIB interface to the Matec system.

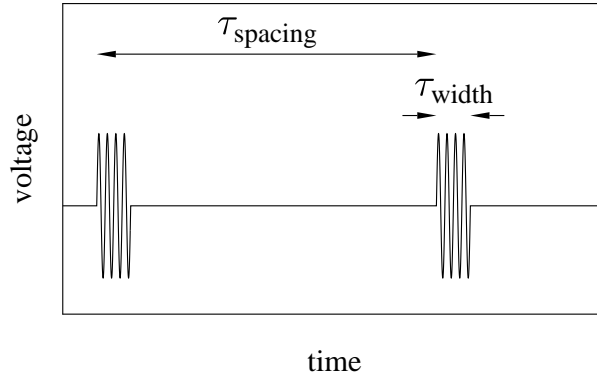


Figure 2.5: Schematic diagram showing definition of  $\tau_{\text{spacing}}$  and  $\tau_{\text{width}}$  from Matec box. Typically the frequency used is  $f = 5 \text{ MHz}$ ,  $f\tau_{\text{spacing}} = 4000 = 800 \mu\text{s}$ , and  $f\tau_{\text{width}} = 40 = 8 \mu\text{s}$ . The round-trip transit time for a pulse in the experiment is  $260 \mu\text{s}$ ; a pulse width of  $8 \mu\text{s}$  corresponds to a pulse length of  $1.2 \text{ cm}$ .

### 2.6.2 Ultrasound software

The signals from the Matec system are measured by a WAAG II data acquisition card from Markenrich Corporation, using a 486 computer. The data acquisition program was originally written by Paul Umbanhowar, and was modified to improve performance in the presence of noise. The WAAG card has two data acquisition channels, measuring the  $0^\circ$  phase component (channel A) and the  $90^\circ$  phase component (channel B).

We use a “buffer rod” provided by Matec (model BR-30) to test the ultrasound system. When a single burst of RF is sent into the buffer rod, the rod provides several ( $\sim 12$ ) distinct reflections. These appear similar to reflections that would be seen from twelve particles at different distances from the probe; as the buffer rod does not ever change, the reflections always occur at the same location and thus appear as non-moving particles. The buffer rod provides clean data to test our data acquisition software.

Figure 2.6 shows reflections from the buffer rod. Raw data measured by channel A is shown in Fig. 2.6(a). A series of ten reflection groups is read in by the

WAAG card. A section of one reflection group is shown in Fig. 2.6(b): each pulse is one reflection. The time  $t$  each reflection is seen is related to the particle position  $x$  by the speed of sound  $c$ :

$$x = ct/2 \quad ; \quad (2.23)$$

the ultrasound pulse travels twice the distance to the particle, as it travels to the particle and then back to the probe, which is why the factor of 1/2 is needed.

The raw data from channels A and B is processed to determine the phase of each reflected pulse. The amplitude is given by  $v = \sqrt{v_a^2 + v_b^2}$ , shown in Fig. 2.6(c). This can be used to determine when a reflection has occurred (the amplitude will be large). The phase is given by  $\phi = \text{Arctan}(v_b/v_a)$ . In practice,  $v_a$  and  $v_b$  vary somewhat across the pulse (as can be seen in Fig. 2.6(b)), but  $\phi$  is steady for the duration of each reflected pulse (Fig. 2.6(d)).  $\phi$  is not as steady at the beginning and end of each reflected pulse, so to determine the phase of a given pulse,  $\phi$  is averaged over the pulse excluding the endpoints. As the pulse width (duration) generated by the Matec system is fixed and set by the user, this information is used to scan the amplitude signal (Fig. 2.6(c)) to find the beginning and end of each pulse. In practice, we set a threshold of 0.4 V; a valid pulse has an amplitude above this threshold for the duration of the pulse.

To find the velocity, the phases of each reflection from the same particle are examined. Figure 2.7(a) shows the phase of ten reflections from the same pulse. The phase is less well-determined compared with Fig. 2.6(d) as this is a real particle, not the buffer rod. By averaging the phase within each reflection (disregarding the endpoints of the pulse), and finding the least-squares fit to a line (Fig. 2.7(b)), the velocity of the particle can be determined. The standard deviation of the phase within each reflection is used as an uncertainty of the phase for that reflection, which is then used for the least-squares fit. The least-squares fit provides an uncertainty for the velocity as well as a  $\chi^2$  statistic; these are used to determine whether or not

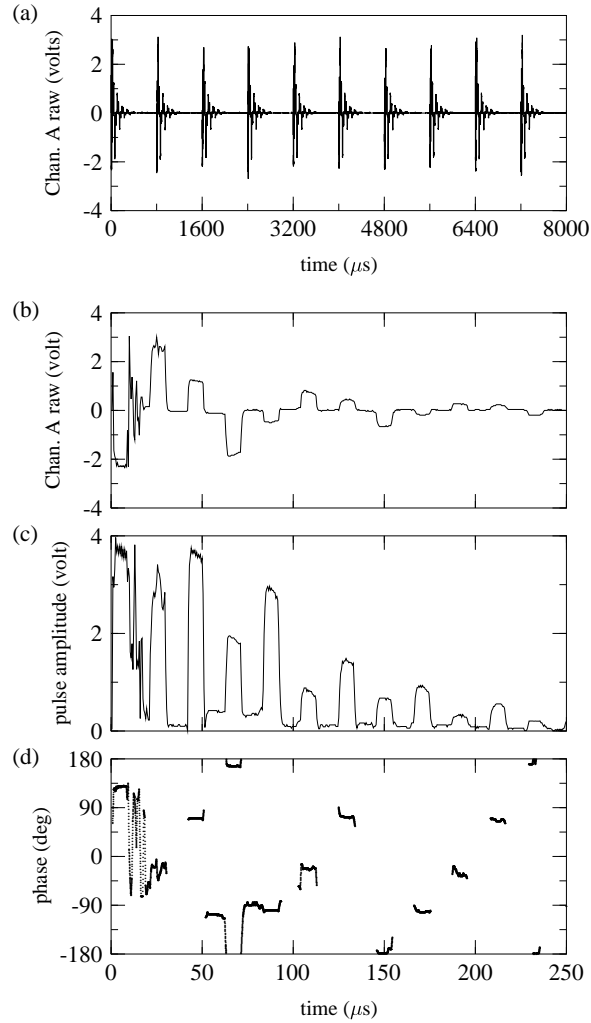


Figure 2.6: Reflections from the Matec buffer rod. Ten bursts of ultrasound with spacing  $\tau_{\text{spacing}} = 800 \mu s$  and width  $\tau_{\text{width}} = 8 \mu s$  are sent into the buffer rod; each burst reflects multiple times. (In the annulus, the maximum round-trip travel time is  $260 \mu s$ .) Normally each reflection corresponds to a particle; here the pulses are internal reflections from the buffer rod. (a) The ten sets of reflections, used for a velocity measurement. The voltage  $v_a$  is proportional to the  $0^\circ$  phase component of the reflected wave (for channel A, pictured). (b) A close-up view of the first reflection group from (a). (c) The amplitude of the reflected pulses from (b); the amplitude is given by  $v = \sqrt{v_a^2 + v_b^2}$ . (d) The phase  $\phi = \text{Arctan}(v_b/v_a)$  for each reflected pulse from (b); the phase is only plotted for points with an amplitude larger than 0.2 volts, an arbitrary cutoff.

that measurement is valid [112]. The velocity  $u$  is given by

$$u = \frac{1}{2} \frac{d\phi}{dt} \frac{\lambda}{2\pi} = \frac{d\phi}{dt} \frac{c}{4\pi f} \quad . \quad (2.24)$$

For the particle shown in Fig. 2.7,  $u = 0.75 \pm 0.03$  cm/s.

### 2.6.3 Choosing parameters

There are several somewhat arbitrary parameters: the pulse width  $\tau_{\text{width}}$ , the pulse spacing  $\tau_{\text{spacing}}$ , and the frequency  $f$ . Increasing  $\tau_{\text{width}}$  allows for a more accurate determination of the phase. However, particles within a distance of  $(c\tau_{\text{width}})$  can be confused. This distance is 1.2 cm for typical parameters  $f = 5$  MHz and  $\tau_{\text{width}} = 8\mu\text{s}$  (40 cycles of the RF signal). Estimating that particles should be at least 2.4 cm apart for the ultrasound system to resolve them, approximately 7000 particles could be put in the experiment without causing problems.

The pulse spacing  $\tau_{\text{spacing}}$  affects the velocity determination. As  $\tau_{\text{spacing}}$  is increased, slower velocities can be determined accurately as the particle has moved farther between each ultrasound burst. However, the particle must remain in the cone of ultrasound while the measurement occurs, placing a restriction on the horizontal velocity based on  $\tau_{\text{spacing}}$ . Typically we use ten reflections to determine the velocity of a particle, so the particle must remain inside the measurement region for at least  $10\tau_{\text{spacing}}$ . The measurement region is  $O(1$  cm) wide, and so the horizontal speed of the particle must be less than  $1 \text{ cm}/(10\tau_{\text{spacing}}) \approx 125$  cm/s. This is a generous estimate as many particles do not cross through the widest point. As  $\tau_{\text{spacing}}$  is increased the horizontal speeds are further restricted.

The frequency can be varied independently of  $\tau_{\text{width}}$  and  $\tau_{\text{spacing}}$ . Increasing the frequency decreases the wavelength and thus improves the spatial resolution (aiding in determining the velocity; see Eq. (2.24)). However, increasing the frequency also increases the attenuation of the signal, as discussed above.



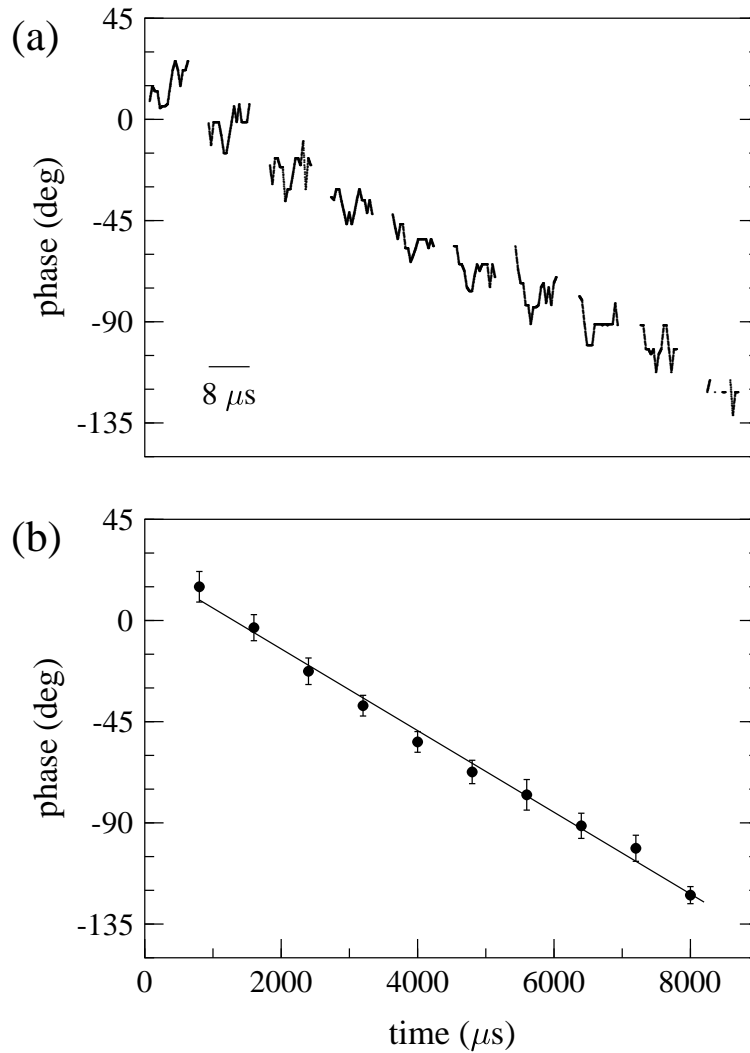


Figure 2.7: (a) The phase measured in ten reflections from the same particle. The pulses are spaced at  $800 \mu\text{s}$ , shown in (b), and are  $8 \mu\text{s}$  wide. A bar of length  $8 \mu\text{s}$  is drawn to show the time scale for each pulse, but the inter-pulse spacing is not to scale. (b) By averaging the phase from each pulse shown in (a), a least-squares fit to the data can be used to find the velocity of the particle. The line has a slope  $d\phi/dt = -0.018^\circ/\mu\text{s}$ . The error bars are from the standard deviation of the phase for each pulse.

#### 2.6.4 Clock signal box

An important consideration is the digitization rate of the WAAG card. The faster the signals from the Matec box are digitized, the more points are available to be used to determine the phase of a given pulse, thus decreasing errors. However, the WAAG card is limited to 128 kB of memory. When using the built-in clock on the WAAG card, the data acquisition rate can be no faster than 2 MHz (the only faster clock available on the WAAG card is 20 MHz). With a fixed data acquisition rate of 2 MHz, the number of points per pulse is  $\tau_{\text{width}}/0.5 \mu\text{s}$ .

Paul Umbanhowar has built a system which can be used to increase the data acquisition rate. The principle of this box is illustrated in Fig. 2.8. The Matec system generates a square wave at the frequency of the ultrasound. It also produces a short pulse (on the pulse width monitor output) which signals the beginning of the transmitted ultrasound burst. These two signals are sent into Umbanhowar's clock signal box. The output of the clock signal box is sent to the WAAG external clock input. The clock signal box starts with the WAAG clock signal off. When the Matec signals the beginning of an ultrasound burst, the clock signal box starts counting clock cycles. After a set number, the clock signal box produces a fixed number of clock pulses, after which it resets (see Fig. 2.8).

The WAAG card, when using the external clock, waits for the external clock to go high before taking a data point. Thus, when the external clock is off (held low by Umbanhowar's clock signal box), the WAAG card does not acquire data. When the clock signal box is passing through a clock signal, the WAAG card acquires data. As the clock signal box is using the ultrasound frequency for its clock, the data acquisition occurs at the faster rate  $f$  of the ultrasound (typically 5 MHz) rather than the slower rate of the internal WAAG clock (2 MHz).

The purpose of turning the external clock on only for a short duration is twofold. First, a smaller amount of data is acquired, which easily fits in the WAAG

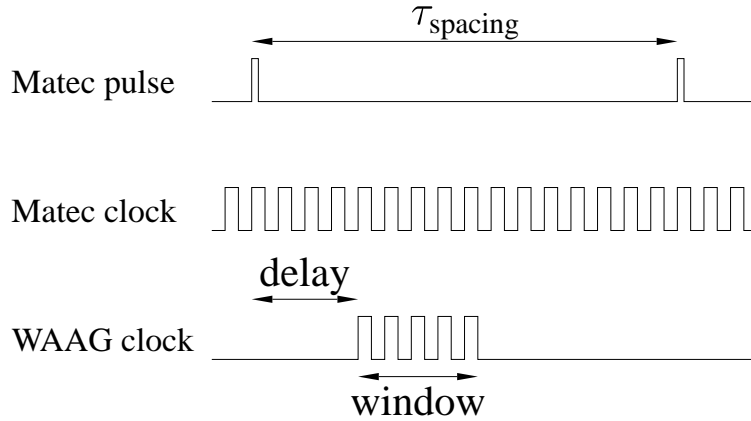


Figure 2.8: The clock signal box takes two inputs, the clock signal from the Matec box (a square wave with the frequency of the ultrasound pulses) and the pulse signal from the Matec box (a short pulse which occurs when the Matec box generates a burst of ultrasound). The output is a modified clock signal which is sent to the WAAG card (bottom time series). The modified clock signal starts a set number of clock cycles after receiving the Matec pulse signal, and it lasts for a set duration.

128 kB memory. The memory restriction is the chief problem preventing a faster clock from being used, and by turning the external clock off for large portions of time, less data is acquired. Second, the clock signal box can be adjusted to only generate a clock signal when useful data should be taken. The round-trip transit time for an ultrasound burst in the experiment is  $260 \mu\text{s}$ ; the typical pulse spacing is  $\tau_{\text{spacing}} = 800 \mu\text{s}$ . Thus useful data is only available for a quarter of the time. Also, for a brief time ( $\sim 20 \mu\text{s}$ ) after the ultrasound burst is transmitted, the probe reads erroneous data (which can be seen in Fig. 2.6(b-d)). By adjusting the two parameters of the clock signal box, the delay time and the clock window width, data can be acquired only when appropriate. Umbanhowar's box contains DIP<sup>3</sup> switches for adjustment of those two parameters. The software program can adapt to either the external or internal clock being used for the WAAG card (see Appendix B).

In the future a frequency doubler could be added between the Matec clock

---

<sup>3</sup>DIP stands for dual-inline-package.

output and Umbanhowar’s clock signal box. This would further improve the ability of the software to determine the phase of a pulse.

### 2.6.5 Additional considerations

Note that our method relies on having particles inside the cone of ultrasound directly beneath the probe, so a large number of particles are needed. As the distribution of particles beneath the probe is random and fluctuates, this method is best for time-averaged quantities, similar to the Doppler techniques discussed in Refs. [141, 142, 143].

We found that new slip rings needed to be installed, in order to carry RF pulses to the annulus without picking up unacceptable amounts of noise. We installed IEC Corporation model IEL-BX slip rings above the annulus (12 rings, with 6 dedicated for carrying two RF signals on coaxial cable lines). These slip rings can handle signals from DC–100 MHz with very little distortion or noise pickup.

We are still determining what tracer particles are best to use. The important characteristic of a particle is an acoustic impedance mismatch with water. The acoustic impedance of a material is given by  $(\text{speed of sound}) \times (\text{density})$  [70]. However, most materials with a density similar to water (needed for neutral buoyancy concerns) also have a similar speed of sound, and thus are acoustically matched rather than mismatched. Thus, an ideal tracer particle would be a shell composed of a dense material surrounding a bubble of air, such as a hollow stainless steel sphere [70]. We are currently looking for hollow ceramic or glass particles of the correct density and size.

## 2.7 Temperature control

Temperature control is important for our experiment for two main reasons. First, we wish to conduct barotropic experiments, that is, experiments without a buoy-

ancy force as would be caused by temperature gradients in the annulus. Second, it is important to know the temperature as the viscosity of the fluid is strongly temperature dependent.

There are several sources of heat. The pump generates a certain amount of heat, and the motor which drives the pump generates additional heat. As all of the fluid passes through the pump, this is a significant problem. A second source of heat is the halogen lights used to illuminate the particles for flow visualization (Sec. 2.2). Originally we used 300 W halogen bulbs; by switching to 100 W bulbs, the heating was greatly reduced. Additionally, an infrared absorbent coating is placed over the light fixtures which reduces the amount of heat passing through. The illumination is still sufficient for the particle tracking technique discussed in Sec. 2.2. A third source of heat is the 2 kW motor which drives the rotating tank; a fan could be mounted on this motor to cool it.

We use a Thermometrics glass-encapsulated thermistor to monitor the temperature of the fluid. The thermistor is inside a hose upstream of the flow meter, through which all of the fluid passes. By monitoring this thermistor we can maintain a constant temperature for the duration of an experiment. An air-conditioning vent is attached to a hose which is aimed at the experiment; by adjusting the position of this hose the temperature of the experiment can be controlled. Typically the hose points at the underside of the experiment, and the distance to the experiment is adjusted by hand as necessary (the temperature changes on a time scale of 10 minutes, although often an equilibrium between the heating and the air conditioning can be reached, keeping the temperature stable for hours without any adjustments). Also, by pre-heating the tank and fluid, the experiment can be conducted at a higher temperature where the heating caused by the pump and halogen lights is balanced by the cooling of the rapid rotation and ambient air temperature. The pre-heating is accomplished with a small portable heater placed near the annulus, while slowly

rotating the annulus and pumping the fluid. Typically we conduct experiments at  $25.5 \pm 0.5^\circ \text{ C}$ .

For the experiments discussed in Chap. 4, low flow rates are used and it is important to ensure the fluid is well mixed to minimize thermal variations. For these experiments, the tank was spun up to 1.5 Hz and back down several times, while pumping at a high rate, in order to thoroughly mix the fluid. For the experiments of Chaps. 5 and 6, higher flow rates are used and thus the fluid is well-mixed during the experiment. For all experiments, it is important to know the temperature to determine the viscosity of the fluid.

## 2.8 Flow meter

To measure the flow rate, a flow meter has been installed on the rotating annulus. When the small Micropump was used, it provided calibrated, known flow rates. The larger Tri-Rotor pump requires a flow meter, as it is uncalibrated and the flow rate fluctuates. Also, the pump rate drifts occasionally, necessitating feedback to keep the rate stable.

We use an EG & G Instruments flow meter, model FT-10AEYW-LEG-1. This is a turbine flow meter designed to work at flow rates between 50 and 2400  $\text{cm}^3/\text{s}$ . The flow meter is installed immediately upstream of the pump, that is, the flow goes through the flow meter and next into the pump; this placement improves performance. Two flow straighteners are installed on either side of the flow meter (10 diameters length of pipe upstream, and 5 diameters downstream). The flow meter is designed to function in one direction only, although it does provide a signal for flow in either direction. Because of the design of the turbine, the flow straighteners, and the placement upstream of the pump, the accuracy in the reverse direction is unknown.

The flow meter works with a modulated carrier (RF) pickoff. An oscillator

circuit is next to the turbine blades, and the oscillation frequency is modulated by the turning turbine blades. An EG & G model CA51 signal conditioner converts this modulated carrier signal to a pulse output. This signal conditioner is mounted on the annulus near the flow meter.

The pulses from the EG & G signal conditioner pass through the slip rings of the annulus, which adds noise to the pulses. The signal is then passed through a circuit we built which reconditions the pulses before sending them to the National Instruments data acquisition card. The data acquisition program used for the hot film probes (Sec. 2.5) also samples the pulses to determine the flow rate. The frequency of the pulses is proportional to the flow rate, and thus the uncertainty of the flow rate measurement is proportional to the time used to sample the frequency. We typically use a sampling time of 1 s, resulting in an uncertainty of 1 Hz in measuring the pulse frequency, corresponding to an uncertainty of  $0.4 \text{ cm}^3/\text{s}$  in flow rate (typical flow rates are 100–400  $\text{cm}^3/\text{s}$ ).

When we first used the flow meter, we were excited to be able to directly measure the flow rate, but the results were disappointing. Figure 2.9(a) shows data from an early measurement. The flow rate has fluctuations with a typical standard deviation of  $4 \text{ cm}^3/\text{s}$ . Occasionally even larger fluctuations are seen. The large fluctuations were determined to be caused by a misalignment of the pump motor and the pump; occasionally this would cause the pump to stick for a fraction of a second and the pump rate would exhibit a large change. The misalignment was also responsible for the smaller fluctuations. In addition, over a long period of time (several hundred seconds) often the flow rate would drift, sometimes by as much as  $40 \text{ cm}^3/\text{s}$ . This was especially the case when particles were in the annulus; as they clogged the holes (Sec. 2.2) the impedance of the plumbing rose, and the flow rate dropped.

To prevent these problems, the pump was realigned and feedback was added.

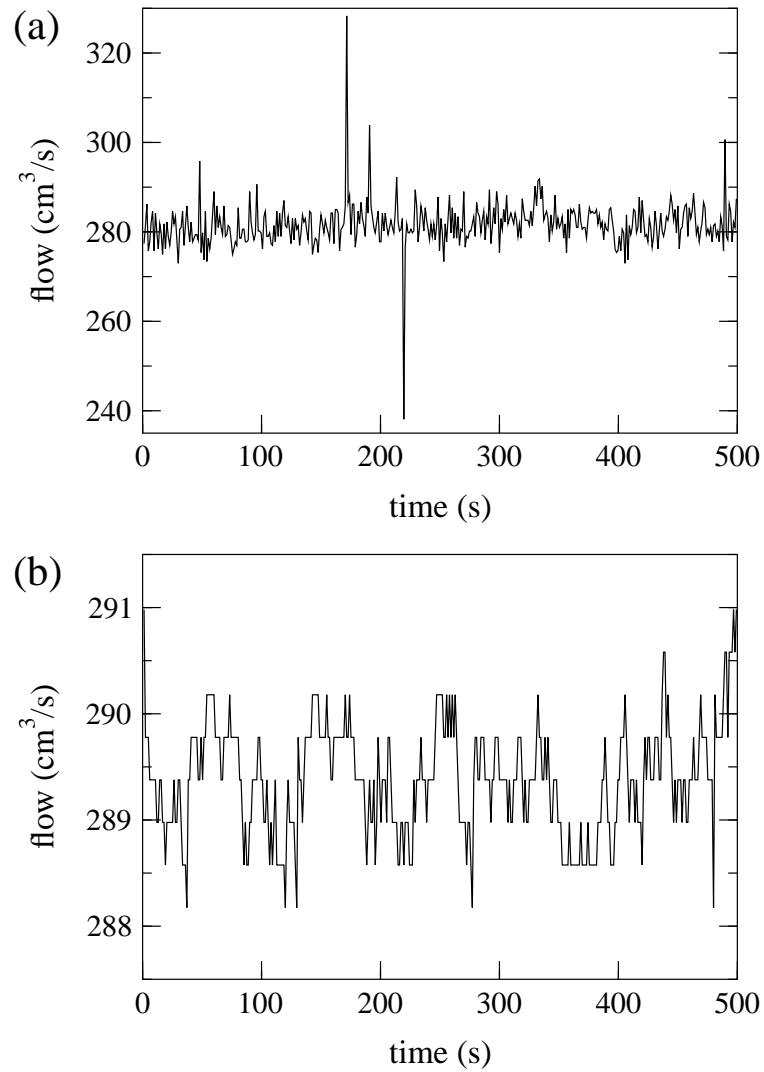


Figure 2.9: Flow rate measured (a) before active control and (b) after active control (spring 1997). Note the difference in vertical scales. The fluctuations seen in (b) are smaller due to better alignment of the pump shaft with the pump motor, and the active control. The quantization of the measurement is due to the sampling time (1 s for both (a) and (b)); see the text for details.



M. A. Bawany modified the hot film data acquisition program to provide a voltage to the pump motor controller, which sets the motor speed. The flow rate is measured by the program (as discussed above), and the output voltage is adjusted slightly to compensate for the discrepancies between the measured and desired flow rates. There is a tradeoff based on the sampling time for measuring the frequency of the pulses coming from the flow meter: as this time is increased, the flow rate is determined more precisely, but the feedback occurs less often. A sampling time of 1–2 s appears adequate. The adjustment of the output voltage is *not* proportional to the mismatch in flow rate. Instead, the output voltage is raised or lowered by a constant amount, unless the difference between the measured and target flow rates is less than  $1 \text{ cm}^3/\text{s}$ , in which case no adjustment is made. This was chosen to avoid problems of overcompensation, and to allow the motor changes to be smooth.

Figure 2.9(b) shows the improvement in the flow rate control with the pump realigned and the active feedback. The fluctuations have a standard deviation of  $0.5 \text{ cm}^3/\text{s}$ , 8 times smaller than the results shown in Fig. 2.9(a). The alignment is believed to have cured the high frequency fluctuations, and the feedback compensates for lower frequency drift. Typically the feedback voltage is observed to change on a time scale of 5 s or longer.

The data acquisition program has an additional feature which is unused for the experiments described in this dissertation. By allowing the target voltage to change in time, the active feedback can adjust the flow rate in the experiment over time. This allows us to adiabatically change the pump flux with a fixed rate of change while taking data. This is discussed further in Appendix B.

Note that the flow meter has an inner diameter of  $7/16$ ". All of the flow from the pump passes through the flow meter, and it is likely that the flow meter accounts for a large portion of the impedance of the annulus plumbing system. The hoses attached to the pump have an inner diameter of 1". Originally the flow was reduced

from 1" to 7/16" over a length of about 12". After constructing a fitting reducing the flow over a length of 2 1/2", the maximum possible flow rate increased by 30%. It is probable that purchasing a new flow meter with a larger inner diameter will increase the flow rate even further, although room must be made to accommodate the flow straighteners (whose length is proportional to their diameter).

## 2.9 Pressure sensor

We have installed a pressure sensor between the inlet and outlet holes of the tank. This sensor was not used for measurements in this dissertation.

We use a Motorola model MPX2010 (case 352-02) sensor, a silicon piezoresistive pressure sensor. The voltage output is linearly proportional to the applied pressure. This voltage can be measured by the data acquisition program used for the hot film probes (Sec. 2.5), that is, the voltage is read by a National Instruments data acquisition card. The pressure sensor is installed to measure the pressure difference between a valve going to an inlet ring, and a valve going to an outlet ring (see Sec. 2.1).

We found that the pressure sensor measurements were extremely noisy, one reason these measurements are not reported in this dissertation.

## 2.10 Achieving high rotation rates

As discussed in Sec. 1.2.2, rapid rotation forces the flow to be predominantly two-dimensional. For the turbulence experiments discussed in Chap. 6, high rotation rates are especially important. To achieve high rotation rates, the annulus walls are constructed from 2.8 cm thick pieces of Plexiglas, and held under compression with several steel bands. 24 vertical clamps are placed around the outer edge of the annulus to help hold the lid in place and to further reinforce the outer walls.

Additionally, the Plexiglas lid is 5 cm thick, to prevent warping which had occurred at high rotation rates in thinner lids (2 cm).

We wish to estimate the maximum possible rotation rate before the steel bands will break. A conservative estimate of the yield strain of steel is  $1.4 \times 10^8$  N/m<sup>2</sup>; at this strain, steel deforms elastically but the stress and strain are no longer linearly related. The steel bands are 3.8 cm wide and 0.1 cm thick; their cross section is 0.38 cm<sup>2</sup>, smaller than the cross section of the bolts holding the bands together (0.50 cm<sup>2</sup>). Thus a tension of  $5.3 \times 10^3$  N could result in significant extension of a band; we will use this force as a conservative estimate of the breaking force.

To find the pressure on the outer wall, we can assume the entire mass of water is rotating at the outer radius  $r = 43.2$  cm. The pressure is then  $F_{\text{centripetal}}/A$  using  $A = 2\pi rh = 0.55$  m<sup>2</sup> for the area of the outer wall.  $F_{\text{centripetal}} = \rho V r \Omega^2$  and so the pressure is  $P = 3.1f^2$  kPa, where  $f$  is the rotation rate of the annulus in Hz. For  $f = 2$  Hz,  $P = 124$  kPa = 18 psi = 1.2 atm.; for  $f = 4$  Hz,  $P = 500$  kPa = 72 psi = 4.9 atm. Assuming this pressure is transmitted uniformly to the steel bands, this pressure generates a tension in the steel bands. By drawing a free-body diagram for a small arc of the band and then letting the arclength go to zero, the relationship between the pressure on a band and the tension is found to be  $T = Phr$ . For the steel bands,  $h = 3.8$  cm and  $r = 45$  cm, producing  $T = 53f^2$  N when  $f$  is measured in Hz. Our estimate for the breaking tension is  $5.3 \times 10^3$  N, so at  $f = 10$  Hz the bands could break.

Our estimate for the pressure on the outer wall overestimates the pressure of the water; a more careful calculation found the pressure to be  $1.9f^2$  kPa [88], 60% of our estimate. However, it is reasonable to assume the Plexiglas outer walls themselves can exert additional pressure on the steel bands, and so using the higher value for the pressure is reasonable.

An additional consideration at high rotation rates is the balancing of the

annulus. Dynamic balancing of the annulus was done by Brian Murphy, a research engineer at the UT Center for Electromechanics, who advised us on dynamic balancing techniques. His work is continued by Charles Baroud who has re-balanced the annulus as new equipment has been added. Currently a Silicon Microstructures model SM7130-002 accelerometer is mounted on the I-beams supporting the annulus, on the side near the center, to measure horizontal shaking of the supports. By monitoring vibrations of the accelerometer, the imbalance of the tank can be detected. To balance the tank, a small weight ( $\sim 500$  g) is added near the edge of the annulus. The tank is spun, and the amplitude of the accelerometer vibrations is measured; the important quantity is the amplitude of the Fourier spectrum peak at the rotation frequency (see Fig. 2.10). By adjusting the angular position of the weight, and then adjusting the amount of the weight, this Fourier peak can be minimized, at which point the tank is dynamically balanced.

An additional test by Murphy examined the resonant frequency of the annulus system. By tapping lightly on the annulus with a mallet, a ringing at approximately 7.0 Hz can be observed; the resonant frequency when tapped in the orthogonal direction is 9.4 Hz. The annulus does not appear to have any resonant frequencies below 7 Hz. To increase these resonant frequencies the system would need to be made stiffer.

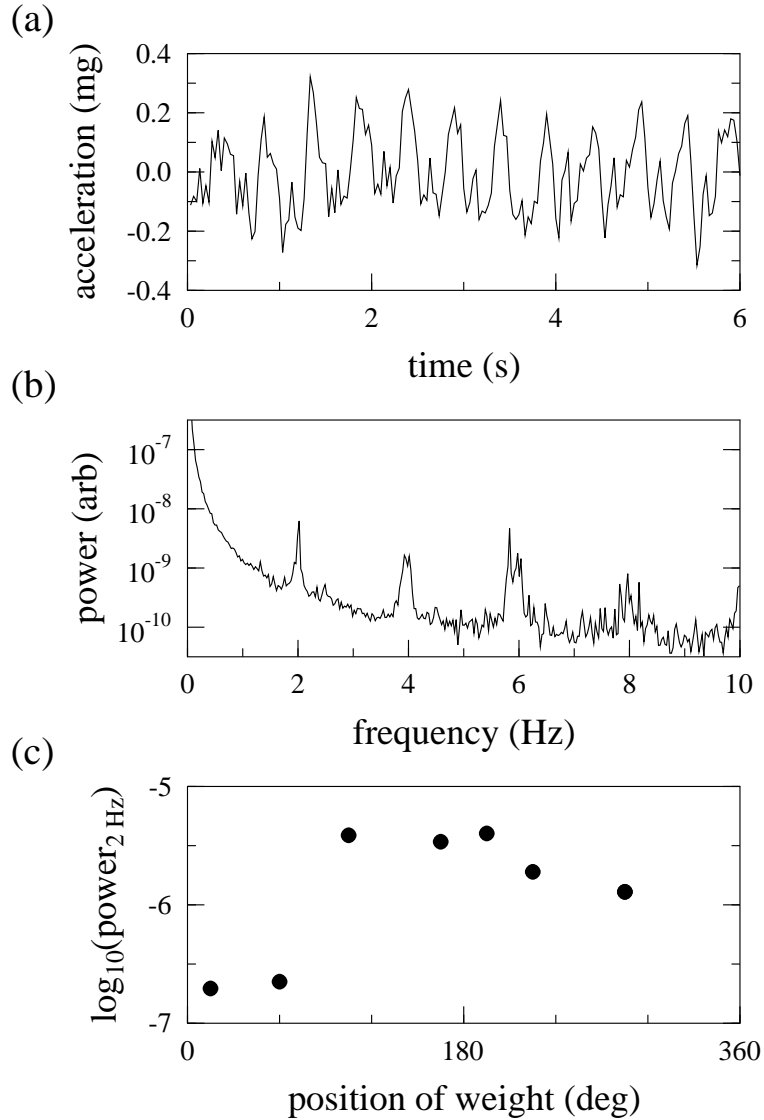


Figure 2.10: Accelerometer data taken at  $\Omega/2\pi = 2$  Hz. (a) Time series from the accelerometer (when a 600 g weight is placed on the edge of the annulus,  $r = 45$  cm). (b) Power spectrum corresponding to (a); the vertical axis is in arbitrary units. (c) The power at 2 Hz for various positions of the weight. For (a) the weight is at  $195^\circ$ . By placing a weight near  $45^\circ$ , the vibrations of the annulus can be minimized thus balancing the annulus. The data shown in (c) are useful for finding the best position of a weight, but do not determine the best size of the weight. Data taken by C. Baroud.

## Chapter 3

# Theory of Random Walks

### 3.1 Introduction to Random Walks

A wide range of diffusive processes can be interpreted as random walks. For example, the Brownian motion of a passive particle in a homogeneous fluid is described as a sequence of steps generated by random collisions with fluid molecules. As Einstein showed [38], an ensemble of such particles will spread out with a variance

$$\sigma^2(t) = \langle x^2(t) \rangle - \langle x(t) \rangle^2 = 2Dt \quad (3.1)$$

where  $D$  is the diffusion coefficient. The broad applicability of this simple result is a consequence of the Central Limit Theorem (CLT): a collection of sums of a large number of statistically independent events will be Gaussian distributed, provided that the distribution of the individual event sizes is not too broad. As applied to random walks, the CLT implies that whenever the mean time between steps and the mean square step size (second moment of the step size distribution) are finite, normal diffusion will result.

In general, anomalous diffusion ( $\sigma^2 \propto t^\gamma$ , with  $\gamma \neq 1$ ) in physical systems is a consequence of correlations generated by spatial or temporal coherence, and the associated breakdown of the assumptions of the CLT [13, 68, 92, 126]. It is

often still possible to describe the transport in terms of a random walk, with broad distributions of step sizes or waiting times accounting for the correlations in the motion. For a distribution  $P(l)$  of step sizes  $l$  given by  $P(l) \propto l^{-\mu}$  with  $\mu < 3$ , the second moment is divergent, and the CLT is no longer applicable. The long excursions which result in a divergent second moment are called Lévy flights. The presence of Lévy flights usually leads to superdiffusion, defined by  $1 < \gamma < 2$ .

An example of a normal random walk is shown in Fig. 1(a,b), and a superdiffusive random walk is shown in Fig. 1(c,d). In both cases,  $P(l) \sim l^{-\mu}$  for large  $l$ ; for the normal random walk shown  $\mu = 3.8 > 3$  and for the superdiffusive random walk  $\mu = 2.2 < 3$ . For the normal random walk, after many steps, the displacement is the average effect of all of the steps. For the anomalous case, the displacement is dominated by a few rare steps. This is the signature of anomalous random walks: the motion is always determined by a few steps, no matter how many steps have been taken.

Quantitative connections between the behavior of the distribution functions and the exponent  $\gamma$  have been made by many authors for symmetric random walks [46, 66, 67, 124, 125, 153, 155]; this work is discussed in Sec. 3.4. We extend this work by considering *asymmetric*, or biased, one-dimensional random walks, where steps in one direction occur with a higher probability than steps in the opposite direction. This can occur in situations such as charged particles moving in an electric field, or particles carried by an asymmetric flow. We will examine the case of flights with finite velocity. (Some authors use the term Lévy walks for motions with constant velocity and reserve flights for instantaneous jumps.) When the CLT applies, it is always possible to shift to a reference frame where  $v_{\text{ave}} = 0$ , and the presence of asymmetry only affects the diffusion coefficient, not the exponent ( $\gamma = 1$ ). When the CLT is not applicable, we find that the asymptotic behavior for symmetric and asymmetric random walks can be quite different.

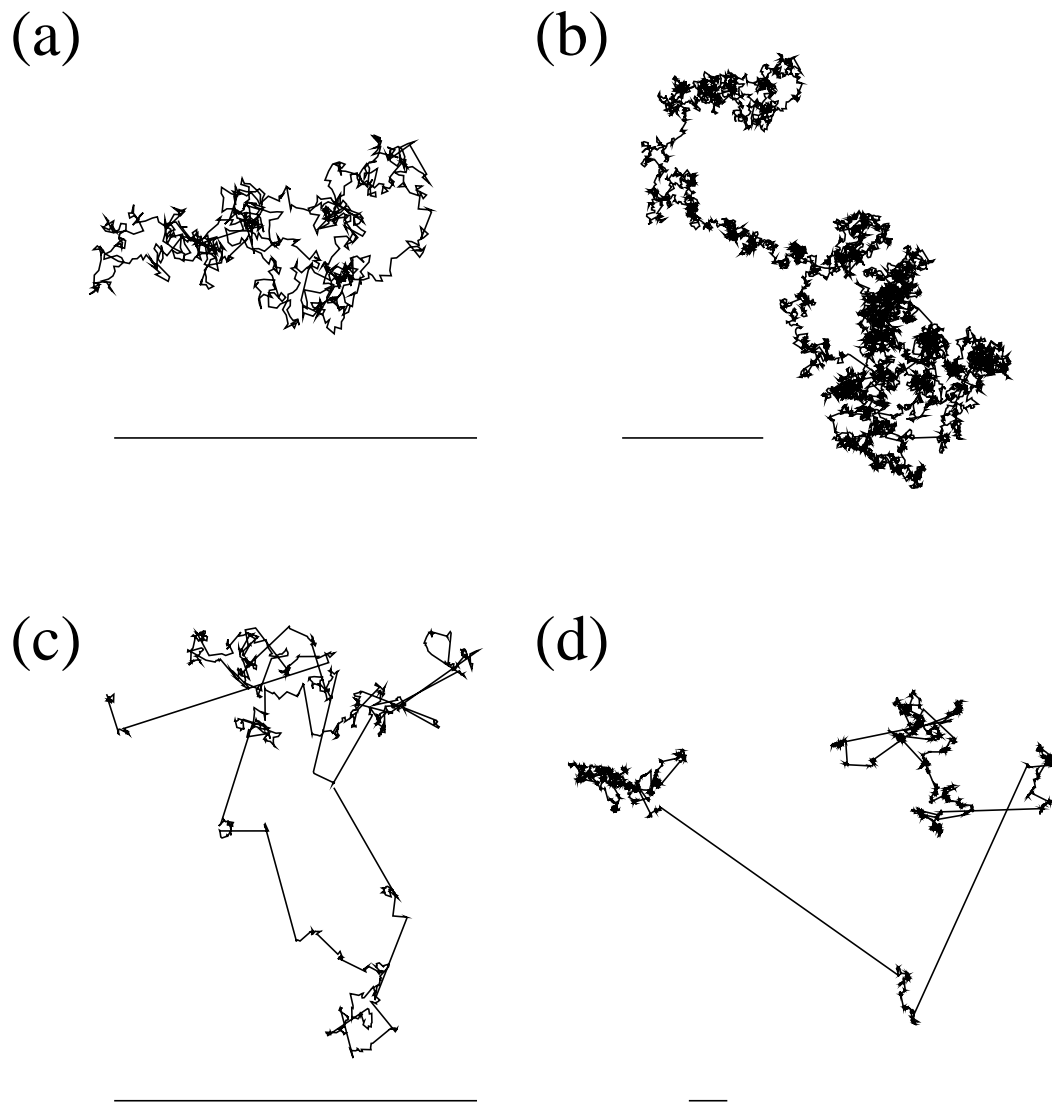


Figure 3.1: Random walk leading to normal diffusion (a) after 1000 steps; (b) after 10000 steps; random walk (Lévy flight) leading to superdiffusion (c) after 1000 steps; (d) after 10000 steps. For both random walks, the mean step size  $\langle l \rangle = 1$ , and the angle is chosen randomly for each step. A horizontal bar of length 50 is beneath each walk. For (a) and (b), the step size distribution decays as  $P(l) \sim l^{-3.8}$  for large  $l$ , and for (c) and (d)  $P(l) \sim l^{-2.2}$ ; see the text for further explanation.



The model we present examines anomalous diffusion arising from 1D (one-dimensional) random walks with discrete steps of constant velocity, separated by pauses (sticks) of random duration. Asymmetric random walks of this form were used to model the first experimental observations of anomalous diffusion (of electrons in amorphous materials) [109, 123], and were studied theoretically for cases with broad distributions of sticking times (but with narrow distributions for flight lengths) [124]. We consider power law forms for both sticking and flight distribution functions, and provide the first comprehensive analysis of the relationship between  $\gamma$  and the sticking and flight distribution exponents for both symmetric and asymmetric random walks. Additionally, we analyze the case where the flight distribution has a different power law decay for leftward and rightward flights. This case has not been considered before, and can be strikingly different from the cases with identical power laws.

Several other mechanisms can lead to anomalous diffusion, e.g., when the successive discrete steps of a random walk have strong correlations [13]. Also, random walks occurring in a random environment can lead to ultra-slow diffusion ( $\sigma^2(t) \sim (\ln t)^\alpha$ ,  $\alpha > 0$ ) [82, 128]. Fractional Brownian motion, a generalization of Brownian motion that leads to anomalous diffusion, was proposed by Mandelbrot and Van Ness in 1968 [76]. Fractional Brownian motion is characterized by the displacement  $\Delta X(t)$  having the same distribution function as the scaled displacement  $a^{-H}\Delta(at)$  for all  $a$  and a specific Holder exponent  $H$  ( $0 < H < 1$ );  $H = 1/2$  is the case of normal Brownian motion. As in regular Brownian motion, individual steps cannot be resolved. A comprehensive review of other mechanisms leading to anomalous diffusion can be found in Ref. [13]. We do not consider these mechanisms.

## 3.2 Random Walks in Experiments

Experiments done in fluids provide many instances of random walks and anomalous diffusion [16, 17, 19, 97, 113, 132, 133]. A collection of particles in a nonuniform flow will disperse as a consequence of the shear in the velocity field as well as the effects of molecular diffusion. In most situations, advection due to fluid motion is much faster than molecular diffusion, and large scale structures, such as eddies, jets, or convection rolls, will dominate the transport [144]. This results in correlations in particle velocities for large distances and/or times, and can lead to a failure of the assumptions of the CLT. In fully-developed turbulence, for example, the presence of eddies distributed over many spatial scales results in superdiffusion ( $\sigma^2 \propto t^\gamma, \gamma > 1$ ), and in 1926 Richardson argued that the separation of two particles in the atmosphere is described by  $\sigma^2 \propto t^3$  [120].

Extremely long time transport of passive tracer particles in fluid flow will be normally diffusive due to Brownian motion [165]. However, for many important flows this time scale is enormously large; for example, in oceanic flows typical length scales are  $L \approx 10$  km; for a diffusion constant  $D \approx 10^{-5}$  cm<sup>2</sup>/s, the diffusive time scale is  $\tau_d = L^2/D \approx 10^9$  yr, while time scales of interest are typically  $\sim 1$  yr.

Subdiffusion has been observed in both linear and planar arrays of vortices of alternating sign [16, 17, 19]. The results have been interpreted as a simple random walk comprised of sticking and flight events [19]. Particles carried by capillary waves were found to move superdiffusively [113, 114], linked to the fractional Brownian motion of the particle trajectories. Tracers in the ocean showed evidence of superdiffusion, although lack of statistics prevented study of underlying mechanisms [96]. In addition, experiments studying mixing of polymer-like micelles found that transport was superdiffusive, and well described by a Lévy flight model [14, 97], although direct observation of flight motions was not possible. In addition to fluid experiments, anomalous diffusion has been observed in photoconductivity of amor-

phous materials [109, 123] and motion of low density lipoprotein receptors on the surface of human skin fibroblasts [49]. Lévy flights also appear in an analysis of sub-recoil laser cooling of atoms [4, 115], where the mean time for atoms to leave an optical trap is infinite.

### 3.3 Higher dimensions

There is little difference between 1D, 2D, and 3D random walks, unless there are correlations between the steps of the random walk. For any random walk, the variance can be broken up into components:

$$\sigma^2 = \langle \vec{r} \cdot \vec{r} \rangle - \langle \vec{r} \rangle \cdot \langle \vec{r} \rangle = \sigma_x^2 + \sigma_y^2 + \sigma_z^2 \quad (3.2)$$

in three dimensions, for example.

Usually it is simplest to consider a one-dimensional random walk when deriving theoretical results. This is the approach taken for the work discussed in this chapter. The results derived for a one-dimensional walk apply equally well to higher dimensions when the steps of the random walk are taken in a random (symmetrically chosen) angular direction. Difficulties arise when there are extreme asymmetries in the motion. For example, if a random walker moves in 2D, and alternates between Lévy flight steps in the  $x$ -direction (with  $y$  held constant) and short steps in the  $y$  direction (with  $x$  held constant), the random walk will be superdiffusive in the  $x$  direction and would be normally diffusive or even subdiffusive in the  $y$  direction. The overall variance would be superdiffusive, as seen in Eq. (3.2), dominated by the  $x$  contribution to the variance.

The random walk model presented in this chapter is a one-dimensional model. In Chap. 4 we discuss our experimental investigations of transport in a rotating fluid flow consisting of an circular chain of vortices bounded on one or both sides by a jet. The motion of tracer particles in the flow is naturally described as a 1D random

walk, alternating between motion in the jet corresponding to steps, and waiting times between steps while the particles are trapped in the vortices. As the jets are asymmetric (one is near the outer wall of the annulus, one near the inner wall), the resulting random walk has some asymmetries as well. The results will be compared with the theoretical results in this chapter.

### 3.4 Previous Theoretical Work

For simple cases, the variance of an ensemble of random walkers grows linearly with time, as given by Eq. (3.1), with the diffusion constant  $D$  being given by

$$D = \frac{\langle l^2 \rangle - \langle l \rangle^2}{2T}. \quad (3.3)$$

The moments of  $l$  are based on  $P_F(l)$ , the distribution of step sizes (or *flight* sizes, as we will use), and  $T$  is the mean time between the start of successive flights. This result depends only on the first two moments of the flight Probability Distribution Function (PDF) and finite nonzero  $T$ , but no other details of the random walk. The mean position of random walkers is

$$\langle x \rangle = \frac{\langle l \rangle}{T} t, \quad (3.4)$$

which is zero for a symmetric ( $\langle l \rangle = 0$ ) random walk [13]. These results are true in the limit  $t \rightarrow \infty$ ; at short times the behavior depends on the details of the random walk.

For PDF's that decay sufficiently slowly, the Central Limit Theorem no longer applies. If  $P_F(|l|) \sim |l|^{-\mu}$  and  $\mu < 3$ , the second moment  $\langle l^2 \rangle$  is infinite ( $\mu > 1$  for the distribution to be normalizable). A random walk for this type of PDF is a Lévy flight, and it has been shown that [46, 66, 125, 153] the variance scales with time  $\sigma^2(t) \sim t^\gamma$  with

$$\gamma = 2 - \frac{1}{\mu} \quad 1 < \mu < 3 \quad (3.5)$$

$$\gamma = 4 - \mu \quad 2 < \mu < 3 \quad (3.6)$$

$$\gamma = 1 \quad \mu > 3 \quad (3.7)$$

In addition, for  $\mu = 2$  the variance grows as  $t^2/\ln t$ , and for  $\mu = 3$  the variance grows as  $t \ln t$  [153]. These results are valid when the random walker moves at constant velocity, taking flights with a length distribution given by  $P_F(|l|)$ , or equivalently, a distribution of flight times having the same asymptotic power law behavior. In addition, the time  $T$  must be finite. Superdiffusive transport,  $1 < \gamma < 2$ , occurs for  $2 < \mu < 3$ . When  $\gamma = 2$ , the transport is ballistic, that is, the exponent is the same as that of a collection of particles moving in different directions in straight lines, with no pauses or changes in direction.

To consider cases where the  $T \rightarrow \infty$ , we allow the random walker to pause (stick) between steps, and introduce the sticking time distribution (also called “trapping” distribution). Again, we assume the behavior at large times decays as a power law:  $P_S \sim t^{-\nu}$ . When  $\nu < 2$  (with  $\nu > 1$  for normalization), the first moment of the sticking PDF  $\langle t_s \rangle$  is infinite and the variance has the possibility of scaling subdiffusively. Shlesinger investigated the case where random walkers were stuck for varying times between random (symmetrically chosen) steps with finite mean square step size ( $\mu > 3$ ), finding [124]

$$\gamma = 1 \quad \nu > 2 \quad (3.8)$$

$$\gamma = \nu - 1 \quad 1 < \nu < 2 \quad (3.9)$$

Shlesinger [124] also considered random walks with asymmetric steps ( $\langle l \rangle \neq 0$ ) and found the scaling of the mean,  $\langle x \rangle \sim \langle l \rangle t^\beta$ , with

$$\beta = 1 \quad \nu > 2 \quad (3.10)$$

$$\beta = \nu - 1 \quad 1 < \nu < 2 \quad (3.11)$$

and the scaling of the variance,  $\sigma^2 \sim t^\gamma$ , with

$$\gamma = 4 - \nu \quad 2 < \nu < 3 \quad (3.12)$$

$$\gamma = 2\nu - 2 \quad 1 < \nu < 2 \quad . \quad (3.13)$$

In the asymmetric case, the possibility for superdiffusion exists with broad sticking PDFs. For example, when  $\nu = 2.5$ ,  $\gamma = 4 - 2.5 = 1.5$ . This will be discussed further in Sec. 3.5. Asymmetric random walks of this type describe transport of electrons in amorphous materials [109, 123], where the asymmetry is introduced by a bias voltage.

The case with power law sticking PDFs combined with symmetric Lévy flights was examined by Klafter and Zumofen, who found for flights with constant velocity [67]

$$\gamma = 2 + \nu - \mu \quad \nu < 2, \quad 2 < \mu < 3 \quad (3.14)$$

$$\gamma = 4 - \mu \quad \nu > 2, \quad 2 < \mu < 3 \quad , \quad (3.15)$$

where Eq. (3.15) is the same as Eq. (3.6). This formula allows for the behavior to be subdiffusive ( $\gamma < 1$ ) for sufficiently small values of  $\nu$  ( $1 < \nu < \mu - 1$ ).

Random walks with broad sticking and flight distributions can be found in Hamiltonian systems. Sticking behavior is usually associated with island chains near closed, ordered regions of phase space, while flights occur between island chains or in chaotic jets [68, 84, 85, 126]. The distributions were found to be well described by power laws for both sticking [84, 85, 106, 159, 166] and flights [45, 46, 166]. In some cases, sticking events in a map representation are equivalent to flights in the full phase space [45, 46, 65, 167]. Maps with power law sticking behavior [43, 84] and flight behavior [44] appear to be common. Transport in Hamiltonian systems can be either normal or anomalous, depending on the structure of the phase space [1, 26, 105].

### 3.5 A model for asymmetric random walks

In results such as Eqs. (3.5)-(3.7) and (3.14), (3.15), the random walk was assumed to be symmetric ( $P_F(l) = P_F(-l)$ ). In the absence of left-right symmetry, many of these results change. For example, if the flights are exclusively in one direction ( $P_F(l) = 0$  when  $l < 0$ ), the sticking occurrences will appear as flights in the opposite direction when viewed from a reference frame centered on  $\langle x(t) \rangle$  (which might not be moving at constant velocity; e.g., Table 3.4). In cases such as this the divergence of the second moment of the sticking PDF can lead to superdiffusive behavior (Eq. (3.12)), because the sticking events will be Lévy flights as seen in the moving reference frame.

In this section we use a model based on a one-dimensional random walk to predict the asymptotic scaling of the variance: as  $t \rightarrow \infty$ ,  $\sigma^2(t) \sim t^\gamma$ . The goal is to find the dependence of  $\gamma$  on the parameters of the model, and to examine differences between symmetric and asymmetric random walks.

Consider a particle that alternates between sticking events (remaining at the same location for some period of time), and constant velocity flights (moving to the left ( $-x$ ) or the right ( $+x$ )). The velocity of the leftward flights is  $v_l$ , and the rightward  $v_r$ . (If  $v_l$  and  $v_r$  have the same sign, the motion is in the same direction. Thus if  $v_l < 0$  and  $v_r > 0$  the flights are in the “leftward” and “rightward” directions, respectively.) The probability of a leftward flight is  $p_l$ ; rightward,  $p_r = 1 - p_l$ . The particles originally start at the origin  $x = 0$ , and at time  $t = 0$  start flight events with probability  $p_F^0$  or sticking events with probability  $p_S^0 = 1 - p_F^0$ .

Both flight and sticking events are of random duration. The PDF for flights in either direction is given by the function  $P_F(t)$ , and the PDF for sticking events is given by  $P_S(t)$ . For the moment, we make no assumptions about the forms of these PDFs. Our goal is to find the PDF  $X(x, t)$  of the particle positions for large times, following the procedure used in Ref. [155] which is similar to that of Ref. [66]. From

this PDF we can calculate the variance  $\sigma^2(t) = \langle x^2(t) \rangle - \langle x(t) \rangle^2$ , and extract the scaling exponent  $\gamma$ . The moments of  $x$  are obtained from the Fourier transform of  $X$ :

$$(i^n) \frac{\partial^n \tilde{X}(k, t)}{\partial k^n} \Big|_{k=0} = \langle x^n \rangle . \quad (3.16)$$

We construct  $\tilde{X}(k, t)$  from simpler PDFs related to the particle motion. Let  $\xi(x, t)$  be the probability that a flight event has a distance of  $x$  and a duration of  $t$ :

$$\xi(x, t) = [p_r \delta(x - v_r t) + p_l \delta(x - v_l t)] P_F(t) . \quad (3.17)$$

The Dirac delta functions ensure that the flights are made with the correct constant velocity. Define  $\Psi(x, t)$  to be the probability that the particle has moved a distance  $x$  in time  $t$  in a single flight event, and possibly is still moving:

$$\Psi(x, t) = [p_r \delta(x - v_r t) + p_l \delta(x - v_l t)] \int_t^\infty d\tau P_F(\tau) . \quad (3.18)$$

Similarly for sticking events,  $\Phi(t)$  is the probability that the particle has been motionless for at least duration  $t$  and possibly will remain motionless:

$$\Phi(t) = \int_t^\infty d\tau P_S(\tau) . \quad (3.19)$$

In addition, we define two functions related to  $X$ . Let  $Y(x, t)$  be the probability of just starting a sticking event at  $x, t$  and  $Z(x, t)$  be the probability of just starting a flight event at  $x, t$ . Then

$$Y(x, t) = p_S^0 \delta(x) \delta(t) + \int_{-\infty}^\infty dx' \int_0^t dt' Z(x', t') \xi(x - x', t - t') \quad (3.20)$$

$$Z(x, t) = p_F^0 \delta(x) \delta(t) + \int_0^t dt' Y(x', t') P_S(t - t') . \quad (3.21)$$

The delta functions represent the initial conditions at  $t = 0$ . The integrals evaluate the probability of being at the correct location earlier, and then having moved to (or stayed at) the current location to begin the sticking or flight event.  $X(x, t)$  can



be defined in terms of these new functions, and we get:

$$X(x, t) = \int_0^t dt' \Phi(t-t') Y(x, t') + \int_{-\infty}^{\infty} dx' \int_0^t dt' \Psi(x-x', t-t') Z(x', t'). \quad (3.22)$$

$X(x, t)$  is the probability of getting stuck at location  $x$  at an earlier time  $t'$  multiplied by probability of still being stuck there now (at time  $t$ ), added to the probability of starting a flight somewhere earlier (at  $x', t'$ ) multiplied by probability of flying to location  $x$  now.

The integral equations can be solved by Fourier transforming in space and Laplace transforming in time. Thus:

$$\begin{aligned} \tilde{X}(k, s) &= \tilde{\Phi}(s) \tilde{Y}(k, s) + \tilde{\Psi}(k, s) \tilde{Z}(k, s) \\ &= [s^{-1}(1 - \tilde{P}_S)] \left[ \frac{p_S^0 + p_F^0 \tilde{\xi}(k, s)}{1 - \tilde{\xi}(k, s) \tilde{P}_S} \right] \\ &\quad + [p_r \tilde{\lambda}(s_r) + p_l \tilde{\lambda}(s_l)] \left[ \frac{p_F^0 + p_S^0 \tilde{P}_S(k, s)}{1 - \tilde{\xi}(k, s) \tilde{P}_S} \right] \end{aligned} \quad (3.23)$$

where  $s_l = s + ikv_l$ ,  $s_r = s + ikv_r$ . (Each of the four terms in square brackets [ ] corresponds to one of the terms in the previous line). The function  $\tilde{\lambda}$  has been introduced for convenience:

$$\tilde{\lambda}(s) = s^{-1}(1 - \tilde{P}_F(s)) \quad . \quad (3.24)$$

Note that

$$\tilde{\xi}(k, s) = p_r \tilde{P}_F(s_r) + p_l \tilde{P}_F(s_l) \quad . \quad (3.25)$$

At this point  $\tilde{X}(k, s)$  has been completely expressed in terms of the Laplace transforms of the two elementary PDFs for flight and sticking events,  $\tilde{P}_F(s)$  and  $\tilde{P}_S(s)$ .

Using Eq. (3.16), we obtain  $\langle x \rangle$  and  $\langle x^2 \rangle$  by taking derivatives of  $\tilde{X}(k, s)$ :

$$\langle x \rangle = \frac{v_{\text{ave}}(p_F^0 + p_S^0 \tilde{P}_S)(1 - \tilde{P}_F)}{s^2(1 - \tilde{P}_F \tilde{P}_S)} \quad (3.26)$$

$$\begin{aligned} \langle x^2 \rangle &= 2[v_{\text{rms}}^2(1 - \tilde{P}_F + s \tilde{P}_F')(1 - \tilde{P}_F \tilde{P}_S) + v_{\text{ave}}^2 \tilde{P}_S(\tilde{P}_F - 1)s \tilde{P}_F'] \\ &\quad \times \frac{(p_F^0 + p_S^0 \tilde{P}_S)}{s^3(1 - \tilde{P}_F \tilde{P}_S)^2} \end{aligned} \quad (3.27)$$

Table 3.1: List of common symbols used in Sec. 3.6.

| Symbol                                     | Meaning  |
|--|--|
| $T$  | mean time between the start of successive steps  |
| $t_F, t_S$                                 | minimum time for short flight, sticking events (see Eqs. (3.28) and (3.29))                                  |
| $\langle t_f \rangle, \langle t_s \rangle$ | first moment of flight, sticking PDFs  |
| $\mu$                                      | power law decay exponent for the flight PDFs (see Eq. (3.28))  |
| $\nu$                                      | power law decay exponent for the sticking PDFs (see Eq. (3.29))  |
| $\gamma$                                   | variance exponent: $\sigma^2 \sim t^\gamma$  |
| $P_F^0, P_S^0$                             | probability that first event is a flight event, sticking event   |
| $p_l, p_r$                                 | probability a flight is to the left ( $-x$ ), right ( $+x$ )   |
| $v_l, v_r$                                 | velocity in left direction, right direction<br>$v_l < 0$ for leftward motion, $v_r > 0$ for rightward motion |

where  $v_{\text{ave}} = p_r v_r + p_l v_l$ ,  $v_{\text{rms}} = \sqrt{p_r v_r^2 + p_l v_l^2}$ , and  $\tilde{P}_F' = \partial \tilde{P}_F / \partial s$ . It is easy to verify that  $X(k=0, s) = \langle x^0 \rangle = 1$  as required for normalization. If  $v_{\text{ave}}$  is set to zero, the expressions provide the behavior for a symmetric random walk. The results in Eqs. (3.26) and (3.27) are exact for any form of  $P_F(t)$  and  $P_S(t)$ ; no approximations have been made.

### 3.6 Results: symmetric and asymmetric random walks

Table 3.1 contains a summary of the important notation used in this section. For a random walk alternating between flight events and sticking events,  $T = \langle t_f \rangle + \langle t_s \rangle$  when both moments are finite ( $\mu > 2, \nu > 2$ ).

At this point we assume specific forms for the PDFs, and use them to expand Eqs. (3.26) and (3.27). The probability distribution function (PDF) for flights in either direction is given by the function  $P_F(t)$ :

$$P_F(t) = 0 \quad t < t_F$$

$$At^{-\mu} \quad t \geq t_F \quad (3.28)$$

where  $t_F$  is a cutoff at short times to allow the function to be normalizable; the normalization constant is  $A = (\mu - 1)t_F^{\mu-1}$ . Similarly, the sticking PDF is given by the function  $P_S(t)$ :

$$P_S(t) = \begin{cases} 0 & t < t_S \\ Bt^{-\nu} & t \geq t_S \end{cases} \quad (3.29)$$

with  $B = (\nu - 1)t_S^{\nu-1}$ . The scaling exponent  $\gamma$  of the variance only depends on the asymptotic behavior of the sticking and flight PDFs (the exponents  $\mu$  and  $\nu$ ), although some results that follow will depend slightly on the exact behavior at short times; this will be clarified later. This particular short time behavior was chosen for convenience in comparison with experimental results (see Sec. 4).

The asymptotic behavior of  $\langle x(t) \rangle$  and  $\langle x^2(t) \rangle$  at large  $t$  (small  $s$ ) can be obtained from an expansion of Eqs. (3.26) and (3.27) in powers of  $s$ . The Laplace transforms of  $P_F(t)$  and  $P_S(t)$  (Eqs. (3.28) and (3.29)) are

$$\tilde{P}_F(s) = As^{\mu-1}\Gamma(1-\mu, st_F) \quad (3.30)$$

$$\tilde{P}_S(s) = Bs^{\nu-1}\Gamma(1-\nu, st_S) . \quad (3.31)$$

Expanding the incomplete Gamma function for small arguments yields:

$$\begin{aligned} \tilde{P}_F(s) &= -\Gamma(2-\mu)t_F^{\mu-1}s^{\mu-1} + 1 - \langle t_f \rangle s \\ &\quad + \frac{1}{2!}\langle t_f^2 \rangle s^2 - \frac{1}{3!}\langle t_f^3 \rangle s^3 \dots \end{aligned} \quad (3.32)$$

with a similar result for  $\tilde{P}_S(s)$ . The expression in terms of the moments of the PDFs is correct only for these particular PDF's.

We begin with the symmetric case,  $v_{\text{ave}} = 0$ , so that  $\langle x \rangle = 0$  and the variance  $\sigma^2(t) = \langle x^2(t) \rangle$ . The asymptotic behavior is found by putting the expansions into Eq. (3.27) and keeping only the leading term. The results, summarized in

Table 3.2: Anomalous diffusion results for symmetric random walks. The variance scales asymptotically as  $\sigma^2(t) \sim Ct^\gamma v_{\text{rms}}^2$  ( $v_{\text{rms}} = (p_l v_l^2 + p_r v_r^2)^{1/2}$ ), with coefficient  $C$  and exponent  $\gamma$  listed below for different values of the flight PDF exponent  $\mu$  and the sticking PDF exponent  $\nu$ .  $\gamma$  is correct for any PDF with the same asymptotic scaling, while the values shown for  $C$  are correct only for the specific form of the PDFs with the cutoff times  $t_F$  and  $t_S$  (Eqs. (3.28) and (3.29)). Terms such as  $\langle t_f \rangle$  and  $\langle t_s \rangle$  are the moments of the flight and sticking PDFs, respectively.

| Conditions      |               | Exponent $\gamma$ | Coefficient $C$  |
|-----------------|---------------|-------------------|--|
| $\mu > 3$       | $\nu > 2$     | 1                 | $(\frac{\langle t_f^2 \rangle}{\langle t_f \rangle + \langle t_s \rangle})$                  |
| $2 < \mu < 3$   | $\nu > 2$     | $4 - \mu$         | $(\frac{2}{(4-\mu)(3-\mu)}) (\frac{t_F^{\mu-1}}{\langle t_f \rangle + \langle t_s \rangle})$ |
| $1 < \mu < 2$   | $\nu > \mu$   | 2                 | $2 - \mu$  |
| $\mu > 3$       | $1 < \nu < 2$ | $\nu - 1$         | $(\frac{1}{\Gamma(2-\nu)\Gamma(\nu)}) \langle t_f^2 \rangle t_S^{1-\nu}$                     |
| $\nu < \mu < 3$ | $1 < \nu < 2$ | $2 + \nu - \mu$   | $(\frac{2\Gamma(3-\mu)}{\Gamma(2-\nu)\Gamma(3-\mu+\nu)}) t_F^{\mu-1} t_S^{1-\nu}$            |

Fig. 3.2(a) and Table 3.2, are in the form  $\sigma^2(t) = C(v_{\text{rms}})^2 t^\gamma$ . Figure 3.2(a) shows the asymptotic diffusive behavior in the form of a phase diagram, with the different shadings representing the ballistic, superdiffusive, normal, and subdiffusive regimes. The transitions from one phase to another that occur as the exponents of the PDF's are varied are sharply defined only in the infinite time limit.

The results for the exponent  $\gamma$  are in agreement with the earlier work discussed in Sec. 3.4. In addition we calculate the coefficients of the power law terms which are also presented in Table 3.2.

The behavior displayed in Fig. 3.2(a) can be understood in terms of the underlying behavior of the random walker. In all cases the variance is directly proportional to  $(v_{\text{rms}})^2 = p_l v_l^2 + p_r v_r^2$ , and this is the only dependence on  $p_l$  or  $p_r$  and  $v_l$  or  $v_r$  (assuming  $v_{\text{ave}} = p_r v_r + p_l v_l = 0$ ). For the case of normal diffusion,  $\mu > 3$  and  $\nu > 2$ ,  $\gamma = 1$  and  $C = \langle t_f^2 \rangle / (\langle t_f \rangle + \langle t_s \rangle)$ . Writing  $\langle t_f^2 \rangle v_{\text{rms}}^2 = \langle l^2 \rangle$  and

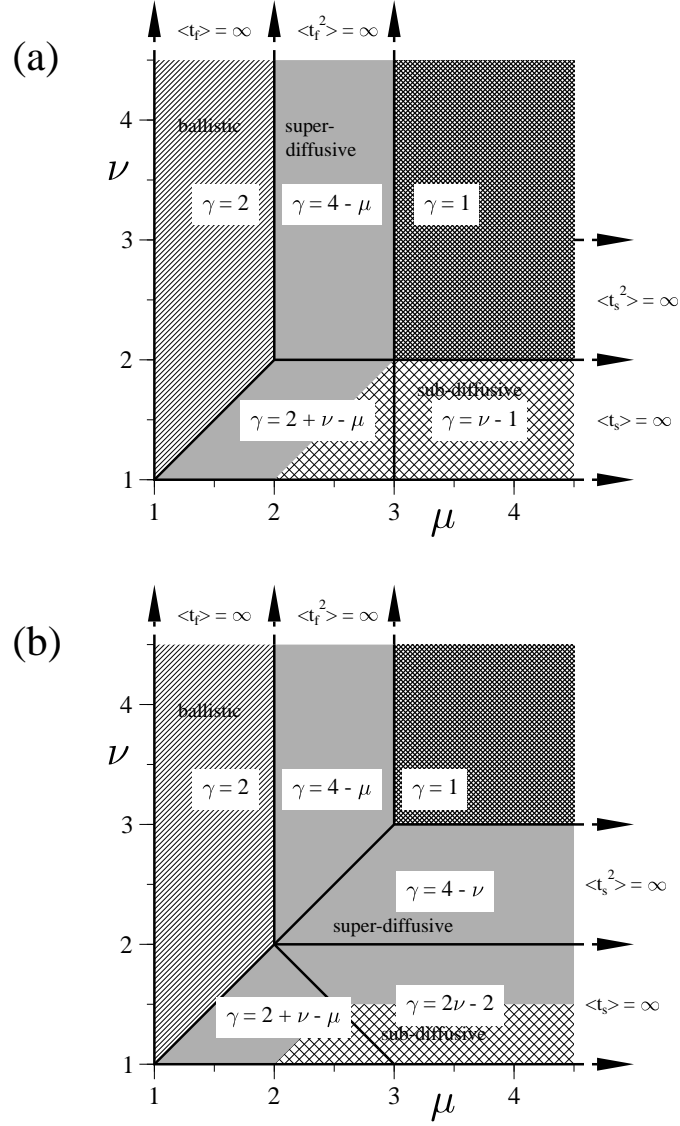


Figure 3.2: Phase diagrams for variance of (a) symmetric and (b) asymmetric (or biased) random walks.  $\mu$  and  $\nu$  are the exponents controlling the asymptotic power law decay of the flight and sticking PDFs, respectively:  $P_F(t_f) \sim t_f^{-\mu}$  and  $P_S(t_s) \sim t_s^{-\nu}$ , as  $t \rightarrow \infty$ . For each region, bordered by the solid lines, the relationship between the variance exponent  $\gamma$  [ $\sigma^2(t) \sim t^\gamma$ ] and  $\mu$  and  $\nu$  is shown. The shadings indicate areas where the behavior is normally diffusive ( $\gamma = 1$ ), subdiffusive ( $\gamma < 1$ ), superdiffusive ( $\gamma > 1$ ), and ballistic ( $\gamma = 2$ ).

$\langle t_s \rangle + \langle t_f \rangle = T$  reproduces the result for Brownian motion, Eqs. (3.1) and (3.3). When the flight PDF exponent  $\mu$  becomes less than three,  $\langle l^2 \rangle$  diverges and the behavior becomes superdiffusive. When  $\langle |l| \rangle$  diverges as well, we have the limiting case of ballistic motion. (In this case,  $\langle t_f \rangle$  and therefore  $T$  also has diverged, thus the flight motion dominates the transport completely, leading to ballistic motion.) Likewise, when the sticking PDF exponent  $\nu$  becomes less than 2,  $T$  becomes infinite because of the divergence of  $\langle t_s \rangle$ , leading to subdiffusive behavior as the transport is inhibited. For both  $\mu < 3$  and  $\nu < 2$ , competition between the Lévy flights and the sticking leads to behavior that can be either subdiffusive or superdiffusive, depending on which process is stronger (see Fig. 3.2(a)).

For the case when  $v_{\text{ave}} \neq 0$ , we first compute the asymptotic behavior of the mean  $\langle x \rangle \sim K v_{\text{ave}} t^\beta$  using Eq. (3.26). The results are presented in Table 3.3. Again, these results can be interpreted through the underlying PDFs. In all cases the mean is proportional to  $v_{\text{ave}}$ , which contains all of the relevant information about the asymmetry. When  $\mu > 2$  and  $\nu > 2$ ,  $\langle l \rangle$  is finite and the mean grows linearly with time, at a rate given by  $K v_{\text{ave}} = \langle l \rangle / T$ . When  $\langle l \rangle$  becomes infinite ( $\mu < 2$ ),  $T$  also diverges and the ratio  $\langle l \rangle / T$  is equivalent to  $v_{\text{ave}}$ . As predicted in Sec. 3.1, when the sticking PDF has an infinite first moment, behavior becomes more complicated, with the result that the mean grows slower than linearly in time.

The results for the variance in the asymmetric case are presented in Table 3.4 and Fig. 3.2(b). The phase boundaries are significantly different from the symmetric case. The result in the region of normal diffusion ( $\mu > 3, \nu > 3$ ) is once again equivalent to Eqs. (3.1) and (3.3), with  $\langle l^2 \rangle$  having a more complicated form because of the asymmetry. When either  $\mu$  or  $\nu$  is between 2 and 3, the resulting superdiffusion can be thought of as arising from a Lévy flight mechanism. For  $2 < \mu < 3$ , the flights are Lévy flights; for  $2 < \nu < 3$ , when shifting to a reference frame moving at constant velocity (equal to  $\langle t_f \rangle / (\langle t_f \rangle + \langle t_s \rangle)$ ); see Table 3.3), sticking events appear as Lévy

Table 3.3: Scaling of the mean position for asymmetric random walks ( $v_{\text{ave}} = p_r v_r + p_l v_l \neq 0$ ),  $\langle x \rangle \sim K v_{\text{ave}} t^\beta$ .  $\beta$  is correct for any PDF with the same asymptotic scaling, while the values shown for  $K$  are correct only for the specific form of the PDFs (Eqs. (3.28) and (3.29)).  $\mu$  is the exponent for the decay of the flight PDF, and  $\nu$  for the sticking PDF.

| Conditions    |                 | $\beta$         | Coefficient $K$  |
|---------------|-----------------|-----------------|--|
| $\mu > 2$     | $\nu > 2$       | 1               | $\frac{\langle t_f \rangle}{\langle t_s \rangle + \langle t_f \rangle}$          |
| $1 < \mu < 2$ | $\nu > \mu$     | 1               | 1  |
| $\mu > 2$     | $1 < \nu < 2$   | $\nu - 1$       | $(\frac{1}{\Gamma(2-\nu)\Gamma(\nu)}) \langle t_f \rangle t_S^{1-\nu}$           |
| $1 < \mu < 2$ | $1 < \nu < \mu$ | $1 + \nu - \mu$ | $(\frac{\Gamma(2-\mu)}{\Gamma(2-\nu)\Gamma(2-\mu+\nu)}) t_F^{\mu-1} t_S^{1-\nu}$ |

flights moving “backwards” with the speed of the moving reference frame. Ballistic motion occurs in the same region as the symmetric case, for similar reasons. When  $1 < \nu < 2$ , motion can be either super- or subdiffusive. For larger values of  $\nu$  in this range, motion is dominated by the “backwards” Lévy flight mechanism. For smaller values,  $\langle x \rangle$  grows too slowly (see Table 3.3), and the divergence of  $T$  leads to subdiffusion.

### 3.7 Strongly Asymmetric Random Walks

In this section we consider strongly asymmetric random walks. We allow the flight PDF to be different for leftward and rightward flights, in addition to the two sources of asymmetry considered previously (different probability for leftward and rightward flights, different velocities for leftward and rightward flights). Specifically, we assume that leftward and rightward flights have a different power law decay exponent.

Table 3.4: Anomalous diffusion results for asymmetric random walks ( $v_{\text{ave}} = p_r v_r + p_l v_l \neq 0$ )  $\sigma^2 \sim C t^\gamma$ , with the coefficients  $C$  and exponent  $\gamma$  given in the table.  $T$  is defined to be  $\langle t_s \rangle + \langle t_f \rangle$ .  $\mu$  is the exponent for the decay of the flight PDF, and  $\nu$  for the sticking PDF.  $\gamma$  is correct for all PDFs with the same asymptotic scaling, while the values shown for  $C$  are correct only for the specific form of the PDFs (Eqs. (3.28) and (3.29)).

| Conditions            |               | $\gamma$        | Coefficient $C$  |
|-----------------------|---------------|-----------------|--|
| $\mu > 3$             | $\nu > 3$     | 1               | $[\frac{\langle t_f \rangle^2 (\langle t_s \rangle^2 + \langle t_f \rangle^2) - 2 \langle t_f \rangle^2 \langle t_s \rangle^2}{T^3}] v_{\text{ave}}^2 + \frac{\langle t_f \rangle^2}{T} [v_{\text{rms}}^2 - \frac{2 \langle t_f \rangle}{T} v_{\text{ave}}^2]$ |
| $2 < \mu < 3$         | $\nu > \mu$   | $4 - \mu$       | $\frac{2}{(4-\mu)(3-\mu)} [v_{\text{rms}}^2 - \frac{(T + \langle t_s \rangle) \langle t_f \rangle}{T^2} v_{\text{ave}}^2] (\frac{t_F^{\mu-1}}{T})$   |
| $\mu > \nu$           | $2 < \nu < 3$ | $4 - \nu$       | $\frac{2}{(4-\nu)(3-\nu)} (\frac{t_S^{\nu-1} \langle t_f \rangle^2}{T^3}) v_{\text{ave}}^2$  |
| $1 < \mu < 2$         | $\nu > \mu$   | 2               | $(2 - \mu) (v_{\text{rms}}^2 - v_{\text{ave}}^2)$  |
| $\mu > 4 - \nu$       | $1 < \nu < 2$ | $2\nu - 2$      | $(\frac{2\Gamma^2(\nu) - \Gamma(2\nu-1)}{\Gamma^2(2-\nu)\Gamma^2(\nu)\Gamma(2\nu-1)}) \langle t_f \rangle^2 t_S^{2-2\nu} v_{\text{ave}}^2$   |
| $\nu < \mu < 4 - \nu$ | $1 < \nu < 2$ | $2 + \nu - \mu$ | $(\frac{2\Gamma(3-\mu)}{\Gamma(2-\nu)\Gamma(3-\mu+\nu)}) t_F^{\mu-1} t_S^{1-\nu} v_{\text{rms}}^2$   |



### 3.7.1 Model

Again we consider a random walker alternating between sticking (remaining at the same location for some length of time) and constant velocity flights. The flights consist of two types: flights of velocity  $v_l$ , with a distribution function  $P_{Fl}(t)$ , and flights of velocity  $v_r$ , with a distribution  $P_{Fr}(t)$ . The  $l$  and  $r$  subscripts are meant to be suggestive of leftward and rightward flights, but the direction of the flights are determined by the signs of  $v_l$  and  $v_r$ ; if  $v_l$  and  $v_r$  have the same sign, the flights are in the same direction. When ending a sticking event, the probability of a leftward flight is  $p_l$ , and the probability of a rightward flight is  $p_r = 1 - p_l$ . The random walker begins at the origin  $x = 0$ , and at time  $t = 0$  begins a flight (with probability  $p_F^0$ ) or a sticking event (with probability  $p_S^0 = 1 - p_F^0$ ). The duration of sticking events is given by the PDF  $P_S(t)$ .

For the moment, we make no assumptions about the forms of the flight and sticking PDFs. Our goal is to find the PDF  $X(x, t)$  of the random walker position for large times, following the same procedure used in the previous section.

We reconstruct  $\tilde{X}(k, t)$  for the case of distinct leftward and rightward flight PDFs. We need  $\xi(x, t)$ , the probability that a flight event has a distance of  $x$  and a duration of  $t$ :

$$\xi(x, t) = p_r \delta(x - v_r t) P_{Fr}(t) + p_l \delta(x - v_l t) P_{Fl}(t) \quad . \quad (3.33)$$

Following exactly the method used in the previous section, we find the Fourier-Laplace transform (in space and time respectively) of  $X(r, t)$  to be:

$$\begin{aligned} \tilde{X}(k, s) &= \left[ s^{-1} (1 - \tilde{P}_S(s)) \right] \left[ \frac{p_S^0 + p_F^0 \tilde{\xi}(k, s)}{1 - \tilde{\xi}(k, s) \tilde{P}_S(s)} \right] \\ &+ \left[ p_r \tilde{\lambda}_r + p_l \tilde{\lambda}_l \right] \left[ \frac{p_F^0 + p_S^0 \tilde{P}_S(s)}{1 - \tilde{\xi}(k, s) \tilde{P}_S(s)} \right] \end{aligned} \quad (3.34)$$

where the function  $\tilde{\lambda}$  has been introduced for convenience:

$$\tilde{\lambda}_r(s) = p_r (s + ikv_r)^{-1} (1 - \tilde{P}_{Fr}(s + ikv_r)) \quad (3.35)$$

and similarly for  $\tilde{\lambda}_l(s)$ . Noting that

$$\tilde{\xi}(k, s) = p_r \tilde{P}_{Fr}(s + ikv_r) + p_l \tilde{P}_{Fl}(s + ikv_l) \quad , \quad (3.36)$$

$X$  has been completely expressed in terms of the three elementary PDFs,  $\tilde{P}_S(s)$ ,  $\tilde{P}_{Fl}(s)$ , and  $\tilde{P}_{Fr}(s)$ .

Using Eq. (3.16), we obtain  $\langle x \rangle$  and  $\langle x^2 \rangle$  by taking derivatives of  $\tilde{X}(k, s)$ :

$$\langle x \rangle = \frac{(p_F^0 + p_S^0 \tilde{P}_S)[\tilde{Z}_r + \tilde{Z}_l]}{s^2(1 - \tilde{\xi} \tilde{P}_S)} \quad (3.37)$$

$$\begin{aligned} \langle x^2 \rangle &= [(1 - \tilde{\xi} \tilde{P}_S)(\tilde{Y}_r + \tilde{Y}_l) - s \tilde{P}_S(\tilde{Z}_r + \tilde{Z}_l)(p_r v_r \tilde{P}'_{Fr} + p_l v_l \tilde{P}'_{Fl})] \\ &\quad \times \frac{2(p_F^0 + p_S^0 \tilde{P}_S)}{s^3(1 - \tilde{\xi} \tilde{P}_S)^2} \end{aligned} \quad (3.38)$$

where

$$\tilde{Y}_r(s) = p_r v_r^2 (1 - \tilde{P}_{Fr} + s \tilde{P}'_{Fr}), \quad (3.39)$$

$$\tilde{Z}_r(s) = p_r v_r (1 - \tilde{P}_{Fr}), \quad (3.40)$$

and similarly for  $Y_l(s)$  and  $Z_l(s)$ . If  $P_{Fl}(t) = P_{Fr}(t)$ , these results reduce to Eqs. (3.26) and (3.27). The results in Eqs. (3.26) and (3.27) are exact for any form of  $P_{Fl,r}(t)$  and  $P_S(t)$ ; no approximations have been made.

### 3.7.2 Results

The asymptotic behavior of  $\langle x(t) \rangle$  and  $\langle x^2(t) \rangle$  as  $t \rightarrow \infty$  ( $s \rightarrow 0$ ) can be obtained from an expansion of Eqs. (3.37) and (3.38) in powers of  $s$ . This depends on  $\tilde{P}_{Fl,r}(s)$  and  $\tilde{P}_S$ , which in turn depend on the particular form of  $P(t)$  for these functions. After expanding for small  $s$ , the leading terms can be inverse Laplace transformed to find the behavior for large  $t$ .

We choose flight and sticking PDFs to be of the same form as those used previously (Eqs. (3.28 and (3.29)). All PDFs have the form:

$$\begin{aligned} P_\alpha(t) &= 0 & t < t_\alpha \\ &A_\alpha t^{-\alpha} & t \geq t_\alpha \end{aligned} \quad (3.41)$$

where  $\alpha$  is either  $\eta$ ,  $\mu$ , or  $\nu$  for  $P_{Fr}$ ,  $P_{Fl}$ , and  $P_S$  respectively, and  $t_\alpha$  is a cutoff at short times to allow the function to be normalizable; the normalization constant is  $A_\alpha = (\alpha - 1)t_\alpha^{\alpha-1}$ . As before, the cutoff times  $t_\eta$ ,  $t_\mu$ , and  $t_\nu$  may be different. The scaling exponent  $\gamma$  of the variance only depends on the asymptotic behavior of the sticking and flight PDFs (the exponents  $\eta$ ,  $\mu$ , and  $\nu$ ), although again the coefficient of  $t^\gamma$  will depend slightly on the exact behavior at short times. The Laplace transforms of the PDFs  $P_\alpha(t)$  (Eq. (3.41)) have the same form as Eq. (3.30), allowing us to use the expansion given in Eq. (3.32) again.

We start by computing the behavior of the mean  $\langle x \rangle \sim Kt^\beta$  using Eq. (3.37). The results are presented in Table 3.5. These results can be understood in relationship to the underlying PDFs. When all PDF exponents are larger than 2, the mean grows proportional to  $\langle l \rangle / T$ , that is, the mean step displacement divided by the time between step. When a flight exponent is less than 2, the mean flight time is infinite. In this situation, for an ensemble of random walkers, for any time  $t$  the typical random walker is still undergoing its first flight, so the mean position for the ensemble of walkers grows as  $v_r$ , the velocity of those walkers (assuming  $\mu < \eta$ ; otherwise the relevant velocity is  $v_l$ ). When the sticking PDF has an infinite first moment ( $\nu < 2$ ), the mean position grows slower than linearly in time, with the growth dependent on the flight behavior; on average, random walkers are undergoing their first sticking event, and the growth of the mean is dependent on the rare walkers not sticking.

Similarly, we expand Eq. (3.38) using Eq. (3.32) to find  $\langle x^2 \rangle$ , and ultimately to find  $\sigma^2(t) = \langle x^2 \rangle - \langle x \rangle^2$ . The results are shown in Fig. 3.3(a) and Table 3.6. The results depend only on the smallest two PDF decay exponents, but are almost completely symmetric between flight and sticking behavior. The variance growth exponent  $\gamma$  in particular is determined by the smallest exponent, and in some cases the second smallest exponent. Note that the transitions from one phase to another that occur as the exponents of the PDF's are varied are sharply defined only in the

Table 3.5: Scaling of the mean position for strongly asymmetric random walks.  $\langle x \rangle \sim Kt^\beta$ .  $\beta$  is correct for any PDF with the same asymptotic scaling, while the values shown for  $K$  are correct only for the specific form of the PDFs (Eq. (3.41)). Without loss of generality, we assume that  $\mu$  is the smaller of the two flight decay exponents.  $\nu$  is the decay exponent for the sticking PDF. In the expressions for  $K$ ,  $\langle l \rangle = p_l v_l \langle t_{Fl} \rangle + p_r v_r \langle t_{Fr} \rangle$  and  $T = p_l \langle t_{Fl} \rangle + p_r \langle t_{Fr} \rangle + \langle t_S \rangle$ . These results are similar to those given in Table 3.3.

| Conditions    |                 | $\beta$         | Coefficient $K$   |
|---------------|-----------------|-----------------|---|
| $\mu > 2$     | $\nu > 2$       | 1               | $\langle l \rangle / T$   |
| $1 < \mu < 2$ | $\nu > \mu$     | 1               | $v_r$   |
| $\mu > 2$     | $1 < \nu < 2$   | $\nu - 1$       | $(\frac{\langle l \rangle}{\Gamma(2-\nu)\Gamma(\nu)})t_\nu^{1-\nu}$                         |
| $1 < \mu < 2$ | $1 < \nu < \mu$ | $1 + \nu - \mu$ | $(\frac{v_r \Gamma(2-\mu)}{\Gamma(2-\nu)\Gamma(2-\mu+\nu)})p_r t_\mu^{\mu-1} t_\nu^{1-\nu}$ |

infinite time limit.

As is the case for the mean  $\langle x \rangle$  discussed above, the behavior can be understood through the PDFs. Let  $\alpha_1$  be the smallest of the PDF decay exponents. If  $\alpha_1 > 3$  then all three PDFs have finite first and second moments, and the Central Limit Theorem must apply. In this case the growth is normally diffusive, that is,  $\gamma = 1$ . If  $2 < \alpha_1 < 3$ , the second moment for that PDF is infinite; this is the situation where flights are Lévy flights. The mean position scales as  $\langle x \rangle \sim t$ , and the growth in the variance results from spreading about this mean position. As expected for situations with Lévy flights, the growth is superdiffusive. If the smallest exponent is the sticking exponent (that is, if  $\alpha_1 = \nu$ ), the sticking events appear to be Lévy flights in the reference frame co-moving with the mean position  $\langle x \rangle$ , and this accounts for the superdiffusive growth of the variance.

For the case when  $1 < \alpha_1 < 2$ , the first moment for the corresponding PDF is infinite. On average, all random walkers are undergoing their first flight (or sticking) event corresponding to this PDF. Thus, the growth in the variance comes from the

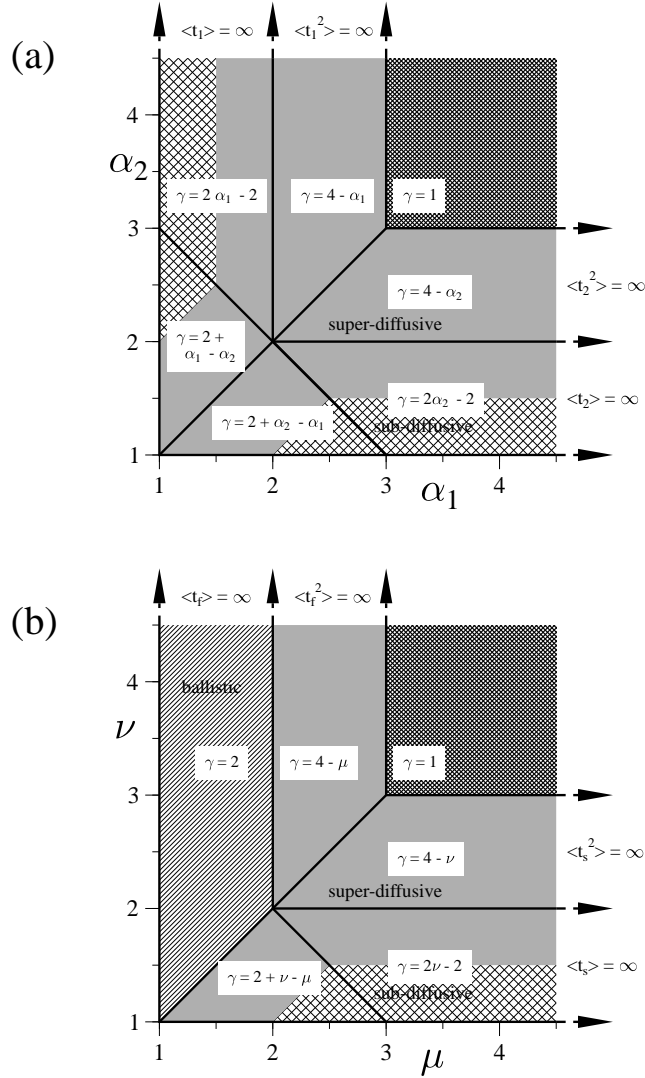


Figure 3.3: (a) Phase diagram for the variance for strongly asymmetric random walks.  $\alpha_1$  and  $\alpha_2$  are the exponents controlling the asymptotic power law decay of the PDFs:  $P_\alpha(t) \sim t^{-\alpha}$  for  $t \rightarrow \infty$ . Of the three PDFs controlling the behavior (flights to the left, flights to the right, sticking),  $\alpha_1$  and  $\alpha_2$  are the lowest two exponents, although by symmetry of the results for this graph it does not matter which exponent is the smallest. For each region, bordered by the solid lines, the relationship between the variance exponent  $\gamma$  [ $\sigma^2(t) \sim t^\gamma$ ] and  $\alpha_1$  and  $\alpha_2$  is shown. The shadings indicate areas where the behavior is normally diffusive ( $\gamma = 1$ ), sub-diffusive ( $\gamma < 1$ ), and superdiffusive ( $\gamma > 1$ ). (b) A copy of Fig. 3.2(b) for comparison (asymmetric random walks). The axes for (b) are analogous to the axes for (a).

Table 3.6: Anomalous diffusion results for strongly asymmetric random walks:  $\sigma^2 \sim Ct^\gamma$ , with the coefficients  $C$  and exponent  $\gamma$  given in the table. In the table, the  $\alpha_i$ 's represent the sorted decay exponents of the PDFs ( $\alpha_1 < \alpha_2 < \alpha_3$ ). The variable  $p_i$  represents  $(p_l, p_r, 1)$  if  $\alpha_i$  corresponds with  $(\eta, \mu, \nu)$  respectively; similarly  $v_i$  represents  $(v_l, v_r, 0)$ .  $\tau_i$  is defined in terms of the cutoff times (see Eq. (3.41)):  $\tau_i = (t_{Fl}, t_{Fr}, t_S)$  if  $\alpha_i$  corresponds with  $(\eta, \mu, \nu)$  respectively.  $T = \sum_{j=1}^3 p_j \langle t_j \rangle$  and  $L_i = \sum_{j=1}^3 p_j (v_i - v_j) \langle t_j \rangle$ . (Note that this definition for  $T$  is equivalent to the one given in Table 3.1.)  $\gamma$  is correct for all PDFs with the same asymptotic scaling, while the values shown for  $C$  are correct only for the specific form of the PDFs (Eq. (3.41)).

| Conditions         |                           | $\gamma$                  | Coefficient $C$   |
|--------------------|---------------------------|---------------------------|---|
| $\alpha_1 > 3$     |                           | 1                         | $2\langle t_s \rangle^2 \langle l \rangle^2 T^{-3} + \sum_{i=1}^3 p_i \langle t_i^2 \rangle T^{-3} L_i^2$   |
| $2 < \alpha_1 < 3$ |                           | $4 - \alpha_1$            | $\frac{2L_1^2}{(4-\alpha_1)(3-\alpha_2)} \left( \frac{p_1 \tau_1^{\alpha_1-1}}{T^3} \right)$  |
| $\alpha_1 < 2$     | $\alpha_2 > 4 - \alpha_1$ | $2\alpha_1 - 2$           | $\left( \frac{2\Gamma^2(\alpha_1) - \Gamma(2\alpha_1 - 1)}{\Gamma^2(2-\alpha_1)\Gamma^2(\alpha_1)\Gamma(2\alpha_1 - 1)} \right) L_1^2 (p_1 \tau_1^{\alpha_1-1})^{-2}$ |
| $\alpha_1 < 2$     | $\alpha_2 < 4 - \alpha_1$ | $2 + \alpha_1 - \alpha_2$ | $\left( \frac{2\Gamma(3-\alpha_2)}{\Gamma(2-\alpha_1)\Gamma(3+\alpha_1-\alpha_2)} \right) \frac{p_2 \tau_2^{\alpha_2-1}}{p_1 \tau_1^{\alpha_1-1}} (v_1 - v_2)^2$      |

rare random walkers which finish those events. If the second smallest PDF exponent  $\alpha_2$  is sufficiently small,  $\gamma$  depends on both  $\alpha_1$  and  $\alpha_2$  as shown in Fig. 3.2.

The results for the exponent  $\gamma$  are similar to those shown in Fig. 3.2(b), with the exception of the ballistic area for  $\mu < 2$  in Fig. 3.2(b). The ballistic motion for the case with  $\mu = \eta$  results as on average, random walkers are undergoing their first flight, but the flight can either be leftward or rightward; for the strongly asymmetric case ( $\mu \neq \eta$ ) one direction dominates. With  $\mu = \eta$ , random walkers going left diverge from those going right; with  $\mu \neq \eta$ , random walkers spend most of their time going in the same direction, and thus the divergence no longer occurs. Thus, for  $\mu \neq \eta$  and either  $1 < \mu < 2$  or  $1 < \eta < 2$ , the growth is no longer ballistic, and can in fact be subdiffusive (see Fig. 3.3(a)).

The results can be easily extended to random walks with multiple types of flights, by slightly modifying the coefficients listed in the Tables: all sums over the three types of events (leftward flights, rightward flights, sticking events) are modified to account for the additional flight types.

## 3.8 Discussion

### 3.8.1 Exponential PDFs

Exponential PDFs, either sticking or flight, are common in physical situations. In this case, all moments are finite, and the PDF can be treated as a power law with  $\mu \rightarrow \infty$  or  $\nu \rightarrow \infty$ . If *both* flight and sticking PDFs have exponential tails, the Central Limit Theorem applies, and the behavior is normally diffusive.

For random walks with exponential sticking PDFs, there is no difference between symmetric and asymmetric random walks in the asymptotic transport behavior, and the results of Eqs. (3.5)-(3.7) (e.g.,  $\gamma = 4 - \mu$  when  $1 < \mu < 2$ ) apply. Random walks without sticking events can be treated the same way (all moments

are finite and equal to zero) and again Eqs. (3.5)-(3.7) describe the behavior as a function of  $\mu$ . The mean of asymmetric random walks when the sticking PDF is exponential grows linearly in time ( $\langle r \rangle \sim v_{\text{ave}} t$ ) for all values of  $\mu$ .

Exponential flight PDFs can lead to different behavior, depending on the symmetry. If  $2 < \nu < 3$ , asymmetric random walks are superdiffusive while symmetric walks are normally diffusive, as seen in the preceding subsection. The case where “flights” are actually steps of constant length, as has been considered previously [13], is equivalent to exponential flight PDFs – again, the important aspect is that all moments of the flight PDF are finite, and again, asymptotic behavior depends on the presence or absence of symmetry.

Using a decay exponent of  $\infty$  for exponential PDFs allows a comparison to be made with the Hamiltonian model of Ref. [33]. This model describes a 2D flow consisting of a chain of vortices in a shear flow. Tracer particles alternate between being trapped in vortices and moving in jets. In several cases, flight times in the jets and sticking times in the vortices are well-described by power law PDFs. In particular, this Hamiltonian model yields different PDFs for leftward and rightward flights, and thus the results can be compared with our model.

Reference [33] considers three cases in detail, and finds for the exponents  $(\mu, \eta, \nu)$  the values  $(\infty, \infty, 2.9)$  (case a);  $(3.26, \infty, 2.4)$  (case b); and  $(\infty, 1.89, 2.0)$  (case c) (where an exponent equal to  $\infty$  represents non-power law decay). The values of  $\gamma$  for cases (a), (b), and (c), respectively, are 1.42, 1.53, and 1.80, while the corresponding predictions of our analyses are 1.10, 1.60, and 1.89. The agreement is good for cases (b) and (c) but not for (a). This suggests that perhaps the trajectories in the Hamiltonian model have hidden correlations, that is, that the motions in the jets and vortices are correlated. It is also possible that the asymptotic time limit hasn't been reached for case (a). For both cases (a) and (c), the exponent  $\beta$  in  $\langle x \rangle \sim t^\beta$  is unity, in agreement with the predictions of our model. A value of  $\beta$



could not be determined for case (b).

### 3.8.2 Correlated Random Walks

Our results have been derived for independent steps and pauses. For cases where the steps are correlated, the results can be different (for example, if all of the steps are in the same direction for a given random walker, or if all pauses are the same length). In some cases, random walks with short-range correlations can be treated as random walks with uncorrelated steps on a longer time scale. In this way the results for the asymptotic behavior can still apply. This approach is discussed in Ref. [13].

### 3.8.3 Higher order terms

The asymptotic behavior of  $\langle x \rangle$  and  $\langle x^2 \rangle$  depends only on the leading terms in the expansion of Eqs. (3.26), (3.27), (3.37), and (3.38). In order to study the approach to the asymptotic limit, it is necessary to calculate higher order terms. In Appendix A, we use Eq. (3.32) for the expansion of the Laplace transform of the PDFs to produce the second order terms, which are tabulated there. The variance will scale in time, generally, as  $\sigma^2(t) \sim Ct^\gamma + C't^{\gamma'}$  with  $\gamma' < \gamma$ . The asymptotic behavior, given in the previous sections, will always be given by the largest exponent.

As discussed in Chap. 4, crossover times must be considered in deducing the anomalous diffusion exponent from data. If the variance  $\sigma^2$  is given by:

$$\sigma^2(t) = at^\gamma + bt^{\gamma'}, \quad \gamma > \gamma' \quad , \quad (3.42)$$

then the slope on a log-log plot is given by  $d(\ln \sigma^2)/d(\ln t)$ :

$$\text{slope}(t) = \frac{\gamma + \gamma'(b/a)t^{\gamma'-\gamma}}{1 + (b/a)t^{\gamma'-\gamma}} \quad , \quad (3.43)$$

which as  $t \rightarrow 0$  has the value  $\gamma'$  and as  $t \rightarrow \infty$  has the value  $\gamma$ , as expected. If  $\gamma - \gamma'$  is small, the time to crossover to the asymptotic behavior is very large. For

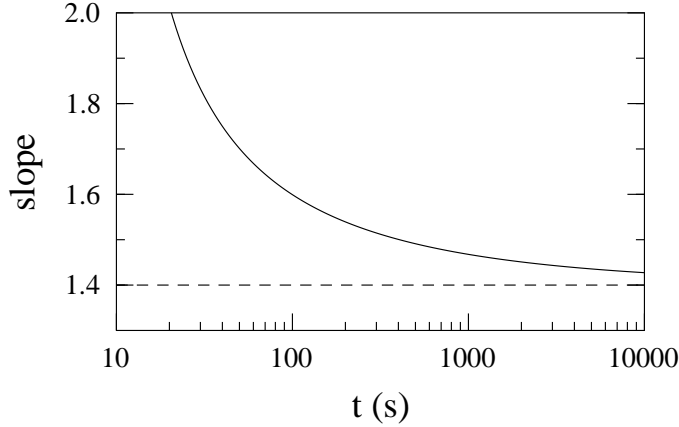


Figure 3.4: Graph of slope of the function  $Ct^\gamma + C't^{\gamma'}$  for  $\gamma = 1.40$ ,  $\gamma' = 1.05$ , corresponding to the predictions of the model for  $\mu = 1.95, \nu = 1.35$  (measured from the experiment; see Chap. 4). The constants are  $C = 0.055$  and  $C' = -0.10$  (from Table A.4, with  $p_l = 0, p_r = 1, v_{\text{rms}}^2 = v_{\text{ave}}^2 = 0.0058 \text{ rad/s}, t_F = 22 \text{ s}, t_S = 10 \text{ s}$ , and  $P_S^0 = P_F^0 = 0.5$ ; again, these values are taken from the experiment). There is a broad region with changing slope. (Figure from Ref. [155].)

example, in Fig. 3.4, with  $b/a = -1.82$ ,  $\gamma = 1.40$  and  $\gamma' = 1.05$ , it takes 400 s for the measured exponent to get below 1.5, within 0.1 of the correct asymptotic value. (When  $b/a$  is negative, as in Fig. 3.4, there is a divergence of the slope when the denominator vanishes in Eq. (3.43).)

### 3.8.4 Conclusions

For most random walks, the Central Limit Theorem applies and the variance grows as  $\sigma^2(t) \sim t^\gamma, \gamma = 1$ . We have investigated cases where the random walk alternates between flight (movement) and sticking (motionless) behavior, and where the flights consist of two distinct types. When the Central Limit Theorem no longer applies, the variance can grow either superdiffusively or subdiffusively, depending on the exact behavior of the random walk. If the random walkers spend part of their time in either flight or sticking behavior with  $\langle t^2 \rangle = \infty$  for that type of behavior, anomalous diffusion usually occurs (with one exception shown in Fig. 3.2(a).) We find that

adding asymmetries to the random walk can have strong qualitative changes to the behavior. In particular, when the first moment of any of the flight or sticking PDFs is infinite, the variance can grow either subdiffusively, superdiffusively, or even ballistically, depending on the decay rate of each PDF.

## Chapter 4

# Random Walks in Experiments

### 4.1 Motivation

The mixing of passive impurities in fluid flows depends critically on the structure and time dependence of the velocity field. In the absence of a flow, Brownian motion of individual tracer particles results in molecular diffusion. If the fluid is moving, advection of tracer particles by the flow results in significant enhancements in the transport rates.

In this chapter we present experimental measurements of Lévy flights and superdiffusive transport in a two-dimensional flow in a rotating annulus [132, 133, 154, 155]. Transport in a two-dimensional flow can be analyzed from a Hamiltonian perspective [3]. Given a stream function  $\psi(x, y, t)$ , the equations describing particle motion in the flow are given by

$$dx/dt = -\partial\psi/\partial y, \quad dy/dt = \partial\psi/\partial x, \quad (4.1)$$

which are Hamilton's equations of motion with  $\psi$  as the Hamiltonian and  $x$  and  $y$  as the conjugate coordinates. The path of a passive tracer in a two-dimensional flow is, therefore, the phase space trajectory of a Hamiltonian system. If  $\psi$  is time-independent, the equations of motion are fully integrable and trajectories lie

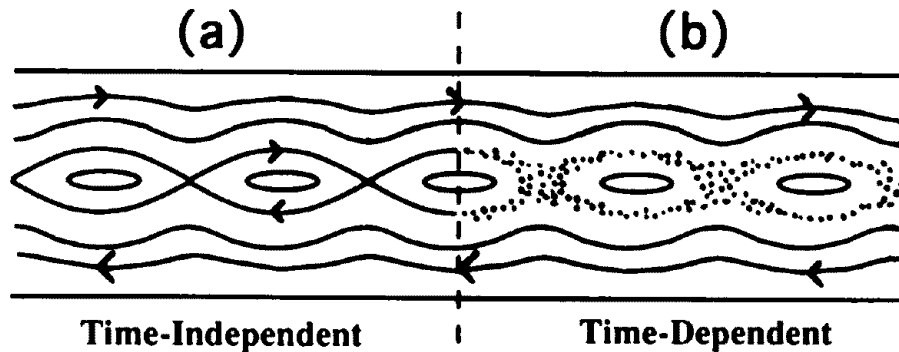


Figure 4.1: (a) Phase space portrait for an ideal time-independent (integrable) system; all trajectories are closed curves. (b) Poincaré section for a time-dependent (non-integrable) system; some trajectories lie on closed curves (“KAM tori”), but there are large regions (the chaotic sea) with chaotic trajectories, represented by the dotted areas. For the fluid flow in the annulus, the phase space is *real* space. (Figure from Ref. [133].)

on closed curves. In time-independent cellular flows, for example, particles within a vortex (a cell) ideally remain trapped indefinitely; see Fig. 4.1(a). In reality [17, 130, 165], molecular diffusion allows tracers eventually to escape from the vortices, although the time scale for the escape can be quite long compared to the characteristic times for the dynamics (e.g., vortex turnover time).

If the flow is time-dependent, the Hamiltonian phase space (real space for fluid mixing) can be divided into ordered and disordered regions; see Fig. 4.1(b). Tracer particles in the disordered regions follow chaotic trajectories. This behavior is termed Lagrangian chaos or chaotic advection [3, 98]. The resultant particle trajectories are often far more complicated than might be expected for a laminar flow. In the absence of molecular diffusion, the curves (invariant surfaces) dividing the ordered and disordered regions act as impenetrable barriers that tracer particles cannot cross.

The motion of tracer particles within the disordered regions is affected by the invariant surfaces (KAM tori) or their remnants (Cantori). Particles that pass

close to an invariant surface remain in the vicinity of that surface for a long (but finite) time [84, 166]. The persistence of trajectories near closed surfaces results in long-time *sticking* of particles. Similarly, if a flow contains jet regions and Cantori, long-range and long-time excursions called *flights* are possible. As discussed in the previous chapter (Sec. 3.4), flights and sticking behavior are both common in Hamiltonian systems.

## 4.2 Flows Studied

For these experiments, a 6 cm tall Plexiglas annulus with inner (outer) radius of 10.8 (19.4) cm is inserted into the tank to act as a barrier; this barrier, by the Taylor-Proudman theorem, divides the flow into inner and outer regions. The flows are studied in the outer region. In all cases, the flows have a sharp velocity gradient above the edge of the Plexiglas barrier. This shear layer is a Stewartson boundary layer, so it does not become unstable. Two fluids are used for these flows, a water-glycerol mixture (38% glycerol by weight) with a kinematic viscosity  $\nu = 0.03 \text{ cm}^2/\text{s}$ , and water with  $\nu = 0.009 \text{ cm}^2/\text{s}$ .

Flows are produced in the annulus by pumping the fluid into and out of the tank through the 0.26 cm diameter holes in the bottom. The holes are arranged in three concentric rings of 120 holes each at radii 18.9, 27.0, and 35.1 cm, as discussed in Chapter 2. We study transport in flows generated with six different forcing techniques. The time-dependence of some of the flows are similar, so in this dissertation we label some of the flows by their structure (number of vortices). The six flows are:

1. *Time-independent flow* with six vortices. The pumping rate is  $45 \text{ cm}^3/\text{s}$ , and the water-glycerol mixture is used. The tank rotation rate is 1.5 Hz. The inner (outer) ring of holes acts as a source (sink) through which fluid is pumped into (from) the tank. The resulting radial forcing flow couples with the Coriolis

effect to produce a strong azimuthal jet that rotates (relative to the tank) in the direction opposite the rotation of the tank. The counter-rotating jet results in a shear layer above the outer ring of holes, which is unstable to the formation of a chain of vortices that precesses around the tank [131] (see for example Fig. 4.3). A similar vortex chain would form above the inner ring of holes, but the Plexiglas barrier suppresses this shear instability (and this is the reason for the barrier — to simplify the resulting flow).

For the time-independent flow, six vortices were present. In the reference frame co-rotating with the vortex chain, the flow is time-independent (Fig. 4.2(a)). This flow should not have chaotic mixing; tracers should follow the streamlines.

2. *Seven-vortex flow* with quasi-periodic time dependence (Fig. 4.3). The pump rate is  $45 \text{ cm}^3/\text{s}$ , and the water-glycerol mixture is used; the difference between this flow and the time-independent flow is the initial condition used, which for this flow resulted in the presence of seven vortices. To generate the seven-vortex flow instead of the time-independent flow, the pump was quickly turned to its final value immediately after the final rotation rate of the annulus was reached, but before the bulk fluid had spun up to this rotation rate. For the time-independent flow, the bulk fluid was allowed to come to rest relative to the tank before the pump was turned on.

In the reference frame co-rotating with the vortex chain, this flow is time-periodic; in the reference frame of the tank, the motion of the vortices around the annulus results in quasi-periodic time dependence (Fig. 4.2(b)). This flow is termed “modulated wave flow” in Ref. [154].

3. *Six-vortex flow* with quasi-periodic time dependence. This flow is generated with the same techniques as the time-independent flow, with one difference: the radial forcing has a non-axisymmetric perturbation. The forcing flow

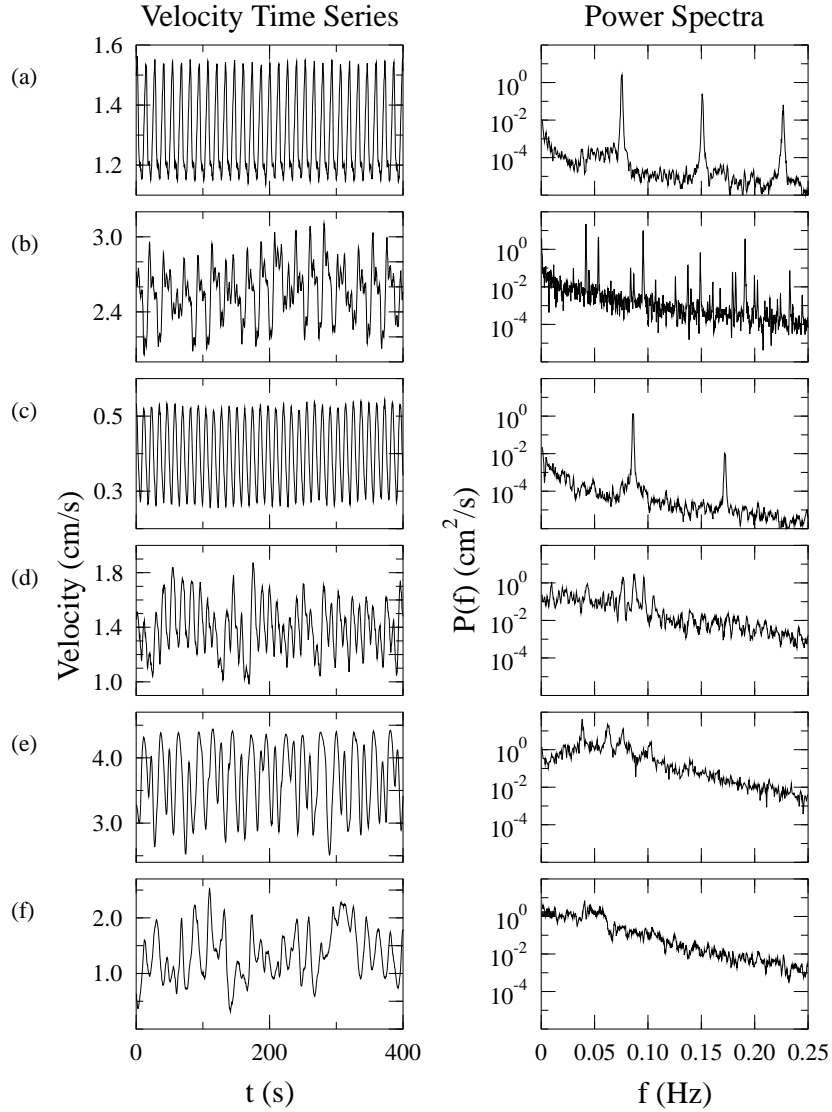


Figure 4.2: Velocity time series and power spectral density  $P(f)$  obtained from hot film probe measurements of the azimuthal velocity component at  $r = 35.1$  cm: (a) *time-independent flow*; (b) *seven-vortex flow* with periodic time dependence in the reference frame co-rotating with the vortex chain (see Fig. 4.3); (c) *six-vortex flow* with periodic time dependence in the vortex chain reference frame; (d) *five-vortex flow* with chaotic time dependence; (e) *four-vortex flow* with chaotic time dependence (see Fig. 4.4); (f) *weakly turbulent flow* (see Fig. 4.5). These data are taken in the *tank* frame of reference, as opposed to the co-moving frame of reference used for the particle pictures in this chapter.



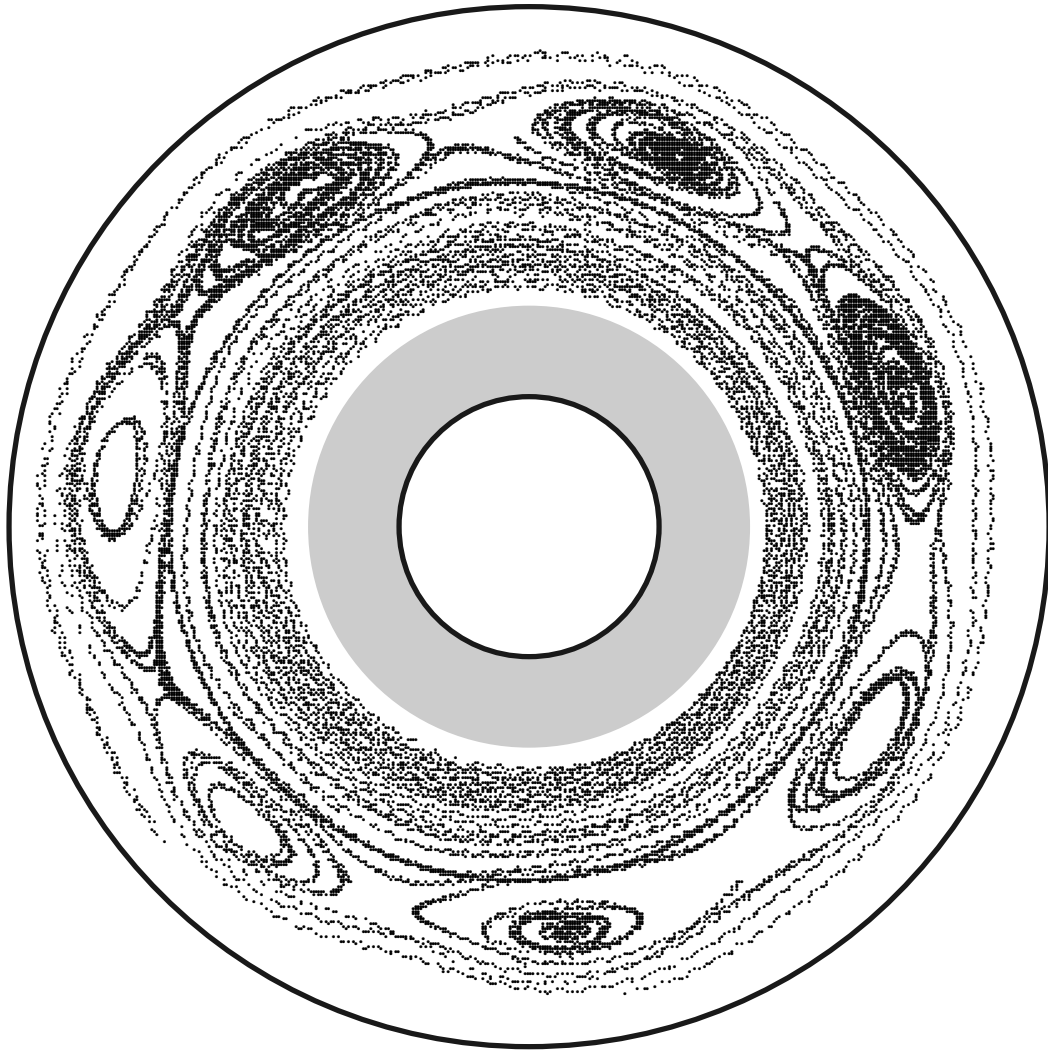


Figure 4.3: The *seven-vortex flow* is revealed by the trajectories of 20 particles tracked for 300 s in a reference frame co-rotating with the vortices. In this reference frame, the vortex chain is sandwiched between two azimuthal jets. This flow has periodic time dependence in this reference frame. The inner and outer circles represent the annulus boundaries, and the grey circle indicates the location of the Plexiglas barrier. (Figure from Ref. [154].)

through one  $60^\circ$  sector of source and sink holes is restricted to less than half that for the rest of the forcing holes. Thus the vortex chain is perturbed as it moves past this constricted sector, with the period of the perturbation being the time for a vortex to precess around the annulus (70.0 s).

In the reference frame of the vortex chain, the flow is time-periodic. In the reference frame of the tank, the flow is also time-periodic (Fig. 4.2(c)), as the perturbation is stationary with respect to the tank. In all other reference frames, the flow is quasi-periodic in time. This flow is termed “time-periodic flow” in Refs. [133, 154].

4. *Five-vortex flow* with chaotic time dependence. This flow is similar to the six-vortex flow, except that the flux through the perturbing sector is completely shut off. There are still well-defined vortices in this flow, but the number of vortices alternates between five and six over long periods of time.

This flow has chaotic time-dependence, as can be seen from the hot film probe measurements (Fig. 4.2(d)). The word chaotic in this case denotes Eulerian chaos, that is, a chaotic velocity field, as distinct from Lagrangian chaos of the particle trajectories (defined in Sec. 4.1). This flow is termed “chaotic flow” in Refs. [133, 154]. We do not actually know this flow is chaotic in the sense of positive Lyapunov exponents; the noise floor shown in Fig. 4.2(d) is higher than the previous flows, a signature of chaos.

5. *Four-vortex flow* with chaotic time dependence (see Fig. 4.4). The pump flux is  $52 \text{ cm}^3/\text{s}$ , water is used rather than water-glycerol, and the rotation rate is 1.0 Hz rather than 1.5 Hz. Rather than the inner and outer forcing rings, this flow uses the inner and middle forcing rings ( $r = 18.9 \text{ cm}$  and  $27.0 \text{ cm}$ ), to allow the vortices to be larger, and prevent an inner jet from forming, as can be seen in Fig. 4.4.



Figure 4.4: The *four-vortex flow* is revealed by the trajectories of 12 particles tracked for 100 s in a reference frame co-rotating with the vortices. The inner and outer circles represent the annulus boundaries, and the grey circle indicates the location of the Plexiglas barrier. (Figure from Ref. [155].)

At this high pumping rate, the motion of the vortices is chaotic, as shown in the velocity power spectrum shown in Fig. 4.2(e). As for the five-vortex flow, this is Eulerian chaos. This flow was termed “chaotic flow” in Ref. [155]. (Again, the chaos of this flow has not been rigorously confirmed, but the power spectrum is reasonable evidence of the chaos of the flow, as are the qualitative observations of the vortex motion.)

6. *Weakly turbulent flow* (see Fig. 4.5). This flow was generated using water and a special forcing configuration. Only the outer ring holes were used ( $r = 35.1$  cm). The ring is divided into  $60^\circ$  sectors, alternating between sources and sinks. The resulting flow consists of vortices of both signs, and there are no persistent jets or other structures. The pump flux is  $45 \text{ cm}^3/\text{s}$ , but all of this flux goes through only one ring of forcing holes rather than two. The rotation rate was 1.5 Hz. Note that the previous flows are all laminar; this is the only velocity field that is turbulent.

The velocity power spectrum consists of broadband noise and no dominant spectral components; see Fig. 4.2(f). This flow is termed “turbulent flow” in Ref. [133] and “weakly turbulent flow” in Ref. [154].

The flows are summarized in Table 4.1.

### 4.3 Analysis techniques

After a typical experimental run of 4 hours, we have tracked typically 5-10 trajectories with duration greater than 20 minutes, 30 with 10-20 minutes duration, and several hundred with 2-10 minutes duration. Statistics for the longer times are improved by repeating the experiments with the same control parameters (but see discussion in Sec. 4.5).

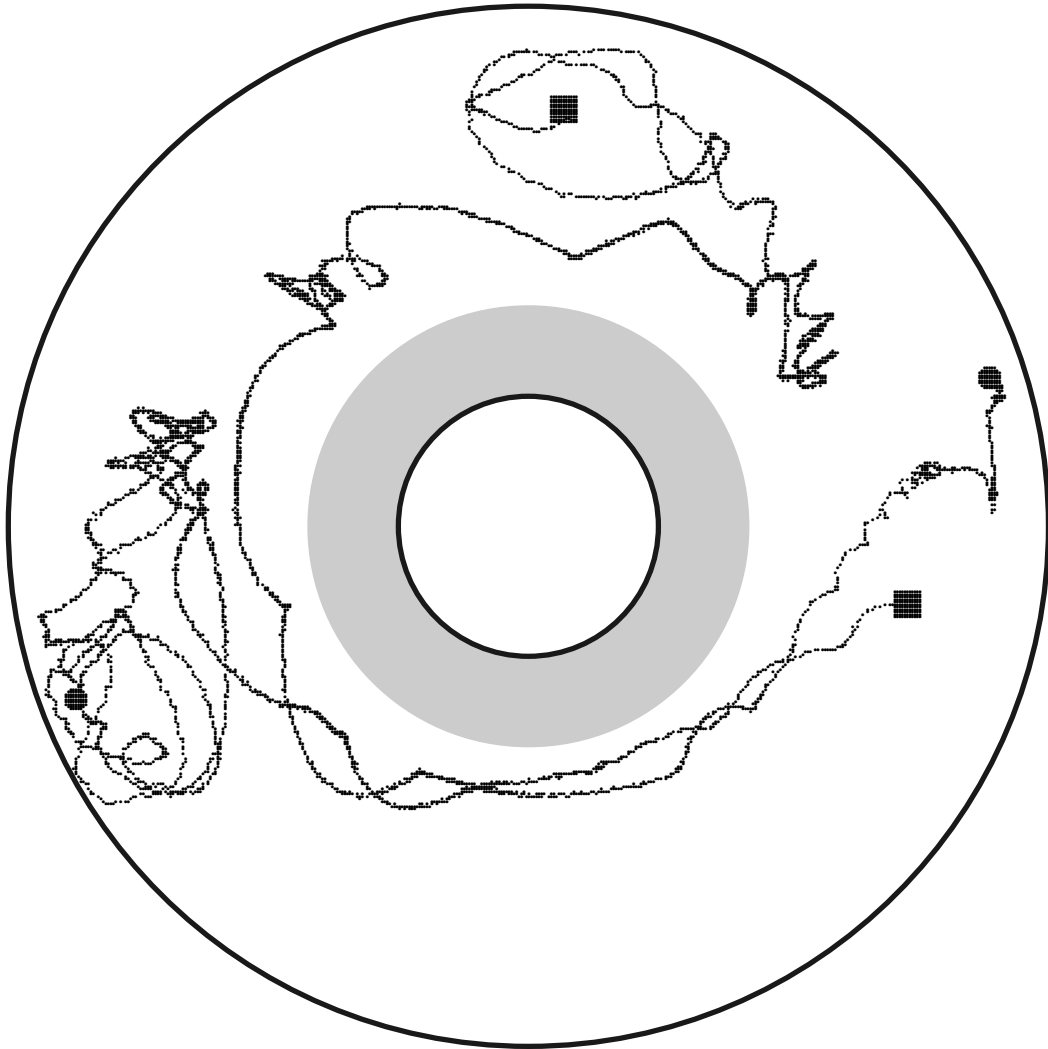


Figure 4.5: Two trajectories show the lack of long-lived coherent structures in the *weakly turbulent flow*. The beginning and end of one trajectory is marked with circles, the other with squares; both particles start at the far right. The inner and outer circles represent the annulus boundaries, and the grey circle indicates the location of the Plexiglas barrier. (Figure based on Ref. [154].) The particles are shown in the reference frame of the annulus.

Table 4.1: Summary of the flows investigated in this chapter, with kinematic viscosity  $\nu$ , pump flux  $F$ , and dimensionless numbers  $Ro$ ,  $Ek$ , and  $Re$  (calculated using  $U = 3$  cm/s as the typical velocity for all flows). The rotation rate  $\Omega = 1.5$  Hz for all flows (except the four-vortex flow as noted). Time dependence listed is in the reference frame co-rotating with the vortex chain.

| Flow name                                    | $\nu$ (cm <sup>2</sup> /s) | $F$ (cm <sup>3</sup> /s) | $Ro \times 10^2$ | $Ek \times 10^6$ | $Re$ |
|--|----------------------------|--------------------------|------------------|------------------|------|
| Time-independent<br>(with six vortices)      | 0.03                       | 45                       | 4.0              | 4.0              | 400  |
| Seven-vortex <sup>a</sup><br>(time-periodic) | 0.03                       | 45                       | 4.0              | 4.0              | 400  |
| Six-vortex <sup>b</sup><br>(time-periodic)   | 0.03                       | 45                       | 4.0              | 4.0              | 400  |
| Five-vortex <sup>c</sup><br>(Eulerian chaos) | 0.03                       | 45                       | 4.0              | 4.0              | 400  |
| Four-vortex <sup>d</sup><br>(Eulerian chaos) | 0.009                      | 52                       | 12               | 2.0              | 1000 |
| Weakly turbulent <sup>e</sup>                | 0.009                      | 45                       | 16               | 1.2              | 1100 |

<sup>a</sup>different initial conditions.

<sup>b</sup>azimuthally asymmetric forcing perturbation.

<sup>c</sup>azimuthally asymmetric forcing perturbation, even stronger than for the six-vortex flow.

<sup>d</sup>using middle forcing ring, rather than outer;  $\Omega = 1.0$  Hz rather than 1.5 Hz.

<sup>e</sup>special forcing used, see text.

The transport is analyzed as a one-dimensional process in the azimuthal direction  $\theta$ . The variance is calculated by the relations

$$\begin{aligned}\sigma^2(t) &= \langle (\Delta\theta(t, \tau) - \langle \Delta\theta(t, \tau) \rangle)^2 \rangle, \\ \Delta\theta(t, \tau) &= \theta(\tau + t) - \theta(\tau),\end{aligned}\tag{4.2}$$

where the ensemble average is over  $\tau$  for individual trajectories and over the different trajectories in the run. This procedure treats each tracer as though starting from the same angle at the same time. This method is accurate for times greater than typical vortex turnover times (typically 10-20 s) but results in a variance that grows as  $t^2$  for short times. Only those trajectories that display both sticking and flight events are used in the calculation of the variance. The first and last events (sticking or flight) are removed to avoid any biasing. (That is, when a particle is first observed, it is in the middle of an event; we consider the trajectory only after this event has finished, so that all particles are considered at the beginning of a flight or sticking event, rather than in the middle of an event.) Different analysis techniques were examined to insure that the results are not strongly dependent on the biasing effects.

Sticking and flight time probability distribution functions (PDFs) are determined from local extrema of  $\theta(t)$ ; see, e.g., Fig. 4.8. A flight is identified by an angular deviation  $\Delta\theta > \Theta_{\text{vortex}}$  (angular width of a single vortex) between successive extrema, and the sticking events are the intervals between flights. The PDFs are normalized histograms of these events. Care must be taken when constructing these PDFs from the data. Our procedure is:

1. Take the logarithm (base 10) of all times.
2. Make a histogram of the logarithm of the times.
3. Convert from the histogram to probability by taking the number of counts in each histogram bin, and dividing by the width (in seconds) of the bin; each bin has a different width as the bins are spaced evenly in logarithm-time.

4. Normalize the resulting distribution function such that the integral is 1 (as required for a probability distribution function); again, the normalization must take into account the variable width of each bin.
5. Plot the resulting PDF on log-log or log-linear scales. At this point, the PDF is correct as plotted. These techniques have been checked with artificially constructed data sets with known power law forms.

The PDFs are adjusted to correct for biases toward shorter sticking/flight times, due to the finite duration of the measured trajectories. The adjustment is determined by generating long, artificial trajectories numerically with known, ideal power law sticking and flight time distributions. These long trajectories are then chopped randomly into smaller sections with a distribution of durations comparable to those in the experiment. PDFs determined from these chopped trajectories are also biased toward smaller times. The adjustment is determined by comparing the PDFs from the chopped trajectories to the ideal PDFs (both from numerical data); the exponents characterizing the PDFs for the chopped time series are about 0.3 larger than for the original long time series. Note that all reported exponents in this chapter are the *corrected* values; the values measured directly from the PDFs are reported in footnotes for each PDF figure.

## 4.4 Results

### 4.4.1 Time-independent flow: no chaotic mixing

Ideally, particle trajectories in a time-independent flow fall on closed streamlines and there is no chaotic advection. While molecular diffusion of the tracer particles is completely negligible on the time scale of the experiments, slight imperfections due to noise (mainly from variations in the pumping, although see discussion in Sec. 4.5), Ekman pumping, and finite-size particle effects can have a noticeable effect



on the trajectories (as discussed in Sec. 2.3). Such imperfections are inevitable in an experiment, even when Fourier spectra indicate that the velocity field is time-independent, as is the case for the flow in Fig. 4.6. The imperfections allow tracers to wander between neighboring streamlines, apparently filling the interior of a vortex; see Fig. 4.6(a). The imperfections occasionally lead to the escape of a tracer particle near a separatrix, but we find that in practice tracers remain trapped for long periods of time. Trapping times of 800 s (approximately 40 vortex turnover times) are common; see Fig. 4.6(a). Similarly, tracers that start in a jet remain in the jet for long times; see Fig. 4.6(b).

The azimuthal coordinate  $\theta(t)$  for a particle in a vortex oscillates about a constant value, while for a particle in a jet with constant velocity,  $\theta(t)$  grows linearly with time, as shown in Fig. 4.6(c). In the absence of noise, the variance of a distribution of particles grows as  $t^2$  (ballistic separation) [89].

#### 4.4.2 Time-periodic flows: power law flights

Chaotic advection is observed in the seven- and six-vortex flows, the two flows with periodic time dependence in the reference frame co-rotating with the vortex chain. Particles frequently make transitions to and from vortices. This is seen in Fig. 4.7. Instead of being trapped indefinitely, particles have sticking events interspersed with flights in the jet regions.

This intermittent sticking/flight behavior is apparent in plots of  $\theta(t)$ , as shown in Fig. 4.8. The observed sticking times and flight times range from  $\sim 10$  s to  $\sim 600$  s. The lower boundary of  $\sim 10$  s is half a vortex turnover time. The vortex turnover time,  $\sim 23$  s, can be measured from Fig. 4.9, a graph showing the time a particle takes to move halfway around a vortex plotted against the angle moved through (with respect to the center of the annulus, in the reference frame moving with the vortex chain). This graph was obtained by taking the difference in time and

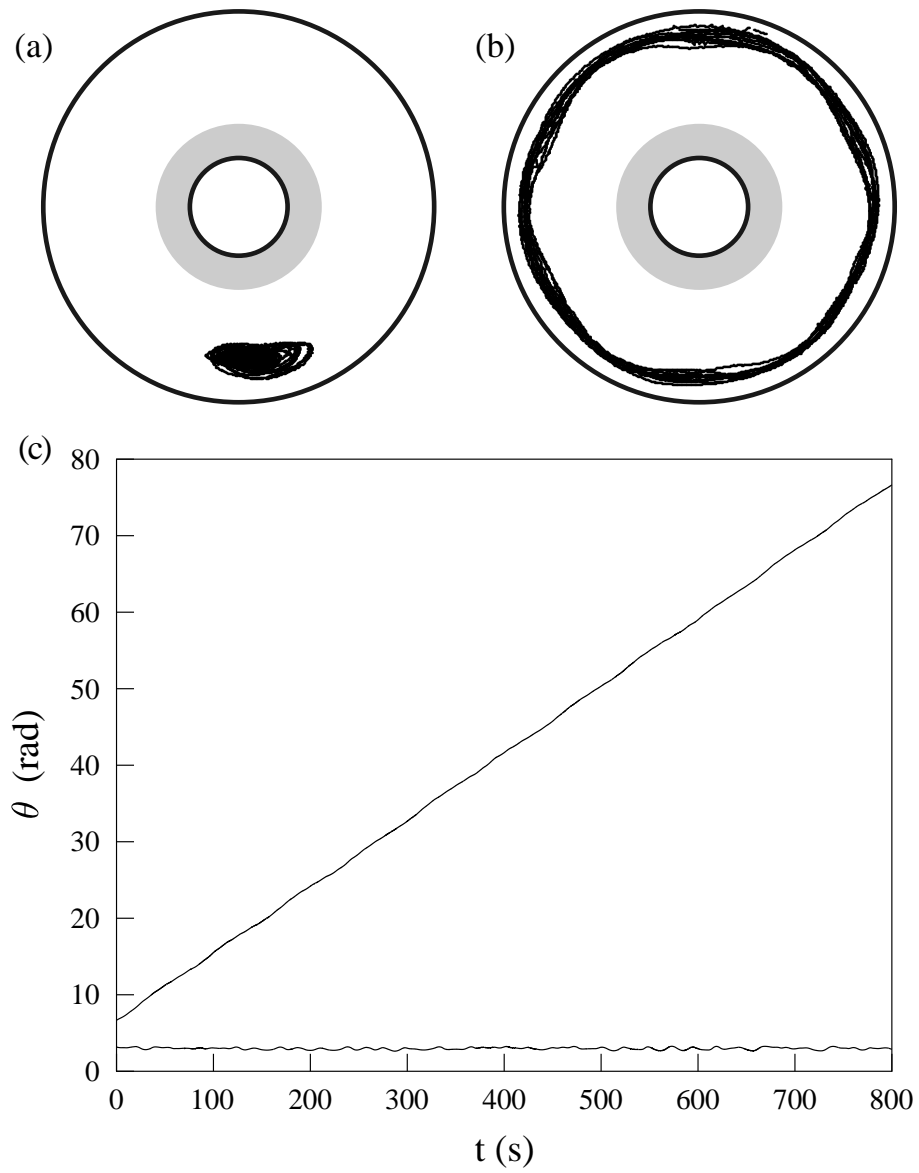


Figure 4.6: (a) and (b) Tracer particle trajectories in the time-independent flow, viewed in a reference frame co-rotating with the vortex chain. (c) The azimuthal displacement as a function of time for the particles in (a) and (b); the starting angle  $\theta(t = 0)$  is arbitrary. The inner and outer circles represent the annulus boundaries, and the grey circle denotes the Plexiglas barrier. (Figure based on Ref. [133].)

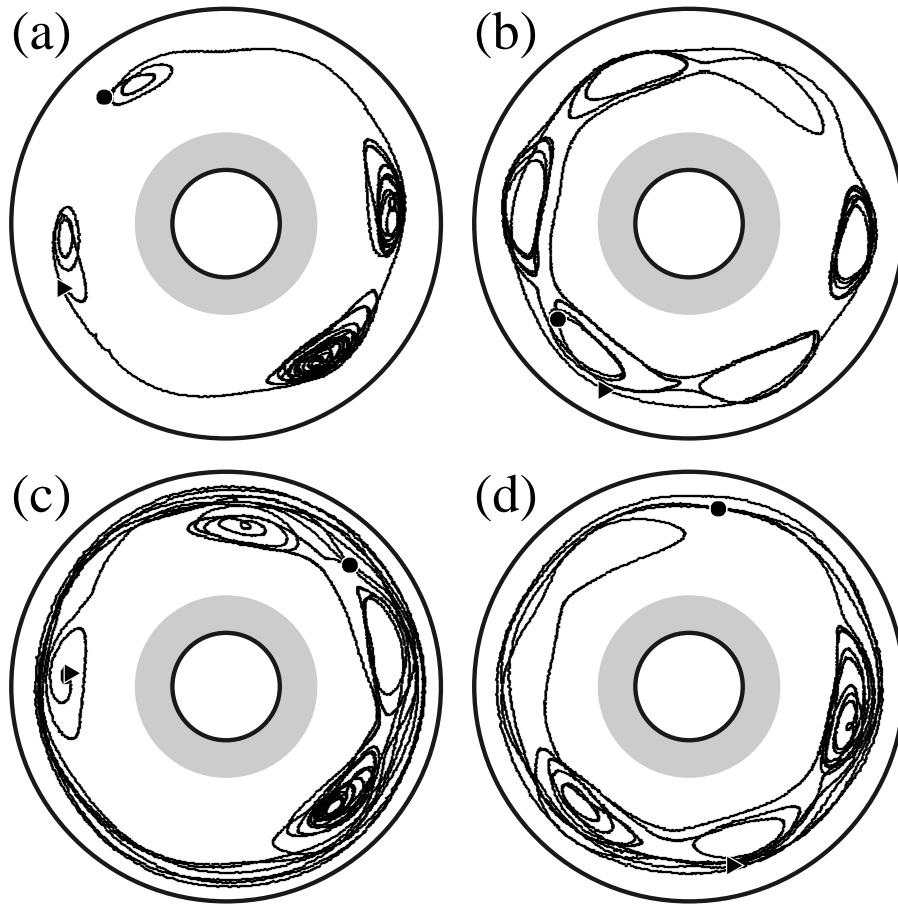


Figure 4.7: Chaotic particle trajectories in the six-vortex flow (time-periodic in the reference frame of the vortex chain). Long sticking events can be seen in each case, and flights of length greater than one rotation about the annulus can be seen in (c), (d). Hyperbolic fixed points, near which the particle motion is particularly sensitive to transitions between flights and sticking events, are evident in all of the trajectories. The particle motion is viewed from a reference frame that is co-rotating with the vortex chain, and the beginning of each trajectory is marked by a triangle, the end by a circle. (Note that this is incorrectly labeled in Ref. [133], as can be seen by comparing Fig. 6(a) and Fig. 7(a) in that article. It is also incorrectly labeled in Ref. [132]; compare Fig. 1(b) and Fig. 2(b).) These trajectories correspond to the six-vortex flow, but are typical in appearance for the seven-vortex and five-vortex flows. (Figure based on Ref. [133].)

angle between successive pairs of maxima and minima in  $\theta(t)$  for a sticking event; see Fig. 4.8. Small angles correspond to particles near the center of the vortex. The average time for all of the particles shown in Fig. 4.9 is 11.7 s, giving a vortex turnover time of 23.4 s. The five-vortex and six-vortex flows have similar vortex turnover times,  $\sim 20$  s.

In Fig. 4.8 it can be seen that the slopes of the flight segments are approximately constant, indicating that the azimuthal velocity,  $\omega = d\theta/dt$ , remains steady during the flights, except when the tracer passes near a hyperbolic point, where both  $\omega$  and the radial component of velocity can decrease nearly to zero. This is also shown by Fig. 4.10, which shows the distance each flight moves against the time for the flight, showing a linear dependence as expected for constant velocity flights. The constant velocity of flights indicate that the results of Chapter 3 are applicable. Figure 4.8 also shows there is an asymmetry between positive and negative displacements, due to a higher probability for co-rotating than for counter-rotating flights. This asymmetry in the flights is likely due to the curvature of the system, which results in longer and more curved separatrices outside the vortex chain than inside (see Fig. 4.8) and a larger exchange rate between the vortices and the outer jet [32]. In addition, Fig. 4.10 shows the velocity of flights in the outer jet is larger than that in the inner jet.

To find the PDFs for the flight and sticking events, the trajectories of 1300 particles were analyzed for the seven-vortex flow, and 1700 particles for the six-vortex flow. The cleanest data (of all six flows) were obtained for the quasi-periodic seven-vortex flow, and the results are shown in Fig. 4.11. The flight PDF shows clear power law decay,  $P_F(t) \sim t^{-\mu}$  with<sup>1</sup>  $\mu = 3.2 \pm 0.2$ . The PDFs for flights in the  $+\theta$  and  $-\theta$  directions were compared and found to have similar decay exponents. The sticking PDF has a curvature indicating asymptotic behavior steeper than a

---

<sup>1</sup>after the correction for finite trajectory duration, discussed in Sec. 4.3

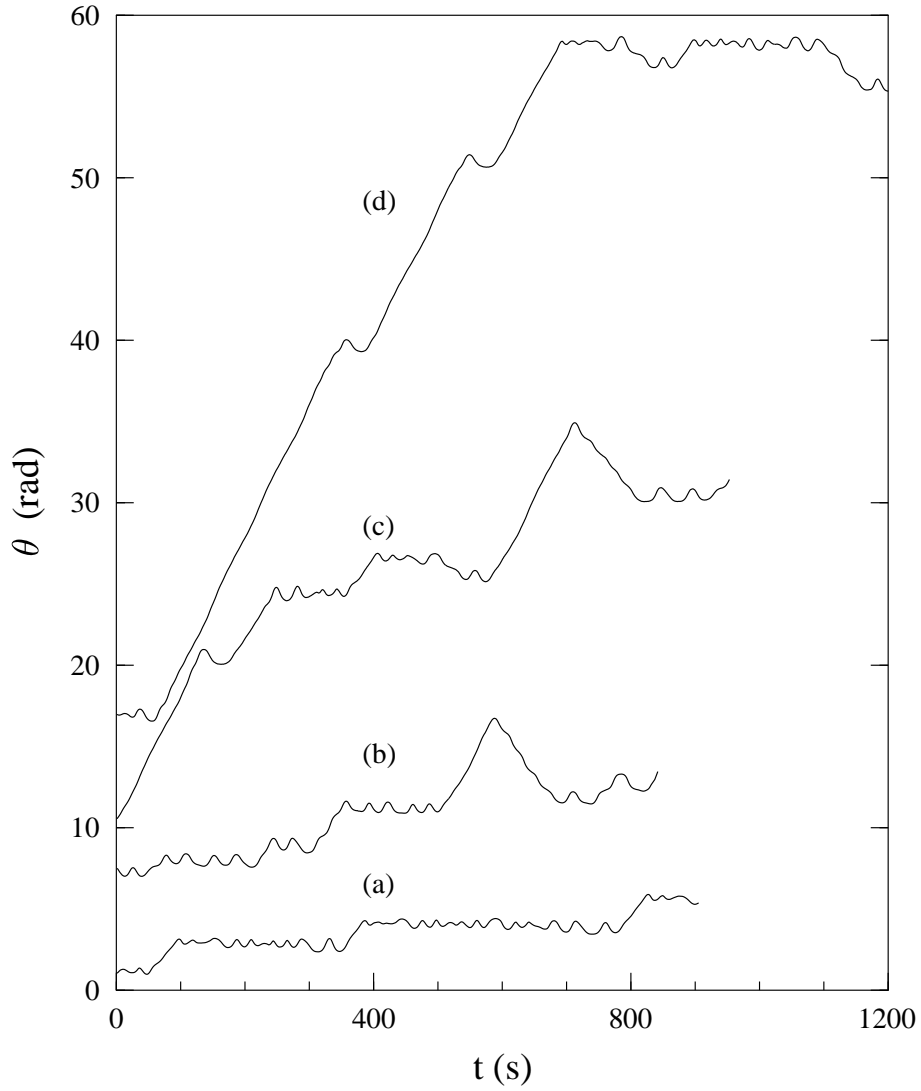


Figure 4.8: Azimuthal displacement  $\theta(t)$  as a function of time for the particle trajectories in Fig. 4.7. The oscillations of the tracer particle trajectories correspond to motion around a vortex, and the diagonal lines correspond to flights. The starting angle  $\theta(t=0)$  is arbitrary. These trajectories correspond to the six-vortex flow, but are typical in appearance for the seven-vortex and five-vortex flows. (Figure from Ref. [133].)

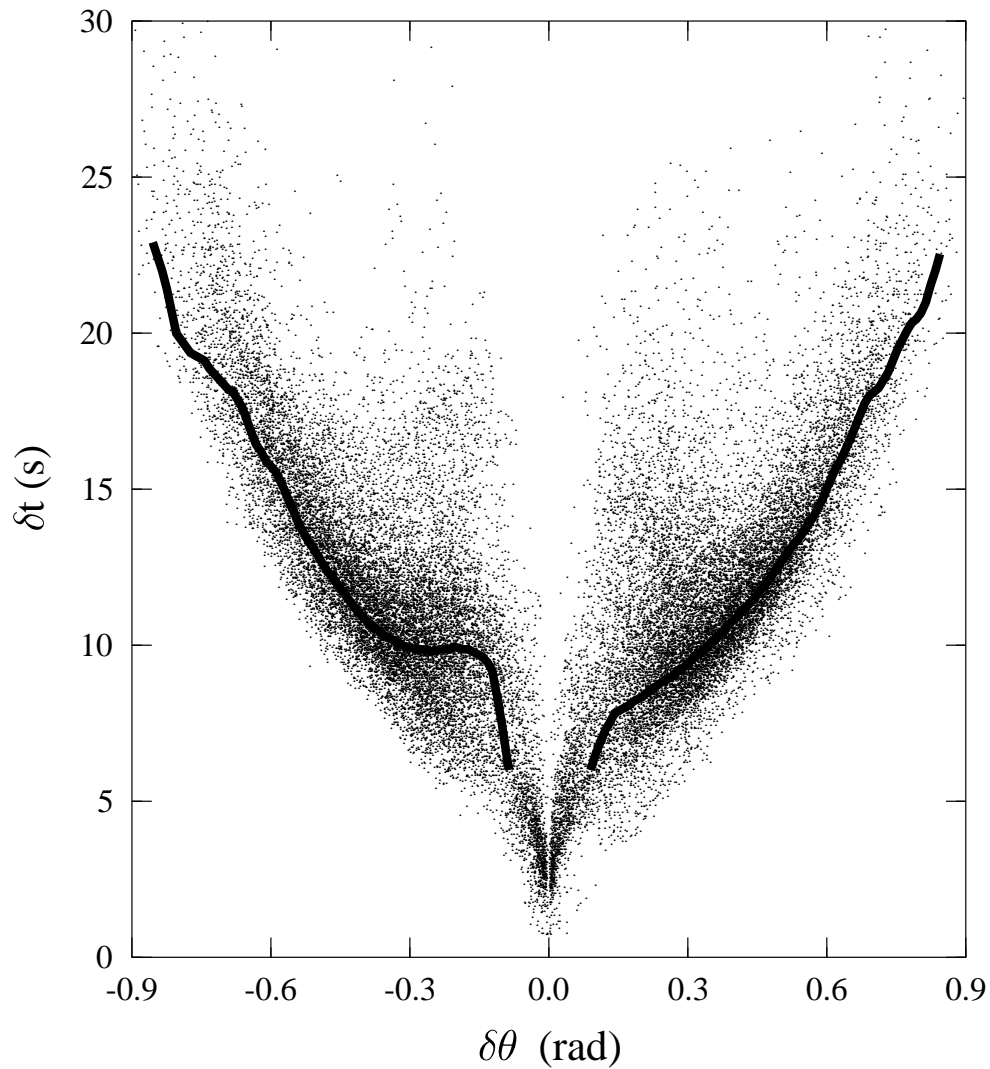


Figure 4.9: Time to move halfway around a vortex plotted against angular displacement (measured relative to the center of the annulus, not the center of the vortex). The scattered points are the measured points for the seven-vortex flow, and the solid line is drawn through the regions of highest density. The plot extends the full width of a vortex,  $2\pi/7 = 0.898$  rad. The points near the top of the plot ( $\delta t > 25$  s) reflect the slowing down the particles experience near hyperbolic points. The left-right asymmetry is presumably due to differences in the vortex shape between the outside (excursions with  $\delta\theta > 0$ ) and the inside of the vortex. (Figure from Ref. [154].)

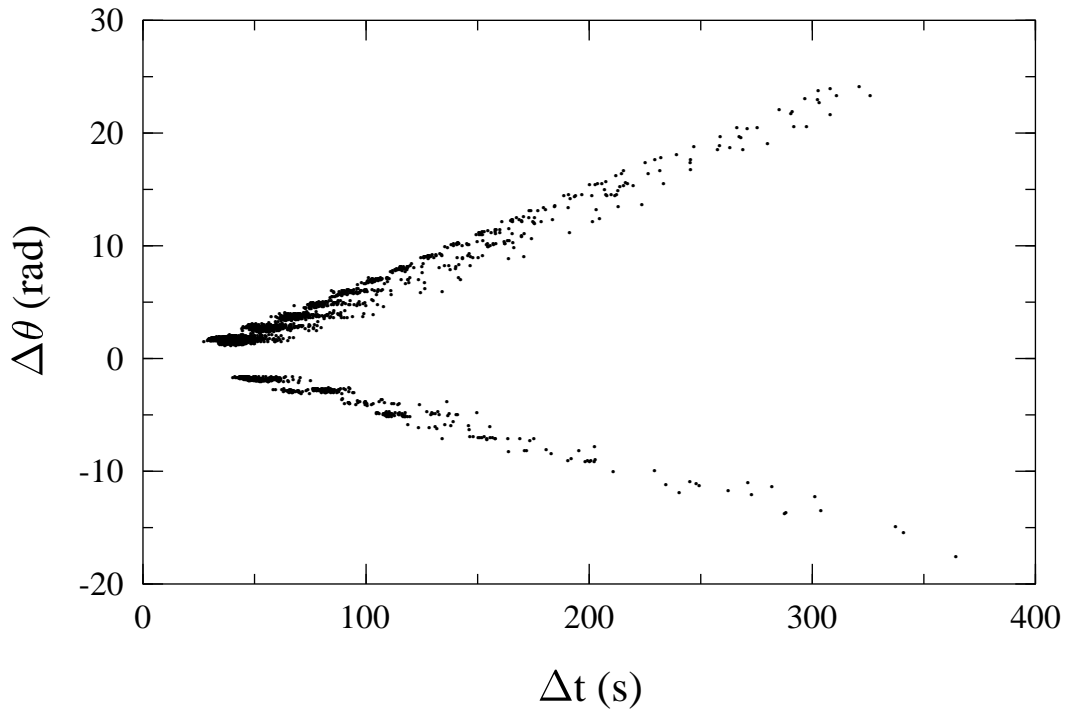


Figure 4.10: Flight length  $\Delta\theta$  versus flight duration  $\Delta t$ . The approximately linear relationship shows that flights have roughly constant velocity. The horizontal bands differ in spacing by  $\pi/3$ , which is the angular spacing between vortices (for the six-vortex flow shown). The spread of times within each horizontal band is due to the slowing down of particles which pass close by the hyperbolic point. The velocity in the  $+\theta$  direction (outer jet) is 0.078 rad/s, that in the opposite direction is -0.047 rad/s. This figure is for the six-vortex flow, although similar results are obtained for the other flows. (Figure from Ref. [154].)

power law (but does not appear exponential).

The results of Chapter 3 can be applied to the seven-vortex flow. Figures 4.8 and 4.10 show that particle trajectories should be treated as an asymmetric random walk, although for the flight exponent  $\mu > 3$  and a rapidly decaying sticking PDF ( $\nu \rightarrow \infty$ ) the distinction between a symmetric and asymmetric random walk is unimportant. For this flow, the Central Limit Theorem predicts normal diffusion ( $\sigma^2(t) \sim t^\gamma$  with  $\gamma = 1$ ). We compute the variance as discussed in Sec. 4.3, with the results shown in Fig. 4.12. The slope of the variance plot is shown in the inset, and suggests that the variance grows superdiffusively. For short times ( $t < 10$  s), the variance grows ballistically,  $\gamma = 2$ . This is because of the vortex turnover time: for times less than  $\sim 10$  s, particles in flight are undistinguished from those stuck in a vortex [144]. Particles all appear to be moving with a constant velocity (different for each particle), some in opposite directions, and thus the variance must grow ballistically.

For longer times,  $\gamma$  cannot be determined accurately, most likely due to a lack of trajectories with long durations. It is clear that for our data  $\gamma$  does not ever approach 1, the value expected for normal diffusion. The discrepancy may possibly be understood by the Berry-Esséen theorem, which strictly only applies to a symmetric random walk with a finite third moment, which is *not* the case for these data [41, 127]. This theorem predicts that the time for random walk to reach normally diffusive behavior scales as

$$t \sim \left( \frac{\langle |l|^3 \rangle}{\langle l^2 \rangle^{3/2}} \right)^2, \quad (4.3)$$

where the moments are for the flight length PDF. For a power law decay  $P(l) \sim l^{-\mu}$  with  $\mu < 4$ ,  $\langle |l|^3 \rangle$  is infinite. While the Berry-Esséen theorem does not apply directly to our results, it is suggestive that the convergence to normally diffusive behavior may be very slow for the seven-vortex flow.



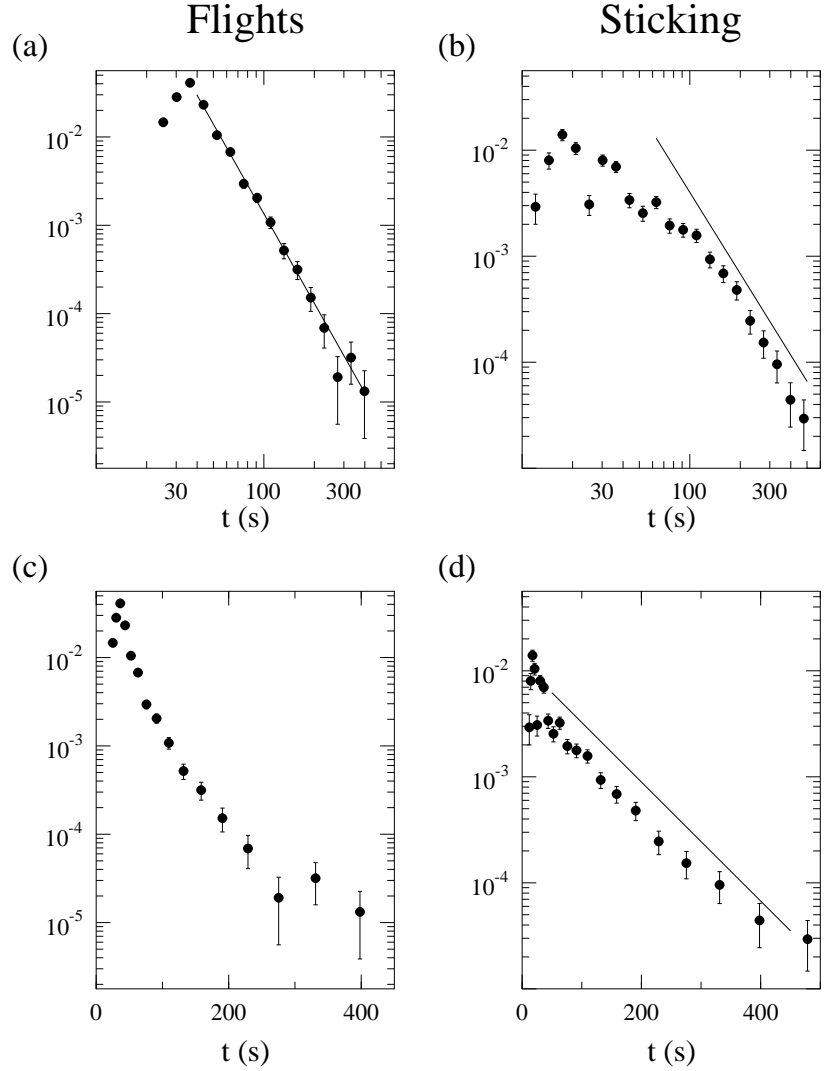


Figure 4.11: Seven-vortex flow: (a,c) flight and (b,d) sticking probability distribution functions, shown on (a,b) log-log axes and (c,d) log-linear axes. The error bars show the statistical uncertainty ( $\sqrt{N}$ ). The flight PDF shows power law decay,  $P_F \sim t^{-\mu}$ ; the line drawn in (a) is a least squares fit to the decaying data yielding<sup>a</sup>  $\mu = 3.2 \pm 0.2$ . The sticking PDF does not show a clear power law decay nor an exponential decay; the straight line (drawn for comparison) in (b) has a slope of -2.55, with the slope obtained from a least squares fit to the last 8 points in the tail. (Figure based on Ref. [154].)

<sup>a</sup>The uncorrected value of  $\mu$  is  $3.4 \pm 0.2$ ; see Sec. 4.3 for details of the correction.

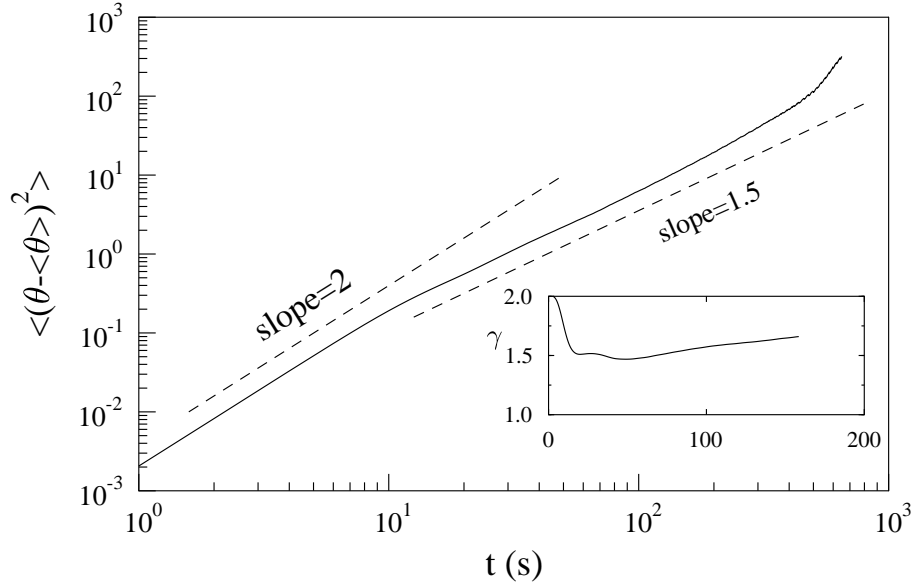


Figure 4.12: Variance  $\sigma^2(t)$  for the ensemble of tracer particles for the seven-vortex flow (solid line). The slope, shown in the inset, indicates that the variance grows superdiffusively. (Figure based on Ref. [154].)

The flight and sticking PDFs for the six-vortex flow are shown in Fig. 4.4.2. Again, the flight PDF shows clear power law decay, with a slope of  $\mu = 2.5 \pm 0.2$  after the correction for finite duration of trajectories (Sec. 4.3). The PDFs for leftward and rightward flights separately had similar decay exponents (within their uncertainties). The sticking PDF clearly decays faster than a power law, although it is unclear if the decay is exponential. Note that this interpretation is different from Refs. [132, 133], where it is stated that the sticking-time PDF appears to show power law decay. The PDFs in those articles were constructed with constant-width bins, rather than variable width bins (see Sec. 4.3), which resulted in misleading results.

Again, the results can be compared with the analysis from Chapter 3. The six-vortex flow particles are undergoing an asymmetric random walk with  $\mu = 2.5$  and  $\nu \rightarrow \infty$ , suggesting that the variance should grow as  $\sigma^2(t) \sim t^\gamma$  with  $\gamma = 4 - \mu =$

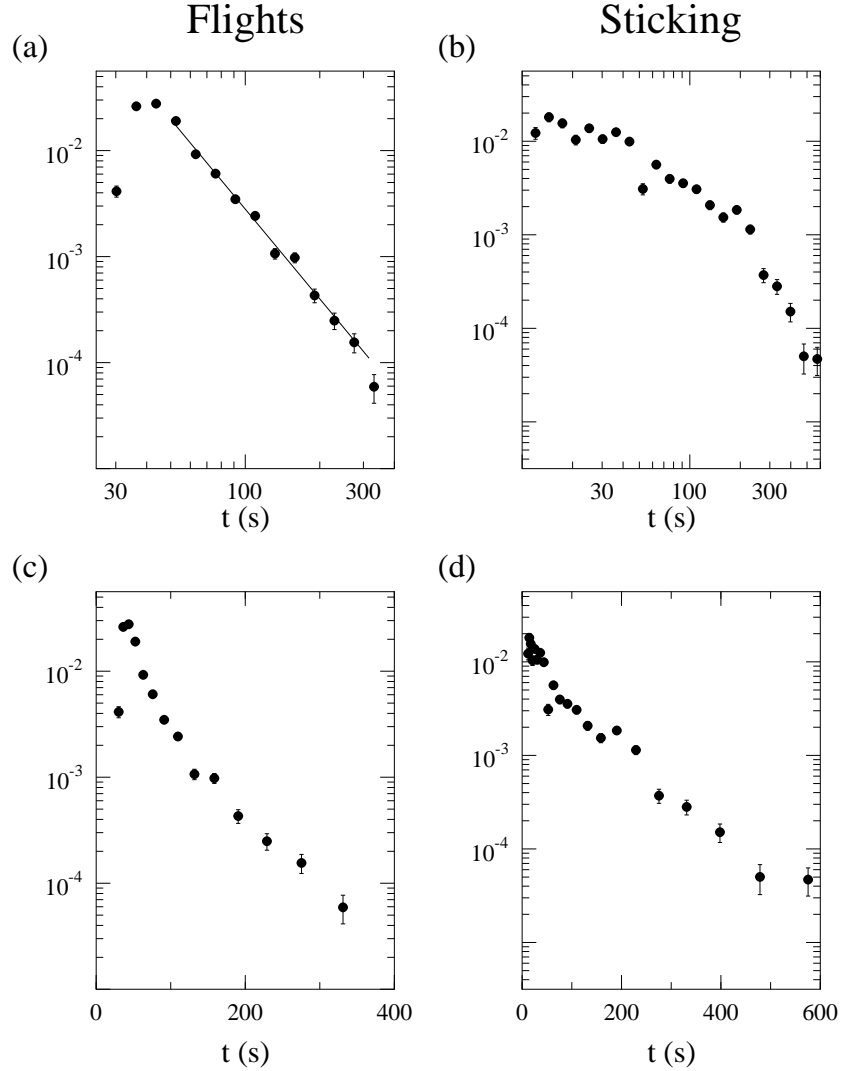


Figure 4.13: Six-vortex flow: (a,c) flight and (b,d) sticking probability distribution functions, shown on (a,b) log-log axes and (c,d) log-linear axes. The error bars show the statistical uncertainty ( $\sqrt{N}$ ). The flight PDF shows power law decay,  $P_F \sim t^{-\mu}$ ; the line drawn in (a) is a least squares fit to the decaying data yielding<sup>a</sup>  $\mu = 2.5 \pm 0.2$ . The sticking PDF does not show a clear power law decay nor an exponential decay. Note that these PDFs are slightly different from those shown in Refs. [132, 133] due to the improvement in binning technique (Sec. 4.3). (Figure based on Ref. [132].)

<sup>a</sup>The uncorrected value of  $\mu$  is  $2.8 \pm 0.2$ ; see Sec. 4.3 for details of the correction.

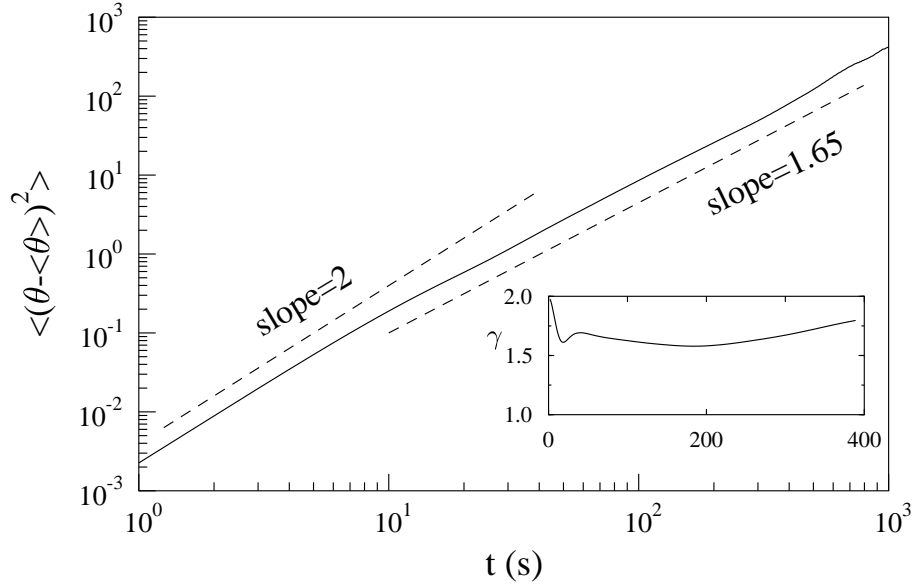


Figure 4.14: Variance  $\sigma^2(t)$  for the ensemble of tracer particles for the six-vortex flow (solid line). The slope, shown in the inset, indicates that the variance grows superdiffusively, with  $\gamma = 1.65 \pm 0.15$ . (Figure based on Ref. [132].)

1.5, that is, superdiffusively (see Fig. 3.2(b)). Figure 4.14 shows that for  $t > 20$  s, the variance grows with  $\gamma = 1.65 \pm 0.15$ . Given the uncertainty of  $\mu$  ( $\pm 0.2$ ), the predicted and measured values for  $\gamma$  are in accord. As noted above for the seven-vortex flow, the variance grows ballistically for times shorter than a vortex turnover time.

While both the seven-vortex flow and the six-vortex flow have periodic time dependence, it is not surprising that the mixing results are different. The seven-vortex flow has naturally arising time-dependence, while the six-vortex flow is perturbed periodically by an artificial change in the forcing (as described in Sec. 4.2). In the vortex reference frame, the instability of the seven-vortex flow has a frequency of 0.00033 Hz and a mode number of 3 (measured from particle tracking). The mechanical perturbation of the six-vortex flow appears with a frequency of 0.014 Hz (in the vortex reference frame) and is mode number 1.

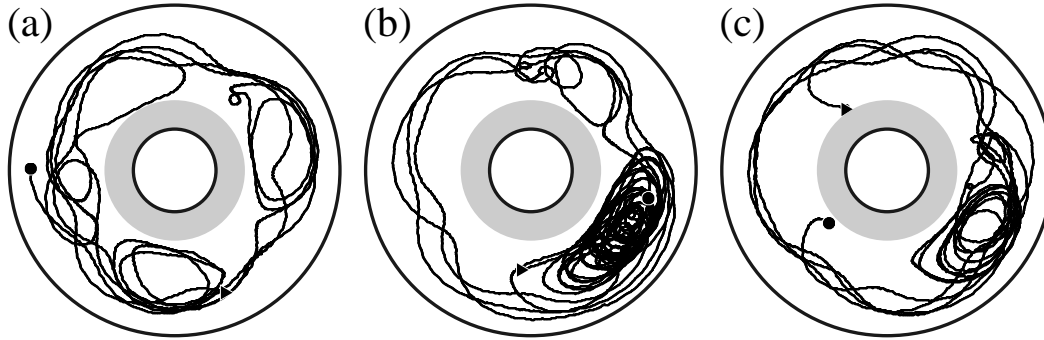


Figure 4.15: Chaotic particle trajectories in the four-vortex flow (chaotic time dependence). Nearly all of the flight behavior is in the outer jet; a brief flight in the inside can be seen in (a). The chaotic motion of the four vortices can be seen in (b), where the particle spends most of its time in the same vortex which moves erratically. The beginning of each trajectory is marked by a circle, the end by a triangle. (Figure from Ref. [155].)

#### 4.4.3 Chaotic flows

The two chaotic flows, the five-vortex flow and the four-vortex flow, also exhibited chaotic mixing. Similar to the seven- and six-vortex flows, the difference between the two chaotic flows is the nature of the forcing: the chaotic time dependence of the five-vortex flow is due to the mechanical perturbation, while the chaotic time dependence of the four-vortex flow arises due to natural instabilities.

The trajectories for the five-vortex flow appear similar to those shown in Fig. 4.7, while typical trajectories of the four-vortex flow are shown in Fig. 4.15. The four vortices are not stationary but move erratically. (The pictures shown are taken in a frame of reference co-rotating with the *average* speed of the vortex chain, but there is substantial variation in the *instantaneous* speed of each vortex.)

Figure 4.16 shows the angular position of the particles as a function of time in the four-vortex flow. The oscillatory behaviors correspond to motion when the particle is “sticking” in a vortex, and the longer diagonal lines are flights in the outer jet. Flights are distinguished from sticking motions by examining the azimuthal

distance traveled before reversing direction: particles travel in a vortex for at most  $\pi/2$  radians before changing directions, while a particle that leaves one vortex and enters the next (the minimum flight distance) will move at least  $\pi/2$  radians. Unlike the other flows, for the four-vortex flow there is no strong inner jet and particles do not travel long distances on the inner side of the vortex chain. Approximately 10% of the flights seen in the four-vortex flow are short hops on the inner side of the vortex chain, from one vortex to an adjacent vortex; these hops take less than 40 s, and do not contribute to the long-time statistics.

To compile the flight and sticking PDFs, 1100 particles were examined for the five-vortex flow and 210 particles were examined for the four-vortex flow. (The four-vortex flow had difficulties in tracking particles for long times; particles disappeared from the visible area rapidly. Because of this lack of data, we checked the accuracy of the PDFs by considering smaller portions of the total data, forming PDFs, and finding the resultant PDFs to be similar to the PDFs formed using all of the data.)

The flight and sticking PDFs for the five-vortex flow are shown in Fig. 4.17. Neither PDF shows power law decay, nor do they show convincing exponential decay. Note that this interpretation is different from that given in Ref. [133]. As discussed in Sec. 4.4.2, this is presumably due to an improvement in the analysis technique.

Given the uncertainty of the decay rate of the flight and sticking PDFs, comparison with the results of Chapter 3 is difficult. The most reasonable interpretation of Fig. 4.17 would be  $\mu \rightarrow \infty$ ,  $\nu \rightarrow \infty$ , yielding  $\gamma = 1$  by the Central Limit Theorem. The growth of the variance measured from the experiment is shown in Fig. 4.18, and shows superdiffusive growth with  $\gamma = 1.55 \pm 0.15$ .

The PDFs for the four-vortex flow are shown in Fig. 4.19. This is the only flow for which both flight and sticking PDFs show power law decay. The decay exponents, adjusted for finite trajectory duration, are  $\mu = 2.0 \pm 0.2$  (flight) and  $\nu = 1.3 \pm 0.2$  (sticking). It is remarkable that these PDFs have a power law form

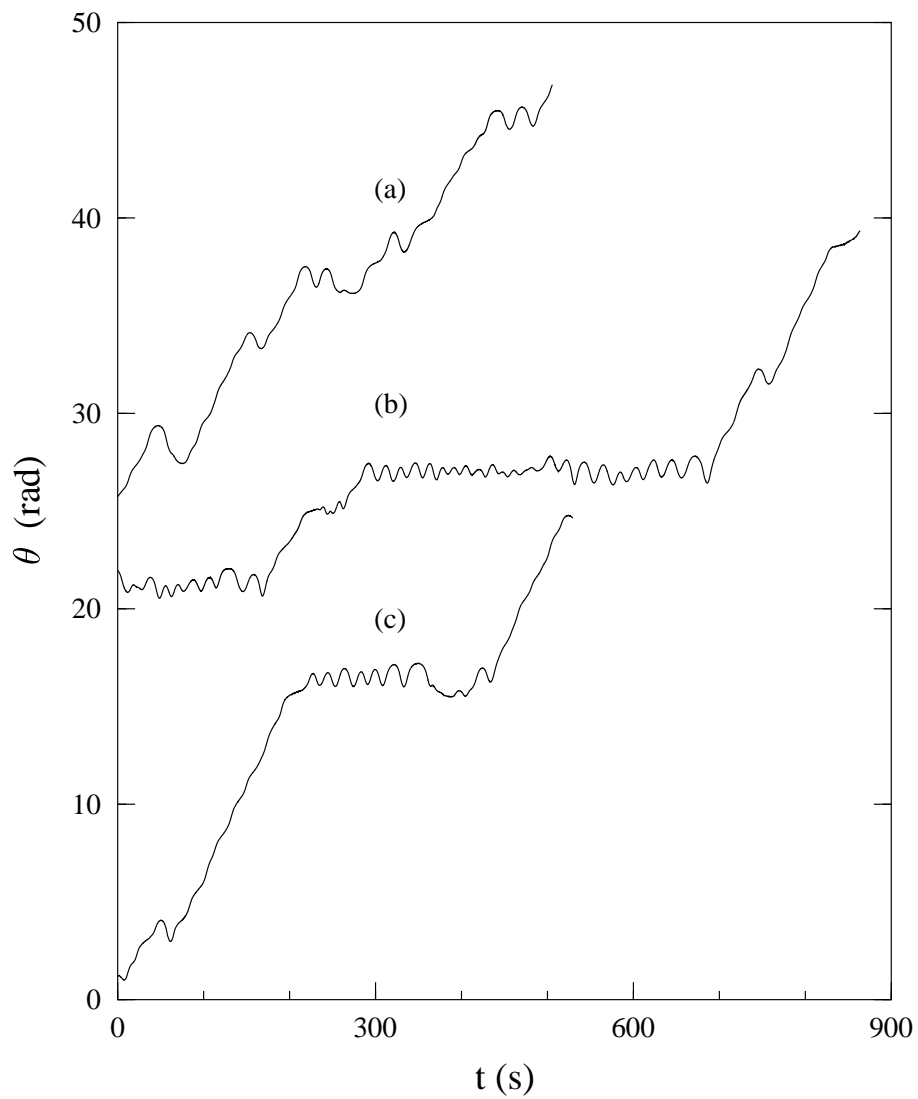


Figure 4.16: Angular displacement  $\theta(t)$  as a function of time for the trajectories shown in Fig. 4.15. Diagonal lines indicate flights, while the small oscillations correspond to particle motion within a vortex. Despite the chaotic motion of the vortices, a clear distinction can be made between flight behavior and sticking behavior. (Figure from Ref. [155].)

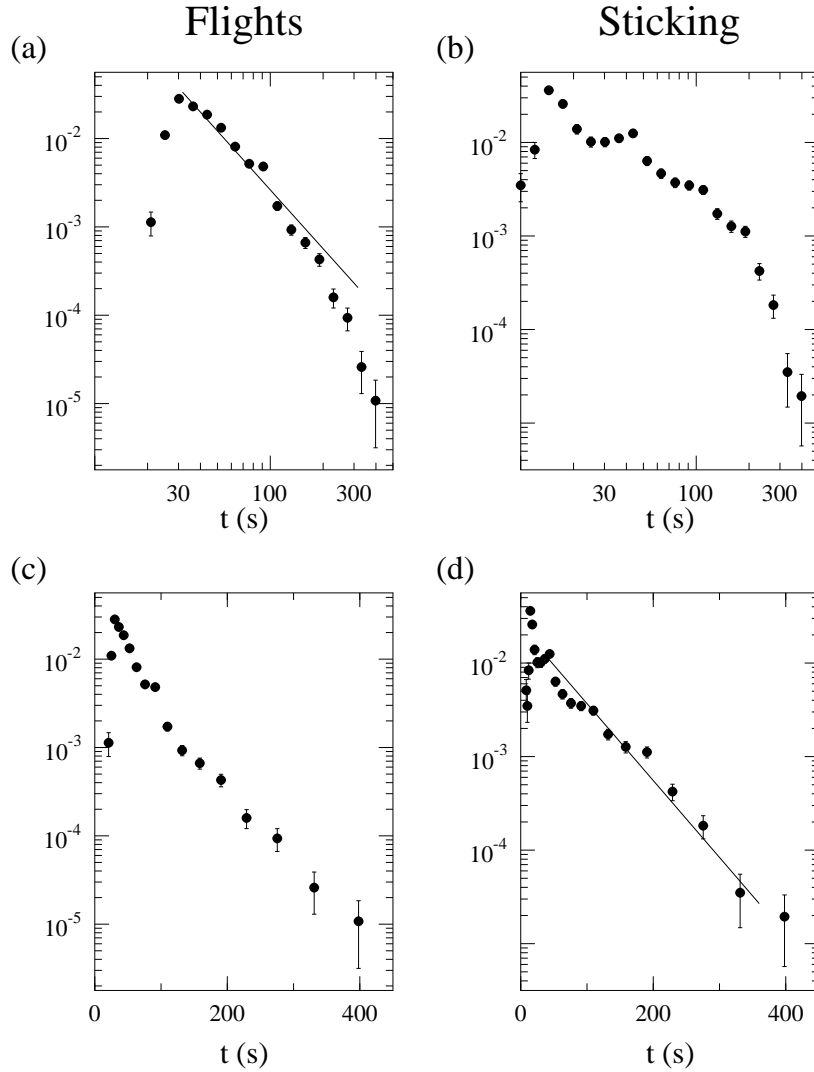


Figure 4.17: Five-vortex flow: (a,c) flight and (b,d) sticking probability distribution functions, shown on (a,b) log-log axes and (c,d) log-linear axes. The error bars show the statistical uncertainty ( $\sqrt{N}$ ). The flight PDF appears to decay faster than a power law; the line drawn for comparison has a slope of -2.2, and is a least squares fit to the data for  $t > 30$  s. The sticking PDF does not show a clear power law decay nor an exponential decay, although the data in (d) look possibly linear; a least squares fit line is shown. Note that these PDFs are slightly different from those shown in Ref. [133] due to the improvement in binning technique (Sec. 4.3). (Figure based on Ref. [133].)



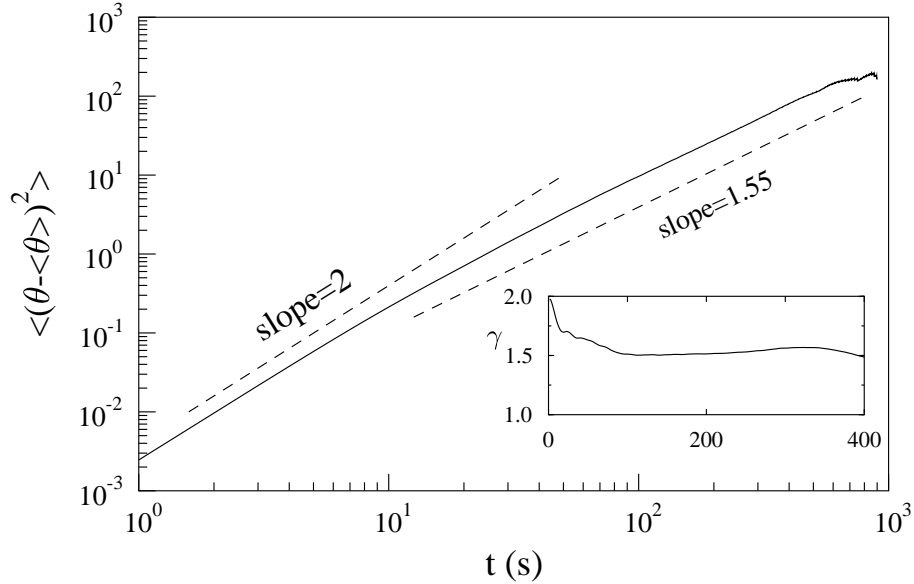


Figure 4.18: Variance  $\sigma^2(t)$  for the ensemble of tracer particles for the five-vortex flow (solid line). The slope, shown in the inset, indicates that the variance grows superdiffusively with  $\gamma = 1.55 \pm 0.15$ . (Figure based on Ref. [133].)

despite the presence of Eulerian chaos. Although the vortices are moving erratically with respect to each other, particle motion still displays the effects of long-time correlations.

The long term transport can be deduced from Chapter 3 for the four-vortex flow. Taking  $\nu = 1.3$  and  $\mu = 2.0$ , the variance should grow as  $t^\gamma$  with  $\gamma = 2 + \nu - \mu \approx 1.3$ . The experimentally determined variance for this flow is shown in Fig. 4.20. It is difficult to track particles for long enough times in this flow to gather the statistics necessary to determine the variance accurately; hence quantitative comparison with the results of Chapter 3 is difficult. However, the behavior appears superdiffusive with an exponent  $\gamma$  between 1.5 and 2.0. At longer times, the exponent drops below 1.5, and the prediction is for  $t \rightarrow \infty$ , so the experimental results appear reasonable.

The failure of the variance to reach its asymptotic behavior despite the large number of long time trajectories can be understood from an analysis of crossover

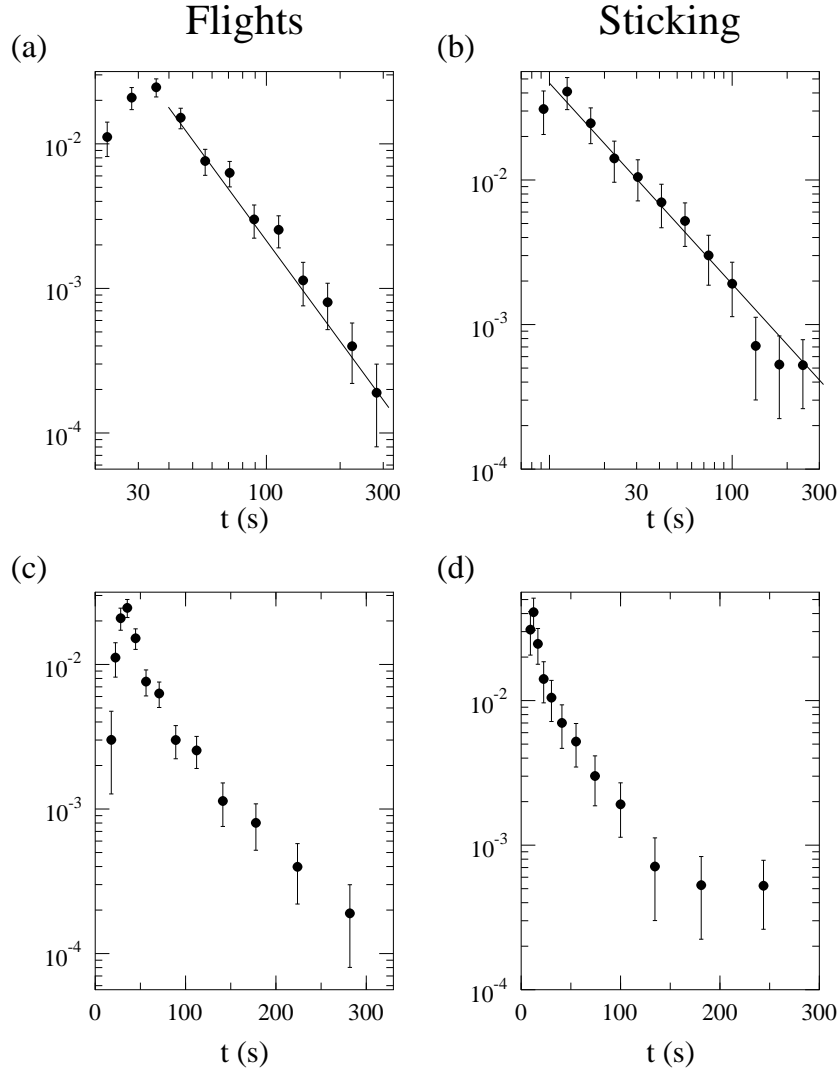


Figure 4.19: Four-vortex flow: (a,c) flight and (b,d) sticking probability distribution functions, shown on (a,b) log-log axes and (c,d) log-linear axes. The error bars show the statistical uncertainty ( $\sqrt{N}$ ). The flight PDF decays as a power law,  $P_F(t) \sim t^{-\mu}$ , with<sup>a</sup>  $\mu = 2.0 \pm 0.2$ . The sticking PDF also appears to decay as a power law, with a decay exponent of<sup>b</sup>  $\nu = 1.3 \pm 0.2$ . The error bars for these PDFs are much larger than for Figs. 4.11, 4.4.2, and 4.17 as this flow had much less data. (Figure based on Ref. [155].)

<sup>a</sup>The uncorrected value of  $\mu$  is  $2.3 \pm 0.2$ ; see Sec. 4.3 for details of the correction.

<sup>b</sup>The uncorrected value of  $\nu$  is  $1.4 \pm 0.2$ ; see Sec. 4.3.

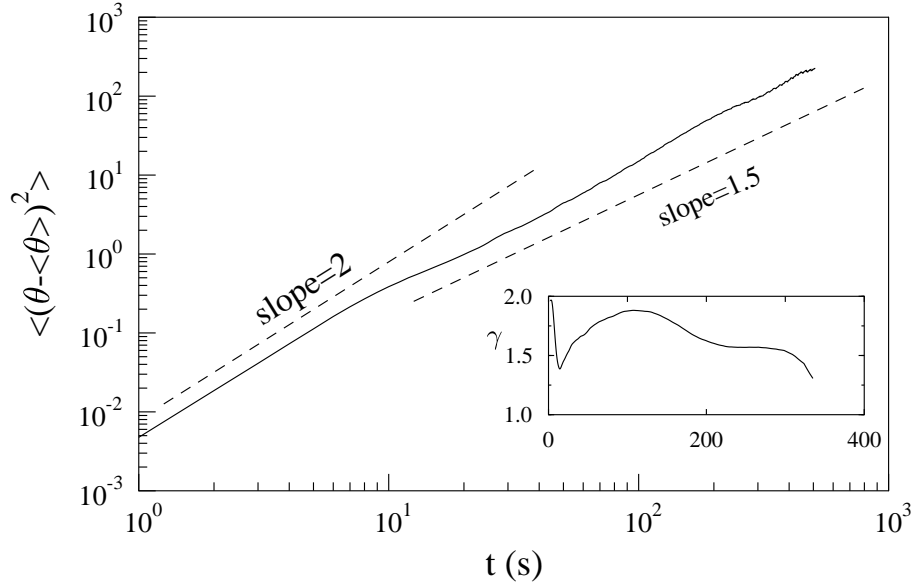


Figure 4.20: Variance  $\sigma^2(t)$  for the ensemble of tracer particles for the four-vortex flow (solid line). The slope, shown in the inset, indicates that the variance grows superdiffusively. (Figure based on Ref. [155].)

times in the model. The time necessary to approach the asymptotic state can be calculated by retaining lower order terms in the expansion for  $\sigma$  (see Appendix A for details). Using the values of  $\mu = 1.9$ ,  $\nu = 1.3$ , and cutoff times  $t_F = 22$  s,  $t_S = 10$  s, yields  $\sigma \sim 0.055t^{1.4} - 0.10t^{1.1}$ . A plot of this function on a log-log scale (Fig. 3.4) does not reach a slope of 1.5 until 400 s, and our data only extend to  $\sim 500$  s. This slow convergence to asymptotic behavior is a generic feature of Lévy processes and complicates analysis in many experimental situations and numerical simulations. (See discussion in Sec. 4.5.)

Figure 4.21 shows that the mean particle position  $\langle x \rangle$  grows approximately linearly with time for most of the range. For longer times,  $\langle x \rangle$  appears to start growing faster than linearly in time. For times less than a vortex turnover time, linear growth is expected, as all particles are moving with constant velocity (whether in a vortex or in the jet). For longer times, the model predicts (for  $\mu = 2.0$  and

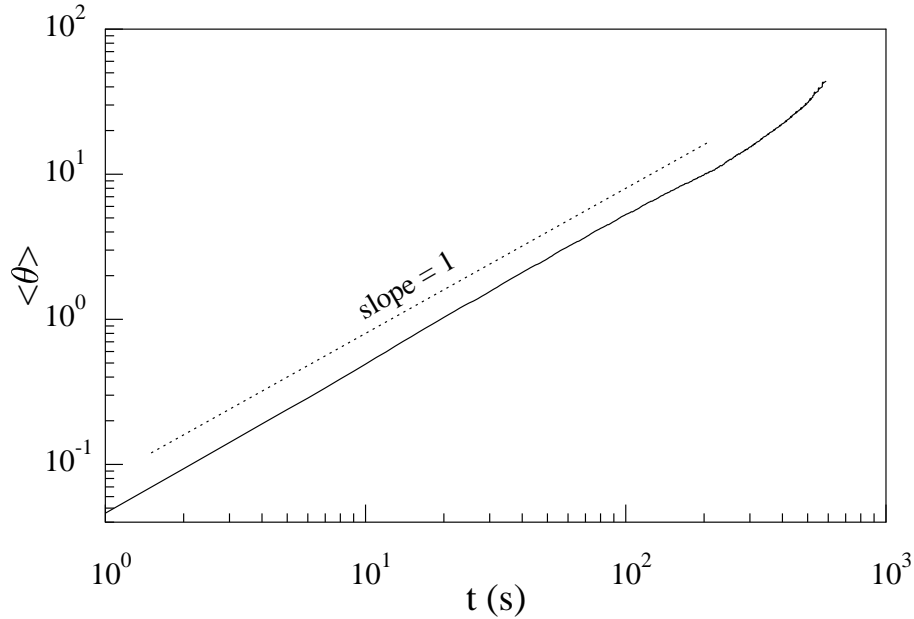


Figure 4.21: Mean particle position for four-vortex flow,  $\langle \theta(t) \rangle$  (solid line). (Figure from Ref. [155].)

$\nu = 1.3$ ) that  $\langle x \rangle \sim t^{0.3}$ ; if the sticking PDF has an exponential tail,  $\langle x \rangle \sim t$ . It is probable that the asymptotic scaling is not reached due to lack of statistics at long times (see discussion in Sec. 3.8.3).

#### 4.4.4 Weakly turbulent flow: no long flights

The large Reynolds number and the absence of azimuthal jets leads to a behavior in the turbulent regime that contrasts markedly with that in the laminar and chaotic regimes. Tracers in the turbulent flow wander erratically, and there are no well-defined flights (which are dependent on jet regions) or sticking events: compare plots of trajectories in the turbulent flow, Fig. 4.5, with those for the six- and four-vortex flows, Figs. 4.7 and 4.15, and compare plots of azimuthal displacement  $\theta(t)$  in Fig. 4.22 with Figs. 4.8 and 4.16.

There are no flights or sticking events in the turbulent flow, but by treating

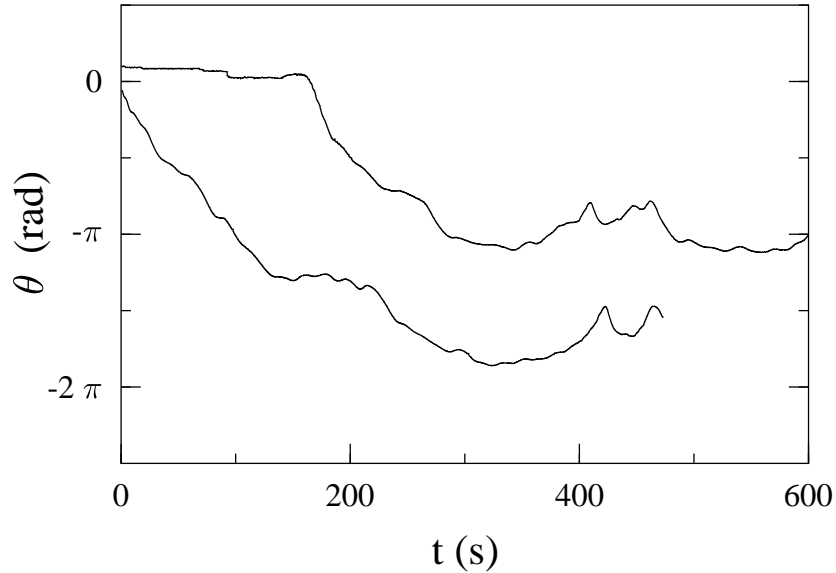


Figure 4.22: Angular displacement  $\theta(t)$  as a function of time for the trajectories shown in Fig. 4.5. The upper trace is for the particle marked with circles. (Figure from Ref. [154].)

the trajectories as random walks, we can define a step as the time between two successive extrema in  $\theta(t)$ . We find that the probability distribution function is exponential,  $P(t) = Ae^{-t/\tau}$ , with  $A = 0.158$  and  $\tau = 15.2$  s (see Fig. 4.23), in contrast to the power law PDFs observed for flights in the time-periodic and chaotic regimes.

The slope  $\gamma$  of a log-log plot of the variance  $\sigma^2(t)$  (Fig. 4.24) drops steadily from 2 and appears to approach the value expected for normal diffusion ( $\gamma = 1$ ) at long times; however, we cannot follow particles for long enough times to determine the asymptotic behavior. This is in agreement with the Central Limit Theorem, which predicts  $\gamma = 1$  for an exponentially decaying flight PDF. This also agrees with a result derived in 1921 by Taylor [144]. Taylor showed that for very short time scales, a turbulent flow should have ballistic mixing ( $\sigma^2(t) \sim t^2$ ). This ballistic behavior lasts until particle motions become uncorrelated; for our weakly turbulent

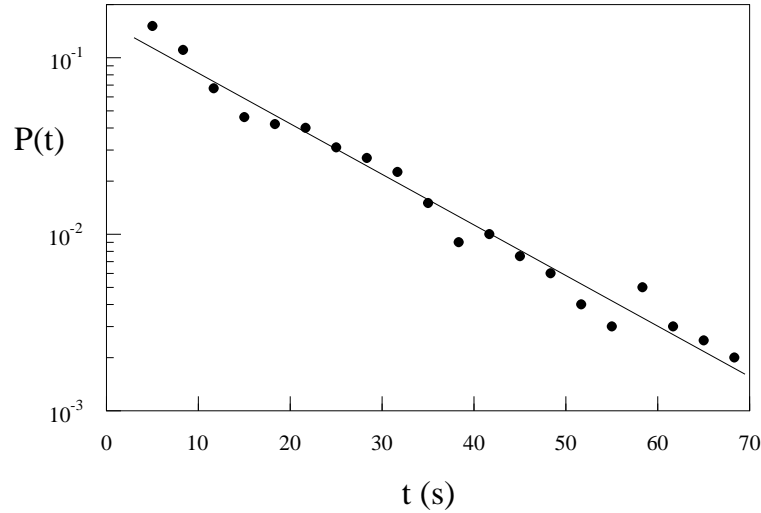


Figure 4.23: Probability distribution for azimuthal displacement in the turbulent flow. The distribution is exponential with a decay time of 15.2 s. (Figure from Ref. [133].)

flow, this time scale appears to be about 6 s.

A diffusion coefficient can be found for the turbulent flow by fitting the variance data, yielding  $D = 0.010 \pm 0.003 \text{ rad}^2/\text{s}$ . The data was fit for  $t > 10 \text{ s}$  and  $t > 100 \text{ s}$ , both giving a similar value. By using  $r = 30 \text{ cm}$  as the typical radius for the vortices, the diffusion coefficient can be written as  $D_{\text{real}} = 9 \text{ cm}^2/\text{s}$ . For particles diffusing purely due to Brownian motion, the Einstein relation for the diffusion coefficient is  $D = RT/6\pi\eta aN$  with  $R$  the universal gas constant,  $\eta$  the dynamic viscosity,  $a$  the particle radius, and  $N$  Avagadro's number [13]. For our tracer particles, the diffusion coefficient due to Brownian motion is  $D = 4.4 \times 10^{-12}$ , a factor of  $10^{12}$  smaller.

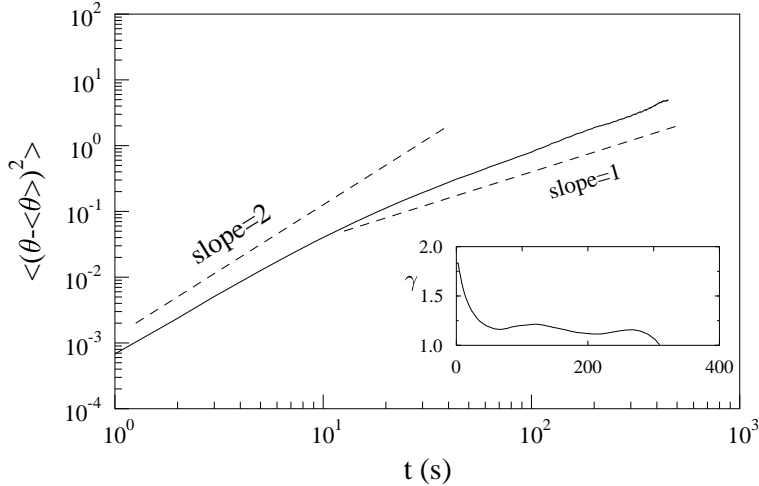


Figure 4.24: Variance  $\sigma^2(t)$  for the ensemble of tracer particles for the weakly turbulent flow (solid line). The slope, shown in the inset, suggests the long term behavior may be normally diffusive. (Figure based on Ref. [133].)

## 4.5 Discussion

We have found superdiffusion in a variety of flows. The data from the six regimes are summarized in Table 4.2. Except for the five-vortex flow, all experiments with jets had power law flight behavior. The variance grows super-diffusively for all flows with nontrivial time dependence, except the weakly turbulent flow which appears to tend to normal diffusion for very long times, as expected.

A significant concern for interpreting the results is the convergence to asymptotic behavior. The PDFs are fairly easy to measure, as they appear to begin a power law decay for times  $t > 30$  s. The lack of long trajectories slightly affects the decay observed for  $t > 200$  s, although this is correctable as discussed in Sec. 4.3. However, the asymptotic behavior of the variance is harder to determine with our data. As discussed in Sec. 3.8.3, the predictions for the variance are only correct as  $t \rightarrow \infty$ ; for finite  $t$ , the variance is composed of several terms. Competition between these terms controls the approach to the asymptotic behavior. As shown in Fig. 3.4, these

Table 4.2: Exponents  $\nu$  and  $\mu$  characterizing the power law decay of probability distribution functions for the sticking and flight times, respectively, and the exponent  $\gamma$  for the power law time dependence of the variance of the azimuthal displacement (measured and predicted). A — entry indicates the exponent is undefined.

| Flow name                               | $\mu$         | $\nu$         | $\gamma_{\text{expt}}$ | $\gamma_{\text{theory}}$ |
|---|---------------|---------------|------------------------|--------------------------|
| Time-independent<br>(with six vortices) | —             | —             | 2                      | 2                        |
| Seven-vortex<br>(time-periodic)         | $3.2 \pm 0.2$ | ?             | $\sim 1.5$             | 1                        |
| Six-vortex<br>(time-periodic)           | $2.5 \pm 0.2$ | $\infty$      | $1.65 \pm 0.15$        | 1.5                      |
| Five-vortex<br>(Eulerian chaos)         | ?             | ?             | $1.55 \pm 0.15$        | 1?                       |
| Four-vortex<br>(Eulerian chaos)         | $2.0 \pm 0.2$ | $1.3 \pm 0.2$ | $\sim 1.5$             | 1.3                      |
| Weakly turbulent                        | $\infty$      | —             | $\sim 1.2$             | 1                        |

higher order terms can cause the variance to grow faster than its asymptotic growth ( $\gamma$  to appear larger at short times).

This slow convergence rate would be less of a problem if the particles in our experiments were observable for longer times. For the results in this chapter, typically 1000-1700 particles were observed. However, only 200-600 particles per flow had a duration longer than 200 s, and only 40-190 had a duration longer than 500 s. For the four-vortex flow, these numbers drop to 210 particles total, with only 28 particles having a duration longer than 200 s. Thus, for the variance graphs, the asymptotic behavior is being determined by only a few particles.

There are several reasons that particles are not observable for long periods of time. The most significant reason is probably Ekman pumping. Particles are illuminated only in a narrow horizontal region (see Sec. 2.2), and Ekman pumping provides a small vertical velocity which can move particles into and out of this



illuminated slice. Additionally, the camera cannot see particles when they are too close to the outer wall of the annulus, as the outer wall reflects light upwards and particles cannot be distinguished from this background. Thus particles which reach the outside of the annulus are lost, although they may be tracked as a new particle if the particle returns to the visible region. A third problem is that the tracking program itself sometimes, for no known reason, loses a particle temporarily and then retracks it as a new particle. Some work has been done trying to catch these errors by post-processing the tracked data, although it must be done by hand. A final concern is the non-neutral-buoyancy of the particles, as discussed in Sec. 2.3; centrifugal effects could cause particles to drift out of the illuminated region.

If there are any correlations linking the particle behavior to their longevity in the visible region, this could further affect results. For example, if particles stuck in vortices have a faster vertical drift (perhaps due to Ekman pumping which should be stronger in a vortex), then the observations of long-lived particles will be biased towards flights.

## Chapter 5

# Interaction of Eastward Jets with Topography

### 5.1 Atmospheric Observations of Blocking

For decades, weather prediction has been based on the assumption that mid-latitude storms arise from linear instabilities of large-scale eastward zonal flow [23, 37, 50, 51, 56, 102]. In fact, one to three times each Northern Hemisphere winter — and occasionally during other seasons — large high-pressure anticyclones form and persist for at least ten days and sometimes longer than a month [25, 35, 95], exceeding the usual 5-7 day life of mid-latitude storms. These anticyclones block the nearly zonal flow and deflect it poleward (see Fig. 5.1(b)). The prediction of these blocking events has become central to improving extended-range weather prediction [7, 91, 148]. Blocking events are an example of an *anomaly*, when the large-scale atmospheric flow strongly differs from the normal flow for a significant period of time [48]. (“Normal” flow in this context would be the the average over several years for that particular month.)

Blocking events were known in the 1940’s and 50’s [48], and were first care-

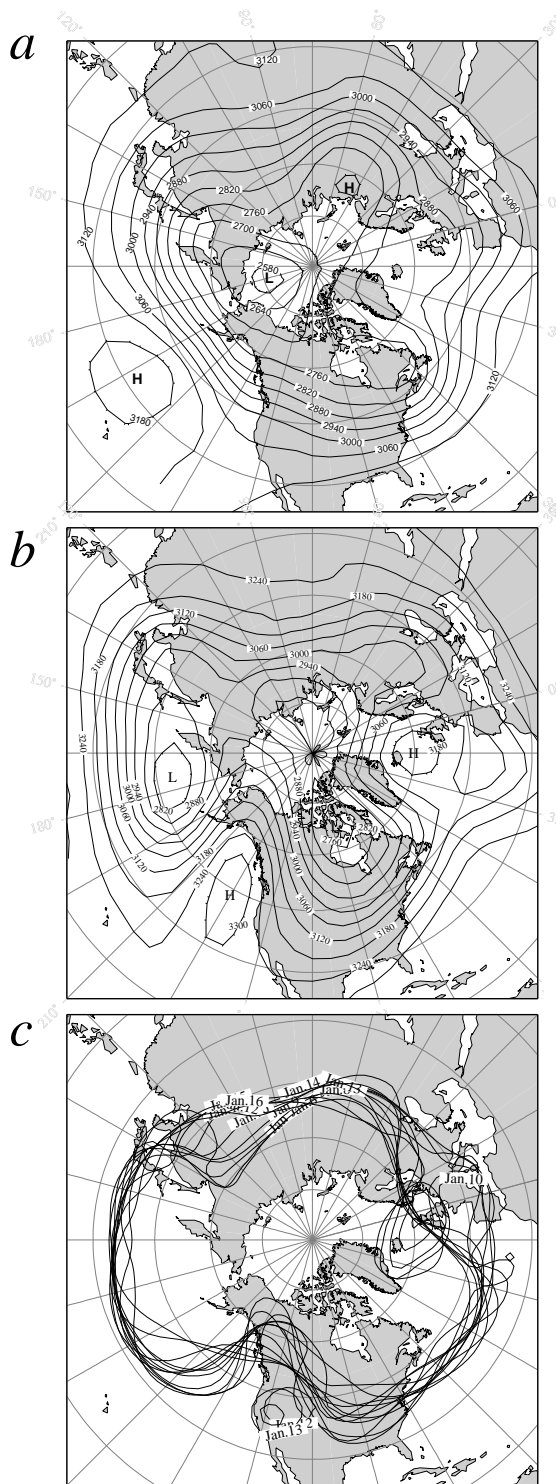


Figure 5.1: Atmospheric pictures of (a) zonal and (b) blocked flow; showing contour plots of the height (m) of the 700-hPa (700 mb) surface, with a contour interval of 60 m for both panels. The flow follows the contours; the flow in the jet stream is from west to east. The plots are obtained by averaging over ten days of twice-daily data for (a) 13–22 December 1978 and (b) 10–19 January 1963 [168]. The nearly zonal flow of panel (a) includes quasi-stationary, small-amplitude waves [52, 152]. Blocked flow advects cold Arctic air southward over eastern North America or Europe. The 2940-m contour corresponds roughly to the mean position of the jet axis; variations in its daily position (using a weighted three-day mean) are shown in panel (c) for the time interval 5–16 January 1997, to illustrate switching between the two types of flow [169]. Figure adapted from Ref. [157].

fully studied by Rex [117, 118]. Rex proposed subjective criteria to define a blocking case [117]:

1. the eastward zonal flow splits into two branches, each carrying an appreciable mass of air;
2. the double-jet flow extends over at least  $45^\circ$  of longitude;
3. the flow is zonal upstream, and meridional downstream of the splitting; and
4. the pattern must persist for at least ten days.

These criteria have been refined by later authors (e.g. [35]) in order to find objective criteria which computers could use to determine blocking events from data, but Rex's criteria are still the most widely used [147]. As the flow is typically split by a local high pressure region (an anticyclone), often a characteristic sign of blocking is the presence of a persistent anticyclone which strongly distorts the eastward jet flow. Blocking anticyclones typically appear singly (over the Atlantic or over the Pacific [48, 117]), although occasionally a double-blocking event occurs such as that pictured in Fig. 5.1(b). In general, blocking occurs more frequently in the Northern Hemisphere, and has more significant consequences for Northern Hemisphere weather [48], although blocked flow does occur in the Southern Hemisphere as well.

Several clues led to the development of models for blocking (discussed in Sec. 5.2). First, there is a suggestion that blocking could be understood as a barotropic (two-dimensional) phenomenon. Daily mid-latitude weather evolves on a time scale of 1–10 days. This evolution is largely driven by three-dimensional, baroclinic instabilities of the nearly zonal flow [23, 37] that convert the potential energy in the atmosphere's density stratification into the kinetic energy of storms [50, 56, 102]. In contrast, low-frequency atmospheric variability on the time scale of 10–100 days is predominantly barotropic, i.e., nearly two-dimensional [24, 25, 71].

Thus, it seems appropriate to first consider blocking anomalies as a barotropic phenomenon which is then perturbed by baroclinic effects (e.g., the baroclinic effects drive the transition from the normal, nearly zonal flow to a blocked flow).

The second clue used to develop models is the axial asymmetry of blocking events. In the Northern Hemisphere, blocking anticyclones occur in either the Pacific or the Atlantic [48, 118]. Thus it is reasonable to assume that asymmetries of the Earth fix the location of these anticyclones. Two likely candidates are the ocean-land contrasts, and the topography immediately upstream of the anticyclones. For North America, the Rocky Mountains are of significant height and extent, extending from  $70^\circ$  N to  $20^\circ$  in latitude, ranging from 110 to 650 km in width, and having an elevation from 1.5 km to 4.4 km at the tallest point. In Europe, the topographic features linked to blocking events consist of the Spanish Plateau, the Pyrenees, the Alps, the Apennines, and the Scandinavian mountain ranges [24]. These mountains extend from  $70^\circ$  N to  $35^\circ$  N in latitude, and are more than 125 km wide at their widest point. One possible reason that blocking occurs more frequently in the Northern Hemisphere is that the mountain ranges in that hemisphere are more pronounced and of larger extent than mountain ranges in the Southern Hemisphere (such as the Andes).

## 5.2 Models of Blocking

Models have suggested the plausibility of a topographic origin of these blocking events [8, 24, 62, 72, 99, 101, 116]. Barotropic models of large-scale flow over idealized Northern Hemisphere topography explain some features of blocking episodes [7, 8, 24, 72, 101, 140], while recent numerical simulations using a general circulation model [79] provide further evidence for the barotropic character of the low-frequency variability and support the results of the simpler models.

The first model was developed by Charney and DeVore [24]. They studied a

two-dimensional model with mode-2 topography (two symmetrically placed “mountains” which perturb the quasi-geostrophic equation for potential vorticity conservation, similar to the way a sloping bottom can perturb a nearly two-dimensional flow, as discussed in Sec. 1.2.6). In the Northern Hemisphere, the topography is dominated by wave number 2 [103], making this a reasonable choice for their model. They used simple eastward zonal forcing, and did a spectral expansion of their equation of motion, keeping the three most significant spectral terms.

They found two equilibria which qualitatively resembled atmospheric blocked and zonal flows<sup>1</sup> [24]. The blocked flow had a jet which was extremely wavy and bent around anticyclones, while the zonal flow was less wavy. The *ridge* of the jet, the area where the jet is furthest poleward and curves back away from the pole, lies over the mountains for the zonal flow and shifts upstream to the valleys for the blocked flow. The zonal jet flow was approximately twice as strong as the blocked jet flow. For a range of parameters, both types of flow patterns were stable, and the initial conditions would determine which flow pattern would ultimately develop.

Further modeling work extended the results of Charney and DeVore. Their model used a  $\beta$ -plane approximation (see Sec. 1.2.6); later models used more realistic geometry and considered more modes in spectral expansions, or otherwise made fewer approximations. The models confirmed that blocked and zonal flows appeared from the interaction of eastward jets with topography; in such models zonal and blocked flows appear as two stable equilibria [8, 24, 101] or two separate chaotic flow regimes [62, 72, 99, 116]. In all models, for very low forcing the blocked flow was the only stable solution. As the forcing was increased, both blocked and zonal flows became possible. For very high forcing, only the zonal solution was stable, and this solution resembles the forcing for any particular model as the forcing is

---

<sup>1</sup>Charney and DeVore used the terms blocked flow and “low index” flow interchangeably, and zonal flow and “high index” flow. The index terminology is related to the zonally averaged pressure gradient across latitudes 35-55° N. Due to the structure of the equations, the blocked flow was also identified as sub-resonant, and the zonal flow as super-resonant.

increased to infinity. For models with chaotic flow regimes, the time spent in the blocked state compared to the time spent in the zonal-like state decreased as the forcing was increased [72].

An additional barotropic model by Wu [163] used azimuthally asymmetric forcing, rather than topography. This study found blocked and zonal flows, and found that the flow would actually alternate between these two flows. This model and the earlier work by Legras and Ghil support the hypothesis that the mechanism allowing switching between blocked and zonal flows may be barotropic, rather than needing to be baroclinic (as hypothesized by Charney and DeVore originally [24]).

### 5.3 Previous Experiments

Laboratory experiments in rotating annuli with a radial temperature gradient have helped in the understanding of the mechanism of baroclinic instability and the atmosphere's general circulation [53, 75]. Introducing wavenumber-two topography in such annuli produced new phenomena [10, 63, 74, 107] but did not adequately explain the spatio-temporal features of the atmosphere's observed and modeled low-frequency variability. Several barotropic experiments were conducted [22, 108, 110] but did not examine questions of blocking and zonal patterns. Stream functions shown in Ref. [108] resemble our nearly-zonal patterns (see Fig. 5.3(a)), but the Reynolds numbers for those experiments were very low and the flows examined were time-independent.

### 5.4 Experimental Observations

We model Northern Hemisphere atmospheric flow experimentally in the rotating annulus with topography added. As discussed in Sec. 2.1, because of the rapid rotation the flow is essentially two-dimensional and can be compared with barotropic

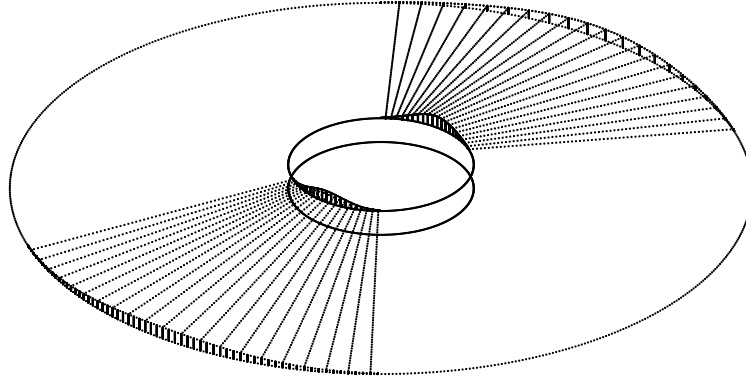


Figure 5.2: Bottom topography placed in the rotating annulus. The topography is Gaussian in profile, has a height of 1.5 cm (approximately 7 % the mean height of the annulus), and an angular extent of  $72^\circ$ . The ridge height is independent of radius, although the topography rests on the sloping bottom of the annulus and thus the topography has this overall slope (0.1). The raised inner circle at the center of this figure reflects the sloping bottom.

model results. These experiments facilitate exploration of the flow’s behavior over a wide parameter range: an hour at a rotation frequency of 2 Hz corresponds to 20 simulated years.

#### 5.4.1 Apparatus

For these experiments, to increase the Reynolds number, the annulus is filled with a fluid with a low viscosity, water (kinematic viscosity  $\nu = 0.009 \text{ cm}^2/\text{s}$ ). The pumping is from the outer ring ( $r_{\text{outer}} = 35.1 \text{ cm}$ ) to the inner ring ( $r_{\text{inner}} = 18.9 \text{ cm}$ ), resulting in a co-rotating (“eastward”) jet (see Sec. 1.2.8). This forcing is similar to the forcing assumed for the barotropic models discussed in Sec. 5.2. Two radial aluminum ridges are symmetrically placed on the bottom of the annulus, each having a Gaussian profile:  $h(r, \theta) = h(\theta) = h_0 \exp[-(\theta/\theta_0)^2]$  with  $h_0 = 1.5 \text{ cm}$  and  $\theta_0 = 21^\circ$  (see Fig. 5.2). This profile extends over  $72^\circ$ ; at  $\pm 36^\circ$  the Gaussian profile is smoothly tapered from 0.9 mm to zero using silicone glue.



Unfortunately, the holes drilled in the aluminum ridges do not perfectly align with the forcing holes in the annulus, and as a result the forcing flow through the ridges is reduced by an unknown amount. The mis-alignment of the holes is the same for both ridges. This presumably results in a perturbation with mode number 2 symmetry and the same phase as the topography, and thus does not significantly change the interpretation of the results. However, any future work should attempt to precisely align the holes, and should keep in mind this discrepancy when comparing future results with these results.

A quick argument can compare the effective height of the experimental mountains with the height of mountains on the Earth [81]. We consider the change in potential vorticity due to flow across a mountain, compared with the change in potential vorticity due to a change in position along the mountain (change in latitude on the Earth, change in radial position in the annulus). From Sec. 1.2.6 it can be seen than

$$\Delta q_{\text{mountain}} = \frac{f_0 \Delta h}{h_0^2} \quad (5.1)$$

for both real mountains and the experimental ridges;  $f_0 = 2\Omega \sin \theta$  for the Earth,  $f_0 = 2\Omega$  for the annulus,  $h_0$  is the effective height of the atmosphere for the Earth and the mean height of the annulus, and  $\Delta h$  is the height of the mountains. Next,

$$\Delta q_{\text{latitude}} = \frac{f_{\text{Mexico}} - f_{\text{Canada}}}{h_0} \quad (5.2)$$

and

$$\Delta q_{\text{radial}} = \frac{f_0 s \Delta r}{h_0^2} \quad (5.3)$$

with  $s = 0.1$  as the slope of the bottom of the annulus. For the experiment, we take  $\Delta r = 43.2 - 10.8 \text{ cm} = 32.4 \text{ cm}$ , producing

$$\frac{\Delta q_{\text{ridge,expt}}}{\Delta q_{\text{radial,expt}}} = \frac{\Delta h}{s \Delta r} = \frac{1.5 \text{ cm}}{(0.1)(32.4 \text{ cm})} \approx 2 \quad . \quad (5.4)$$

For the Earth,  $\Delta h \approx 2$  km and  $h_0 \approx 10$  km; taking  $\theta_0 = 45^\circ$ ,  $\theta_{\text{Canada}} = 30^\circ$ , and  $\theta_{\text{Mexico}} = 65^\circ$ , we find

$$\frac{\Delta q_{\text{mountains}}}{\Delta q_{\text{latitude}}} = \frac{(\sin \theta_0)(\Delta h)}{h_0(\sin \theta_{\text{Mexico}} - \sin \theta_{\text{Canada}})} = \frac{(0.707)(2\text{km})}{10\text{km}(0.91 - 0.50)} \approx 0.35 \quad . \quad (5.5)$$

Some of the numbers used in this calculation are somewhat arbitrary, but it appears that the annular mountains are of roughly the correct order of magnitude in height, perhaps six times larger than they ought to be. Future experiments should use smaller hills rather than mountains for the ridges. Note also that the effect of the land/ocean contrasts is unknown, and may be the primary mechanism for localizing the blocking anticyclones in the atmosphere [24, 48]: the above calculation cannot take the oceans into account, but it is reasonable to conjecture that to model the effect of land/ocean contrasts the experimental ridges must be taller than they would need to be for modeling purely topographic effects.

Our two control parameters are the pump flux rate  $F$ , which ranges from 0 to 400 cm<sup>3</sup>/s, and  $\Omega$ , which for these experiments ranges from  $2\pi$  to  $6\pi$  rad/s (1–3 Hz). These two control parameters determine the nondimensional Rossby ( $Ro$ ) and Ekman ( $Ek$ ) numbers (Sec. 1.2.1). The Rossby number  $Ro = U/2\Omega L$  is given in terms of  $L$ , the spacing between the forcing rings (16.2 cm), and the maximum velocity  $U$  that would result from a steady, axisymmetric flow in the absence of topography,  $U = (F/2\pi)(\Omega/\nu)^{1/2} r_{\text{sink}}^{-1}$  (see Eq. (1.36)). The Ekman number  $Ek = (T_{\text{annulus}}/T_{\text{Ekman}})^2$  is given by the squared ratio of the annulus rotation period,  $T_{\text{annulus}} = 2\pi/\Omega$ , to the relaxation time for unforced disturbances,  $T_{\text{Ekman}} = h_0/2(\nu\Omega)^{1/2}$  (see Sec. 1.2.3), yielding  $Ek = (4\pi/h_0)^2(\nu/\Omega)$ . This differs from the definition of  $Ek$  given in Sec. 1.2.1 by a constant. In the present experiments,  $0.10 < Ro < 0.35$  and  $0.4 \times 10^{-3} < Ek < 10^{-3}$ .

### 5.4.2 Results

In the absence of topography, the flow in this parameter range is characterized by eastward propagating Rossby waves [132, 138]. With the topography in place, however, we observe two stationary wave patterns with dramatically different characteristics, as illustrated by the contour plots of typical time-averaged stream functions in Fig. 5.3 (see Sec. 2.4 for a discussion of stream function calculation). At high Rossby numbers (i.e., high pumping or low rotation) a nearly *zonal* flow (Fig. 5.3(a)), resembling the more frequently occurring atmospheric patterns (see Fig. 5.1(a)), is observed: a strong co-rotating jet smoothly flows around the annulus, with a small-amplitude wave of zonal wavenumber two induced by the two mountains. At lower Rossby numbers a *blocked* flow is observed (Fig. 5.3(b)): the jet is wavier and its speed much lower (see also Figs. 5.9(a,c)). A strong wavenumber-four component of the flow field has arisen, with one anticyclone (counter-rotating vortex) present upstream of each mountain, the other one downstream, like in a Rossby lee wave [64]. In the atmosphere, though, unlike in the experiment here, it is the upstream ridge (poleward curvature of the jet) which is more pronounced. There is some evidence that the downstream vortex will move towards the equator in a real atmosphere [60, 100], and thus the upstream anticyclone seen in the experiment is more important; in the atmosphere, the blocking anticyclone is upstream of the topography.

Blocking anticyclones appear most often separately, in either the North-Atlantic/European or the Pacific/North-American sector, although double-blocking episodes (see Fig. 5.1(b)) do occur [7, 25, 35, 118, 122]; the two-fold symmetry of the apparatus presumably favors the double-blocking pattern. The drop in jet intensity, increase in wave amplitude, and upstream shift of the two stronger highs that we observe for blocked flow are in agreement with the simplified barotropic models [24, 72, 101, 140], which are supported by results from general circulation models

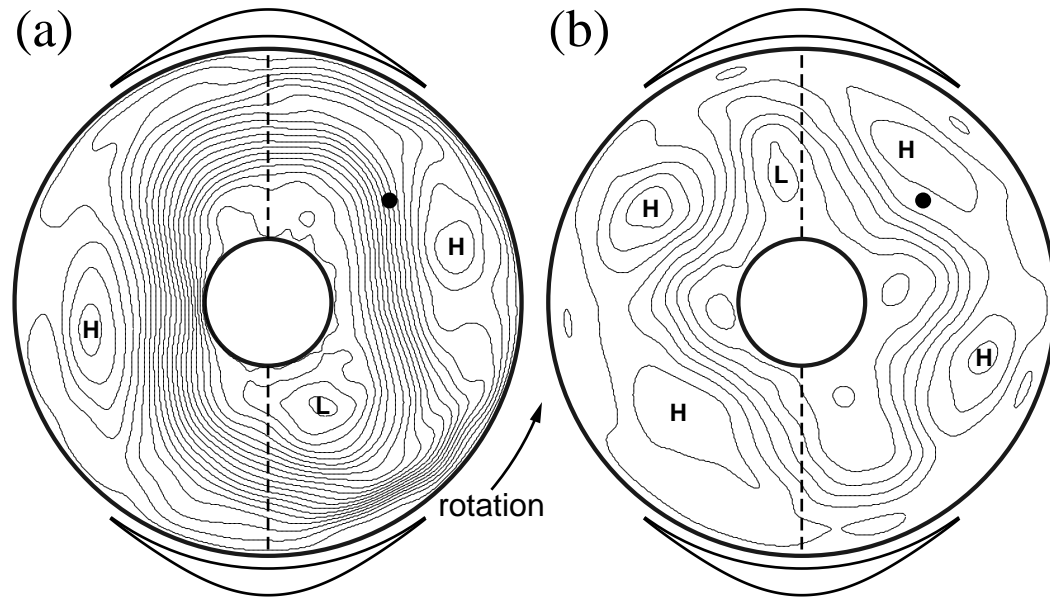


Figure 5.3: Time-averaged stream function contours calculated from experimental data for (a) zonal flow and (b) blocked flow. The peaks of the ridges are indicated by heavy dashed lines, and the profile of each ridge is shown by black curves outside the rim of the round panels. The contour interval is  $15 \text{ cm}^2/\text{s}$  for both plots. The annulus rotates counter-clockwise, and the flow is in the direction of rotation (eastward). The Rossby numbers  $Ro$  for the zonal and blocked flows are  $0.33 \pm 0.02$  and  $0.22 \pm 0.02$ , respectively (pump flux  $F=390 \text{ cm}^3/\text{s}$  and  $260 \text{ cm}^3/\text{s}$ ); for both flows, the Ekman number is  $Ek = 4.8 \times 10^{-4}$  ( $\Omega = 3\pi \text{ rad/s}$ ). The highs and lows of the stream function are indicated by bold letters H and L respectively. The black dots indicate the horizontal location of the hot film probe.

[79]. Still, direct comparison of the experimental observations with the atmosphere is not possible since the spectrum of Northern Hemisphere topography is dominated by wavenumbers 2 and 3, thermal contrasts between continents and oceans complicate the barotropic forcing, and baroclinic phenomena also play an important role [8, 62, 101, 116].

The azimuthal flux carried by the jet is typically 3 times smaller than in the zonal case, even for similar pumping rates and Ekman number (not shown). The azimuthal flux can be determined by integrating the radial velocity profiles, shown in Fig. 5.4. The blocked flow shown ( $Ro = 0.22 \pm 0.02$ ) has a net azimuthal flux of  $1100 \text{ cm}^3/\text{s}$ , while the zonal flow shown ( $Ro = 0.33 \pm 0.02$ ) has a net azimuthal flux of  $4900 \text{ cm}^3/\text{s}$ , over 400% larger, despite the change in forcing by only 50%. The velocity profiles relative to the center of the jets are shown in Fig. 5.5. Here, a contour representing the position of the jet has been chosen, and data are shifted by this radial position before averaging. The zonal jet appears slightly narrower and has a steeper velocity gradient.

The variability of the blocked flow in the experiments is much higher than that of the zonal flow. For zonal flow (Fig. 5.3(a)), the variations from the mean spatial pattern are small, and instantaneous stream function fields resemble their time average. This can be seen in Fig. 5.6: a sequence of stream photographs reveal the zonal flow structure. For blocked flow (Fig. 5.3(b)), the instantaneous patterns differ considerably from the time average over most of the parameter range investigated; see Figs. 5.7 and 5.8.

The velocity time series for zonal flow, measured at a fixed point in the fluid, also shows nearly periodic variations superimposed on a noisy background (Figs. 5.9(a,b)), with an associated period of 17 annulus rotations. The blocked flow has a broad-band spectrum, with spectral power  $P$  decreasing with frequency  $f$  (Fig. 5.9(d)). However, its fluctuations decrease with  $Ro$  and, at very low  $Ro$ ,

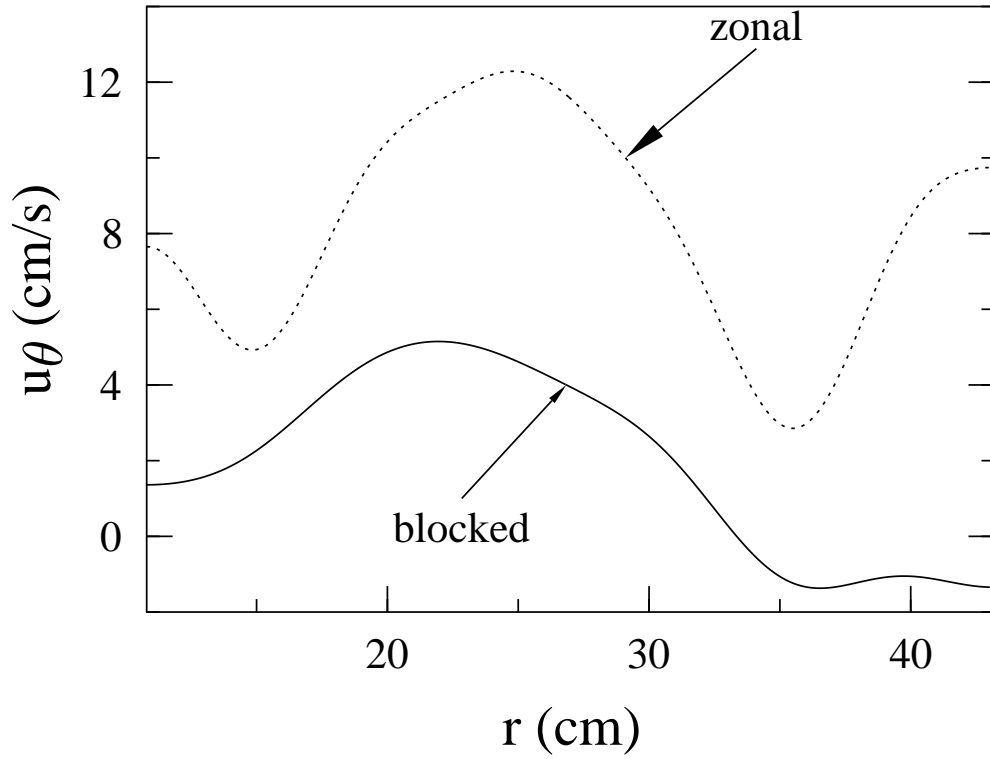


Figure 5.4: Azimuthally averaged azimuthal velocity profile. The data correspond to the stream functions shown in Fig. 5.3. These velocity profiles are from time-averaged data.

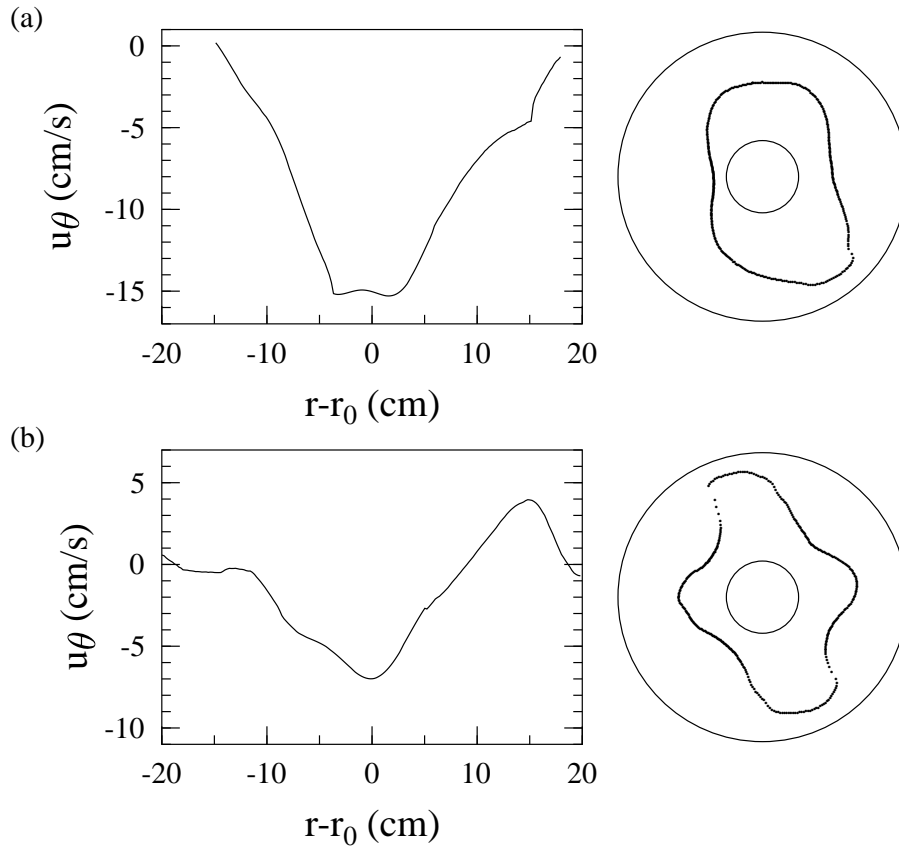


Figure 5.5: Azimuthally averaged azimuthal velocity profile, relative to the center of the jet, for (a) zonal flow and (b) blocked flow. At right, the contour giving  $r_0$  is indicated; the data are shifted relative to  $r_0$  for a given value of  $\theta$  and then averaged azimuthally. The zonal contour is given by  $\psi(r, \theta) = 200$ , the blocked contour by  $\psi(r, \theta) = 70$ ; these values are somewhat arbitrary and the velocity profiles are similar for different contours (except for a radial offset). The vertical axes have the same scales for (a) and (b). The data correspond to the stream functions shown in Fig. 5.3. These velocity profiles are from time-averaged data.

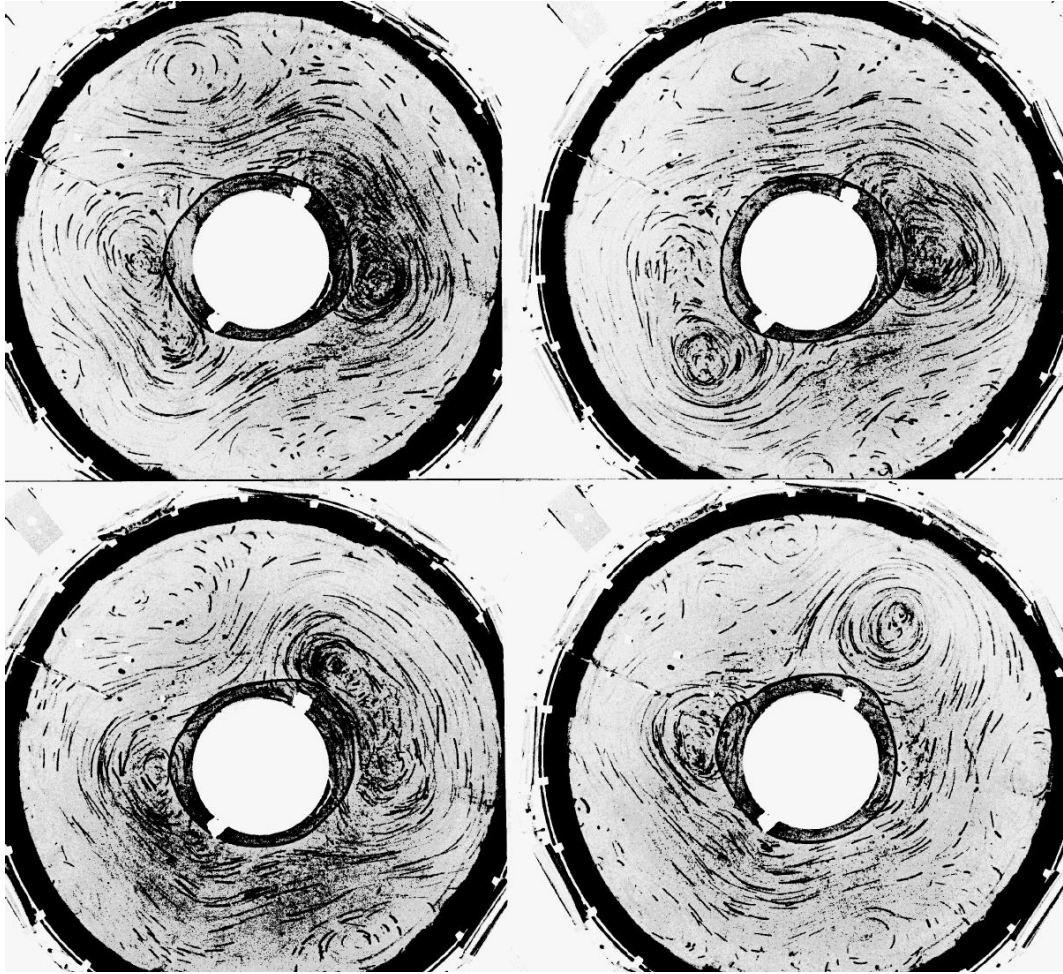


Figure 5.6: A sequence of four photographs of tracer particles in the zonal flow, taken at ten second intervals, with exposure times of 0.25 s to show particle motion. The rotation rate is 1.5 Hz, and the pump rate is  $380 \text{ cm}^3/\text{s}$ ;  $Ek = 4.8 \times 10^{-4}$  and  $Ro = 0.32 \pm 0.4$ . The mountain crests are located at 2 o'clock and 8 o'clock. The fourth picture is dissimilar to the first three, and may be the beginning of a transition to blocked flow: given the uncertainty in  $Ro$  for this particular experimental run, it is possible the flow is actually in the intermittent region (see Fig. 5.11). The flow is co-rotating (counter clockwise). The wavy continuous line around the center of the annulus is the edge of a bubble; for these pictures (and Figs. 5.7 and 5.8) this bubble was present, although not for most data presented in this chapter. The pictures are printed as negative images to enhance the contrast.



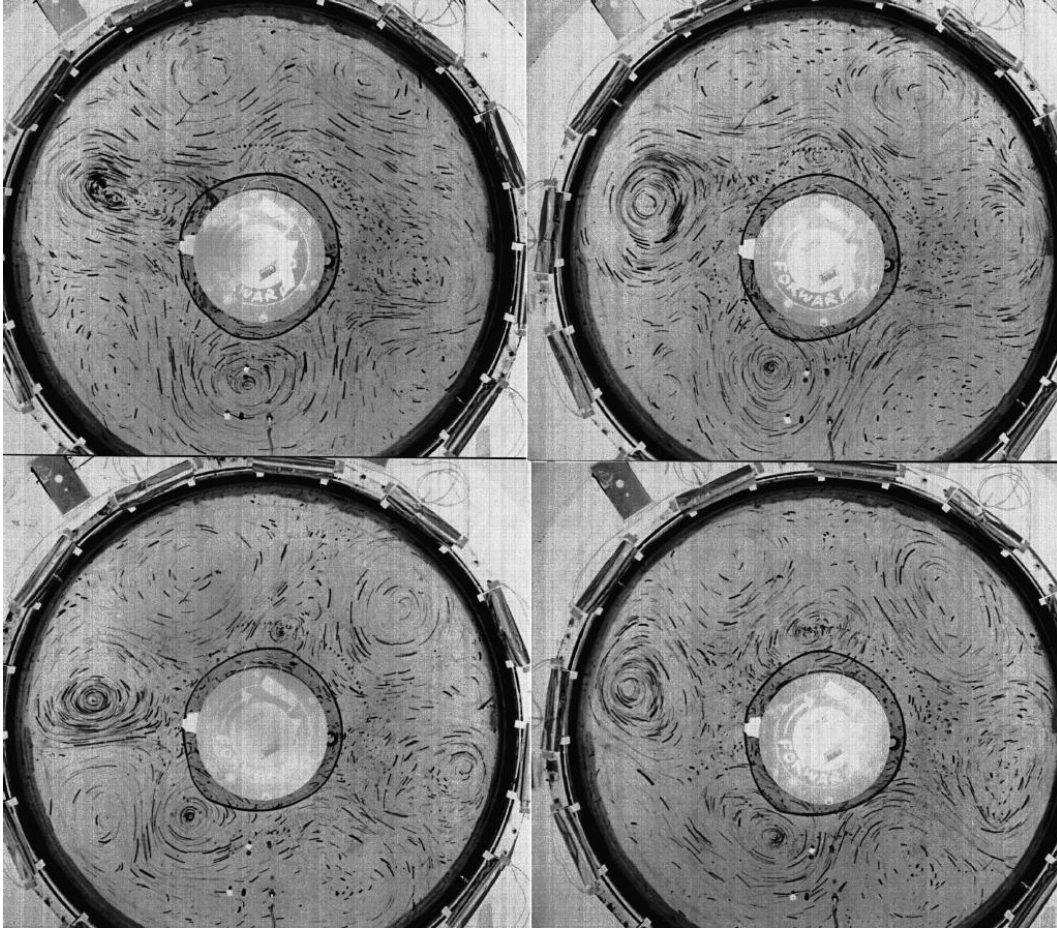


Figure 5.7: A sequence of four photographs of tracer particles in the blocked flow, taken at two second intervals, with exposure times of 0.25 s to show particle motion. The rotation rate is 1.5 Hz, and the pump rate is  $170 \text{ cm}^3/\text{s}$ ;  $Ek = 4.8 \times 10^{-4}$  and  $Ro = 0.14 \pm 0.04$ . The mountain crests are located at 4 o'clock and 10 o'clock. For further details, see the caption to Fig. 5.6.

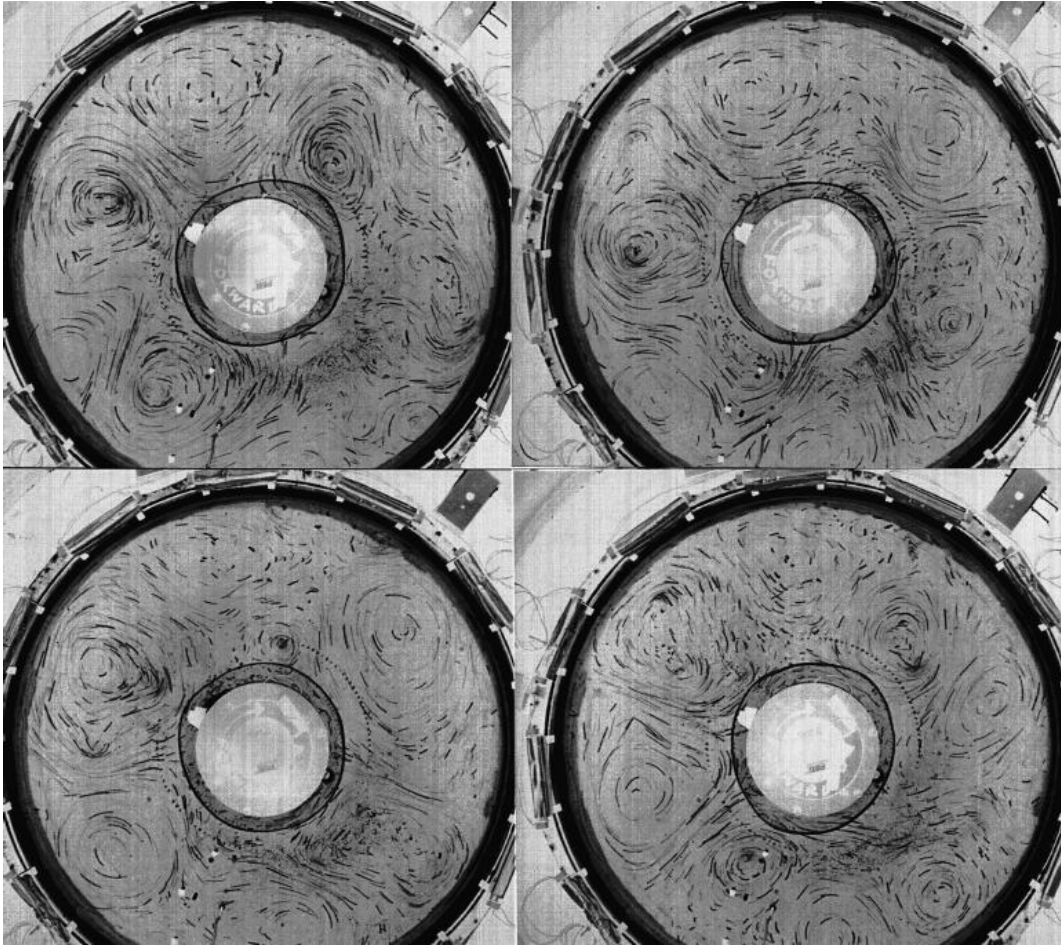


Figure 5.8: A sequence of four photographs of tracer particles in the blocked flow, taken at two second intervals, with exposure times of 0.25 s to show particle motion; the forcing rate is 40% higher than Fig. 5.7. The rotation rate is 1.5 Hz, and the pump rate is  $240 \text{ cm}^3/\text{s}$ ;  $Ek = 4.8 \times 10^{-4}$  and  $Ro = 0.20 \pm 0.03$ . At this high forcing rate, the blocked flow is quite erratic in time; compare with Fig. 5.7. The mountain crests are located at 5 o'clock and 11 o'clock. For further details, see the caption to Fig. 5.6.

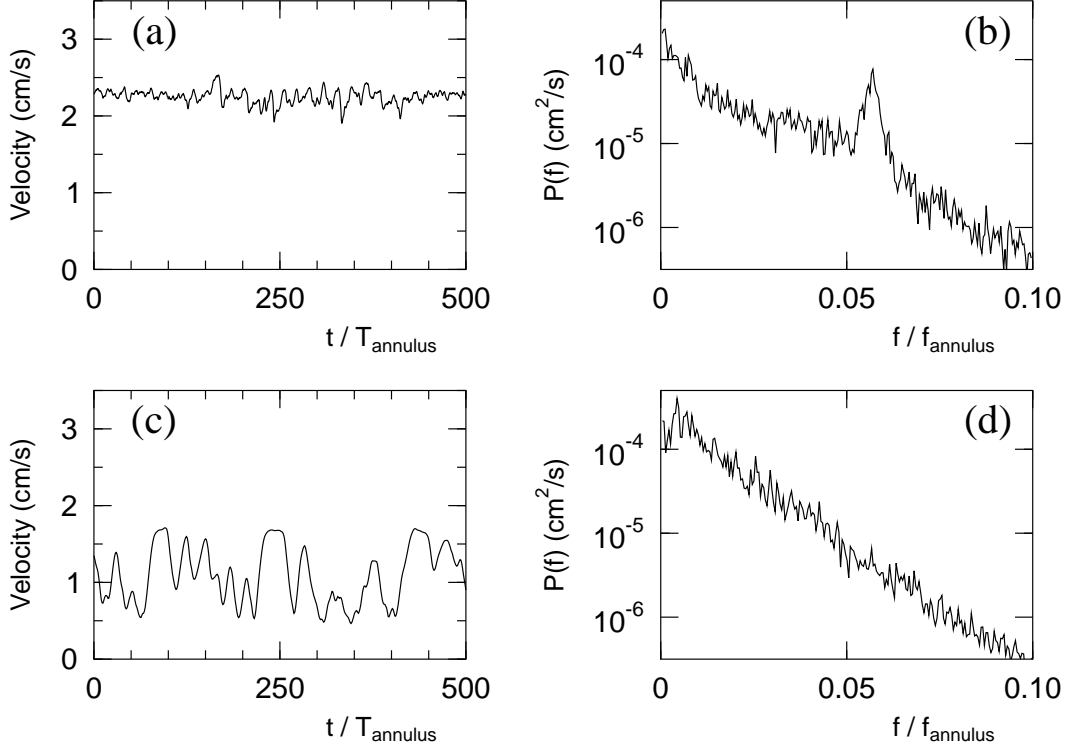


Figure 5.9: (a,c) Velocity time-series and (b,d) associated power spectra obtained from a hot-film probe located in the lid at  $r = 27.0$  cm; its position is indicated in Fig. 5.3 by a black dot. (a,b) Zonal and (c,d) blocked flows correspond to  $Ro = 0.332 \pm 0.005$  and  $0.124 \pm 0.005$  (pump flux  $F=320$  cm<sup>3</sup>/s and 120 cm<sup>3</sup>/s), with  $Ek = 7.2 \times 10^{-4}$  for both flows ( $\Omega = 2\pi$  rad/s). The peak in (b) has a period 17 s  $= 17T_{\text{annulus}}$ .

the blocked flow becomes time-independent and two-fold symmetric in space. Figure 5.10 shows a sequence of time series taken at varying  $Ro$  values for fixed  $Ek$ . In Fig. 5.10(a) can be seen periodic oscillations which are only present for very low values of  $Ro$ ; below this point, the flow is time-independent, although because of limitations of our current pump and flow meter, it was impossible to precisely determine the onset point of this periodic time-dependence.

Figure 5.11 is a regime diagram, showing blocked flow at low Rossby number, zonal flow at high  $Ro$ , and an intermediate regime where, for *fixed* experimental

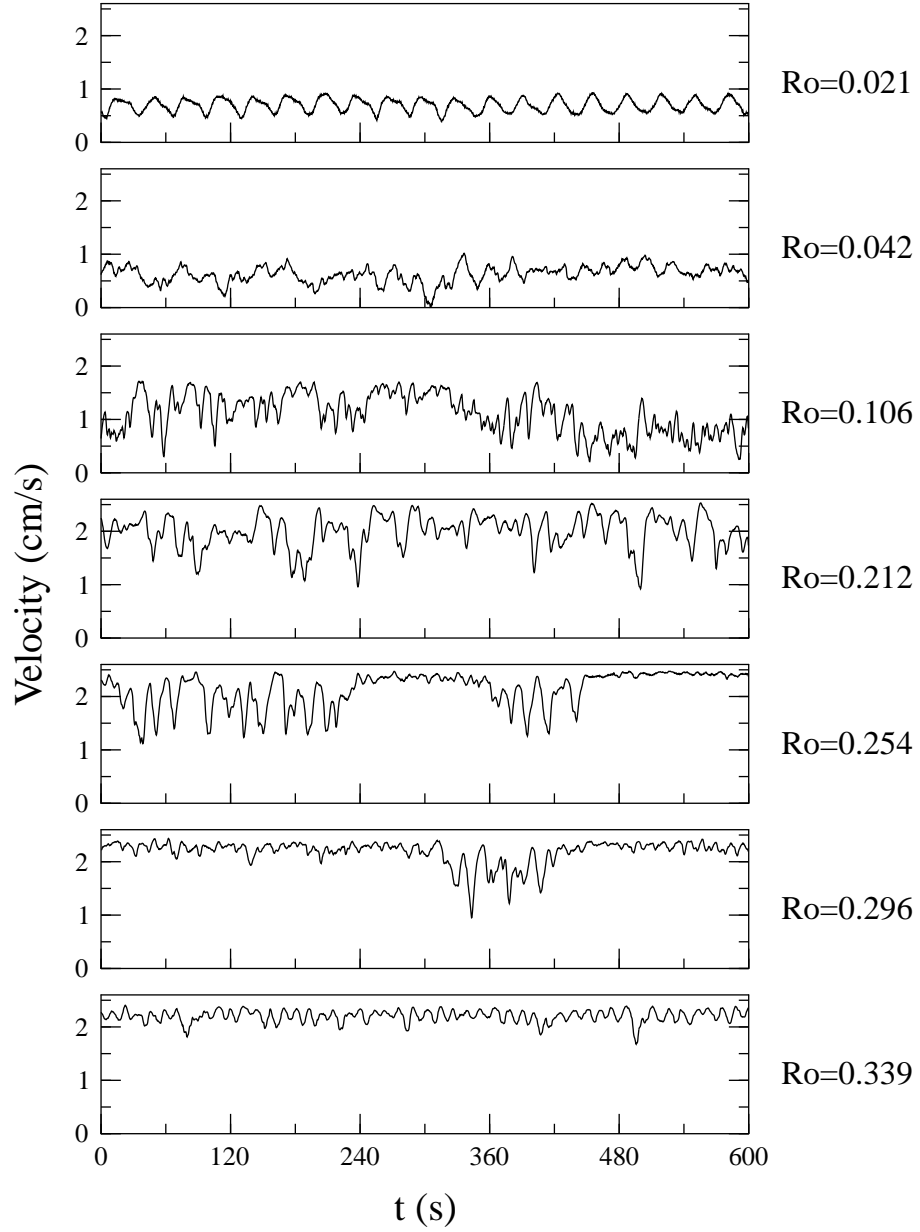


Figure 5.10: Velocity time-series obtained from a hot-film probe located in the lid at  $r = 27.0$  cm; its position is indicated in Fig. 5.3 by a black dot. The Rossby numbers are indicated for each flow at right, with uncertainties  $\pm 10\%$ , and  $Ek = 4.8 \times 10^{-4}$  for all flows ( $\Omega = 3\pi$  rad/s). For the first time series ( $Ro = 0.021$ ), the period is  $32 \text{ s} = 48 T_{\text{annulus}}$ .

conditions ( $Ro$  and  $Ek$ ), there are spontaneous transitions between distinct zonal and blocked flows (Fig. 5.12(a)). Similar spontaneous transitions are seen both in the atmosphere (see Fig. 5.1(c) and Refs. [25, 35]) and in simple deterministic models with a sufficient number of degrees of freedom [62, 72, 116]. Our blocked and zonal flows, however, both persist for many more annulus rotation periods than blocked and zonal flows persist in atmospheric observations. This is presumably due to the absence of baroclinic instabilities in the present annulus (cf. [10], for instance), as is the greater stability of the experimental zonal flow [72].

In the intermediate region, the fraction of time spent in one state varies as a function of the Rossby number (Fig. 5.12(b)). Similarly, as the pole-to-equator temperature gradient changes — from season to season or year to year in the same season [24, 62, 72, 99, 122, 140] — the relative prevalence of zonal- or blocked-flow episodes can change. Our experimental results are consistent with the idealized barotropic models [72] in that the frequency of blocking events increases when approaching the parameter range where blocking is the stable regime (see also [99]). The seasonal and interannual variability of persistent non-zonal flow patterns, such as blocking, in the atmosphere is subtler and has been documented to some extent in the Pacific/North-American sector, for both observations and general circulation models [59].

### 5.4.3 Symmetry of Flow Patterns

The flow patterns pictured in Fig. 5.3 are slightly asymmetric. There are several possible reasons for this asymmetry.

The first and simplest explanation is that the forcing may be asymmetric, for a variety of reasons. As described in Sec. 2.1, the forcing rings are divided into six sectors, and the plumbing controlling each sector may have slight variations resulting in asymmetric forcing. Also, as the experiment progresses, particles are sucked into

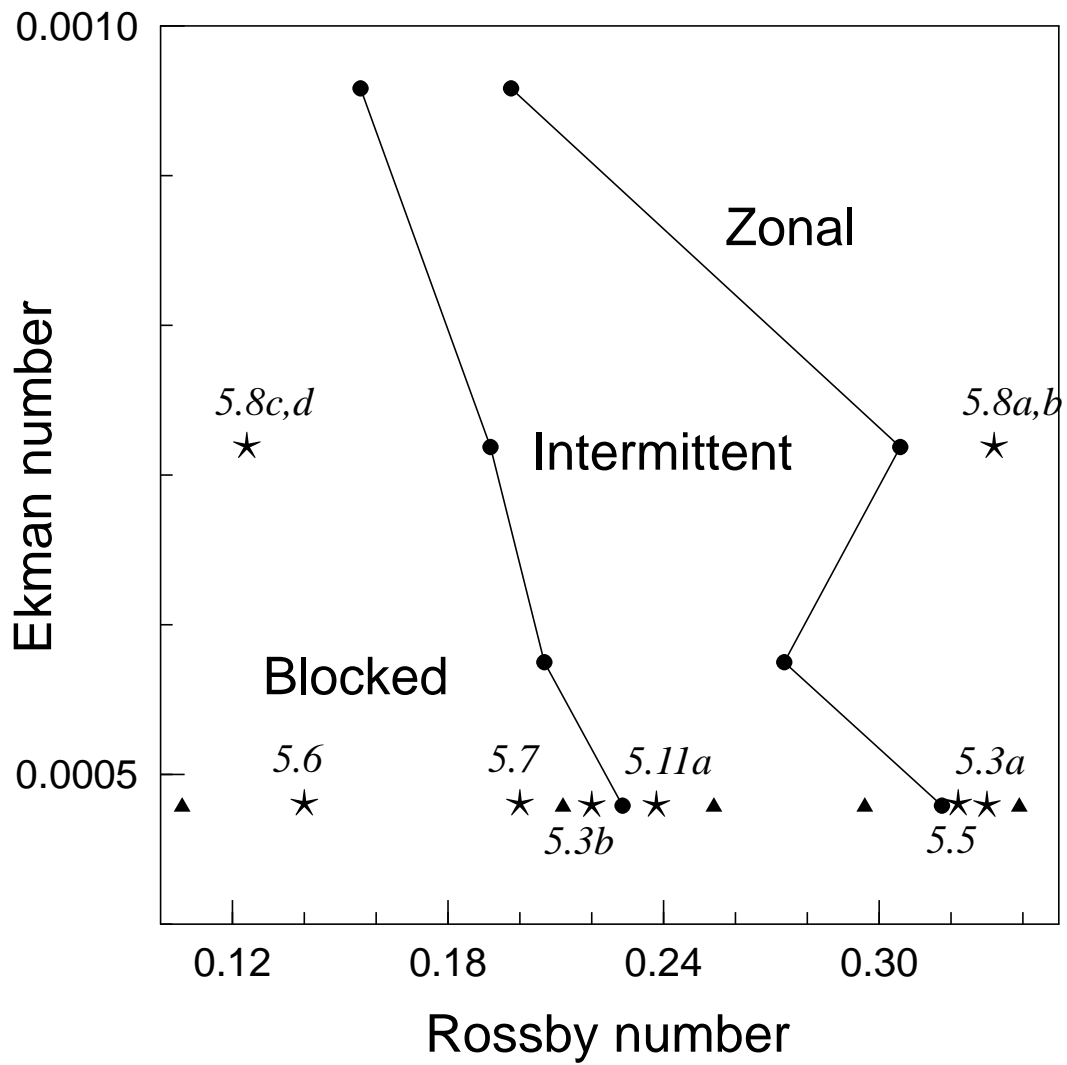


Figure 5.11: Diagram showing boundaries between the three observed flow regimes: pure zonal, pure blocked, and intermittent regime. In the intermittent regime, spontaneous switching between blocked and zonal flows occurs at irregular intervals. Stars indicate the positions in this diagram of the experimental runs used for Figs. 5.3(a,b), 5.9(a-d), and 5.12(a). The triangles indicate the positions of the last five time series from Fig. 5.10.

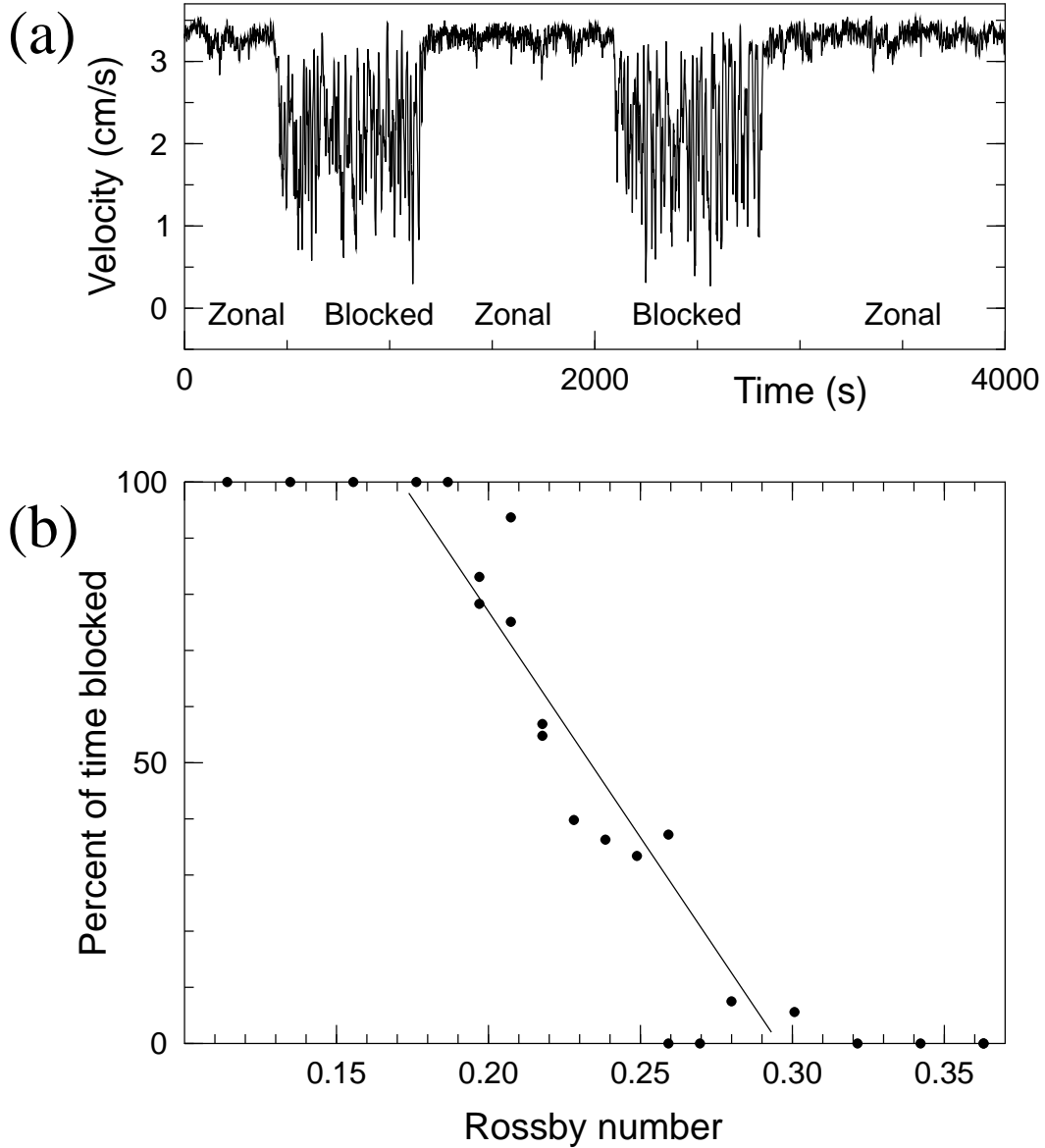


Figure 5.12: (a) Velocity time series showing intermittent transitions between zonal and blocked flow (cf. Figs. 5.9 and 5.11);  $Ro = 0.237 \pm 0.005$  and  $Ek = 4.8 \times 10^{-4}$  (pump flux  $F = 280 \text{ cm}^3\text{s}$  and  $\Omega = 3\pi \text{ rad/s}$ ). (b) The fraction of time spent in the blocked state as a function of the Rossby number (compare with similar plots for the atmosphere [35] and barotropic models [72]);  $Ek = 7.2 \times 10^{-4}$  ( $\Omega = 2\pi \text{ rad/s}$ ). To guide the eye, the straight line shows the least-squares fit to the intermittent data.

the sink ring of holes, where they are trapped by the netting (Sec. 2.2). Spatial variations of the amount of obstruction of flux through individual holes results in azimuthally asymmetric forcing.

The second reason the stream functions may be asymmetric is the amount of data used to produce the stream functions. As described in Sec. 2.4, a large amount of data is averaged to find the velocity field, which is then fit to basis functions to determine the stream function. In practice, the particle observations do not completely cover the annulus. Also, some areas have sparse observations where one or two particle trajectories solely determine the velocity in those areas, while other areas may have many particle trajectories which are averaged. As discussed in Sec. 2.4, both of these cases are given equal weight. Thus, the lack of data may result in asymmetries of the resulting stream functions, which significantly more data would smooth out. This was tested by taking portions of the data and generating stream functions, and observing that they were indeed more asymmetric. Additionally, the asymmetries observed in the stream functions generated from these truncated data sets typically showed no overall bias. This suggests that perhaps the forcing asymmetries are fairly insignificant, otherwise all stream functions would show similar asymmetries (i.e., one blocking anticyclone always with larger vorticity than the other, or a constant deformity of the jet on one side of the annulus.)

A third possibility was suggested by Panetta [100]. It is possible that the flow pattern itself has a scale larger than what will fit around the annulus. In such a situation, the topography may fix the phase of this large scale pattern. The flow could choose an alignment with the topography which is easiest, e.g., the pattern may be constructively interfering with the topographic forcing of one ridge and destructively interfering with the other ridge. It is even possible to imagine that for high forcing rates, where the flow structures are moving around somewhat turbulently (see Fig. 5.8 for example), that the flow pattern may alternate between



favoring one ridge and the other. Future work will be done with one mountain ridge which will hopefully illuminate this question.

## 5.5 Conclusions

Our barotropic laboratory experiments with topographic forcing yield two flow states qualitatively similar to atmospheric blocking and nearly zonal flow. Spontaneous transitions between the two flow states resemble those observed in the atmosphere and occur in the annulus for a wide range of control parameters. Our experiments suggest that, in agreement with the results of both simple models [8, 24, 72, 101] and general circulation models [71, 79], atmospheric blocking can be understood as a nonlinear, predominantly barotropic phenomenon that is strongly affected by topography.

Further experimental and numerical work [146] should examine the dynamical mechanisms responsible for the intermittency, and their effect on the long-term mean properties of atmospheric, oceanic, and laboratory flows. Studies should investigate the dependence of the current observations on mountain height. Tsimering suggested trying experiments without topography but with the forcing reduced through two opposite sectors of forcing holes; if this could cause similar blocking and zonal patterns, it would be an easy parameter to vary by controlling the valves to each sector [151]. Also, it would be interesting to examine the flows which occur when only one mountain ridge is used in the annulus. Several people have additionally suggested trying to control the transitions between blocked and zonal flow. Given the uncertainty of the transition mechanism and the difficulty of obtaining clear instantaneous pictures of the flow, probably a control method would need to be one which has the possibility of learning directly from the limited measurements available [156].

Another question worth examining is the pressure drop across the jet; this

should change when a transition between zonal and blocked flows occurs. We expect that the pressure drop should be greater for a zonal flow. An indirect way to measure this might be to investigate the pump speed or power as the pump flux is held constant and the flow undergoes a transition. This would be easy to measure, given our current data acquisition software (and might be easier than installing a pressure sensor). Either the control voltage sent to the pump controller could be measured, or the power lines connecting the controller to the pump motor could be monitored. By measuring the pressure drop across the jet, either directly or indirectly, a connection could be made to the “index cycle” terminology often used to describe blocking and zonal patterns [24, 48].

## Chapter 6

# Two-Dimensional Turbulence

### 6.1 Introduction

Three dimensional (3D) turbulence has been widely studied, but remains an unsolved mystery with few well established results [42]. The most well-known result is due to Kolmogorov, who originally considered the question of the energy spectrum  $E(k)$  when energy is injected into isotropic, homogeneous 3D turbulence at a length scale  $L_{\text{inj}}$ . He found that energy starting at wavenumber  $k_{\text{inj}} = 2\pi/L_{\text{inj}}$  “cascades” to smaller length scales, eventually reaching the dissipation scale  $k_d = (\epsilon/\nu^3)^{1/4}$  where the energy is dissipated by viscosity; the energy injection rate (per unit mass)  $\epsilon$  is equal to the energy dissipation rate. For length scales  $k_{\text{inj}} < k < k_d$ , the energy spectrum function is independent of the details of the forcing, and independent of the scales  $k_{\text{inj}}$  and  $k_d$ ; dimensional analysis shows  $E(k) \sim \epsilon^{2/3} k^{-5/3}$ , the famous Kolmogorov -5/3 law. While Kolmogorov’s law has been closely studied and modified slightly, it is clear that this result is reasonably correct and the decay exponent of the energy spectrum is close to -5/3 [42, 93, 139, 150].

Two dimensional (2D) turbulence is strikingly different as *enstrophy*, the total squared vorticity of the flow, is conserved, in contrast to 3D flows where

vortex tubes can be stretched. This constraint, in addition to the constraint of energy conservation (true for 2D and 3D flows), results in sharply different behavior. The classical picture of Kraichnan [69] and Batchelor [5] of forced 2D turbulence includes two scaling regimes, an inverse cascade of energy to large length scales,  $E(k) \sim \epsilon^{2/3} k^{-5/3}$ , and a cascade of enstrophy to small length scales,  $E(k) \sim \eta^{2/3} k^{-3}$  (see Fig. 6.1) (the directions of these two cascades are a consequence of Fjortoft's theorem [73]).  $\eta$  is the enstrophy injection rate,  $\eta = k_{\text{inj}}^2 \epsilon$ . As is the case for the original Kolmogorov -5/3 law, new analyses find corrections to these cascade laws [12, 111] while leaving the qualitative aspects of these laws unchanged.

In idealized forced 2D turbulence, the energy is never dissipated, unlike 3D turbulence. The energy continues cascading to large length scales, with the largest scale always increasing (see Fig. 6.1). In practice, two considerations limit this growth. First, practical systems have a finite size, and when the energy reaches length scales of the size of the system, the boundary prevents energy from reaching larger scales and boundary effects can dissipate energy. Second, all experimental flows at very high Reynolds number are really 3D rather than 2D [73]. As the energy at large length scales increases, the local Reynolds number can increase and dissipate energy through 3D turbulence.

Ekman pumping (Sec. 1.2.3) is a third dissipative mechanism present in rotating experiments. Ekman pumping provides damping acting at large scales rather than small scales [73]. In some cases, dissipation due to Ekman pumping is strong enough to completely inhibit the inverse energy cascade [73]; this appears to occur when  $Ro < \sqrt{Ek}$  [15]. The scale at which lateral friction becomes relevant is given by  $L_\nu = \sqrt{\nu/\omega'}$ , and the Ekman dissipative scale is given by  $L_E = u' \tau_E$ , using the viscosity  $\nu$ , rms value of the vorticity and velocity  $\omega'$  and  $u'$ , and the Ekman time  $\tau_E = h_0/(2\sqrt{\nu\Omega})$  (see Sec 1.2.3) [28]. The energy dissipation rates due to Ekman friction and lateral friction are given by  $\epsilon_E = \langle u \rangle^2 \tau_E^{-1}$  and  $\epsilon_\nu = \nu \langle \omega \rangle^2$ , with the

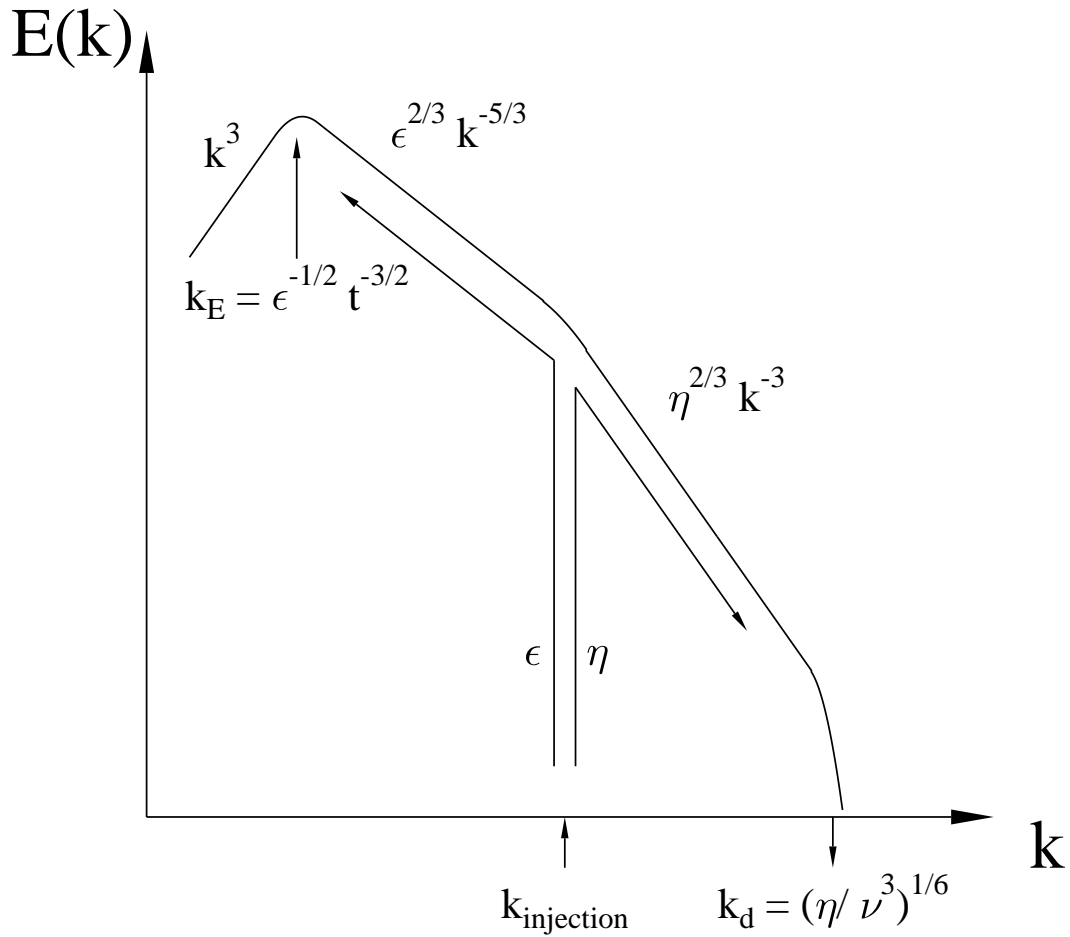


Figure 6.1: Schematic view of energy spectrum for 2D turbulence, adapted from Ref. [73]. Energy and enstrophy are injected into the flow at wavenumber  $k_i$  with injection rates  $\epsilon$  and  $\eta$  respectively. Energy cascades upwards to large scales (small wavenumber  $k$ ) and enstrophy cascades to small scales (large  $k$ ) where it is dissipated by vorticity. The largest scales for the energy grow in time and are eventually affected by the size of the system (see text for discussion). For the experiment,  $k_{\text{inj}}$  and  $k_d$  can be estimated as  $k_{\text{inj}} \approx 0.4 \text{ cm}^{-1}$  and  $k_d \approx 10 \text{ cm}^{-1}$ ; see the text for details.

angle brackets denoting a global spatial average [28]<sup>1</sup>. (The consequences of these length scales and dissipation rates for our experiment are discussed in Sec. 6.2.)

Effects such as Ekman pumping are mechanisms allowing the three dimensional nature of an experiment to modify the quasi-2D flow. In turn, 3D forcing can be used to drive a 2D flow (and thus the inverse energy cascade and the enstrophy cascade). Numerical simulations show that for sufficiently rapid rotation (low  $Ro$ ), 3D forcing results in 2D turbulence [129]. This is supported by past experimental work, discussed in Sec. 6.3.

An additional consideration for geophysical flows is the  $\beta$  effect (Sec. 1.2.6). Vortices above a certain size are distorted by the  $\beta$  effect; this size is known as the Rhines length, and is given by [119]:

$$l_R = \sqrt{\frac{2U}{\beta}} \quad . \quad (6.1)$$

Below this length scale, the turbulence is not affected by the  $\beta$  effect, and thus the turbulence is generally isotropic. Above this length scale vortices are elongated in the zonal direction and growth is blocked in the meridional direction [73]. It is possible that the inverse cascade is blocked at  $l_R$  by the propagation of Rossby waves [28, 119].

A final length scale for rotating experiments is the two-dimensionalization scale. This scale has not been well defined in the literature. As discussed in Sec. 1.2.2, rotating experiments are constrained to be two-dimensional by the Taylor-Proudman theorem. This theorem strictly holds when  $Ro$  and  $Ek$  are zero. For nonzero values, this theorem becomes

$$\left| \frac{\partial \vec{u}}{\partial z} \right| \sim \frac{U}{L} (Ro + Ek) \quad (6.2)$$

---

<sup>1</sup> $\epsilon_E$  can be determined by the following simple argument. The total kinetic energy can be written as  $\frac{1}{2}\rho V \langle u^2 \rangle$ , and the kinetic energy per unit mass as  $\frac{1}{2}\langle u^2 \rangle$ . If the forcing is removed, the flow decays as  $u = u_0 e^{-t/\tau_E}$ , so  $dKE/dt = \frac{1}{2}\langle 2u \, du/dt \rangle = -\langle u^2 \rangle/\tau_E$  (evaluating  $du/dt$  at  $t = 0$ );  $\epsilon_E = -dKE/dt$ .

where  $U$  and  $L$  are typical length and velocity scales. From this equation, a length scale for vertical changes can be estimated as  $L/(Ro + Ek)$ .

This can be compared to experimentally determined results for Taylor columns [54]. A Taylor column forms above a small topographic feature in a tank [145]. In order for the flow to be two-dimensional, the flow in a rotating experiment must move around the topographic obstruction; for the flow to pass over the obstruction, the fluid columns would have to compress, violating the two-dimensionality constraint. A Taylor column is the undisturbed fluid above such a topographic feature; dye injected into the Taylor column region will not mix with the bulk fluid, even far above the topographic feature [145]. However, for finite rotation, the Taylor column becomes unstable sufficiently far from the obstruction which generated the column. This distance has been found to be  $\sim L/Ek^{1/4}$  [54], with  $L$  being the width of the topographic obstacle and  $Ek = \nu/\Omega(L/2)^2$  being the Ekman number based on the length scale  $L/2$ . This result is for a Taylor column existing in a background flow with a velocity relative to the column.

## 6.2 Considerations for our experiment

The parameters discussed in the previous section can be estimated for our experimental apparatus. We start by considering the characteristic length  $L$  and velocity  $U$ , used to define  $Ro$  and  $Re$ . Reference [137] finds an expression for the velocity of the jet  $U$  and its width  $L$  in our rotating annulus:

$$U = a(sd^2/2\pi^2\nu h_0 r_m^2)^{1/3}(F\Omega)^{2/3} \quad . \quad (6.3)$$

$$L = b(h_0 d/4\pi s r_m \nu^{1/2})^{1/3}(F^2/\Omega)^{1/6} \quad (6.4)$$

with typical height  $h_0 = 18.7$  cm, distance between forcing rings  $d$ , bottom slope  $s = 0.1$ , mean radial position of jet  $r_m$ , viscosity  $\nu = 0.01$  cm<sup>2</sup>/s, pump flux  $F$ , and rotation rate  $\Omega$ .  $a$  and  $b$  are nondimensional parameters depending on the details of

the flow and exact definition of  $L$ ; for our experiment with a counter-rotating jet,  $a \approx 0.72$  and  $b \approx 0.69$  [137]. Equations (6.3) and (6.4) were derived by considering the balance of the torque induced by the forcing and the torque caused by Ekman friction, and the balance between advection and the beta effect.

Note that there are differences between co-rotating (eastward) and counter-rotating (westward) jets in our experiment [136, 137, 138]. Co-rotating jets tend to be narrower. Counter-rotating jets are broader, and are much more turbulent; it is for this reason we plan to conduct experiments with counter-rotating forcing. The Great Red Spot was simulated using counter-rotating jets [136].

$L$  and  $U$  depend on the details of the forcing (to determine  $d$  and  $r_m$ ) and the experimental control parameters  $F$  and  $\Omega$ . We consider two forcing configurations in this subsection, narrow forcing and wide forcing. *Wide forcing* uses two forcing rings, at  $r = 18.9$  cm and  $r = 35.1$  cm ( $d = 16.2$  cm and  $r_m = 27$  cm); this results in the largest possible values of  $L$  and  $U$  for a given  $F$  and  $\Omega$ . *Narrow forcing* is done between forcing rings at  $r = 27.0$  cm and  $r = 35.1$  cm ( $d = 8.1$  cm and  $r_m = 31$  cm); this results in the smallest possible values of  $L$  and  $U$ . A third alternative, forcing between rings at  $r = 18.9$  cm and  $r = 27.0$  cm, yields intermediate values of  $U$  and  $L$ . For our experiment,  $U \sim 20\text{--}100$  cm/s for wide forcing and  $\sim 5\text{--}40$  cm/s for narrow forcing,  $L \sim 6\text{--}22$  cm for wide forcing and  $\sim 4\text{--}14$  cm for narrow forcing (see Fig. 6.2).

We examine four separate cases in this subsection: wide forcing and narrow forcing, at  $\Omega/2\pi = 4$  Hz and 1 Hz. The values of  $Ro$ ,  $Re$ , and  $U$  are shown in Fig. 6.3 as a function of the forcing  $F$ .  $Ro$  is  $O(10^{-1})$  and  $Re$  is  $O(10^4 - 10^5)$  for our experiment. It appears that for sufficiently high forcing and low rotation,  $Ro \sim 0.2$ , at which point the Taylor-Proudman theorem may be significantly violated (i.e., the flow will be 3D).

The Ekman number ( $Ek$ ) is purely a function of rotation rate; it does not



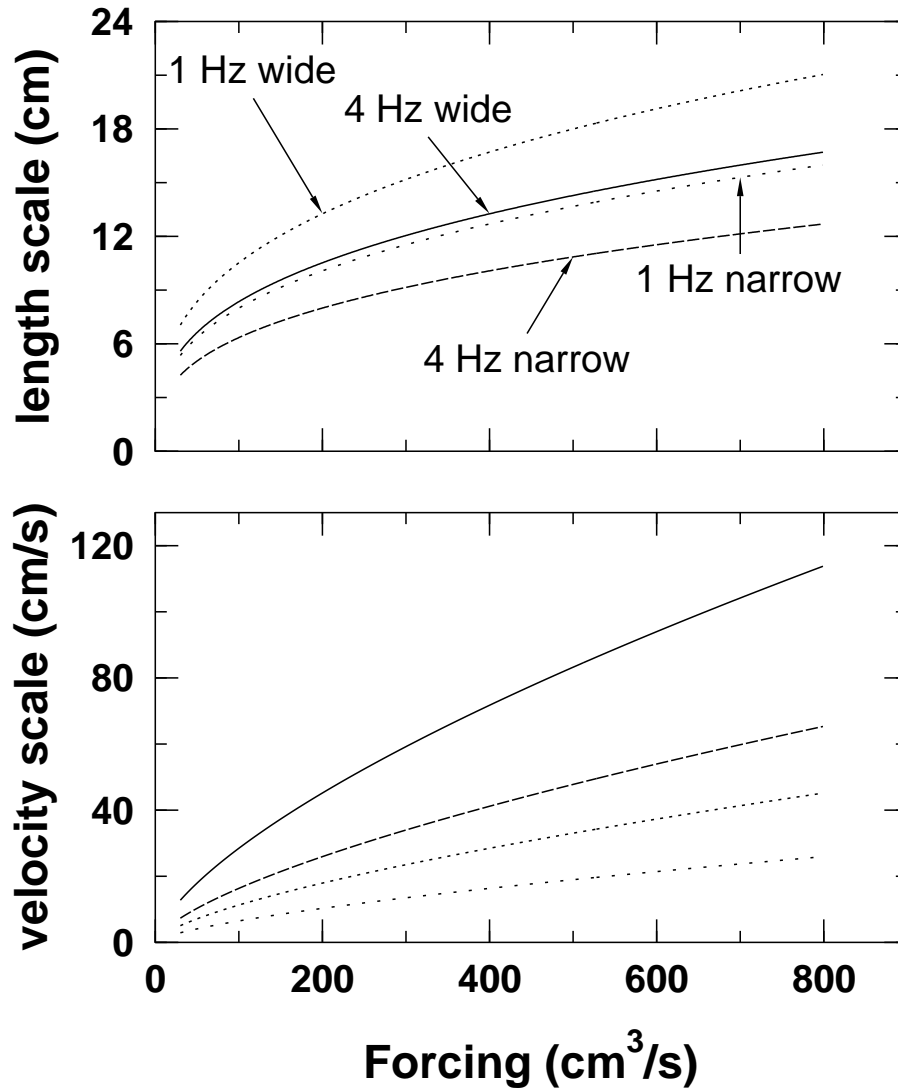


Figure 6.2: Length scale  $L$  and velocity scale  $U$  as a function of pump flux  $F$ , for four experimental configurations. These are empirically checked predictions from Ref. [137] (Eqs. (6.3) and (6.4)).

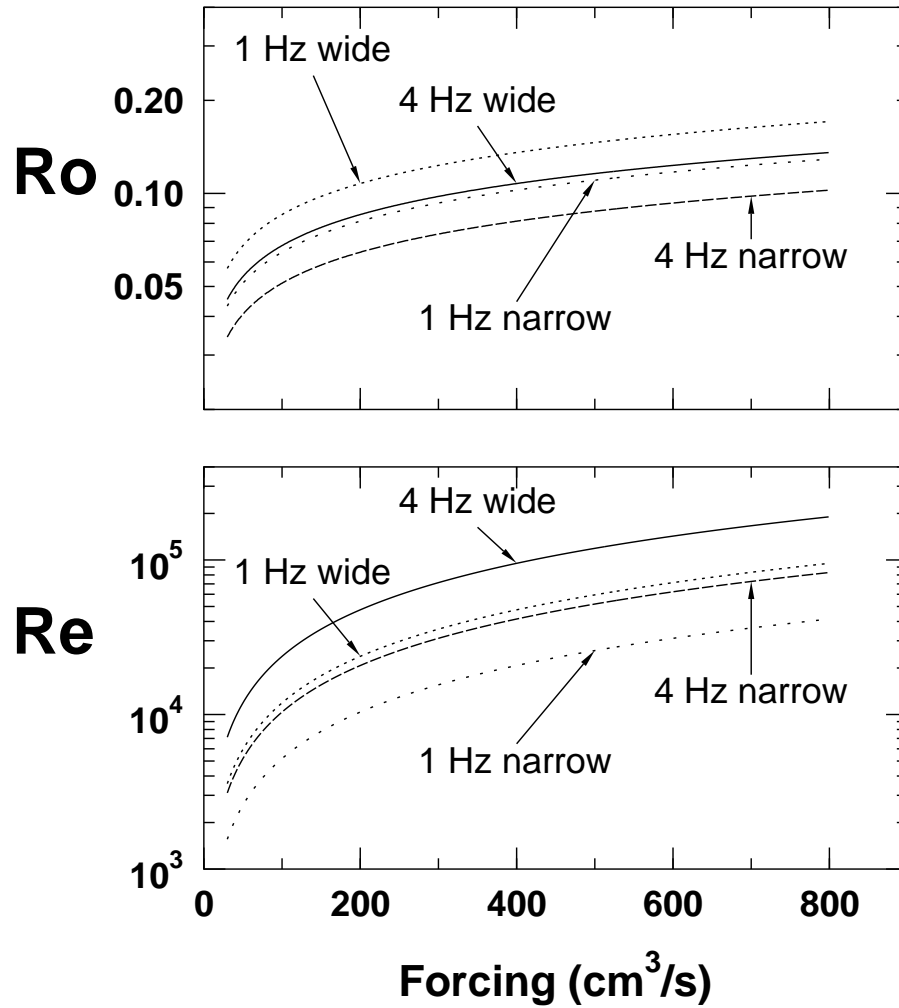


Figure 6.3: Rossby number  $Ro = U/2\Omega L$  and Reynolds number  $Re = UL/\nu$  as a function of forcing (pump flux)  $F$ , for four experimental configurations.

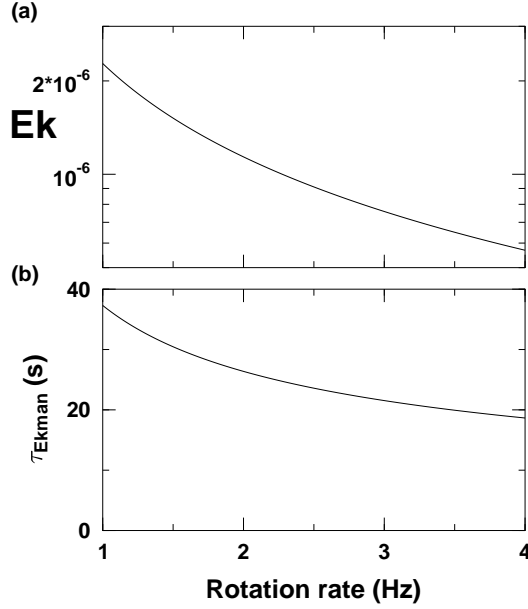


Figure 6.4: (a) Ekman number  $Ek = \nu/2\Omega h^2$  and (b) Ekman time  $\tau_E = h/\sqrt{2\Omega\nu}$  as a function of rotation rate  $\Omega/2\pi$ .

depend on the forcing.  $Ek$  is shown as a function of  $\Omega$  in Fig. 6.4. For our experiment,  $Ek$  is  $O(10^{-6})$ . The Ekman time ( $\tau_E$ ) is also shown in Fig. 6.4, and ranges from 20–40 s; this time scale is separated from the vortex turnover time ( $\sim 2$ –10 s for the turbulence experiments) and the rotation time for the annulus (0.2–1 s). The condition that the tank period is less than the vortex turnover time is equivalent to the condition of low  $Ro$ ; the condition that the vortex turnover time is less than  $\tau_E$  is equivalent to the condition of small  $Ek$  [138].

An additional length scale is the forcing scale. One possible choice is to use  $L = 16.2$  cm for wide forcing, and  $L = 8.1$  cm for narrow forcing (that is,  $L = d$  where  $d$  is the spacing between the forcing rings). Another possible choice is to consider the distance from the forcing rings to the walls of the experiment; turbulence is generated by the shear effects between the fluid forced between the rings and the motionless fluid near the walls. We choose  $l_{\text{inj}} \equiv 8.1$  cm as the shorter

of the two distances,  $d$  and the distance from the forcing rings to the walls. (That is, there are three possible forcing rings and two must be used; one ring used will always 8.1 cm from a wall, and the forcing rings themselves are spaced 8.1 cm apart.)

Using the definitions for  $L$  and  $U$ , we can calculate various important length scales. The forcing scale is always 8.1 cm, as discussed above (and thus  $k_{\text{inj}} = 2\pi/8.1 \text{ cm} = 0.78 \text{ cm}^{-1}$ ). The thickness of the Ekman layer is  $\delta_E \sim \sqrt{\nu/\Omega}$  (Sec. 1.2.3) which is 0.04 cm for  $\Omega/2\pi = 1 \text{ Hz}$  and 0.02 cm for 4 Hz. The dissipation scales for Ekman friction ( $l_E$ ) and viscous friction ( $l_\nu$ ) are calculated as discussed in the previous subsection, as are the Rhines length  $l_R$  and the enstrophy dissipation scale  $l_d = 2\pi/k_d$  (with  $k_d = (\eta/\nu^3)^{1/6}$ ); the results are shown in Figs. 6.5 and 6.6<sup>2</sup>.  $l_E$  is  $O(1000 \text{ cm})$ ,  $l_R$  is  $O(40 \text{ cm})$ ,  $l_d$  is  $O(0.5 \text{ cm})$ , and  $l_\nu$  is  $O(0.05 \text{ cm})$ ; these four length scales are well separated and separate from the forcing scale  $l_{\text{inj}} = 8.1 \text{ cm}$ . As the enstrophy dissipation scale is larger than the viscous dissipation scale (Fig. 6.5), the 2D turbulence cascade model is satisfied (that is, energy cannot cascade to the small scales; it must be removed by Ekman friction). Because  $l_E > 100 \text{ cm}$ , Ekman friction is important for flows in our experiment (size  $\sim 90 \text{ cm}$ ).

Next, we calculate the dissipation due to Ekman pumping ( $\epsilon_E$ ) and viscous dissipation ( $\epsilon_\nu$ ). The results are shown in Fig. 6.7. As  $\epsilon_E$  is two orders of magnitude larger than  $\epsilon_\nu$ , Ekman dissipation is the dominant dissipation mechanism for our experiment.

The vertical distance over which the Taylor-Proudman theorem breaks down can be estimated as  $L/Ro$  (see previous section). As  $L \sim 8 \text{ cm}$  and  $Ro \sim 0.3$  or smaller, this length scale is  $\sim 26 \text{ cm}$ , slightly larger than the height of our experiment (18.7 cm). As  $\Omega$  is increased, this length scale increases (see Fig. 6.3).

A last consideration is whether Ekman pumping can inhibit the inverse cascade for our experiment, that is, if  $Ro < \sqrt{Ek}$  [15] (as discussed in the previous

---

<sup>2</sup>To derive the enstrophy injection rate  $\eta$ , we use  $\eta = k_{\text{inj}}^2 \epsilon$ , with  $\epsilon$  determined from the values shown in Fig. 6.7.

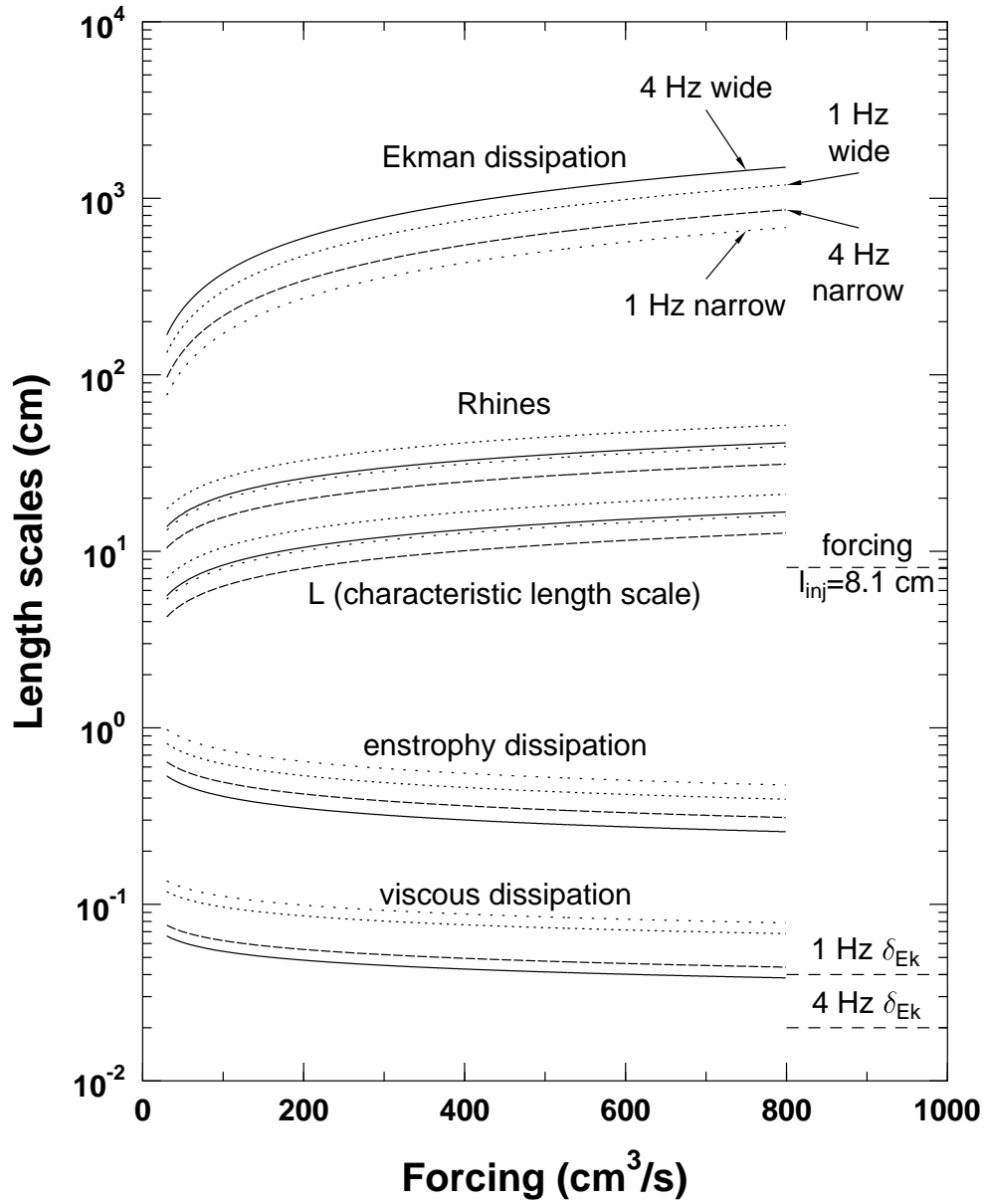


Figure 6.5: Important length scales for the turbulence experiment as a function of pump flux  $F$ . Note that all scales are well separated. In particular, as  $l_R > l_{inj}$ , an inverse cascade can occur.  $l_E = U\tau_E$  (Ekman dissipation),  $l_R = \sqrt{2U/\beta}$  (Rhines length),  $L_d = 2\pi(\nu^3/\eta)^{1/6}$  (enstrophy dissipation), and  $L_\nu = 2\pi(\nu^3/\epsilon)^{1/4}$  (viscous dissipation). See also Fig. 6.6.

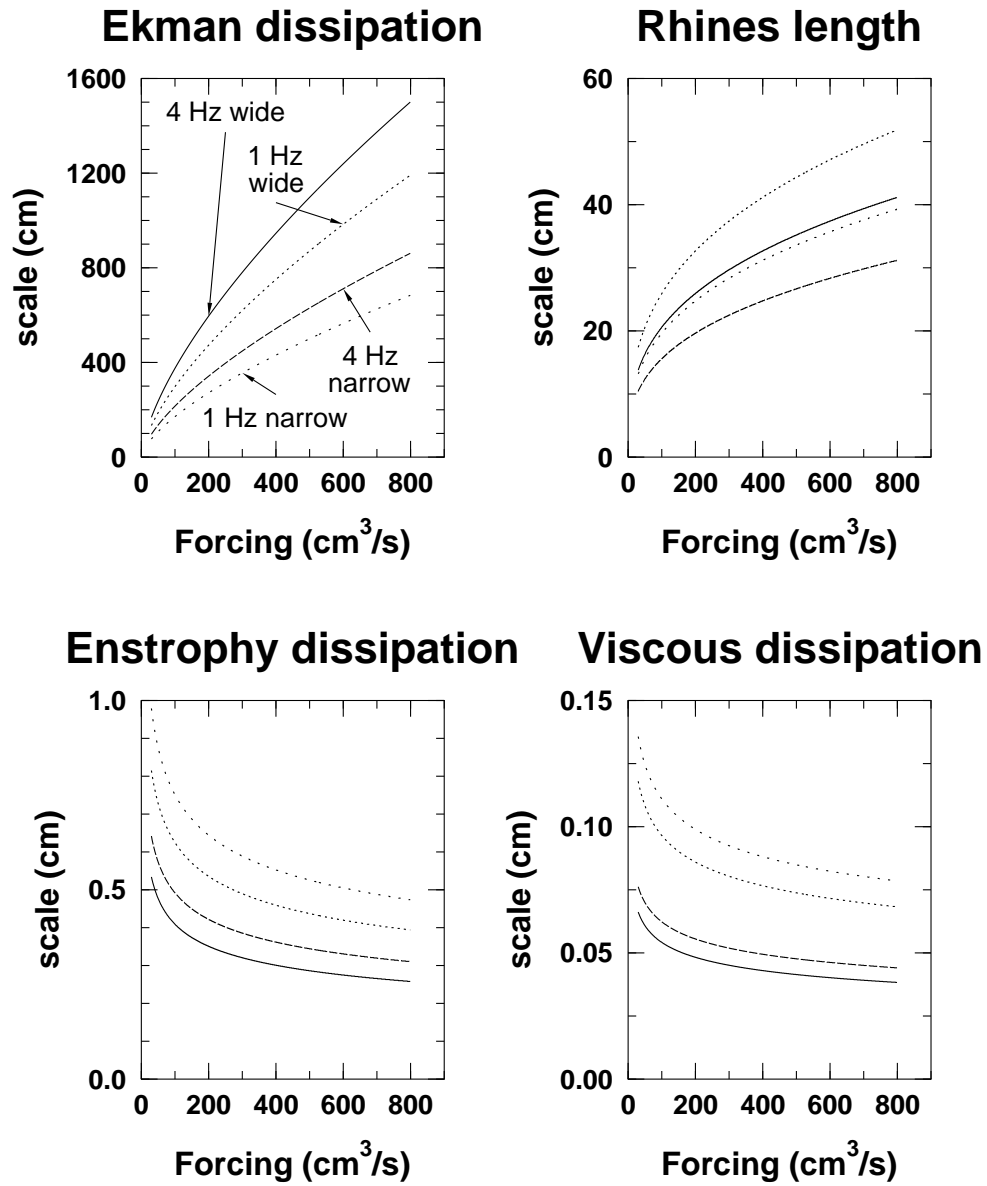


Figure 6.6: Ekman dissipation length scale  $l_E$ , Rhines length  $l_R$ , entrophy dissipation scale  $l_d$ , and viscous dissipation scale  $l_\nu$ , as a function of forcing. See also Fig. 6.5.

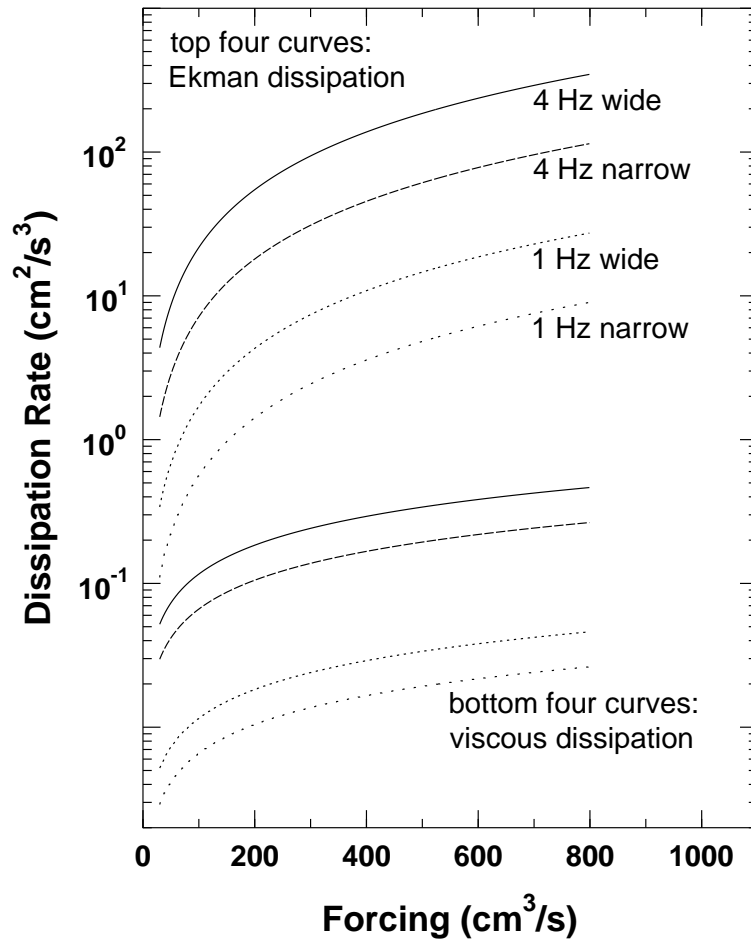


Figure 6.7: Dissipation rates due to Ekman dissipation (top four curves) and viscous dissipation (bottom four curves). For all forcing configurations and rotation rates,  $\epsilon_E \gg \epsilon_\nu$ , indicating that Ekman dissipation is the dominant dissipation mechanism.  $\epsilon_E = \langle U^2 \rangle / \tau_E$  and  $\epsilon_\nu = \nu \langle U^2 \rangle / L^2$ .

subsection). This condition can be rewritten as  $U^2/2\nu < \Omega$ . As  $U > 5$  cm/s for our experiments,  $\Omega$  must be larger than 1250 rad/s to inhibit the inverse cascade. Currently the experiment cannot rotate this rapidly, suggesting that an inverse cascade will occur, although as discussed previously it may be halted at the Rhines length scale [28, 119]. As  $l_R > l_{\text{inj}}$  for our experiment (Fig. 6.5), we should observe an inverse cascade with structures larger than the forcing length. Such structures are expected to be a strong jet for co-rotating forcing [137] or a large persistent vortex (the “Great Red Spot”) for counter-rotating forcing [136], as discussed above. Our experiments will examine the counter-rotating case.

### 6.3 Previous Experiments

Several experiments have studied quasi-2D flows at moderate  $Re$ . These include flows in magnetic fields [11, 18, 161] and in soap films [29, 47, 164]. Because of the geophysical applications, several experiments have examined specifically turbulence in rotating experiments. Two good reviews of rotating turbulence experiments are Refs. [58] and [149]. Generally these experiments used 3D forcing. The resulting flow was 3D near the forcing mechanism and 2D elsewhere. The 3D regions generally showed no qualitative or quantitative difference between the rotating and non-rotating cases.

The earliest experiment examining turbulence in a rotating system was conducted by McEwan [83]. He examined the formation of vortices from turbulence driven by sources and sinks arranged in periodic arrays on the bottom of a rotating tank, finding that the eddies generally had an anisotropic cyclonic form. His experiments were conducted at  $Ek \approx 10^{-6}$ ,  $Ro \approx 10^{-2}$ , and  $Re \approx 10^4$ . These experiments were not able to investigate a wide range of  $Ro$  or  $Re$ .

Colin de Verdière studied rotating 2D turbulence using random sources and sinks in a rotating cylinder [28] (rather than the periodic arrays of McEwan). He



found evidence for an inverse cascade as vortices formed on larger scales than the forcing, although he did not determine a scaling exponent. The flow was strongly anisotropic when  $\beta \neq 0$ . The experiments were conducted at  $Ek \approx 10^{-6}$ ,  $Ro \approx 10^{-2}$ , and  $Re \approx 10^3$ . He did not investigate the possibility of 3D structures for larger  $Ro$ . For steady forcing, energy injected at small scales was dissipated primarily by Ekman pumping at the larger scales.

Hopfinger and co-workers conducted experiments using a rotating tank with an oscillating grid at the bottom [57]. The 3D to 2D transition was difficult to characterize since the flow properties evolved in space, and quantities such as the Rossby number had to be estimated locally. As  $Ro$  decreased (moving away from the grid), at  $Ro \approx 0.2$  a transition from 3D to 2D behavior was observed. Again, in the 2D region, the energy coming from the 3D forcing was dissipated by Ekman friction. These experiments were conducted with  $Ek \approx 10^{-5}$ ,  $Ro \approx 5 \times 10^{-2}$ , and  $Re \approx 10^3$ . The parameter space at higher  $Ro$  and  $Re$  remains uncharted.

Dickinson and Long examined the growth of turbulence in a system similar to Hopfinger's tank [34]. They found that a turbulent layer grew away from the oscillating grid, and eventually a flow would be established similar to Hopfinger's observations: the flow was 3D near the grid, and 2D farther away. Their 3D region was interpreted as similar to an Ekman layer. They also found for extremely strong forcing that the 3D region would grow to fill the tank. However, the experiments were done at low rotation rates ( $\Omega \sim 0.2 - 1.1$  rad/s) and thus could not examine behavior for extremely low  $Ro$ ; the experiments were conducted at  $Ek \approx 10^{-5}$ ,  $Ro \approx 10^{-1}$ , and  $Re \approx 10^4$ .

## 6.4 Experiments

Our experiments will examine continuously forced 2D turbulence rather than the decaying turbulence that has more often been the subject of 2D turbulence stud-

ies [61]. We plan to conduct experiments to determine the conditions for which the experimental flow is predominantly two-dimensional, and for which the experiment is predominantly three-dimensional. For rapid rotation and low forcing,  $Ro$  and  $Ek$  are both small and the flow will be strongly 2D as has been observed in past experiments with our apparatus [131]. When the experiment is no longer rotating, the flow will be three-dimensional.

We plan to use both hot film probes and the ultrasound probe to investigate the character of the flow. We have placed a hot film probe at the top of the experiment at  $r = 27.0$  cm, and another probe directly underneath at the bottom of the experiment. By measuring the correlation of the signals from these two probes, a measure of the two-dimensionality of the flow can be obtained. The ultrasound probe can be used to measure the vertical velocity along one column of fluid at a fixed location 2.6. This probe best measures time-averages. One reasonable measurement of the dimensionality of the flow is to measure the time-averaged vertical velocity as a function of height  $z$ ; if the time-averaged vertical velocity profile is close to zero, the flow can be considered 2D. A second measurement would be to find the time-average of the fluctuations in the vertical velocity, perhaps also as a function of  $z$ .

The character of the transition from 2D to 3D flow is unknown. One possibility is growth of the Ekman boundary layers. This is unlikely; for  $\delta_{Ek} \sim 9$  cm, the half height of the tank, the rotation rate must be  $\Omega \sim 0.0001$  rad/s, and the conditions of small  $Ro$  and  $Ek$  will be violated at larger rotation rates. Also, it is reasonable to suppose that the phase space boundary between 2D and 3D behavior depends on both  $\Omega$  and the pump flux  $F$ , but  $\delta_{Ek}$  is determined solely from  $\Omega$ . The growth of the boundary layers will be monitored by the ultrasound probe. As the hot film probes are located 1 cm from the top lid and the bottom of the annulus, if the boundary layers grow to 1 cm ( $\Omega \sim 0.01$  rad/s), a change in the correlation

should be noticed. We do not expect that growth of the Ekman layers is a significant source of 3D behavior.

A second possibility for the transition from 2D to 3D behavior is through bursting of 3D turbulence [81]. It is possible that, via the inverse energy cascade, energy flows to large length scales; as the energy contained in these large scales increases, possibly it is released through a sudden burst of 3D turbulence. This bursting of 3D flow may be localized, or it may fill the tank. Bursting behavior could be detected by considering the correlation between hot film probes for short periods of time; a burst would be signaled by a sudden low correlation. Also, a 3D burst would be visible as a sudden abnormal vertical velocity profile as measured by the ultrasound probe. By examining ultrasound and hot film data, the fraction of time spent in 2D and 3D behavior could be determined. It is possible that Ekman dissipation will prevent the buildup of energy at large scales; also, the  $\beta$  effect may inhibit the inverse cascade.

A third possibility for the transition from 2D to 3D behavior would be an abrupt transition (as a function of  $F$  and  $\Omega$ ). If such a transition occurs, it would be easy to detect both with the ultrasound probe and the hot film probes. It would be interesting to learn if such a transition was hysteretic.

A last possibility is that the transition is gradual. Perhaps the 3D behavior grows as  $Ro$  (or  $1/Ro$ ) according to Eq. (6.2). In such a case, the 3D behavior could be measured by the correlation coefficient for the top and bottom hot film signals, and by quantities such as the average fluctuations of the vertical velocity, rms average vertical velocity, or other averaged measurements from the ultrasound probe.

We expect to begin conducting these 2D/3D turbulence experiments during the months of October and November 1997.

# Appendix A

## Random Walk Second Order terms

This appendix contains coefficients for the second order terms discussed in Chap. 3.

### A.1 Notation

Table A.1 contains a summary of the important notation used in this appendix. For a random walk alternating between flight events and sticking events,  $T = \langle t_f \rangle + \langle t_s \rangle$  when both moments are finite ( $\mu > 2, \nu > 2$ ).

### A.2 Second order terms

The asymptotic behavior of  $\langle x \rangle$  and  $\langle x^2 \rangle$  depends only on the leading terms in the expansion of Eqs. (3.26) and (3.27). In order to study the approach to the asymptotic limit, it is necessary to calculate higher order terms. (In cases where  $\langle x \rangle \sim t$ , it was necessary to calculate third order terms as the first order terms for  $\langle x \rangle$  and  $\langle x^2 \rangle$  canceled.) In this appendix, we use Eq. (3.32) for the expansion of the Laplace transform of the PDFs to produce the second order terms. The variance

Table A.1: List of common symbols used in this appendix.

| Symbol                                     | Meaning  |
|--|--|
| $T$  | mean time between the start of successive steps                                      |
| $t_F, t_S$                                 | minimum time for short flight, sticking events (see Eqs. (3.28), (3.29), and (3.41)) |
| $\langle t_f \rangle, \langle t_s \rangle$ | first moment of flight, sticking PDFs  |
| $\mu$                                      | power law decay exponent for the flight PDFs   |
| $\nu$                                      | power law decay exponent for the sticking PDFs                                       |
| $\gamma$                                   | variance exponent: $\sigma^2 \sim t^\gamma$  |
| $P_F^0, P_S^0$                             | probability that first event is a flight event, sticking event                       |
| $p_l, p_r$                                 | probability a flight is to the left ( $-x$ ), right ( $+x$ )                         |
| $v_l, v_r$                                 | velocity in left direction, right direction<br>( $v_l > 0$ for leftward motion)      |

will scale in time, generally, as  $\sigma^2(t) \sim Ct^\gamma + C't^{\gamma'}$  with  $\gamma' < \gamma$ . The asymptotic behavior, given in Sec. 3.5, will always be given by the largest exponent.

Regions with different second order terms are shown in Fig. A.1. We calculate the highest order terms for each region; these are listed in Tables A.2-A.4. The calculations are valid to second order, so while several terms are listed for each of the regions shown in Fig. A.1, only the two terms with the largest exponents are useful. The other terms may have exponents which are smaller than neglected third order terms that do not appear in the table.

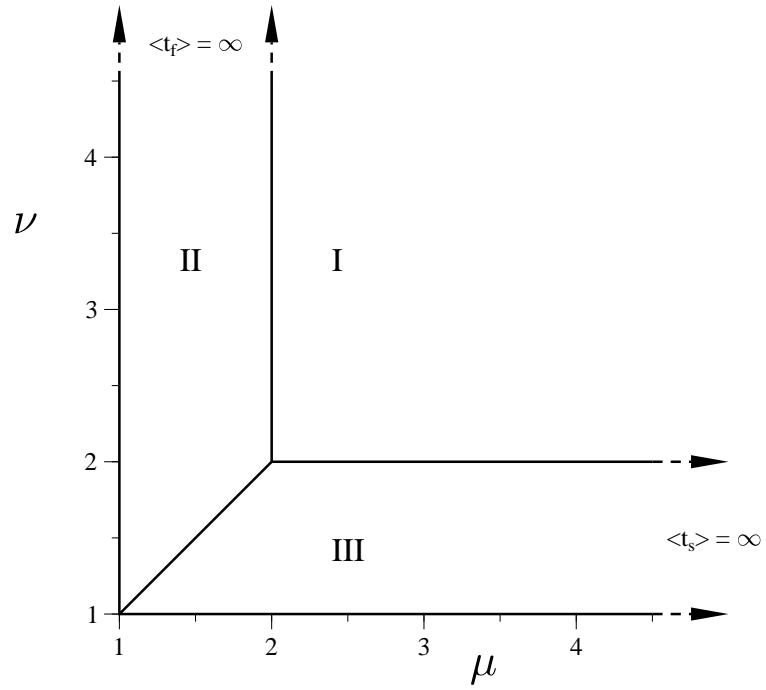


Figure A.1: (a) Phase diagram for the tables in the appendix. The regions shown correspond to the regions discussed in Tables A.2-A.4. The axes are the flight exponent  $\mu$  and sticking exponent  $\nu$ .

Table A.2: Scaling of the mean position for asymmetric random walks ( $v_{\text{ave}} = p_r v_r - p_l v_l \neq 0$ ),  $\langle x \rangle \sim K v_{\text{ave}} t^\beta + K' v_{\text{ave}} t^{\beta'}$ . The terms have been calculated to second order for each region shown in Fig. A.1. To use this table, determine which two terms have the largest exponent for a given value of  $\mu$  and  $\nu$ . The term with the third largest exponent is not necessarily the third order term, as the calculations have only been done to second order. In this table  $T$  is defined as  $\langle t_s \rangle + \langle t_f \rangle$ . Terms containing  $\langle t_f \rangle$  are only valid for  $\mu > 2$ , and terms containing  $\langle t_s \rangle$  are only valid for  $\nu > 2$ .

| Region | exponent $\beta$  | coefficient $K$   |
|--------|-------------------|---|
| I      | 1                 | $\langle t_f \rangle / T$   |
|        | $3 - \mu$         | $\frac{\langle t_s \rangle t_F^{\mu-1}}{(3-\mu)(2-\mu)T^2}$   |
|        | $3 - \nu$         | $\frac{\langle t_f \rangle t_S^{\nu-1}}{(3-\nu)(2-\nu)T^2}$   |
|        | 0                 | $\frac{2\langle t_f \rangle \langle t_s \rangle (P_F^0 \langle t_f \rangle - P_S^0 \langle t_s \rangle) + \langle t_s^2 \rangle \langle t_f \rangle - \langle t_s \rangle \langle t_f^2 \rangle}{2T^2}$ |
| II     | 1                 | 1   |
|        | $\mu - 1$         | $\frac{-\langle t_s \rangle t_F^{1-\mu}}{\Gamma(2-\mu)\Gamma(\mu)}$   |
|        | $1 + \mu - \nu$   | $-\left(\frac{\Gamma(2-\nu)}{\Gamma(2-\mu)\Gamma(2+\mu-\nu)}\right) t_F^{1-\mu} t_S^{\nu-1}$  |
| III    | $\nu - 1$         | $\left(\frac{\mu-1}{(\mu-2)\Gamma(2-\nu)\Gamma(\nu)}\right) t_F t_S^{1-\nu}$  |
|        | $1 + \nu - \mu$   | $\left(\frac{\Gamma(2-\mu)}{\Gamma(2-\nu)\Gamma(2-\mu+\nu)}\right) t_F^{\mu-1} t_S^{1-\nu}$   |
|        | $2\nu - 3$        | $-\left(\frac{1}{\Gamma^2(2-\nu)\Gamma(2\nu-2)}\right) (\langle t_f \rangle + \frac{\nu-1}{\nu-2} t_S) \langle t_f \rangle t_S^{2-2\nu}$  |
|        | $1 - 2\mu + 2\nu$ | $-\left(\frac{\Gamma^2(2-\mu)}{\Gamma^2(2-\nu)\Gamma(2-2\mu+2\nu)}\right) t_F^{2\mu-2} t_S^{2-2\nu}$  |
|        | $2 - \mu$         | $\left(\frac{P_S^0}{\mu-2}\right) t_F^{\mu-1}$  |
|        | 0                 | $-P_S^0 \langle t_f \rangle$  |

Table A.3: Anomalous diffusion results for symmetric random walks ( $v_{\text{ave}} = p_r v_r - p_l v_l = 0$ ),  $\sigma^2 \sim C v_{\text{rms}}^2 t^\gamma + C' v_{\text{rms}}^2 t^{\gamma'}$ . For each region shown in Fig. A.1, the terms for  $\sigma^2$  have been calculated to second order. See caption for Table A.2 for an explanation of how to use this table.

| Region | exponent $\gamma$ | coefficient $C$   |
|--------|-------------------|---|
| I      | 1                 | $\frac{\langle t_f^2 \rangle}{T}$   |
|        | $4 - \mu$         | $\left(\frac{2}{(4-\mu)(3-\mu)}\right) \frac{t_F^{\mu-1}}{T}$   |
|        | $6 - 2\mu$        | $\left(\frac{-2\Gamma(3-\mu)\Gamma(2-\mu)}{\Gamma(7-2\mu)}\right) \left(\frac{t_F^{2\mu-2}}{T^2}\right)$  |
|        | $6 - \mu - \nu$   | $\left(\frac{-2\Gamma(3-\mu)\Gamma(2-\nu)}{\Gamma(7-\mu-\nu)}\right) \left(\frac{t_F^{\mu-1} t_S^{\nu-1}}{T^2}\right)$  |
|        | 0                 | $-\frac{4\langle t_f^3 \rangle}{3T} + \left(\frac{\langle t_f^2 \rangle}{2T^2}\right) [\langle t_f^2 \rangle + \langle t_s^2 \rangle + 2\langle t_s \rangle (P_F^0 \langle t_f \rangle - P_S^0 \langle t_s \rangle)]$ |
| II     | 2                 | $2 - \mu$   |
|        | $\mu$             | $\left(\frac{2}{\Gamma(2-\mu)\Gamma(1+\mu)}\right) [(\mu-1)t_F + (\mu-2)\langle t_s \rangle] t_F^{1-\mu}$   |
|        | $2 + \mu - \nu$   | $\left(\frac{(2\mu-4)\Gamma(2-\nu)}{\Gamma(2-\mu)\Gamma(3+\mu-\nu)}\right) t_F^{1-\mu} t_S^{\nu-1}$   |
| III    | $\nu - 1$         | $\left(\frac{1}{\Gamma(2-\nu)\Gamma(\nu)}\right) \langle t_f^2 \rangle t_S^{1-\nu}$   |
|        | $2 + \nu - \mu$   | $\left(\frac{2\Gamma(3-\mu)}{\Gamma(2-\nu)\Gamma(3-\mu+\nu)}\right) t_F^{\mu-1} t_S^{1-\nu}$  |
|        | $2\nu - 3$        | $\left[\frac{1}{\Gamma(3-\nu)\Gamma(2-\nu)\Gamma(2\nu-2)}\right] ((\nu-2)\langle t_f \rangle + (\nu-1)t_S) \langle t_f^2 \rangle t_S^{2-2\nu}$  |
|        | 0                 | $-P_S^0 \langle t_f^2 \rangle$  |
|        | $2\nu - \mu$      | $\left[\frac{2\Gamma(3-\mu)}{\Gamma(3-\nu)\Gamma(2-\nu)\Gamma(1-\mu+2\nu)}\right] ((\nu-2)\langle t_f \rangle + (\nu-1)t_S) t_F^{\mu-1} t_S^{2-2\nu}$   |
|        | $3 - \mu$         | $\frac{2P_S^0}{\mu-3} t_F^{\mu-1}$  |
|        | $2 + 2\nu - 2\mu$ | $\left(\frac{(2\mu-4)\Gamma^2(2-\mu)}{\Gamma^2(2-\nu)\Gamma(3-2\mu+2\nu)}\right) t_F^{2\mu-2} t_S^{2-2\nu}$   |



Table A.4: Anomalous diffusion results for asymmetric random walks ( $v_{\text{ave}} = p_r v_r - p_l v_l \neq 0$ ),  $\sigma^2 \sim Ct^\gamma + C't^{\gamma'}$ . For each region shown in Fig. A.1, the terms for  $\sigma^2$  have been calculated to second order. For an explanation on how to use this table, see caption for Table A.2.

| Region          | exponent $\gamma$ | coefficient $C$  |
|-----------------|-------------------|--|
| I               | 1                 | $[\frac{\langle t_f \rangle^2 (\langle t_s^2 \rangle + \langle t_f^2 \rangle) - 2 \langle t_f \rangle^2 \langle t_s \rangle^2}{T^3}] v_{\text{ave}}^2 + \frac{\langle t_f^2 \rangle}{T} [v_{\text{rms}}^2 - \frac{2 \langle t_f \rangle}{T} v_{\text{ave}}^2]$   |
|                 | $4 - \mu$         | $\frac{2}{(4-\mu)(3-\mu)} [(\frac{-(T+\langle t_s \rangle) \langle t_f \rangle}{T^2}) v_{\text{ave}}^2 + v_{\text{rms}}^2] (\frac{t_F^{\mu-1}}{T})$  |
|                 | $4 - \nu$         | $\frac{2}{(4-\nu)(3-\nu)} (\frac{t_S^{\nu-1} \langle t_f \rangle^2}{T^3}) v_{\text{ave}}^2$  |
|                 | $6 - 2\mu$        | $(\frac{2\Gamma(3-\mu)\Gamma(2-\mu)}{\Gamma(7-2\mu)}) (\frac{t_F^{2\mu-2}}{T^2}) [\frac{\langle t_f \rangle - \langle t_s \rangle}{T} v_{\text{ave}}^2 - v_{\text{rms}}^2] + (\frac{t_F^{2\mu-2}}{T^4}) \Gamma^2(2-\mu) [\frac{2\langle t_s \rangle^2 - 4\langle t_f \rangle \langle t_s \rangle}{\Gamma(7-2\mu)} - \frac{\langle t_s \rangle^2}{\Gamma^2(4-\mu)}] v_{\text{ave}}^2$   |
|                 | $6 - 2\nu$        | $(\frac{\Gamma^2(2-\nu)(6\Gamma^2(4-\nu) - \Gamma(7-2\nu))}{\Gamma(7-2\nu)\Gamma^2(4-\nu)}) (\frac{\langle t_f \rangle^2 t_S^{2\nu-2}}{T^4}) v_{\text{ave}}^2$   |
|                 | 0                 | $[(\frac{\langle t_f^2 \rangle}{2T^2}) (\langle t_f^2 \rangle + \langle t_s^2 \rangle + 2\langle t_s \rangle (P_F^0 \langle t_f \rangle - P_S^0 \langle t_s \rangle)) - \frac{4\langle t_f^3 \rangle}{3T}] v_{\text{rms}}^2 + (\frac{4}{3T^3}) \langle t_f^3 \rangle \langle t_f \rangle (T + \langle t_s \rangle) v_{\text{ave}}^2 + (\frac{4}{3T^3}) \langle t_s^3 \rangle \langle t_f \rangle^2 v_{\text{ave}}^2 + (\frac{\langle t_f^2 \rangle^2}{4T^4}) (3\langle t_s \rangle^2 - 4\langle t_f \rangle \langle t_s \rangle - 2\langle t_f \rangle^2) v_{\text{ave}}^2 + (\frac{5\langle t_s^2 \rangle \langle t_f \rangle}{4T^4}) (\langle t_s^2 \rangle \langle t_f \rangle - 2\langle t_f^2 \rangle \langle t_s \rangle) v_{\text{ave}}^2 + (\frac{-P_F^0 \langle t_f \rangle^2}{T^4}) [\langle t_f^2 \rangle \langle t_s \rangle (\langle t_f \rangle + 3\langle t_s \rangle) + \langle t_f \rangle^2 \langle t_s^2 \rangle] v_{\text{ave}}^2 + (\frac{\langle t_f \rangle \langle t_s \rangle}{T^4}) [\langle t_f \rangle \langle t_s \rangle (\langle t_f \rangle^2 - 4\langle t_f \rangle \langle t_s \rangle - \langle t_s^2 \rangle) + 3\langle t_f^2 \rangle \langle t_s \rangle^2 + 3\langle t_f \rangle^2 \langle t_s^2 \rangle] v_{\text{ave}}^2 - (\frac{(P_S^0)^2 \langle t_s \rangle^2 \langle t_f \rangle^2}{T^2}) v_{\text{ave}}^2 + (\frac{P_S^0 \langle t_f \rangle}{T^4}) [2\langle t_s \rangle^3 (\langle t_f \rangle^2 + \langle t_f^2 \rangle) + \langle t_f \rangle^2 \langle t_s^2 \rangle \langle t_s \rangle + 2\langle t_f \rangle \langle t_s \rangle^4] v_{\text{ave}}^2$ |
|                 | II                | 2  |
| $\mu$           |                   | $(\frac{2}{\Gamma(2-\mu)\Gamma(1+\mu)}) [(\mu-1)t_F + (\mu-2)\langle t_s \rangle] t_F^{1-\mu} (v_{\text{rms}}^2 - v_{\text{ave}}^2)$   |
| $2 + \mu - \nu$ |                   | $(\frac{2\Gamma(2-\nu)}{\Gamma(2-\mu)\Gamma(3+\mu-\nu)}) [(4-\mu-\nu)v_{\text{ave}}^2 + (\mu-2)v_{\text{rms}}^2] t_F^{1-\mu} t_S^{\nu-1}$  |
| III             | $2\nu - 2$        | $(\frac{2\Gamma^2(\nu) - \Gamma(2\nu-1)}{\Gamma^2(2-\nu)\Gamma^2(\nu)\Gamma(2\nu-1)}) \langle t_f \rangle^2 t_S^{2-2\nu} v_{\text{ave}}^2$   |
|                 | $2 + \nu - \mu$   | $(\frac{2\Gamma(3-\mu)}{\Gamma(2-\nu)\Gamma(3-\mu+\nu)}) t_F^{\mu-1} t_S^{1-\nu} v_{\text{rms}}^2$   |
|                 | $3\nu - 4$        | $(\frac{[2\Gamma(3\nu-3) - 4\Gamma(\nu)\Gamma(2\nu-2)] [(2-\nu)\langle t_f \rangle + (1-\nu)\langle t_s \rangle]}{\Gamma(3-\nu)\Gamma^2(2-\nu)\Gamma(\nu)\Gamma(2\nu-2)\Gamma(3\nu-3)}) \langle t_f \rangle^2 t_S^{3-3\nu} v_{\text{ave}}^2$   |
|                 | $\nu - 1$         | $(\frac{1}{\Gamma(2-\nu)\Gamma(\nu)}) [-\langle t_f \rangle^2 v_{\text{ave}}^2 + \langle t_f^2 \rangle v_{\text{rms}}^2] t_S^{1-\nu}$  |
|                 | $3 - \mu$         | $\frac{2P_S^0 t_F^{\mu-1} v_{\text{rms}}^2}{\mu-3}$  |
|                 | $2 + 2\nu - 2\mu$ | $(\frac{\Gamma^2(2-\mu)((2\mu-2)\Gamma^2(2-\mu+\nu) - \Gamma(3-2\mu+2\nu))}{\Gamma^2(2-\nu)\Gamma^2(2-\mu+\nu)\Gamma^2(3-2\mu+2\nu)}) t_F^{2\mu-2} t_S^{2-2\nu} v_{\text{ave}}^2 - (\frac{2(2-\mu)\Gamma^2(2-\mu)}{\Gamma^2(2-\nu)\Gamma(3-2\mu+2\nu)}) t_F^{2\mu-2} t_S^{2-2\nu} v_{\text{rms}}^2$  |

# Appendix B

## Software documentation

This appendix documents several useful software programs that have been developed in the past five years. All of these programs work using command line options, and for all programs the **-h** option gives a brief help message and a listing of all command line options. The source code for all software discussed in this Appendix can be found on the World Wide Web at the address <http://chaos.ph.utexas.edu/~weeks/thesis/thesis.html>.

### B.1 Ultrasound Data Acquisition

For a conceptual description of the ultrasound programs, see Sec. 2.6. Two programs are needed to operate the ultrasound system, one to operate the Matec system via a GPIB interface and one to read in data from the WAAG II data acquisition card.

#### B.1.1 Matec controller software

The program which sets the parameters for the Matec MBS-8000 system using the GPIB interface is called **matec**. The GPIB bus is accessed through a National Instruments GPIB-PC2A card. The GPIB board is configured with an address of

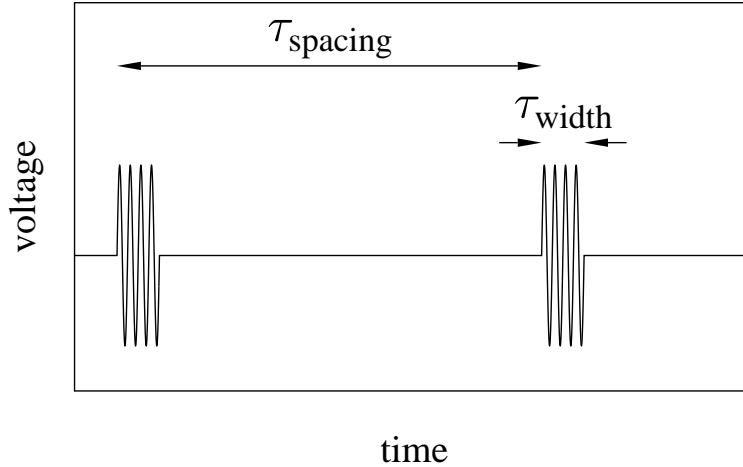


Figure B.1: Schematic view of ultrasound pulses generated by Matec system.

2E1 (hex) using DMA channel 3. The Matec bus address is 11. This program works by giving six numbers on the command line, i.e. **matec 40 0 30 130 0 0**. We will refer to these six numbers as  $A, B, C, D, E$ , and  $F$ .  $A$  and  $B$  set the intra-pulse interval (called  $\tau_{\text{spacing}}$  in Sec. 2.6), by

$$\tau_{\text{spacing}} = A \times 100 \times 10^B \times (1/f) \quad (\text{B.1})$$

where  $f$  is the frequency of the ultrasound (see Fig. B.1).  $C$  sets the number of cycles per pulse, thus  $\tau_{\text{width}} = C/f$ .  $D$  is the pre-amplifier gain in units of 0.5 dB;  $D$  can be set between 0 and 190, and values over 190 are set to 95 dB.  $E$  may be selecting a filter, although it may also be an obsolete variable; we always use  $E = 0$ .  $F$  is a switch for turning on ( $F = 128$ ) or off ( $F = 0$ ) the gated amplifier; we always use  $F = 0$ .

For the GPIB bus to work, the file “GPIB.COM” should be in the directory **C:\**, and the statement **DEVICE=C:\GPIB.COM** must be in the “config.sys” file of the computer.

Note that at low gain values ( $D < 96$ ), the Matec system we have does not always set the gain correctly. Some of the relays may be broken or working poorly;

the actual gain does not increase monotonically as  $D$  is increased. Above  $D = 96$  this is no longer a problem, although a step change in  $D$  does not always increase precisely 0.5 dB.

### B.1.2 Data acquisition software

The ultrasound data acquisition was originally written by Paul Umbanhowar. This program has been modified in several ways: the ability to use command-line options to set parameters, the ability to use the internal WAAG clock or an external clock as desired, and an improvement in the algorithm which determines velocities from the raw data. The program works with a Markenrich WAAG II data acquisition card, and is currently running on a 486 computer.

The output of the program is groups of six floating point numbers (4 bytes each). They are the position (in cm), velocity  $v$  (in cm/s), uncertainty  $\Delta v$ , the  $\chi^2$  of the line fit to the data which determines the velocity, the amplitude of the pulse (in V), and the time stamp (in seconds since the program began).

This program has several command line options:

- h:** Provides a list of all command line options and a terse description of their use.
- o:** Allows the user to specify a file name to store the data in. The default file name is "blah.out". Currently our naming scheme is to use the prefix "us", the date, and then a number for the file suffix, i.e., "-o us041097.001" is the first file created on April 10, 1997.
- n:** Number of data points to read in. After the program has read this much data, it will exit. (Actually, the program typically reads in a few more data points past this point.)
- v:** Number of reflection groups  $N$  to read to determine the velocity. Increasing this number improves the velocity measurement, but runs the risk that the

particle isn't visible in each reflection group. Decreasing this number results in a less accurate velocity determination. Typically 8-12 is good.

- f**: The frequency of the RF signal, in MHz. This allows the program to calculate the velocity, and also aids in recognizing pulses.
- p**: Number of pulses between each ultrasound burst. This is the same number as *A* for the **matec** program.
- l**: Pulse length. This is the same number as *C* for the **matec** program.
- R**: This option lets you save the raw data, rather than the velocity information. However, it only saves one measurement (that is, one set of reflections). When used, the output has the velocity data at the top, then a line of large numbers ( $9 \times 10^9$ ), then the raw data. The raw data has six columns: channel a, channel b, amplitude, phase angle (radians), data number, and time stamp. This option was used to create the figures for Sec. 2.6 and can be used for error checking.
- t**: Set the trigger level for the WAAG II card. It is not clear that the trigger level makes much difference. “-t 0” is negative full scale, “-t 255” is positive full scale.
- C**: This option switches between the external clock and the internal 2 MHz clock. This is the data digitization rate. The WAAG card can only take  $2^{16}$  data points (per channel), so  $(\tau_{\text{spacing}} \times N \times f_{\text{clock}}) < 2^{16}$  is required. (Recall *N* is set by the -v option.)
- d**: Set the delay from the clock signal box (Sec. 2.6.4), in units of  $1/f_{\text{clock}}$ . Only used if the external clock is used; this helps the program correctly determine the position of particles.

**-s:** The number of samples in the window set by the clock signal box (Sec. 2.6.4), in units of  $1/f_{\text{clock}}$ . Again, this is only used if the external clock is used.

The defaults for the program can be seen by using the **-h** option, and can be changed by modifying and recompiling the program.

## B.2 Hot Film Probe Data Acquisition

The hot film probe data acquisition program is called **adscan**, as it scans the analog-to-digital inputs of the National Instruments AT-MIO-16 board. The program was originally written by Muhammad Shazad Pervez, but the source code was lost. Muhammad Ali Bawany wrote the next version, and added many improvements. Most recently Eshel Faraggi has added in the ability to control a multiplexer circuit to the program.

This program has many command line options that allow the program to do merely simple data acquisition, or in addition allow the program to control the flow rate. The command line options are:

- h:** Provides a list of all command line options and a terse description of their use.
- s:** The number of samples to take. Typically this is chosen to allow the data to be Fast Fourier Transformed, i.e., a power of 2.
- r:** Sample rate for data acquisition.
- n:** Number of channels to acquire. The total number of data points taken, set by  $(\text{number of samples}) \times (\text{number of channels})$ , must be less than or equal to 65536. For the version of **adscan** using the multiplexer, only one A/D channel is actually read; the successive measurements are interpreted as different channels. This option is not needed when using the multiplexer version.

- m:** Number of multiplexer channels to acquire. As with the **-n** option, the total number of points must be less than 65536. The program steps through the multiplexer channels and once all channels have been read, a reset signal is sent to the multiplexer. In this way, from 1 to 8 multiplexer channels can be read. In the future, it would be possible to add in a second analog multiplexer chip and slightly rewire the counter chip to increase the maximum possible number of channels to 16.
- p:** Gate pulse duration. The program reads digital pulses to find a frequency (for the rotary encoder beneath the annulus used to find the rotation rate of the annulus, or the pulses coming from the flow meter). These pulses are measured for a set duration, and then the frequency is determined based on the count of pulses. **-p** sets this duration.
- ct:** The flow rate required, if a constant flow rate is desired. The program produces an output voltage which is used to control the pump motor, and this voltage is adjusted if the measured flow rate is different from the desired flow rate. **-ct** is set using the flow rate in cm/s; the program converts from the flow meter frequency to flow rate.
- stv:** This is the starting voltage for the pump motor control voltage. Typical usage for pump control is described below.
- inc:** When using pump control, the output voltage is adjusted in small steps. This option sets the step size in units of bits. As the output voltage can vary from -10-10 V, with 12 bits of resolution, each bit is 0.005 V. Setting this option small results in small changes; larger values allow faster response time for the program, but can result in over-compensation.
- rf:** Specify a flow rate file. This option is used instead of the **-ct** option. A flow rate file consists of pairs of points (data point number,flow rate). The first

coordinate is equivalent to the time by (time in seconds  $\times$  data acquisition rate in Hz = data point number). The program then interpolates linearly between pairs of data points to determine the target flow rate at any given instant. This moving target then is used as the basis for the pump control voltage. If the file contains an entry (-1,-1), the flow is held constant at the last previous flow rate given in the file; the (-1,-1) is used to signal the end of the flow rate file.

The files to save the data in must be specified by providing a file suffix on the command line at the end. The file suffix must be at most six characters (plus the standard 3 character MS-DOS file extension). **adscan** then prepends a prefix indicating which data is in a given file. Files begin with "t0," "t1," etc., for the 0th, 1st, and subsequent channels. A special file beginning with "tf" contains the frequency information read by the data acquisition program, typically the frequency of the pulses from the flow meter. This frequency could also be the frequency of pulses from the rotary encoder beneath the annulus. Our naming scheme is to use the date with a version number, thus "t1041097.002" is the second data file taken for channel 1 on April 10, 1997.

Typically **adscan** is used to keep the pump rate constant. One small "feature" of the National Instruments driver software is that the output voltage of the AT-MIO-16 card temporarily drops to zero when the board is reinitialized, that is, at the beginning of the program. We have found the best way to control the pump is to 1) determine the proper starting voltage by turning the knob on the manual pump control box and checking the flow rate; 2) using this starting voltage as the argument for the -stv to **adscan**; 3) starting **adscan** and waiting a few seconds, until a beep is heard on the computer signalling the initialization of the AT-MIO-16 is complete; and 4) switching the pump control box from manual control to computer control. In this way the signal sent to the pump is steady. When exiting, **adscan**



prints the last value of the control voltage, which can be used to specify the next value for `-stv`.

### B.3 Stream Function Programs

There are several programs which work together to process the raw data and then generate stream function pictures.

The first program is **filter2dat**. This program takes data in the form (time stamp,  $\theta$ ,  $r$ ,  $u_\theta$ ,  $u_r$ ) and produces output in the same form. This program interpolates the data onto an evenly spaced mesh (evenly spaced in  $(x, y)$  coordinates rather than  $(r, \theta)$ ). There is one command line option, **-n**. This option sets the number of grid points used to cover the flow domain. The output from the **filter2dat** program should be inspected to make sure that the flow domain is reasonably evenly covered with data. For example, plotting a dot at the second and third coordinates for all of the data should show a grid of dots that cover almost all of the flow domain<sup>1</sup>. If this is not the case, the number of grid points should be decreased, or more raw data obtained.

The second program is **dat2amp**, designed to take the velocity data and find the amplitudes of the basis functions for the stream function. This is the program that does the least squares calculation described in Sec. 2.4. This program has several command line options:

- h**: A help message listing all options.
  
- t**: Set the number of azimuthal basis functions. (See Sec. 2.4 for details of basis functions.)
  
- r**: Set the number of radial basis functions.

---

<sup>1</sup>On the computer 'maytag', this could be done with the command **filter2dat veldata | field 2 3 | plot | newworm**.

- m**: Set the maximum value of  $r$  (default is 43.2 cm).
- n**: Set the minimum value of  $r$  (default is 10.8 cm). If experiments are done with the inner barrier, such as described in Chap. 4, then this value might be changed.

The input of this program is in the form (time stamp,  $\theta$ ,  $r$ ,  $u_\theta$ ,  $u_r$ ), although the first column is ignored. This program can use the data from **filter2dat**, although it can also use the raw data fed into **filter2dat**. See Sec. 2.4.3 for a discussion of the subtleties; results are better when **filter2dat** is used to pre-process the data. The output from **dat2amp** has  $r_{\min}$  on the first line,  $r_{\max}$  on the second line, and then a listing of the coefficients in the form  $(m, n, l, C_{mnl})$ , corresponding to the indices discussed in Sec. 2.4.

Several additional programs (discussed below) take the coefficients from **dat2amp** and convert them into usable forms such as contour plots of the stream function. If desired, the output from **dat2amp** can be filtered, for example only using coefficients with  $|C_{mnl}| > \epsilon$  for some threshold  $\epsilon$ . Also, by examining the magnitudes of the coefficients, the proper number of basis functions to use for **dat2amp** can be determined.

The most useful two programs are **amp2con** and **amp2nat** (the latter named for obscure historical reasons). These programs take the basis function amplitudes produced by **dat2amp** and produce PostScript contour plots. **amp2con** is the simpler of the two programs and is somewhat obsolete; **amp2nat** was designed to create Fig. 5.3 and has more features. The default options of **amp2nat** are designed specifically for the two data sets shown in Fig. 5.3, but can be modified as necessary. Also, **amp2nat** draws in some topography information. This program should probably be revised to allow the user to turn off the topography information for cases when it is not needed. The program is extensively commented and should not be difficult to modify.

The algorithm used by the program is to partition the stream function domain into an  $N \times N$  grid; the stream function is initially calculated on all points of this grid. (Portions of this grid outside the annular flow domain are excluded from this calculation and all subsequent calculations.) Then, each square region with four grid points at the corners is examined (see Fig. B.2). The program determines if a contour line should pass through this square region (if at least one grid point has  $\psi(x, y) > \psi_n$  and at least one has  $\psi(x, y) < \psi_n$ , where  $\psi_n = n\psi_0$  is a multiple of some fixed contour spacing). If so, the program partitions that square region into four smaller square regions, and determines which of these squares the contour lines go through. This process is repeated recursively for several levels until the contour line is drawn through the smallest sized square region in a simple fashion (Fig. B.2(d)). Although all contour lines are drawn at a multiple of  $45^\circ$  to each other, by allowing the initial grid point spacing to be small and the recursion to continue for several levels, smooth-appearing curves are drawn.

Both **amp2con** and **amp2nat** have the following command line options:

- h:** A help message listing all options.
- n:** Set the initial spacing for contours (the value of  $N$  above). This should typically be 200–400; lower values can result in the need for two contour lines to pass through one initial square region, which causes problems. Higher values will work but are usually unnecessary.
- z:** Sets the level of recursion. In Fig. B.2 four levels of recursion are shown. The higher  $N$  is (set by -n), the lower the recursion level is needed.
- c:** The number of contours to use; the contour level spacing  $\psi_0$  is adjusted automatically.
- l:** The value of  $\psi_0$  (overrides the -c option). This is preferred when comparing several stream function pictures and they all need the same contour spacing.

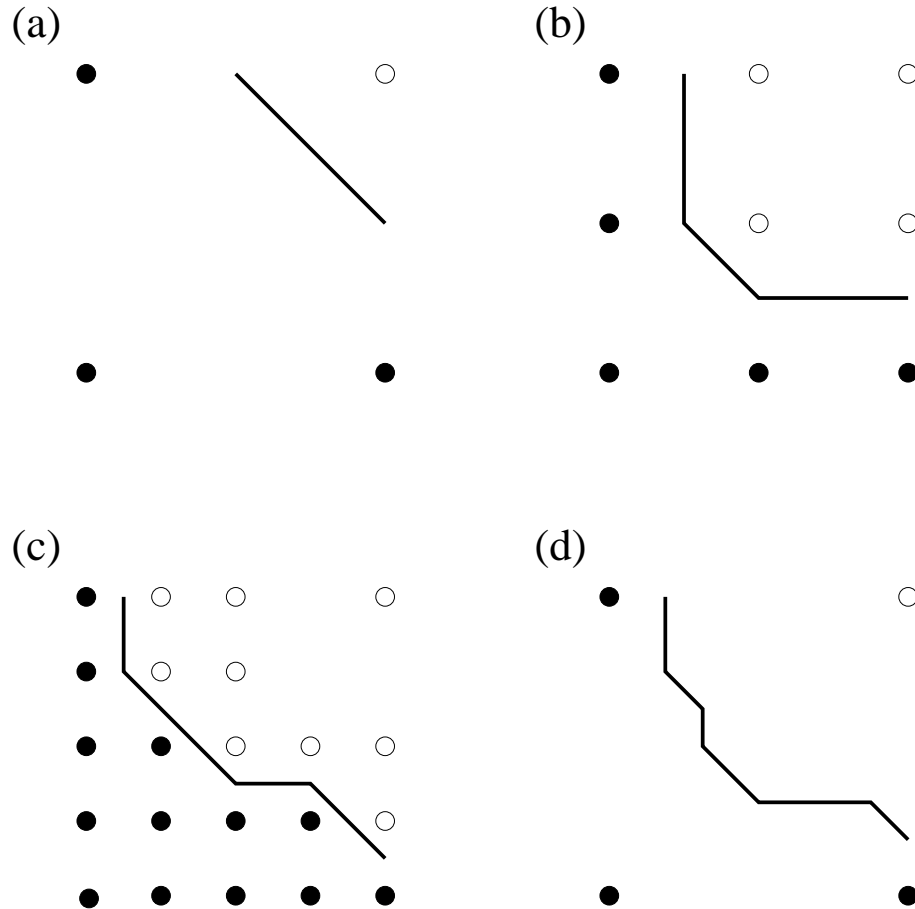


Figure B.2: Partitioning scheme to draw contours for the programs **amp2con** and **amp2nat**. Points colored black are “below” the contour level, and white points are “above.” The recursion is continued until the contour lines are suitably high resolution; see the text.

The default of automatic spacing (adjustable by the `-c` option) would be more useful for a quick qualitative picture.

- A:** Using the `-A` option prints a picture without an annulus outline around it.
- I:** Using the `-I` option toggles the usage of the inner barrier (used in the experiments described in Chap. 4). Normally the inner barrier should not be used.
- L:** This option can be used to change the linewidth of the contour lines.

In addition, the program **amp2nat** has extra command line options. Primarily these command line options are used to generate a figure with two stream functions on the same page (discussed further below).

- N:** This option sets which stream function is being drawn, “1” or “2”. This affects page positioning and also the generation of the PostScript headers.
- m:** Change the orientation of stream function “1.” This is relative to a fixed position on the annulus, i.e., the crest of the topographic ridges for Chap. 5. In particular, this should be the angle that the mountain peak is located at in the reference frame of the raw data. Typical procedure would be to place an LED over the mountain crest in the annulus, then find the angular location of this LED in the reference frame co-rotating with the annulus. This angle is the value to give to the `-m` option.
- M:** Change the orientation of stream function “2.”
- O:** Use only one mountain. This makes the resulting figure fill the entire page rather than leaving room for a second stream function, and prints a complete set of PostScript headers.

- T**: This prints the two stream functions side by side rather than one above the other.
- E**: Normally the symbols “H” and “L” are printed to indicate the highs and lows of the stream function. The -E option turns this feature off.
- e**: This sets the window size for scanning for highs and lows. A local extremum point of  $\psi(x, y)$  must be larger (or smaller) than all nearby grid points within this window radius. Increasing this value typically reduces the number of H’s and L’s that are printed.

To produce two stream functions on the same page, the output of **amp2nat** using the -N1 option can be placed in a file, and the output using -N2 appended to that file.

A third program, **amp2ppm** makes color pictures of stream functions, in PPM format<sup>2</sup>. This program only makes one picture at a time; it cannot be used to make a multiple part figure, although other standard programs such as **xv** which can read PPM format might be useful. The program uses the output from **dat2amp** as input, and the output is the PPM file. The following command line options are available:

- h**: A help message listing all options.
- n**: Width of picture, in pixels.
- i**: Invert color scheme (exchange red and blue ends of the spectrum).
- c**: Adds in contours with a given spacing (spacing set with this option).
- e**: Sets the width of the contours, in pixels; only useful if the -c option is also used.

---

<sup>2</sup>The PPM (Portable Pixel Map) format is a standard graphics format, described at <http://chaos.ph.utexas.edu/~weeks/graphics/mkppm.html>.

- m**: This option puts in outlines indicating where the mountains are positioned; the location of the mountains is specified similar to the -m option for the **amp2nat** program.
- M**: This option puts in a bold dashed line at the mountain crest location, similarly to -m.
- z**: Adds a white border around the edges of the picture. The width of this border in pixels is specified by -z.
- B**: Makes a black and white picture rather than a color picture.
- R**: Rotates the resulting picture 90°.
- C**: Prints a color bar at the side of the picture.

The next program, **amp2slip**, shows the problems caused by the lack of a zero-slip boundary condition imposed at the walls. This program calculates  $u_\theta(r, \theta)$  for  $r = r_{\text{inner}}$  and  $r = r_{\text{outer}}$ , or at an arbitrary radius. Typical results are shown in Fig. B.3. Ideally this should be a constant; due to a lack of data, especially near the outer and inner walls, the velocity is poorly determined near the walls and does not go to a constant.

This program has two command line options. The -n option specifies how many different values of  $\theta$  are calculated (with a default of 1000; usually there is no need to change this value). The -r option specifies the value of  $r$  to use. The default is to print out three columns,  $(\theta, u_\theta(r_{\text{inner}}, \theta), u_\theta(r_{\text{outer}}))$ .

The last program is **amp2base**. This program is used to extract radial velocity profiles. The output is  $(r, u_\theta(r, \theta))$  for a specific (user-chosen) value of  $\theta$ . The command line options are:

- h**: A help message listing all options.

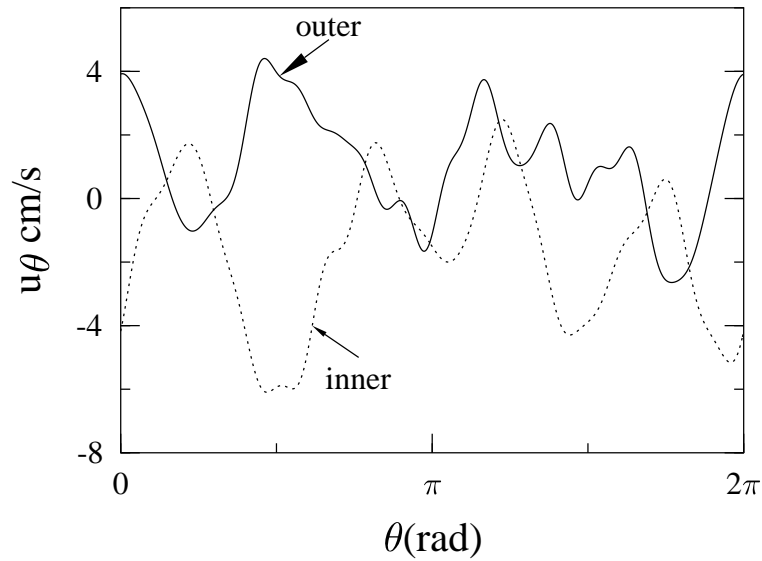


Figure B.3: Azimuthal velocity at outer wall (solid line) and inner wall (dashed line). Due to insufficient data, the velocity does not go to a constant at the walls. These data correspond to Fig. 5.3(b), the blocked flow.

- d: Print the velocity, rather than the stream function value.
- n: Number of radial points to print out.
- r: Print a radial slice at the specified angular location (in degrees). If the -r option is not used, the output is the azimuthally averaged velocity profile (see Fig. 5.4) which may be a more useful way to use this program, and is the default behavior.

The output of this program for the blocked and zonal flows of Fig. 5.3 is shown in Fig. 5.4.



# Bibliography

- [1] V. V. Afanasiev, R. Z. Sagdeev, G. M. Zaslavsky, Chaotic jets with multifractal space-time random walk, *Chaos* **1**, 143 (1991).
- [2] H. L. Anderson, Ed., *A Physicist's Desk Reference: The Second Edition of Physics Vade Mecum* (American Institute of Physics, New York, NY 1989), p. 57.
- [3] H. Aref, Stirring by chaotic advection, *J. Fluid Mech.* **143**, 1 (1984).
- [4] F. Bardou, J. P. Bouchaud, O. Omile, A. Aspect, C. Cohen-Tannoudji, Subrecoil laser cooling and Lévy flights, *Phys. Rev. Lett.* **72**, 203 (1994).
- [5] G. K. Batchelor, Computation of the energy spectrum in homogeneous two-dimensional turbulence, *Phys. Fluids Suppl.* **12**, II-233 (1969).
- [6] R. P. Behringer, S. D. Meyers, H. L. Swinney, Chaos and mixing in a geostrophic flow, *Phys. Fluids A* **3**, 1243 (1991).
- [7] R. Benzi, B. Saltzman, A. C. Wiin-Nielsen, (Eds.), *Anomalous Atmospheric Flows and Blocking*, *Adv. Geophys.* **29** (Academic Press, Orlando, 1986).
- [8] R. Benzi, P. Malguzzi, A. Speranza, A. Sutera, The statistical properties of general atmospheric circulation: observational evidence and a minimal theory bimodality, *Quart. J. Roy. Meteor. Soc.* **112**, 661 (1986).

- [9] R. Benzi, G. Paladin, A. Vulpiani, Power spectra in two-dimensional turbulence, *Phys. Rev. A* **42**, 3654 (1990).
- [10] P. Bernardet, A. Butet, M. Déqué, M. Ghil, R. L. Pfeffer, Low-frequency oscillations in a rotating annulus with topography, *J. Atmos. Sci.* **47**, 3023 (1990).
- [11] N. F. Bondarenko, M. Z. Gak, F. V. Dolzhanskiy, *Izvestiya, Atmospheric and Oceanic Physics* **15**, 711 (1979).
- [12] V. Borue, Spectral exponents of enstrophy cascade in stationary two-dimensional homogeneous turbulence, *Phys. Rev. Lett.* **71**, 3967 (1993); Inverse energy cascade in stationary two-dimensional homogeneous turbulence, *Phys. Rev. Lett.* **72**, 1475 (1994).
- [13] J. P. Bouchaud and A. Georges, Anomalous diffusion in disordered media: statistical mechanisms, models and physical applications, *Phys. Rep.* **195**, 127 (1990).
- [14] J. P. Bouchaud, A. Ott, D. Langevin, W. Urbach, Anomalous diffusion in elongated micelles and its Lévy flight interpretation, *J. Phys. II* **1**, 1465 (1991).
- [15] V. M. Canuto and M. S. Dubovikov, Physical regimes and dimensional structure of rotating turbulence, *Phys. Rev. Lett.* **78**, 666 (1997).
- [16] O. Cardoso and P. Tabeling, Anomalous diffusion in a linear array of vortices, *Europhys. Lett.* **7**, 225 (1988).
- [17] O. Cardoso and P. Tabeling, Anomalous diffusion in a linear system of vortices, *Eur. J. Mech. B/Fluids* **8**, 459 (1989).
- [18] O. Cardoso, D. Marteau, P. Tabeling, Quantitative experimental study of the free decay of quasi-two-dimensional turbulence, *Phys. Rev. E* **49**, 454 (1994).

- [19] O. Cardoso, B. Gluckmann, O. Parcollet, P. Tabeling, Dispersion in a quasi-two-dimensional-turbulent flow: An experimental study, *Phys. Fluids* **8**, 209 (1996).
- [20] G. Carey, private communication (1996).
- [21] G. F. Carnevale, J. C. McWilliams, Y. Pomeau, J. B. Weiss, W. R. Young, Evolution of vortex statistics in two-dimensional turbulence, *Phys. Rev. Lett.* **66**, 2735 (1991); G. F. Carnevale, J. C. McWilliams, Y. Pomeau, J. B. Weiss, W. R. Young, Rates, pathways, and end states of nonlinear evolution in decaying two-dimensional turbulence: scaling theory versus selective decay, *Phys. Fluids A* **4**, 1314 (1992).
- [22] G. F. Carnevale, R. C. Kloosterziel, G. J. F. van Heijst, Propagation of barotropic vortices over topography in a rotating tank, *J. Fluid Mech.* **233**, 119 (1991)
- [23] J. G. Charney, The dynamics of long waves in a baroclinic westerly current, *J. Meteorol.* **4**, 135 (1947).
- [24] J. G. Charney and J. G. DeVore, Multiple flow equilibria in the atmosphere and blocking, *J. Atmos. Sci.* **36**, 1205 (1979).
- [25] X. Cheng and J. M. Wallace, Cluster analysis of the Northern Hemisphere wintertime 500-hPa height field: Spatial patterns, *J. Atmos. Sci.* **50**, 2674 (1993).
- [26] A. A. Chernikov, B. A. Petrovichev, A. V. Rogal'sky, R. Z. Sagdeev, G. M. Zaslavsky, Anomalous transport of streamlines due to their chaos and their spatial topology, *Phys. Lett. A* **144**, 127 (1990).
- [27] D. A. Christensen, *Ultrasonic Bioinstrumentation*, (John Wiley & Sons, Inc., New York, 1988).

- [28] A. Colin de Verdiere, Quasi-geostrophic turbulence in a rotating homogeneous fluid, *Geophys. Astrophys. Fluid Dynamics* **15**, 213 (1980).
- [29] Y. Couder and C. Basdevant, Experimental and numerical study of vortex couples in two-dimensional flows, *J. Fluid Mech.* **173**, 225 (1986).
- [30] B. Cushman-Roisin, *Introduction to Geophysical Fluid Dynamics*, (Prentice-Hall, Inc., New Jersey, 1994).
- [31] D. del Castillo Negrete, Dynamics and transport in rotating fluids and transition to chaos in area preserving nontwist maps, Ph.D. thesis, University of Texas at Austin (1994).
- [32] D. del-Castillo-Negrete and P. J. Morrison, Chaotic transport by Rossby waves in shear flow, *Phys. Fluids A* **5**, 948 (1993).
- [33] D. del-Castillo-Negrete, Asymmetric transport and non-Gaussian statistics of passive scalars in vortices in shear, submitted to *Phys. Fluids* (1997).
- [34] S. C. Dickinson and R. L. Long, Oscillating-grid turbulence including effects of rotation, *J. Fluid Mech.* **126**, 315 (1983).
- [35] R. M. Dole and N. M. Gordon, Persistent anomalies of the extratropical Northern hemisphere winter time circulation: geographical distribution and regional persistence characteristics, *Mon. Wea. Rev.* **111**, 1567 (1983).
- [36] D. G. Dritschel, Vortex properties of two-dimensional turbulence, *Phys. Fluids A* **5**, 984 (1993).
- [37] E. T. Eady, Long waves and cyclone waves, *Tellus* **1**, 33 (1949).
- [38] A. Einstein, Über die von der molekularkinetischen Theorie der Wärme geforderte Bewegung von in ruhenden Flüssigkeiten suspendierten Teilchen, *Annalen der Physik* **17**, 549 (1905) 549.

- [39] S. Elghobashi and G. C. Truesdell, Direct simulation of particle dispersion in a decaying isotropic turbulence, *J. Fluid Mech.* **242**, 655 (1992).
- [40] G. Falkovich and V. Lebedev, Nonlocal vorticity cascade in two dimensions, *Phys. Rev. E* **49**, R1800 (1994).
- [41] W. Feller, *An Introduction to Probability Theory and Its Applications*, (John Wiley & Sons Inc., New York, 1966) Vol. 2, Chap XVI.8, p. 525.
- [42] U. Frisch, *Turbulence: The Legacy of A. N. Kolmogorov*, (Cambridge University Press, Cambridge, 1995).
- [43] T. Geisel and S. Thomae, Anomalous diffusion in intermittent chaotic systems, *Phys. Rev. Lett.* **52**, 1936 (1984).
- [44] T. Geisel, J. Nierwetberg, A. Zacherl, Accelerated diffusion in Josephson Junctions and related chaotic systems, *Phys. Rev. Lett.* **54**, 616 (1985).
- [45] T. Geisel, A. Zacherl, G. Radons, Generic 1/f noise in chaotic Hamiltonian dynamics, *Phys. Rev. Lett.* **59**, 2503 (1987).
- [46] T. Geisel, A. Zacherl, G. Radons, Chaotic diffusion and 1/f-noise of particles in two-dimensional solids, *Z. Phys. B - Condensed Matter* **71**, 117 (1988).
- [47] M. Gharib and P. Derango, A liquid film (soap film) tunnel to study two-dimensional laminar and turbulent shear flows, *Physica D* **37**, 406 (1989).
- [48] M. Ghil and S. Childress, *Topics in Geophysical Fluid Dynamics: Atmospheric Dynamics, Dynamo Theory, and Climate Dynamics* (Springer-Verlag, New York, 1987).
- [49] R. N. Ghosh and W. W. Webb, Automated detection and tracking of individual and clustered cell surface low density lipoprotein receptor molecules, *Biophys. J.* **66**, 1301 (1994).

- [50] A. E. Gill, *Atmosphere-Ocean Dynamics* (Academic Press, San Diego, 1982).
- [51] G. J. Haltiner and R. T. Williams, *Numerical Prediction and Dynamic Meteorology*, 2nd ed. (J. Wiley, New York, 1980).
- [52] I. M. Held, Stationary and quasi-stationary eddies in the extratropical troposphere: Theory, in *Large-Scale Dynamical Processes in the Atmosphere*, eds. B. J. Hoskins and R. P. Pearce, (Academic Press, London, 1983) pp. 127-168.
- [53] R. Hide, An experimental study of thermal convection in a rotating liquid, *Philos. Trans. R. Soc.* **A250**, 442 (1958).
- [54] R. Hide, A. Ibbetson, M. J. Lighthill, On slow transverse flow past obstacles in a rapidly rotating fluid, *J. Fluid Mech.* **32**, 251 (1968).
- [55] J. O. Hinze, *Turbulence* (McGraw-Hill, New York, 1959).
- [56] J. R. Holton, *An Introduction to Dynamic Meteorology* (3rd ed.) (Academic Press, San Diego, 1992).
- [57] E. J. Hopfinger, F. K. Browand, Y. Gagne, Turbulence and waves in a rotating tank, *J. Fluid Mech.* **125**, 505 (1982).
- [58] E. J. Hopfinger, Turbulence and vortices in rotating fluids, in *Theoretical and Applied Mechanics*, eds. P. Germain, M. Piau and D. Callerie (Elsevier, North-Holland, 1989) 117-138.
- [59] J. D. Horel and C. R. Mechoso, Observed and simulated intraseasonal variability of the wintertime planetary circulation, *J. Clim.* **1**, 582 (1988).
- [60] B. J. Hoskins and D. J. Karoly, The steady linear response of a spherical atmosphere to thermal and orographic forcing, *J. Atmos. Sci.* **38**, 1179 (1981).

- [61] A. Ibbetson and D. J. Tritton, Experiments on turbulence in a rotating fluid, *J. Fluid Mech.* **68**, 639 (1975).
- [62] H. Itoh and M. Kimoto, Multiple attractors and chaotic itinerancy in a quasi-geostrophic model with realistic topography: implications for weather regimes and low-frequency variability, *J. Atmos. Sci.* **53**, 2217 (1996).
- [63] P. R. Jonas, Laboratory observations of the effects of topography on baroclinic instability, *Quart. J. Roy. Meteor. Soc.* **107**, 775 (1981).
- [64] E. Kalnay-Rivas and L.-O. Merkin, A simple mechanism for blocking, *J. Atmos. Sci.* **38**, 2077 (1981).
- [65] C. F. F. Karney, Long-time correlations in the stochastic regime, *Physica D* **8**, 360 (1983).
- [66] J. Klafter, A. Blumen, M. F. Shlesinger, Stochastic pathway to anomalous diffusion, *Phys. Rev. A* **35**, 3081 (1987).
- [67] J. Klafter and G. Zumofen, Lévy Statistics in a Hamiltonian System, *Phys. Rev. E* **49**, 4873 (1994).
- [68] J. Klafter, M. F. Shlesinger, G. Zumofen, Beyond Brownian motion, *Physics Today* **49**, 33 (Feb. 1996).
- [69] R. H. Kraichnan, Inertial ranges in two-dimensional turbulence, *Phys. Fluids* **10**, 1417 (1967).
- [70] D. Kupperman, private communication (1997).
- [71] N.-C. Lau and M. J. Nath, Frequency dependence of the structure and temporal development of wintertime tropospheric fluctuations—Comparison of a GCM simulation with observations, *Mon. Wea. Rev.* **115**, 251 (1987).

- [72] B. Legras and M. Ghil, Persistent anomalies, blocking and variations in atmospheric predictability, *J. Atmos. Sci.* **42**, 433 (1985).
- [73] M. Lesieur, *Turbulence in Fluids*, 2nd ed. (Kluwer Academic Publishers, Boston, 1990).
- [74] G.-Q. Li, R. Kung, R. L. Pfeffer, An experimental study of baroclinic flows with and without two-wave bottom topography, *J. Atmos. Sci.* **43**, 2585 (1986).
- [75] E. N. Lorenz, *The Nature and Theory of the General Circulation of the Atmosphere* (World Meteorological Organization, Geneva, 1967).
- [76] B. B. Mandelbrot and J. W. Van Ness, Fractional Brownian motions, fractional noises and applications, *SIAM Review* **10**, 422 (1968).
- [77] P. Marcus, Numerical simulation of Jupiter's Great Red Spot, *Nature* **331**, 693 (1988).
- [78] P. S. Marcus, J. Sommeria, S. D. Meyers, H. L. Swinney, Models of the Great Red Spot, *Nature* **343**, 517 (1990).
- [79] S. L. Marcus, M. Ghil, J. O. Dickey, The extratropical 40-day oscillation in the UCLA general circulation model. Part II: Spatial structure, *J. Atmos. Sci.* **53**, 1993 (1996).
- [80] P. S. Marcus and C. Lee, A model for eastward and westward jets in laboratory experiments and planetary atmospheres, preprint.
- [81] P. S. Marcus, private communication.
- [82] E. Marinari, G. Parisi, D. Ruelle, P. Windey, Random walk in a random environment and  $1/f$  noise, *Phys. Rev. Lett.* **50**, 1223 (1983).



- [83] A. D. McEwan, Angular momentum diffusion and the initiation of cyclones, *Nature* **260**, 126 (1976).
- [84] J. D. Meiss and E. Ott, Markov-tree model of intrinsic transport in Hamiltonian systems, *Phys. Rev. Lett.* **55**, 2741 (1985).
- [85] J. D. Meiss and E. Ott, Markov tree model of transport in area-preserving maps, *Physica D* **20**, 387 (1986).
- [86] S. D. Meyers, J. Sommeria, H. L. Swinney, Laboratory study of the dynamics of jovian-type vortices, *Physica D* **37**, 515 (1989).
- [87] S. D. Meyers and H. L. Swinney, A laboratory study of planetary-type jets in a rotating annulus, in *Nonlinear Structures in Physical Systems*, eds. L. Lam and H. C. Morris (Springer, New York, 1990), 168-172.
- [88] S. D. Meyers, Laboratory studies of coherent structures in quasi-geostrophic flows, Ph.D. thesis, University of Texas at Austin (1990).
- [89] I. Mezic and S. Wiggins, On the dynamical origin of asymptotic  $t^2$  dispersion of a nondiffusive tracer in incompressible laminar flows, *Phys. Fluids* **6**, 2227 (1994).
- [90] E. E. Michaelides, Review—The transient equation of motion for particles, bubbles, and droplets, *J. Fluid Eng.* **119**, 233 (1997).
- [91] F. Molteni and T. N. Palmer, Predictability and finite-time instability of the northern winter circulation, *Quart. J. Roy. Meteor. Soc.* **119**, 269 (1993).
- [92] E. W. Montroll and M. F. Shlesinger, in *Nonequilibrium Phenomena II: From Stochastics to Hydrodynamics*, *Studies in Statistical Mechanics*, Vol. II, eds. J. L. Lebowitz and E. W. Montroll (North-Holland, Amsterdam, 1984), 1-119.

- [93] M. Nelkin, Universality and scaling in fully developed turbulence, *Advances in Physics* **43**, 143 (1994).
- [94] E. A. Novikov, Vortical scales for two- and three-dimensional turbulence, *Phys. Rev. E* **49**, R975 (1994).
- [95] J. F. O'Connor, The weather and circulation of January 1963 — One of the most severe months on record in the United States and Europe, *Mon. Wea. Rev.* **91**, 209 (1963).
- [96] A. R. Osborne, A. D. Kirwan, Jr., A. Provenzale, L. Bergamasco, Fractal drifter trajectories in the Kuroshio extension, *Tellus* **41A** 416 (1989).
- [97] A. Ott, J. P. Bouchaud, D. Langevin, W. Urbach, Anomalous diffusion in “living polymers”: A genuine Lévy flight?, *Phys. Rev. Lett.* **65**, 2201 (1990).
- [98] J. M. Ottino, Mixing, chaotic advection, and turbulence, *Ann. Rev. Fluid Mech.* **22**, 207 (1990).
- [99] T. N. Palmer, Extended-range prediction and the Lorenz model, *Bull. Amer. Meteorol. Soc.* **74**, 49 (1993).
- [100] L. Panetta, private communication (1996).
- [101] J. Pedlosky, Resonant topographic waves in barotropic and baroclinic flows, *J. Atmos. Sci.* **38**, 2626 (1981).
- [102] J. Pedlosky, *Geophysical Fluid Dynamics*, 2nd ed. (Springer-Verlag, New York, 1987).
- [103] J. P. Peixoto, B. Saltzman, S. Teweles, Harmonic analysis of the topography along parallels of the earth, *J. Geophys. Res.* **69**, 1501 (1964).

- [104] M. S. Pervez and T. H. Solomon, Long-term tracking of neutrally buoyant tracer particles in two-dimensional fluid flows, *Exp. Fluids* **17**, 135 (1994).
- [105] B. A. Petrovichev, A. V. Rogal'sky, R. Z. Sagdeev, G. M. Zaslavsky, Stochastic jets and nonhomogeneous transport in Lagrangian turbulence, *Phys. Lett. A* **150**, 391 (1990).
- [106] G. Petschel and T. Geisel, Unusual manifold structure and anomalous diffusion in a Hamiltonian model for chaotic guiding-center motion, *Phys. Rev. A* **44**, 7959 (1991).
- [107] R. L. Pfeffer, J. Ahlquist, R. Kung, Y. Chang, G. Li, A study of baroclinic wave behavior over bottom topography using complex principle component analysis of experimental data, *J. Atmos. Sci.* **47**, 67 (1990).
- [108] R. L. Pfeffer, R. Kung, W. Ding, G.-Q. Li, Barotropic flow over bottom topography—experiments and nonlinear theory, *Dynamics of Atmospheres and Oceans* **19**, 101 (1993).
- [109] G. Pfister and H. Scher, Dispersive (non-Gaussian) transient transport in disordered solids, *Adv. Phys.* **27**, 747 (1978).
- [110] J. M. Pratte and J. E. Hart, Experiments on periodically forced flow over topography in a rotating fluid, *J. Fluid Mech.* **229**, 87 (1991).
- [111] A. Polyakov, The theory of turbulence in two dimensions, *Nucl. Phys. B* **396**, 367 (1993).
- [112] W. H. Press, S. A. Teukolsky, W. T. Vetterling, B. P. Flannery, *Numerical Recipes in C: The Art of Scientific Computer*, 2nd ed. (Cambridge University Press, New York, 1992).

- [113] R. Ramshankar, D. Berlin, J. P. Gollub, Transport by capillary waves. Part I. Particle trajectories, *Phys. Fluids A* **2**, 1955 (1990).
- [114] R. Ramshankar and J. P. Gollub, Transport by capillary waves. Part II: Scalar dispersion and structure of the concentration field, *Phys. Fluids A* **3**, 1344 (1991).
- [115] J. Reichel et al., Raman cooling of cesium below 3 nK: New approach inspired by Lévy flight statistics, *Phys. Rev. Lett.* **75**, 4575 (1995).
- [116] B. B. Reinhold and R. P. Pierrehumbert, Dynamics of weather regimes: Quasi-stationary waves and blocking, *Mon. Wea. Rev.* **110**, 1105 (1982).
- [117] D. F. Rex, Blocking action in the middle troposphere and its effect upon regional climate: I. An aerological study of blocking action, *Tellus* **2**, 196 (1950).
- [118] D. F. Rex, Blocking action in the middle troposphere and its effect upon regional climate: II. The climatology of blocking action, *Tellus* **2**, 275 (1950).
- [119] P. B. Rhines, Waves and turbulence on a  $\beta$ -plane, *J. Fluid Mech.* **69**, 417 (1975).
- [120] L. F. Richardson, Atmospheric diffusion shown on a distance-neighbour graph, *Proc. Roy. Soc. (London) Ser. A* **110**, 709 (1926).
- [121] M. A. Rizk and S. E. Elghobashi, The motion of a spherical particle suspended in a turbulent flow near a plane wall, *Phys. Fluids* **28**, 806 (1985).
- [122] C.-G. Rossby and collaborators, Relation between variations in the intensity of the zonal circulation of the atmosphere and the displacements of the semi-permanent centers of action, *J. Marine Res.* **2**, 38 (1939).
- [123] H. Scher and E. W. Montroll, Anomalous transit-time dispersion in amorphous solids, *Phys. Rev. B* **12**, 2455 (1975).

- [124] M. F. Shlesinger, Asymptotic solutions of continuous-time random walks, *J. Stat. Phys.* **10**, 421 (1974).
- [125] M. F. Shlesinger and J. Klafter, Lévy walk representations of dynamics processes, in: *Perspectives in Nonlinear Dynamics*, eds. M. F. Shlesinger, R. Cawley, A. W. Saenz and W. Zachary (World, Singapore, 1986) pp. 336-349.
- [126] M. F. Shlesinger, G. M. Zaslavsky, J. Klafter, Strange kinetics, *Nature* **363**, 31 (1993).
- [127] M. F. Shlesinger, Comment on “Stochastic process with ultraslow convergence to a Gaussian: The truncated Lévy flight”, *Phys. Rev. Lett.* **74**, 4959 (1995).
- [128] Ya. G. Sinai, The limiting behavior of a one-dimensional random walk in a random medium, *Theo. Prob. Appl.* **27**, 256 (1982).
- [129] L. M. Smith, J. R. Chasnov, F. Waleffe, Crossover from two- to three-dimensional turbulence, *Phys. Rev. Lett.* **77**, 2467 (1996).
- [130] T. H. Solomon and J. P. Gollub, Passive transport in steady Rayleigh-Bénard convection, *Phys. Fluids* **31**, 1372 (1988).
- [131] T. H. Solomon, W. J. Holloway, H. L. Swinney, Shear flow instabilities and Rossby waves in barotropic flow in a rotating annulus, *Phys. Fluids A* **5**, 1971 (1993).
- [132] T. H. Solomon, E. R. Weeks, H. L. Swinney, Observation of anomalous diffusion and Lévy flights in a two-dimensional rotating flow, *Phys. Rev. Lett.* **71**, 3975 (1993).
- [133] T. H. Solomon, E. R. Weeks, H. L. Swinney, Chaotic advection in a two-dimensional flow: Lévy flights and anomalous diffusion, *Physica D* **76**, 70 (1994).

- [134] T. H. Solomon, private communication (1996); the counter-rotating locking case was also briefly experimentally examined by the author, and appeared to be a coincidence of similar rotation rates rather than a true “locking.” See also Ref. [80].
- [135] E. F. C. Somerscales, Fluid velocity measurement by particle tracking, in *Flow: Its Measurement and Control in Science and Industry*, vol. 1, ed. R. E. Wendt, Jr. (ISA, Pittsburgh, 1974) 795-808.
- [136] J. Sommeria, S. D. Meyers, H. L. Swinney, A laboratory simulation of Jupiter’s Great Red Spot, *Nature* **331**, 374 (1988).
- [137] J. Sommeria, S. D. Meyers, H. L. Swinney, Laboratory model of a planetary eastward jet, *Nature* **337**, 58 (1989).
- [138] J. Sommeria, S. D. Meyers, H. L. Swinney, Experiments on vortices and Rossby waves in eastward and westward jets, in *Nonlinear Topics in Ocean Physics*, ed. A. Osborne (North-Holland, Amsterdam, 1991), pp. 227-269.
- [139] K. R. Sreenivasan and R. A. Antonia, The phenomenology of small-scale turbulence, *Ann. Rev. Fluid Mech.* **29**, 435 (1997).
- [140] C. M. Strong, F.-f. Jin, M. Ghil, Intraseasonal oscillations in a barotropic model with annual cycle, and their predicatability, *J. Atmos. Sci.* **52**, 2627 (1995).
- [141] Y. Takeda, Velocity profile measurement by ultrasound Doppler shift method, *Int. J. Heat Fluid Flow* **7**, 313 (1986).
- [142] Y. Takeda, Measurement of velocity profile of mercury flow by ultrasound Doppler shift method, *Nuclear Technology* **79**, 120 (1987).

- [143] Y. Takeda, Development of an ultrasound velocity profile monitor, *Nuclear Engineering and Design* **126**, 277 (1991).
- [144] G. I. Taylor, Diffusion by continuous movements, *Proc. Lon. Math. Soc.* **2** **20**, 196 (1921).
- [145] G. I. Taylor, Experiments on the motion of solid bodies in rotating fluids, *Proc. Roy. Soc. A* **104**, 213 (1923).
- [146] Y. Tian, M.S. thesis, University of California, Los Angeles (1997). Y. Tian et al., in preparation.
- [147] Y. Tian, personal communication (1997).
- [148] M. S. Tracton et al., Dynamical extended range forecasting (DERF) at the National Meteorological Center, *Mon. Wea. Rev.* **117**, 1604 (1989).
- [149] D. J. Tritton, Experiments on turbulence in geophysical fluid dynamics, in *Turbulence and Predictability in Geophysical Fluid Dynamics* (Soc. Italiana di Fisica, Bologna, Italy, 1985) pp. 171–192.
- [150] D. J. Tritton, *Physical Fluid Dynamics*, 2nd ed. (Oxford University Press, New York, 1988).
- [151] L. Tsimring, private communication (1997).
- [152] J. M. Wallace and M. L. Blackmon, in *Large-Scale Dynamical Processes in the Atmosphere*, eds. B. J. Hoskins and R. P. Pearce (Academic Press, London, 1983) pp. 55-94.
- [153] X.-J. Wang, Dynamical sporadicity and anomalous diffusion in the Lévy motion, *Phys. Rev. A* **45**, 8407 (1992).

- [154] E. R. Weeks, T. H. Solomon, J. S. Urbach, H. L. Swinney, Observation of Anomalous Diffusion and Lévy Flights, in: *Lévy Flights and Related Topics in Physics*, eds. M. F. Shlesinger, G. M. Zaslavsky and U. Frisch (Springer-Verlag, Heidelberg, 1995) pp. 51-71.
- [155] E. R. Weeks, J. S. Urbach, H. L. Swinney, Anomalous diffusion in asymmetric random walks with a quasi-geostrophic flow example, *Physica D* **97**, 219 (1996).
- [156] E. R. Weeks and J. M. Burgess, Evolving artificial neural networks to control chaotic systems, *Phys. Rev. E* **56**, 1531 (1997).
- [157] E. R. Weeks et al., Transitions between blocked and zonal flows in a rotating annulus with topography, submitted to *Science* (1997).
- [158] E. R. Weeks and H. L. Swinney, Anomalous diffusion resulting from strongly asymmetric random walks, in preparation.
- [159] J. B. Weiss and E. Knobloch, Mass transport and mixing by modulated traveling waves, *Phys. Rev. A* **40**, 2579 (1989).
- [160] J. B. Weiss and J. C. McWilliams, Temporal scaling behavior of decaying two-dimensional turbulence, *Phys. Fluids A* **5**, 608 (1993).
- [161] B. S. Williams, D. Marteau, J. P. Gollub, Mixing of a passive scalar in magnetically forced two-dimensional turbulence, *Phys. Fluids* **9**, 2061 (1997).
- [162] A. Wolf, S. J. Van Hook, E. R. Weeks, Why electric field line diagrams don't work, *Am. J. of Phys.*, **64**, 714 (1996).
- [163] P. Wu, Nonlinear resonance and instability of planetary waves and low-frequency variability in the atmosphere, *J. Atmos. Sci.* **50**, 3590 (1993).
- [164] X-L. Wu, B. Martin, H. Kellay, W. I. Goldburg, Hydrodynamic convection in a two-dimensional couette cell, *Phys. Rev. Lett.* **75**, 236 (1995).



- [165] W. Young, A. Pumir, Y. Pomeau, Anomalous diffusion of tracer in convection rolls, *Phys. Fluids A* **1**, 462 (1989).
- [166] G. M. Zaslavsky, D. Stevens, H. Weitzner, Self-similar transport in incomplete chaos, *Phys. Rev. E* **48**, 1683 (1993).
- [167] G. M. Zaslavsky, Fractional kinetic equation for Hamiltonian chaos, *Physica D* **76**, 110 (1994).
- [168] Data from the NOAA Climate Analysis Center.
- [169] NCAR/NCEP reanalysis data provided through NOAA Climate Diagnostics Center.

# Vita

Eric Richard Weeks was born in Hinsdale, Illinois, on May 19, 1970. He is the son of Mary Elizabeth Weeks and Richard William Weeks II. He graduated from Downers Grove South High School in Downers Grove, IL, in the spring of 1988, and received a B.S. degree in engineering physics from the University of Illinois Urbana-Champaign in the spring of 1992. He enrolled at the University of Texas at Austin in the fall of 1992 to begin research for a Ph.D. in physics.

Permanent Address: 13743 Janas Pkwy  
Lockport, IL 60441

This dissertation was typeset with  $\text{\LaTeX} 2_{\epsilon}^3$  by the author.

---

<sup>3</sup> $\text{\LaTeX} 2_{\epsilon}$  is an extension of  $\text{\LaTeX}$ .  $\text{\LaTeX}$  is a collection of macros for  $\text{\TeX}$ .  $\text{\TeX}$  is a trademark of the American Mathematical Society. The macros used in formatting this dissertation were written by Dinesh Das, Department of Computer Sciences, The University of Texas at Austin.